

Study of Ozone and other Trace Gases Distribution in the Lower Atmosphere

Thesis Submitted for the Degree of

Doctor of Philosophy

In

Physics

To

Kumaun University, Nainital (India)

By

Narendra Ojha

Aryabhatta Research Institute of Observational Sciences (ARIES)

Manora Peak, Nainital, 263002, Uttarakhand, India

May 2013

DECLARATION

I hereby declare that the work presented in this thesis is a result of investigations carried out by me at the Aryabhata Research Institute of observational sciences (ARIES), Nainital, under the joint supervision of Dr. Manish Naja (ARIES, Nainital) and Prof. H. C. Chandola (Department of Physics, Kumaun University, Nainital). This thesis work has not been submitted for the award of any degree, diploma, associateship or fellowship of any University or Institute.

Place: Nainital

Date: May 2013

Narendra Ojha
27-5-2013

(Narendra Ojha)

CERTIFICATE FROM THE SUPERVISORS

This is to certify that

1. The synopsis of the present thesis entitled “**Study of Ozone and other Trace Gases Distribution in the Lower Atmosphere**” for award of the degree of Doctor of Philosophy in Physics has duly been approved by the Kumaun University, Nainital (Letter no.-Shodh/Physics/2011, dated 12/11/2011).
2. The thesis embodies the work of Mr. Narendra Ojha himself.
3. Mr. Narendra Ojha worked under our joint supervisions for this thesis as a Research Fellow at the Aryabhata Research Institute of Observational Sciences (ARIES), Nainital. He has put in more than 200 days of attendance at ARIES, Nainital during this period.
4. The thesis has not been submitted before for the award of any degree, diploma, associateship or fellowship of any University or Institute.

Manish Naja
27.5.13
Dr. Manish Naja

ARIES, Manora Peak,
Nainital

H. C. Chandola
27/5/2013

Prof. H. C. Chandola,
Department of Physics,
Kumaun University, Nainital

Madan
31/6/13
Head & Convener
BOS/RDG Physics Deptt.
Kumaun University,
NAINITAL (U.K.) 263001

Dedicated to
My
Loving Parents and Teachers

Acknowledgements

I take this opportunity to express my gratitude and deep respect to Dr. Manish Naja for invaluable guidance, continuous encouragement, fruitful discussions and support during the entire period of this work. His suggestions and discussions have benefited me throughout my research work at ARIES. His encouragement to work with new ideas always played a crucial role in my research. I consider it very fortunate to have worked with him and will always be indebted to him.

I express my sincere thanks to Prof. H. C. Chandola, Department of Physics, Kumaun University, for guidance and continuous encouragements and for all the academic and administrative support.

I am deeply grateful to Prof. Ram Sagar, Director, ARIES for his positive outlook, encouragements and invaluable support in establishing various observational facilities. I am highly thankful to Prof. Shyam Lal, PRL, Ahmedabad for his wholehearted support in initiating various observations, fruitful discussions and constructive suggestions. A special thank to S. Venkataramani, PRL, Ahmedabad for his guidance in learning different observational techniques, particularly related with the balloon-borne experiments. I would like to thank Late Dr. P. Pant for encouragements and fruitful discussions during my research work.

I am indebted to Dr. Rajesh Kumar for selfless help, consistent encouragements and personal interest in the progress of my work. He, as a senior and friend, always stood beside me during my hard times, without any invitation. My special thanks to

Dr. Narendra Singh and Tapaswini for fruitful discussions, wonderful company, encouragement and support during this period.

I would like to express my sincere thanks to Drs. K. P. Singh, G. B. Pant University, Pantnagar and Yogesh Kant, IIRS, Dehradun for their support in making the measurements at Pantnagar and Dehradun. I also owe my thanks to Drs. Hitoshi Mukai, T. Machida and A. Sunaga for their efforts in making measurements of greenhouse gases. It gives me immense pleasure to thank Dr. P. P. N. Rao and Dr. C. B. S. Dutt, ISRO GBP ATCTM project for their valuable advice and information. I thank all the colleagues and collaborators under the ISRO GBP ATCTM program for various fruitful discussions.

I am thankful to the Academic Committee, all the faculty members and staff of ARIES, who directly or indirectly helped me, during the course of this work. I gratefully acknowledge the valuable support from Computer section, Engineering staff, and Library staff of ARIES.

I accord my thanks to G. P. Brasseur, Michael Newchurch, D. D. Parrish, Hongyu Liu, Mark Lawrence, Tim Butler, Hartwig Harder, Prabir Patra, Daniel Jacob and Vinayak Sinha for various fruitful discussions and constructive feedback on my thesis work during various conferences and meetings. The critical efforts made by the science team members of various satellite based instruments e.g. MODIS, MOPITT, AIRS, TES, OMI, TRMM and AATSR are highly acknowledged. I acknowledge the use of various models such as WRF-Chem, NCARMM, MATCH-MPIC, MOZART and an air-trajectory model (HYSPLIT).

I express my sincere thanks to Ashish Kumar, Kalpana Pandey, Manav Kumar, Manjul Mungali, Deepak Chausali for their help in the operation and maintenance of various instruments. I am also grateful to Bareilly ATC for their constant support in giving permissions for carrying out our balloon flights at ARIES.

I am deeply thankful to all my teachers in University of Allahabad, who taught me basic courses of Physics and motivated me towards research, particularly, Prof. Avinash Chandra Pandey, Prof. Ranjana Prakash, Dr. Suneet Dwivedi and Dr. Vivek Tiwari.

I would like to thank Ram Kesh, Brajesh and Bindu Rani, my batch mates at ARIES for their wonderful company. I express my heartfelt thanks to my friends and colleagues at ARIES Jay Shreekar, Sanjit Sahu, Dr. Saurabh, Dr. Abhishek Srivastava, Abhishek Sharma, T. S. Kumar, Samaresh, Jai Bhagwan, Piyush, Pradeep, Raman, Krishna Reddy, Ravi, Krishna Shukla, Rupak, Eswar, Sumana, Manash, Amitava for their wonderful company. I acknowledge my friends in PRL, Ahmedabad Chinmay, Shuchita, Arun, Naveen and Sharad for making my stay at PRL pleasant with their company. I would like to acknowledge my close friends Akhil, Abhishek and Romil for their consistent encouragement, support and helpful attitude during my study carrier.

Last but not the least, I express my gratefulness and heartiest regards towards my parents, who always encouraged me during my study carrier. I am grateful to my brother Arvind, sister Sneha, Jija Ji Shri Virendra Pathak for moral support and care. I thank all my relatives and family friends for their support.

Preface

Ozone and other trace gases play key roles in the air quality, atmospheric chemistry and climate change. However, studies of trace gases budget and their contributions to aforementioned processes are not well understood mainly due to lack of sufficient measurements, particularly in the tropics. The existing knowledge on the distribution of trace gases and their controlling processes is presented in the **Chapter 1** of the thesis. Satellite and model studies revealed the elevated levels of ozone and other pollutants over the Indo-Gangetic Plain (IGP) in the Northern India. However, due to lack of in-situ measurements, the understanding of underlying physical, chemical and dynamical processes is rather poor. In view of this, weekly balloon flights have been conducted to measure vertical distribution of ozone (EN-SCI 2ZV7 ECC Ozonesonde) and meteorological parameters (iMet-1-RSB 403 MHz GPS Radiosonde) from a high altitude site Nainital (79.5°E, 29.4°N, 1958 m amsl) in the central Himalayas since January 2011. Additionally, surface ozone is measured at Pantnagar (79.5°E, 29.0°N, 231 m amsl) in the IGP region since 2009. Weekly air samples are also collected at Nainital for analysis of CO and greenhouse gases CO₂ and CH₄ in collaboration with NIES, Japan. Few samples are also collected at Pantnagar and analyzed for CO and CH₄ in collaboration with PRL, Ahmedabad. A chemical box model (NCAR Master Mechanism), a regional chemistry transport model (WRF-Chem) and data from global models (MATCH-MPIC and MOZART) are used to understand the observed variabilities. The detailed descriptions of the observational techniques, satellite datasets and models used in the thesis are discussed in the **Chapter 2**.

The analysis of surface ozone observations at Pantnagar in the IGP region is presented in **Chapter 3**. Surface ozone at Pantnagar shows daytime build-up with levels sometimes as high as 100 ppbv. Ozone seasonal variations exhibit highest levels during spring (39.3 ± 18.9 ppbv in May) and lower levels in summer-monsoon (16.8 ± 8.9 ppbv in August) and winter (10.8 ± 12.1 ppbv in January). This ozone seasonality is in agreement with the meteorological parameters and satellite observations of tropospheric NO_2 and CO (681 hPa). A global model (MATCH-MPIC) captures the seasonality but overestimates the ozone levels. Model simulated daytime $\text{H}_2\text{O}_2/\text{HNO}_3$ values are higher indicating NO_x -limited chemistry over this region. Box model simulations are used to corroborate this and to estimate integrated net ozone production in a day (72.9 ppbv). Strong positive correlation ($r^2 = 0.96$ in May) between the daytime ozone at IGP and nearby Himalayan site suggests transport of pollution from IGP to the cleaner Himalayas via the boundary layer evolution. Estimated 3-monthly AOT40 index, using the observed ozone data, poses threat for vegetations in the IGP region.

The seasonal variations in the vertical distribution of ozone and meteorological parameters obtained from balloon-borne observations are presented in **Chapter 4**. Tropopause pressure from radiosonde observations agrees with the satellites (AIRS and TES) and model results, but shows dramatic variability (150-250 hPa) during winter and early spring. Lower tropospheric (2-6 km amsl) ozone shows a prominent seasonality with spring maxima and summer-monsoon minima, which is consistent with the surface observations. A comparison of ozonesonde profiles with collocated satellite (TES) retrievals shows reasonable agreement. Tropospheric column ozone (TCO) from the ozonesonde observations shows a typical seasonality comprising of spring maxima (47.2 ± 9.8 DU) and winter minima (30.4 ± 10.1 DU).

The balloon-borne observations are used to investigate the influences of dynamical processes and biomass burning on the ozone distribution and are presented in **Chapter 5**. Springtime ozone profiles are classified into high and low fire activity periods using MODIS fire counts. Ozone levels during high fire activity periods are observed to be higher by 19.9 ± 4.6 ppbv in 2-4 km altitude range, as compared with low fire activity period. Signature of ozone downward transport, noticed during winter, is corroborated with observed reduction in relative humidity (radiosonde and AIRS satellite) and enhancement in potential vorticity (WRF). However, model simulated ozone profiles discern enhancements at lower altitudes than observations.

The analysis of long-term CO_2 , CH_4 and CO data obtained from the samples collected at Nainital during September 2006-December 2011 is presented in **Chapter 6**. CO_2 shows a prominent seasonality over Nainital with the spring maximum (395.9 ± 5.9 ppm in May) and post-monsoon/autumn minimum (374.4 ± 5.8 ppm in October). CO_2 seasonal cycle at Nainital is similar to that at Mauna Loa, however, the seasonal amplitude in CO_2 is much larger at Nainital (~ 21.5 ppm) as compared with Mauna Loa (~ 6.5 ppm). Long-term trends in CO_2 , CH_4 and CO have been investigated by deseasonalizing the time series and a linear regression fit. The estimated trend in CO_2 over Nainital (1.88 ppm per year) is consistent with the trends over Mauna Loa (1.60 to 2.43 ppm per year) and global marine observations (1.64 to 2.40 ppm per year). CH_4 levels discern a small positive trend of 4 ppb per year, while, CO levels show a negative trend of 7.3 ppb per year. A summary of the thesis along with its future scope is presented in the **Chapter 7**.

List of Publications

1. Nishanth, T., **N. Ojha**, M.K.S. Kumar, and M. Naja, Influence of solar eclipse of 15 January 2010 on surface ozone, *Atmospheric Environment*, 45, 1752-1758, 2011.
2. Kumar, R., M. Naja, S. K. Satheesh, **N. Ojha**, H. Joshi, T. Sarangi et al., Influences of the springtime Northern Indian Biomass Burning over the central Himalayas, *J. Geophys. Res.*, 116, D19302, doi: 10.1029/2010JD015509, 2011.
3. **Ojha, N.**, M. Naja, K. P. Singh, T. Sarangi, R. Kumar, S. Lal, M. G. Lawrence, T. M. Butler and H. C. Chandola, Variabilities in ozone at a semi-urban site in the Indo-Gangetic Plain region: Association with the meteorology and regional processes, *J. Geophys. Res.*, 117, D20301, doi: 10.1029/2012JD017716, 2012.
4. Girach, I. A., P. R. Nair, L. M. David, P. Hegde, M. K. Mishra, G. M. Kumar, S. M. Das, **N. Ojha** and M. Naja, The changes in near-surface ozone and precursors at two nearby tropical sites during annular solar eclipse of 15 January 2010, *J. Geophys. Res.*, 117, D01303, doi: 10.1029/2011JD016521, 2012.
5. Reddy, K. K., M. Naja, **N. Ojha**, P. Mahesh and S. Lal, Influences of the Boundary Layer Evolution on Surface Ozone Variations at a Tropical Rural Site in India, *Journal of Earth System Science*, 121, No. 4, August 2012, pp. 911-922, 2012.
6. Sarangi, T., M. Naja, K. P. Singh, Y. Kant, **N. Ojha**, R. Kumar, K. Pandey, S. Venkataramani, S. Lal and Ram Sagar, Observations of radiatively and chemically active trace gases in the central Himalaya and Indo-Gangetic Plain region, *Climate change in the Himalayas*, Editors- Vir Singh et al., ISBN 978-81-7387-228-0, pp. 61-74, 2011.
7. Sarangi T., M. Naja, **N. Ojha**, R. Kumar, S. Lal, S. Venkataramani, A. Kumar, H. C. Chandola and R. Sagar, First simultaneous measurements of ozone, CO and NOy at a

high altitude regional representative site in the central Himalayas, for revised submission to *J. Geophys. Res.*, 2012JD019373, 2013.

8. Sarangi, T., M. Naja, **N. Ojha**, R. Kumar, S. Lal and H. C. Chandola, Variability in Meteorological Parameters and Trace Gases over the Central Himalayas: Observations and Model Simulations, Under Review in *Vayumandal Journal*, 2013.
9. Mallik, C., S. Lal, S. Venkaramani, M. Naja, **N. Ojha**, Variability in ozone and its precursors over the Bay of Bengal during post-monsoon: Transport and emission effects, (revised version to be submitted to *J. Geophys. Res.*, 2013.
10. **Ojha, N.**, M. Naja, R. Kumar, T. Sarangi, S. Lal, S. Venkataramani, R. Sagar, A. Kumar and H. C. Chandola, On the Processes Influencing the Vertical distribution of ozone over the central Himalayas, to be submitted, *J. Geophys. Res.*, 2013.

List of Acronyms and Abbreviations

AATSR	Advanced Along Track Scanning Radiometer
AGL	Above Ground Level
AIRS	Atmospheric Infrared Sounder
AOT40	Accumulated Ozone Exposure above a threshold of 40 ppbv
ARW	Advance Research WRF
DU	Dobson Unit
ECC	Electrochemical Concentration Cell
EOS	Earth Observing System
FID	Flame Ionization Detector
FTIR	Fourier Transfer Infrared Spectrometer
GC	Gas Chromatograph
GDAS	Global Data Assimilation System
GFS	Global Forecasting System
GPS	Global Positioning System
HFAP	High Fire Activity Period
HYSPLIT	Hybrid Single Particle Integrated Trajectory Model
IGP	Indo-Gangetic Plain
IGY	International Geophysical Year
IMD	Indian Meteorological Department
INDOEX	Indian Ocean Experiment
INTEX-B	Intercontinental Chemical Transport Experiment–Phase B
LFAP	Low Fire Activity Period
LIDAR	Light Detection and Ranging

LLGHGs	Long-Lived Greenhouse Gases
MATCH- MPIC	Model of Atmospheric Transport and Chemistry-Max Planck Institute for Chemistry
MLS	Microwave Limb Sounder
MODIS	Moderate Resolution Imaging Spectroradiometer
MOZAIC	Measurements of Ozone and water vapor by Airbus In-Service aircraft
MOZART	Model for Ozone and Related chemical Tracers
NCEP	National Centre for Environmental Prediction
NDIR	Non Dispersive Infrared
NH	Northern Hemisphere
NIES	National Institute for Environmental Studies
NMHCs	Non-Methane Hydrocarbons
NMVOCs	Non-Methane Volatile Organic Compounds
NOAA	National Oceanic and Atmospheric Administration
OMI	Ozone Monitoring Instrument
PV	Potential Vorticity
PR	Precipitation Radar
RACM	Regional Atmospheric Chemical Mechanism
REAS	Regional Emission Inventory for Asia
RF	Radiative Forcing
RH	Relative Humidity
STE	Stratosphere-Troposphere Exchange
TCO	Tropospheric Column Ozone
TES	Tropospheric Emission Spectrometer

TKE	Turbulent Kinetic Energy
TMI	TRMM Microwave Imager
TOMS	Total Ozone Mapping Spectrometer
TRMM	Tropical Rainfall Measuring Mission
TUV	Tropospheric Ultraviolet Visible
UTLS	Upper Troposphere Lower Stratosphere
UV	Ultra Violet
VIRS	Visible and IR Radio System
WHO	World Health Organization
WPS	WRF Pre-processing System
WMO	World Meteorological Organization
WRF	Weather Research and Forecast
WRF-Chem	Weather Research and Forecast with Chemistry

Contents

Chapter 1: Introduction.....1

1.1.	Importance of Tropospheric Ozone.....	4
1.1.1.	Role in Global warming.....	4
1.1.2.	Effects on Human Health and Vegetations.....	6
1.1.3.	Oxidation Capacity of the Atmosphere.....	8
1.2.	Sources and Sinks of Tropospheric Ozone.....	9
1.2.2.	Photochemical Production and Loss.....	11
1.2.3.	Natural Source: Stratosphere-Troposphere Exchange (STE)	12
1.2.4.	Surface Deposition.....	14
1.2.5.	Budget of Tropospheric Ozone.....	15
1.3.	Long-Range Transport.....	17
1.4.	Long-Term Trends in Trace Gases.....	19
1.4.2.	Ozone.....	19
1.4.3.	CO ₂ and CH ₄	23
1.5.	Present Scenario over the Indian region.....	26
1.6.	Objectives and Outline of the Thesis.....	29

Chapter 2: Methodology.....33

2.1.	Surface Ozone.....	34
2.2.	Balloon-borne Measurements.....	38
2.2.1.	Radiosonde.....	42
2.2.2.	Ozonesonde.....	43
2.2.3.	Preparation of the Ozonesonde for Flight.....	44
2.2.3.1.	Advance Preparation.....	44
2.2.3.2.	Preparation on the day of Balloon Launch	45
2.3.	Air Sampling for CO ₂ , CO and CH ₄	46
2.4.	Satellite Data.....	47
2.4.1.	Tropospheric Emission Spectrometer (TES)	48
2.4.2.	Moderate Resolution Imaging Spectroradiometer (MODIS)	48
2.4.3.	Ozone Monitoring Instrument (OMI)	49
2.4.4.	Tropical Rainfall Measuring Mission (TRMM)	49

2.4.5.	Atmospheric Infrared Sounder (AIRS)	50
2.5.	Modeling the Atmospheric Processes	50
2.5.1.	Physical Processes.....	52
2.5.2.	Chemical Processes.....	53
2.5.3.	Dynamical Processes.....	54
2.6.	Models Used in the Study.....	55
2.6.1.	Back-Air Trajectories (HYSPLIT).....	55
2.6.2.	Chemical Box Model (NCAR-MM).....	56
2.6.3.	Regional Chemistry Transport Model (WRF-Chem).....	58
2.6.3.1.	The WRF Pre-processing System (WPS).....	59
2.6.3.2.	Types of Emissions used.....	60
2.6.3.3.	Model Physics.....	61
2.6.4.	Global Chemistry Transport Model (MATCH-MPIC).....	62
2.6.5.	Global Chemistry Transport Model (MOZART).....	63

Chapter 3: Surface Ozone Variations at Pantnagar in the Indo-Gangetic Plain.....65

3.1.	Observational site	66
3.1.1.	General Meteorology.....	68
3.2.	Diurnal Variations in Ozone.....	71
3.2.1.	Rate of change in Ozone.....	73
3.3.	Seasonal Variation in Ozone.....	76
3.3.1.	Correlation between Ozone and Mixing depth.....	80
3.4.	Comparison with observations at other sites in India.....	84
3.4.1.	Ozone at Pantnagar and Nainital.....	85
3.5.	Results from a Global Chemistry-Transport Model (MATCH-MPIC).....	87
3.5.1.	Variations in H ₂ O ₂ and HNO ₃ from MATCH-MPIC.....	92
3.6.	Photochemical Ozone Production Rate and Sensitivity to NMHCs and NO _x	95
3.7.	Impacts of Ozone Pollution on the Vegetations in IGP: Estimation of AOT40 index.....	99
3.8.	Summary and Conclusions.....	101

Chapter 4: Vertical distribution of Ozone and Meteorological Parameters over the central Himalayas.....104

4.1. Variations in the Meteorological Parameters.....108
4.1.1. Air Temperature and Relative Humidity.....108
4.1.2. Wind Speed and Wind Direction.....112
4.2. Estimation of Tropopause Pressure.....116
4.3. Vertical Distribution of ozone.....119
4.4. Comparison with the Satellite Data.....125
4.4.1. Collocation Criteria and Application of TES operator.....126
4.4.2. Comparison of the Vertical Profiles.....127
4.4.3. Tropospheric Column Ozone (TCO).....130
4.4.4. Correlation Analysis.....132
4.5. Summary and Conclusions.....134

Chapter 5: Influences of Dynamical processes and Biomass Burning on Ozone Distribution.....136

5.1. Stratosphere-Troposphere Exchange (STE).....137
5.1.1. Seasonal Variations in PV over Nainital.....138
5.1.2. STE Event on 17th February 2011.....140
5.1.2.1. Change in the Potential Vorticity.....141
5.1.2.2. Change in the Relative Humidity.....143
5.1.2.3. Back Air Trajectory.....146
5.1.2.4. Model Simulations.....148
5.2. Secondary Ozone Peaks.....154
5.3. Influence of Biomass Burning.....156
5.3.1. Seasonal Variation in Biomass Burning.....157
5.3.2. Classification of High and Low Fire Activity Periods158
5.4. Summary and Conclusions.....161

Chapter 6: Variations in CO₂, CH₄ and CO over the central Himalayas.....163

6.1. Seasonal Variations.....166
6.1.1. Seasonal Variation in CO₂.....166
6.1.1.1. Comparison with Mauna Loa and Global Marine Observations.....169
6.1.2. Seasonal Variation in CH₄.....170
6.1.3. Seasonal Variation in CO.....172
6.2. Long-Term Trends.....175
6.3. Inter-Species Correlation Analysis.....179
6.3.1. CO-CH₄ Correlations179
6.3.2. CO-CO₂ Correlations.....181
6.4. Summary and Conclusions.....184

Chapter 7: Summary and Future Scope.....186

7.1. Variations in surface Ozone at Pantnagar in the Indo-Gangetic Plain (IGP) region.....186
7.2. Vertical Distribution of Ozone and Meteorological Parameters over the central Himalayas.....189
7.3. Influences of Dynamical Processes and Biomass Burning on Ozone Distribution.....193
7.4. Variations in CO₂, CH₄ and CO over the central Himalayas.....195
7.5. Future Scope198

List of Figures

1.1: A summary of the global mean radiative forcing by major climate forcing agents estimated for year 2005 relative to the start of industrial era (adapted from *Forster et al.*, 2007). Tropospheric ozone is the third most important greenhouse gas after CO₂ and CH₄.

1.2: Response of agricultural crop yields of soybean, wheat, corn and rice with the increase in average ozone [*Adams et al.*, 1989; *Chameides et al.*, 1999].

1.3: A simplified layout of different processes controlling the tropospheric ozone.

1.4: The global photochemical production and loss of ozone simulated by the present day 21 global chemistry transport models for the year 2000. For description of the models, please see *Stevenson et al.* [2006].

1.5: Long term trends in seasonally averaged ozone levels at high altitude sites (~1.9 km) Lassen N. P. in Western North America and Mt. Happon in Japan (Figure is adapted from *Parrish et al.*, 2012).

1.6: Long-term trends in the atmospheric concentrations of long-lived greenhouse gases over the last 2000 years. This figure is obtained from *Forster et al.*, IPCC, [2007].

1.7: Climatological distribution of tropospheric ozone [*Fishman et al.*, 2003] over the India and Southeast Asia along with the distribution of population density.

2.1: A simplified block diagram showing the operating principle of surface ozone measurements using the UV absorption technique.

2.2: An example of responses of the ozone instrument during the zero and span tests carried out on 6 March 2011 at Nainital.

2.3: A strong positive correlation is observed between the simultaneous ozone observations from Thermo and Teledyne.

2.4: Balloon with ozonesonde and radiosonde during the ascent at ARIES, Nainital.

2.5: Ozonesonde, radiosonde, antenna and receiver coupled with the laptop via MODEM as used during the observations.

2.6: Layout of the balloon sounding experiments showing the measurement, data transmission and receiving system.

2.7: Time series of balloon launch times at ARIES, Nainital. In general, launch time was kept around 12 hour IST however; the changes in launch times are mainly due to unavailability of permissions from Air Traffic Controller, Bareilly.

2.8: Picture showing the pump, cooling unit and glass bottle connected to it, as used for collecting air samples at -30 °C.

2.9: A Layout showing various processes influencing the concentration of a species X in an atmospheric box.

3.1: (a) Topographical map of India with zoomed map of the northern India, (b) population density around the observation site, and (c) annual average CO emissions (INTEX-B) over India are shown. A belt of higher CO emissions, from the northern India to the eastern side, is the IGP region. Observation site Pantnagar (PNT) is marked with a black filled triangle, other sites used for comparison namely Delhi (DEL), Ahmedabad (AHM), Gadanki (GAD), Trivandrum (TVM) and Nainital (NTL) are marked with white filled circles.

3.2: Three days backward(1000 AGL) trajectories at Pantnagar for all days in January, April, July and October 2010 are shown. The trajectories are color coded, according to the atmospheric pressure along the trajectories, to portray the altitude range attained by the air masses before arriving at the observation site.

3.3: Seasonal variations in monthly total rainfall from TRMM (2009-2010), solar radiation (Wm^{-2}) and temperature from GDAS data (2009-2011) over Pantnagar.

3.4: Monthly average diurnal variation in ozone at Pantnagar from January to December during March 2009 to June 2011 period. Sunrise times in these months are also shown as dotted lines and total numbers of days for which observations are available in each month are mentioned in the upper right corner in each month plot.

3.5: (a) Average diurnal variations in ozone and (b) diurnal variation in rate of change of ozone (ppbv/hour) at Pantnagar along with those at Delhi [*Ghude et al.*, 2008], Ahmedabad [*Lal et al.*, 2000] and Gadanki [*Naja and Lal*, 2002].

3.6: Seasonal variations in monthly (24 hours), daily (24 hours), daytime (1130-1630 hours) and nighttime (0100-0300 hours) average ozone at Pantnagar. Monthly average ozone mixing ratios at a nearby high altitude site (Nainital) are also shown.

3.7: Seasonal variations in the tropospheric column ozone, tropospheric column NO_2 and CO at 681 hPa over Pantnagar.

3.8: (a) Average diurnal variations in mixing depth at Pantnagar during four different months (January, April, August and October) representing four seasons. Two additional months (May and June) are also shown. (b) Seasonal variations in the daily and monthly average mixing depth at Pantnagar. Mixing depth is obtained from GDAS data.

3.9: Correlation between daytime average ozone and the mixing depth at 1230 hour IST in different seasons at Pantnagar. Filled symbols are daytime average data and open symbols are binned average data for the respective season. The r^2 has been estimated for the binned average data points. In the binned average data points, one sigma horizontally spread is in the bins of 500 m mixing depth and one sigma vertical spread is in the associated ozone data.

3.10: Comparison of the observed monthly average ozone seasonal variations at Pantnagar (PNT) with the observations at other sites Nainital (NTL), Delhi (DEL), Gadanki (GAD) and Trivandrum (TVM) in India.

3.11: Correlation between ozone mixing ratios at Nainital and Pantnagar during afternoon hours (1130-1630 hours) and nighttime (01-03 hours) in May. Open symbols are binned average in 5 ppbv bins and error bars represent one-sigma spread in the binned data.

3.12: MATCH-MPIC simulated spatial distribution of surface ozone over the South Asian region, during four different months January, April, July and October representing four seasons, of the year 2010.

3.13: Comparison of the observed ozone seasonal variation at Pantnagar (PNT) with the results from MATCH-MPIC model. Seasonal variation in ozone, at a nearby high altitude site Nainital, is also shown. Upper range and lower range in grey shaded region is daytime and nighttime ozone data at Pantnagar, respectively.

3.14: Seasonal variations in CO from fossil fuel and biomass burning over Pantnagar simulated from MATCH-MPIC model.

3.15: MATCH-MPIC simulated variations in daytime (1130-1630 hours) H_2O_2 , HNO_3 and $\text{H}_2\text{O}_2/\text{HNO}_3$ ratios at Pantnagar during January to December 2010.

3.16: Box model simulated diurnal variations in surface ozone. Apart from the base run, diurnal variations in ozone for (a) different levels of NO_x and constant level of NMHCs and (b) different levels of NMHCs and constant level of NO_x are also shown.

3.17: Diurnal variations in ozone production rate $P(\text{O}_3)$, ozone loss rate $L(\text{O}_3)$ and net ozone production rate $P-L(\text{O}_3)$ estimated from box model simulations for the base run.

3.18: Seasonal variations in monthly AOT40 over two sites Pantnagar (PNT) and Dehradun (DDN) in the IGP.

4.1: Location of the observation site Nainital, in the map of India, shown by a cyan color balloon. Drift of balloons during flights are shown for different seasons namely winter (DJF), spring (MAM), summer-monsoon (JJA) and autumn (SON).

4.2: The vertical profiles of air temperature during twelve months of the year 2011 obtained from the radiosonde observations at Nainital in the central Himalayas.

4.3: The vertical profiles of relative humidity during twelve months of the year 2011 obtained from the radiosonde observations at Nainital in the central Himalayas.

4.4: The vertical profiles of wind speed during twelve months of the year 2011 obtained from the radiosonde observations at Nainital in the central Himalayas.

4.5: The seasonal variations in the wind direction at different altitudes, as the percentage occurrences in four quadrants (0-90, 90-180, 180-270 and 270-360 degrees).

4.6: (a) The seasonal variation in lapse rate tropopause (LRT) over Nainital estimated from radiosonde measurements for year 2011. Lapse rate tropopause (LRT) data obtained from satellite (AIRS) and model results (WRF) are also shown for the comparison. **(b)** Correlations between LRT from radiosonde and satellite and **(c)** radiosonde and model are shown.

4.7: The vertical profiles of ozone during twelve months of the year 2011 obtained from the ozonesonde observations at Nainital in the central Himalayas.

4.8: The seasonal variations in the seasonally averaged vertical profiles of temperature, relative humidity, wind speed and ozone over Nainital during the year 2011.

4.9: The seasonal variations in the layers of 2-2 km thickness **(a)** 2 to 4 and 4 to 6 km **(b)** 6 to 8 and 8 to 10 km **(c)** 10 to 12 and 12 to 14 km over Nainital during 2011. Monthly mean values are shown by white lines on the boxes while median values are shown by black lines.

4.10: A comparison of the original ozonesonde profile, sonde data smoothed using the TES a priori, TES a priori, TES retrieval and TES operated sonde profile for one day observation on 7th January 2011.

4.11: Comparison of seasonally averaged collocated observations from ozonesonde and TES satellite during winter, spring, summer-monsoon and autumn.

4.12: The vertical profiles of the percentage bias in the TES retrievals during different seasons. Autumn season includes only one day profile and denoted by *.

4.13: The seasonal variation in the daily and monthly values of TCO from the sonde and TES all observations are shown.

4.14: The correlations of TES TCO with Sonde-TCO-TE Sop and Sonde-TCO-TE Sop-TE S-Trop are shown. A linear regression fit has been made to estimate the coefficient of the determination (r^2) between the satellite and sonde datasets. The 95% confidence interval for the fit is also shown.

5.1: Seasonal variations in potential vorticity at three pressure levels over Nainital, on the flight days, obtained using the WRF-Chem simulated meteorology.

5.2: Ozone vertical distribution during the high ozone event on 17th February 2011 along with all the ozone profiles and seasonally averaged profile in winter.

5.3: Contour maps of potential vorticity at 300 hPa pressure level over the South Asian region on 11th February and 17th February 2011 obtained from WRF-Chem meteorology simulation. The location of the balloon launching site Nainital (NTL) is shown as a triangle.

5.4: Relative humidity profiles during the event day (17th February) and two closest observations on 11th and 2nd February. Seasonally Averaged RH profile during winter (DJF) is also shown for the comparison.

5.5: The distribution in relative humidity from AIRS satellite during 10-12 February, 2011 and on 17 February, 2011 at 400, 300 and 200 hPa over the northern Indian subcontinent. The location of the observation site Nainital is shown by a red filled triangle.

5.6: 5-day back air trajectories have been simulated over Nainital using the HYSPLIT model at different altitudes 6, 9, 15, 16, 18 and 20 km above ground level (AGL). Figures a and b are for 11 February 2011 while c and d are showing the trajectories for 17 February 2011.

5.7: A comparison of ozone profiles on 11 and 17 February 2011 obtained from ozonesonde observations, WRF-Chem model and MOZART model simulations.

5.8: MOZART simulated spatial distributions in the ozone and CO at 400 hPa on 11th and 17th February over the South Asian region.

5.9: The contour maps of MOZART simulated ozone and CO as the functions of pressure and latitude at the fixed longitude of the Nainital on 11th and 17th February, 2011.

5.10: The presence of secondary ozone peak in the middle troposphere during different flights. Seasonally average ozone profiles are also shown for the comparison.

5.11: Seasonal variations in the daily total and monthly total fire counts obtained from MODIS satellite over the northern Indian region during 2011.

5.12: The time series of daily total fire counts during spring over the northern Indian region obtained from the MODIS sensors onboard Aqua and Terra.

5.13: Average vertical distribution of ozone over Nainital obtained from ozonesonde observations during low fire activity period (LFAP) and high fire activity period (HFAP).

6.1: The seasonal variation in CO₂ levels at Nainital during September 2006-December 2011 are shown as a box plot. Average monthly values are shown by a thick blue line. All observations are also shown in open red circles to show the week to week variations.

6.2: The comparison of seasonal variation in CO₂ levels over Nainital with the Mauna Loa and global marine observations (obtained from NOAA; <http://www.esrl.noaa.gov/gmd/ccgg/trends/>) during the study period.

6.3: The seasonal variation in CH₄ levels at Nainital during September 2006-December 2011 are shown as a box plot. Average monthly values are shown by a thick blue line. All observations are also shown in open red circles to show the week to week variations.

6.4: The seasonal variation in CO levels at Nainital during September 2006-December 2011 are shown as a box plot. Average monthly values are shown by a thick blue line. All observations are also shown in open red circles to show the week to week variations.

6.5: The time series of CO₂, CH₄ and CO along with the monthly average values with 1-sigma from September 2006 to December 2011 over Nainital.

6.6: The deseasonalized time series of CO₂, CH₄ and CO over Nainital along with a linear regression fit for the 2006-2011 period.

6.7: Scatter plots showing the correlations between CH₄ and CO over Nainital during four seasons. All the data points are shown by open green circles. Coefficient of determination (r^2) have been estimated using the binned data (red filled squares).

6.8: Scatter plots showing the correlations between CO₂ and CO over Nainital during four seasons. All the data points are shown by open green circles. Coefficient of determination (r^2) have been estimated using the binned data (red filled squares).

List of Tables

3.1: Comparison of rate of change in ozone at Pantnagar with those at other sites in India.

Positive rate is for increase in ozone while negative is indication for decrease in ozone.

3.2: Monthly average mixing depth, ozone with one sigma deviation, maximum ozone, number of ozone data counts (15 minutes average), average CO, average CH₄ and number of samples during study period at Pantnagar.

3.3: Environmental conditions, representing spring, opted for the chemical box model simulations.

4.1: Total number of balloon soundings with serial numbers of the radiosonde and ozonesonde launched during different months of year 2011.

4.2: Tropopause pressure (hPa) in four seasons from the radiosonde observations, AIRS and TES satellites and WRF model.

5.1: The seasonal average values of PV at different pressure levels over Nainital using the data of flight days obtained from WRF-Chem simulated meteorology.

6.1: The monthly average values of CO₂ (ppm) during twelve months as well as in the annual dataset along with the maximum and minimum values and counts.

6.2: The monthly average values of CH₄ (ppm) during twelve months as well as in the annual dataset along with the maximum and minimum values and counts.

6.3: The monthly average values of CO (ppb) during twelve months as well as in the annual dataset along with the maximum and minimum values and counts.

6.4: Estimates of Global and East Asian CH₄/CO emission during TRACE-P period as obtained from *Xiao et al.* [2004].

6.5: Estimates of CO₂ and CO emissions and CO₂/CO emission over India for TRACE-P period obtained from *Suntharalingam et al.* [2004].

Chapter 1

Introduction

The problem of climate change is likely the most important global concern for the mankind. Most of the observed changes in global climate are shown to have link with human-induced perturbations starting with commencement of industrial and agricultural evolution in middle of 18th century [*Forster et al.*, 2007]. The chemistry of the atmosphere, involving the gases present in very low amounts (less than 0.1%) known as the “trace gases”, is found to play vital role in bringing about these changes. The important trace gases, for example, include carbon dioxide (CO₂), ozone (O₃), nitrogen oxides (NO_x), carbon monoxide (CO), sulfur dioxide (SO₂), methane (CH₄), non-methane hydrocarbons (NMHCs), nitrous oxide (N₂O) etc. Notably, the roles played by these gases are disproportionate to their atmospheric abundances. Further, most of these gases exhibit large spatial and temporal variability in their atmospheric abundances.

It has been demonstrated that the global average surface temperature has increased by 0.74°C during the last century and the rate of warming has been almost double in the past 50 years [Le Treut *et al.*, 2007]. This “global warming” has in turn led to the melting of the glaciers and rise in the sea level [Bindoff *et al.*, 2007]. Most of this warming is attributed to the observed enhancements in some of the trace gases called as “greenhouse gases”. In addition, trace gases play a key role in the air pollution having adverse influences on the health of living beings and vegetations. Trace gases also play vital role in the atmospheric chemistry and control the oxidizing capacity of the atmosphere. Thus, an adequate understanding of the variability in the distribution of trace gases and their long-term trends is essential to quantify their relative contributions in the climate change and to design policies to mitigate these changes. The major anthropogenic sources of trace gases include industrial emissions, vehicular exhaust, biomass burning and excessive use of fertilizers. These activities have remarkably increased during last couple of centuries and led to a significant enhancement in all the trace gases. Our knowledge of the distribution and variability in the trace gases is mainly obtained from the observations. Numerous attempts have been made to observe these gases [Forster *et al.*, 2007 and references therein] from different platforms including ground-based [e.g. Keeling *et al.*, 1995; Jaffe *et al.*, 2003; Oltmans *et al.*, 2006], satellite-based [e.g. Thompson *et al.*, 2001; Fishman *et al.*, 2003; Richter *et al.*, 2005], balloon-borne [e.g. Logan, 1985; Logan, 1994; Naja *et al.*, 2003; Tarasick *et al.*, 2005], ship-borne [e.g. Lelieveld *et al.*, 2004] and aircrafts [e.g. Lelieveld *et al.*, 2001; Parrish *et al.*, 2004], but our understanding of the distributions and climatic implications of these gases is still limited. This is because in situ observations lack sufficient spatial and temporal coverage. Space-borne sensors can provide global

coverage but have limited ability to see through the clouds and planetary boundary layer.

In many aspects, ozone remains the most important trace gas, which plays contrasting roles depending upon its concentration and altitudinal placement in the atmosphere. High in the stratosphere, ozone filters the harmful UV light from the incoming solar radiation, while, in contrast, higher ozone levels near the earth surface are deleterious for living beings and plants. Also, being the main precursor of the hydroxyl radical (OH), ozone plays the central role in the atmospheric chemistry. Moreover, tropospheric ozone is an effective greenhouse gas and contributes significantly to the global warming. On per molecule basis, the global warming potential of tropospheric ozone is about 1200 to 2000 times higher than that of CO₂ molecule [*Schwarzkopf and Ramaswamy, 1993*]. It has been shown that the contribution of ozone in the global warming is considerably higher in the upper troposphere [e.g. *Wang et al., 1980; Lacis et al., 1990; Forster and Shine, 1997*]. Moreover, the contribution of stratosphere-troposphere exchange in the budget of tropospheric ozone is also not understood quantitatively mainly due to lack of sufficient measurements of ozone and meteorological parameters in the UTLS (Upper Troposphere Lower Stratosphere). Thus, to understand the role of ozone in the climate change and its budget, the measurements of its vertical distribution are essential.

In view of the above, the systematic measurements of ozone vertical distribution were started during 1960s over the USA, Europe and Japan [*SPARC report, 1998*].

However, these are still very limited over the Asia (home to ~60% of the world's population), where anthropogenic emissions are rapidly increasing [Akimoto, 2003, Zhang *et al.*, 2009]. The observations are particularly sparse over the South Asia, including the Indian region, where the increasing emissions are anticipated to intensify the atmospheric chemistry, due to naturally available intense tropical solar insolation and higher water vapor content. Moreover, stronger convection can lift the pollution from this region to higher altitudes from where stronger winds can transport it to other parts of the world [Lawrence *et al.*, 2003b; Park *et al.*, 2007]. Further, the diversity of emission sources in South Asia lead to physical and chemical processes which are much different from those in North America and Europe. For example, observations made during Indian Ocean Experiment (INDOEX) revealed that ozone levels in South Asian outflow are much lower from those observed in North American and European outflows, despite of very high pollution loadings [Lelieveld *et al.*, 2001]. The very limited knowledge on the vertical distribution of ozone over India have relied upon the observations made by Indian Meteorological Department (IMD) using Indian ozonesonde [Shreedharan, 1968] and recent observations over western India [Srivastava *et al.*, 2012]. Additionally, campaign-mode observations were made at Kanpur in the IGP and marine regions surrounding India [Gupta *et al.*, 2007; Srivastava *et al.*, 2011]. Over the northern Indian region, the ozone distribution has been investigated using the MOZAIC (Measurements of Ozone and water vapour by Airbus In-Service Aircraft) observations [Sahu *et al.*, 2009].

The following sections provide a brief overview of tropospheric ozone and the present status of our understanding of the different processes controlling ozone.

1.1. Importance of Tropospheric Ozone

1.1.1. Role in Global warming

The role of various trace constituents in the climate change is generally evaluated in terms of their “radiative forcing”. Radiative forcing is a measure of the perturbation in the energy balance of earth-atmosphere system due to change in the concentration of a greenhouse gas/agent/specie. Quantitatively, it is the rate of energy change per unit area of the globe at the top of the atmosphere (Wm^{-2}). Positive values of radiative forcing are associated with the warming of the Earth system, while, negative values represent the cooling. The radiative forcing of different trace constituents as compared with the pre-industrial era (about 1750) are shown in the Figure 1.1. Among all the greenhouse agents, the highest contribution to the observed warming is seen due to increase in CO_2 .

Ozone absorbs the terrestrial radiation at $9.6 \mu\text{m}$ wavelength, which lies within the so-called “atmospheric window” and makes it an effective greenhouse gas [Fishman *et al.*, 1979; Wang *et al.*, 1986]. Atmospheric warming, induced per molecule of ozone is estimated to be 1200-2000, 217 and 22 times more effective, in comparison with CO_2 , N_2O and CH_4 respectively [Ramanathan *et al.*, 1985; Schwarzkopf and Ramaswamy, 1993; Marengo *et al.*, 1994]. The radiative forcing of tropospheric ozone is generally estimated using the model simulations [e.g. Gauss *et al.*, 2006] as the available observations are sparse and insufficient to make such estimations. The increase in the levels of tropospheric ozone since the preindustrial era [Volz and Kley, 1988; Marengo, 1994; Hauglustaine and Brasseur, 2001; Lamarque *et al.*,

2005; Gauss et al., 2006] has led to a radiative forcing of $0.35 \pm 0.15 \text{ W m}^{-2}$ making ozone the third most important greenhouse gas after CO_2 and CH_4 [Forster et al., 2007].

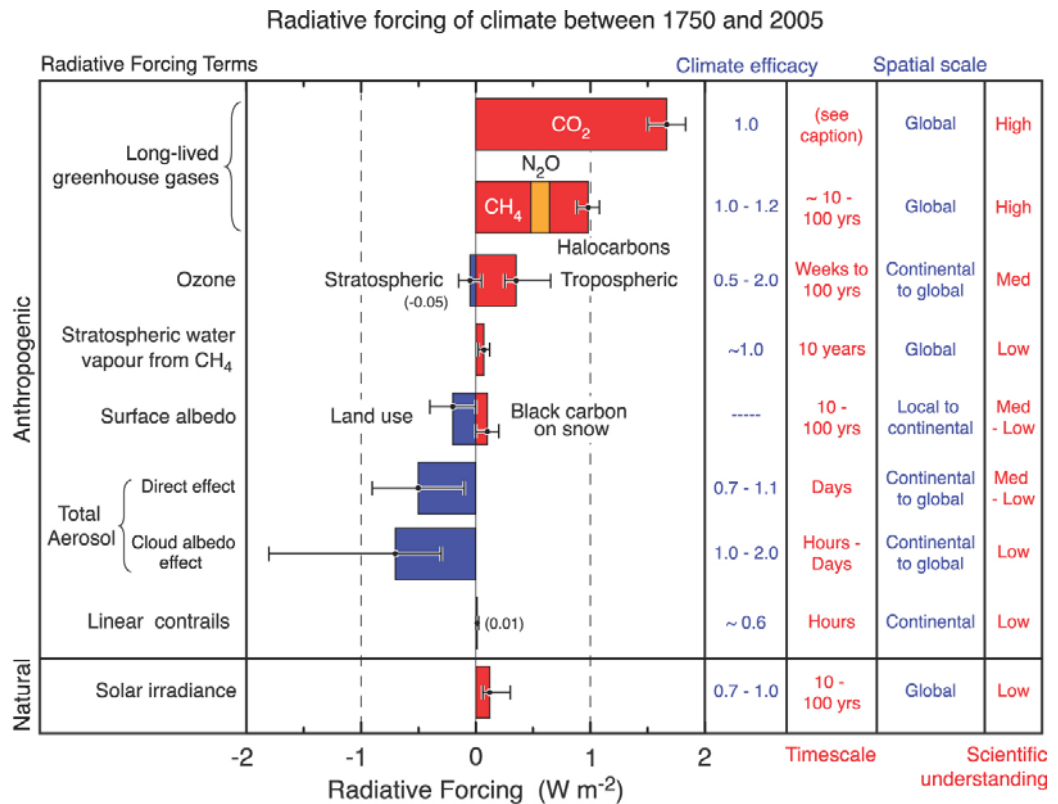


Figure 1.1: A summary of the global mean radiative forcing by major climate forcing agents estimated for year 2005 relative to the start of industrial era (adapted from Forster et al., 2007). Tropospheric ozone is the third most important greenhouse gas after CO_2 and CH_4 .

1.1.2. Effects on Human Health and Vegetations

Tropospheric ozone is an important secondary pollutant of concern due to its deleterious influences on the health of human beings [Desqueyroux *et al.*, 2002]. Exposure to higher ozone levels (e.g. ~70-80 ppbv for 8-hour) can lead to serious health issues including chest pain, increased susceptibility to respiratory diseases, risk of asthma, headache, eye irritation, and even premature death (<http://www.epa.gov/apti/ozonehealth/population.html#content>).

In addition, ozone uptake by plants can significantly damage the cells inside plant leaves affecting their growth. Ozone exposures can reduce the rate of photosynthesis and plants could require more resources to detoxify and repair leaves [Ashmore, 2005]. These adverse effects of ozone result in reduction of crop yield and acute injury on plants [Krupa and Nosal, 1989; Mauzerall and Wang, 2001; Avnery *et al.*, 2011]. The critical levels of ozone, capable of damaging plants significantly, are generally expressed using “Accumulated Ozone Exposure above a threshold of 40 ppbv” (AOT40 index) [Fuhrer *l.*, 1997; Mills *et al.*, 2007]. Crop yields bear a negative linear relationship with the AOT40 indices. The critical levels of AOT40 values over 3-months for wheat and tomato are derived as 3 ppmv*hr and 6 ppmv*hr respectively [Mills *et al.*, 2007]. The estimated economic losses associated with the ozone induced damages in agriculture were estimated to be about 5 billion US dollars in East Asia [Wang and Mauzerall, 2004], Europe [Holland *et al.*, 2006] and the USA [Adams *et al.*, 1998]. The reductions in the agricultural crop yields due to higher ozone levels have been studied for different crops by U.S.A. Environmental Protection Agency (EPA). Figure 1.2 shows the response of

agricultural crop yields of soybean, wheat, corn and rice with the increase in average ozone [Adams et al., 1989; Chameides et al., 1999].

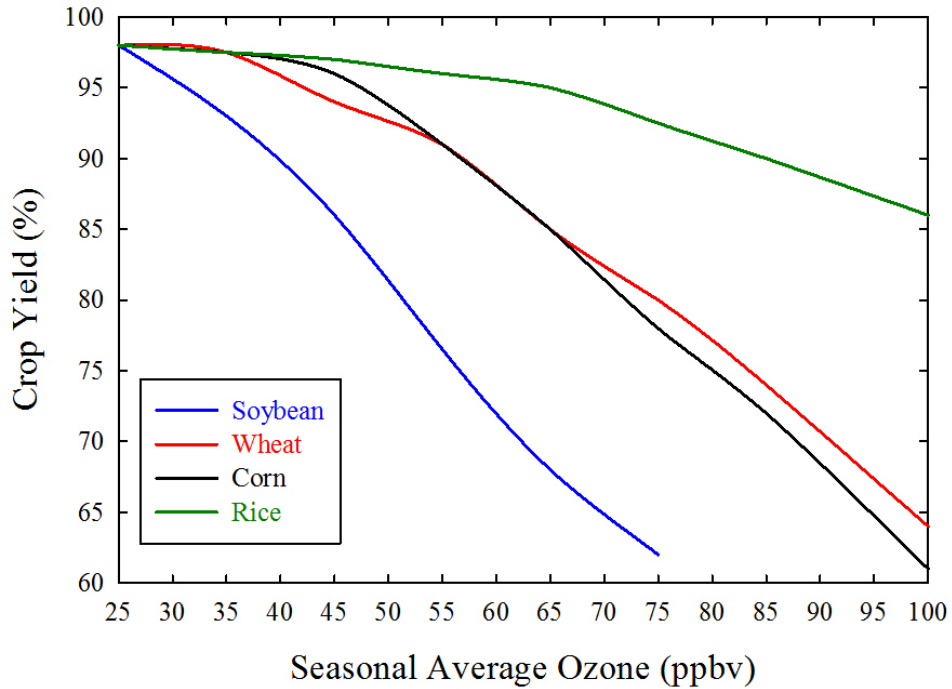


Figure 1.2: Response of agricultural crop yields of soybean, wheat, corn and rice with the increase in average ozone [compiled from Adams et al., 1989; Chameides et al., 1999].

Clearly, Soybean, Wheat and Corn are observed to be more sensitive towards the increase in ozone pollution. For average ozone of more than 75 ppbv, the crop yield of Soybean is reduced to about 62%. Similarly, for Corn and Wheat, ozone levels above 90 ppbv reduce the crop yields to about 70%. A recent global model study [Avnery et al., 2011] have shown that loss in global crop production could be 79-121 million metric tons per year, which translates to an economic loss of about 11-18 billion USD during 2000. The studies of the impact of enhanced ozone levels on the

agricultural activities are few over the Indian region [Ghude *et al.*, 2008a; Van Dingenen *et al.*, 2009]. Considering the estimated losses in global crop productions, it is highly essential to make measurements of surface ozone over a network of sites and plan proper ozone control strategies over the Indian region.

1.1.3. Oxidation Capacity of the Atmosphere

Hydroxyl radical (OH), the photochemical derivative of ozone, is the major oxidant for most of the trace gases such as CO, hydrocarbons, sulfur and nitrogen compounds. Therefore, OH radical is often termed as the “detergent” of the atmosphere. In absence of the oxidation, these trace gases would have accumulated to substantially higher levels than their current levels in the atmosphere [Thompson, 1992; Brasseur *et al.*, 1999]. The photolysis of ozone followed by reaction with water vapor [Levy, 1971] leads to the production of OH radical as follows:



Here, it should be noted that only a fraction of the O (¹D) atoms produced in the reaction (R1.1) react with water vapor (R1.2). The remaining significant fraction of O (¹D) undergoes quenching to the ground state O (³P) through collisions with a third body (N₂ or O₂) [Pitts and Pitts, 2000]. Reportedly, OH radicals oxidize about 3.7 Gt of trace gases including Methane (CH₄), Carbon Monoxide (CO), many Hydrofluorocarbons (HCFs) and Hydrochlorofluorocarbons (HCFCs) every year [Ehhalt, 1999]. Being the main precursor of OH radical, ozone is suggested to control the oxidizing capacity of the atmosphere. Due to very short lifetimes (few

seconds), the direct measurements of OH radicals are very difficult and OH values are often derived using the global measurements of the trace gases (e.g. Methyl Chloroform), for which emissions are known and the primary sink is their reaction with OH. However, the uncertainties in the emissions and lack of sufficient measurements of trace gases could reduce the accuracy of these estimations [O'Doherty *et al.*, 2004].

1.2. Sources and Sinks of Tropospheric Ozone

The key processes controlling the levels of trace gases are emissions, physical and chemical transformations, transport and deposition. The gases, which are directly injected into the atmosphere from a source, are classified as “primary trace gases”, while the gases produced as a result of chemical reactions among primary gases are classified as “secondary trace gases”. CO, NO and SO₂ are few examples of primary pollutants, while, ozone is a secondary pollutant.

A simplified layout of the processes controlling tropospheric ozone is shown in the Figure 1.3. According to the classical view during 1960s-1970s, tropospheric ozone was mainly transported from the stratosphere and destroyed at the surface [Regener, 1949]. Later, the significant contribution of photochemical ozone production was proposed by Crutzen [1973] and Chameides and Walker [1973]. It was suggested in these studies that the oxidation of CO and CH₄, in presence of NO_x and sunlight could lead to significant amount of ozone production even outside the polluted areas. Moreover, the ozone loss due to the chemical processes has been very

important [e.g. Brasseur *et al.*, 1999]. Thus, the key sources of tropospheric ozone are in situ photochemical production supplemented with the downward transport from the stratosphere and loss processes include the chemical losses and deposition.

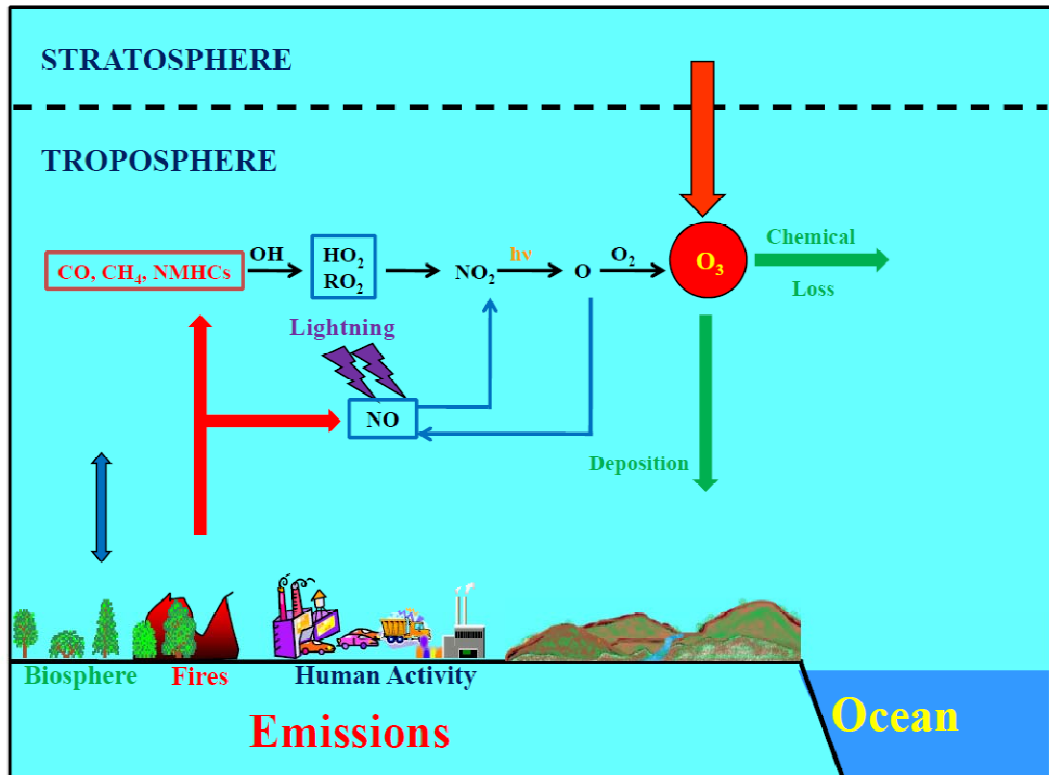


Figure 1.3: A simplified layout of different processes controlling the tropospheric ozone.

1.2.1. Photochemical Production and Loss

The chemical formation of ozone in the atmosphere takes place through the reaction of oxygen molecule (O_2) with the oxygen atom (O), in presence of third molecule.



[R1.3]

In the stratosphere, the ultraviolet radiation of wavelengths shorter than 240 nm dissociates the O₂ molecules to produce the atomic oxygen, which then combines with O₂ to form O₃. However, the UV light ($\lambda < 240$ nm) is not available in the troposphere and therefore O₂ molecules cannot be photo-dissociated in the troposphere. In the troposphere, atomic oxygen is formed by the photo-dissociation of NO₂ ($\lambda > 420$ nm). In the early 1950s, Haagen-Smit proposed that photochemical smog containing ozone could be formed by the photochemistry involving hydrocarbons and NO_x. In the free troposphere and relatively remote marine boundary layers, the levels of NMHCs could be very less and ozone production could be a result of oxidation of CO and CH₄ instead of NMHCs [Brasseur *et al.*, 1999]. CO, NMHCs and NO_x are generally referred to as the precursors of ozone.

First the emitted CO and hydrocarbons react with OH radical and produce peroxy radicals HO₂/RO₂. These peroxy radicals convert NO into NO₂ which ultimately undergoes photolysis and produces the atomic oxygen which combines with oxygen molecule and ozone is formed (R1.3). Apart from ozone producing reaction of peroxy radicals with NO, peroxy radicals can also react with ozone and might lead to ozone loss. Therefore, the reactions rates of both the reactions determine the dominance of ozone production or loss. For net photochemical ozone production, the NO level should be higher than a critical value and this critical value depends upon the ambient ozone level itself. Since, there are hundreds of different hydrocarbons emitted into the atmosphere; the resulting chemistry of ozone production is very complex [e.g. Brasseur *et al.*, 1999]. The relative importance of various hydrocarbons in producing peroxy radicals depends upon their abundances and their reactivity with OH. Generally, the reactivity increases with an increase of

number of C-H bonds available. Unsaturated hydrocarbons are also highly reactive as OH adds to the C=C double bonds rapidly.

The main chemical loss process in the NO_x-rich urban environments is the titration of ozone as follows:



While, in the NO_x-poor environments, the photolysis of ozone molecules at wavelengths shorter than 320 nm and its reaction with OH and HO₂ are the major sinks for ozone on the global scale. More details of the tropospheric chemistry can be seen elsewhere [e.g. *Brasseur et al.*, 1999; *Pitts and Pitts*, 2000; *Seinfeld and Pandis*, 2006].

1.2.2. Natural Source: Stratosphere-Troposphere Exchange (STE)

The troposphere and stratosphere are characterized by different dynamical and chemical properties with strong gradients of ozone and potential vorticity at the tropopause [e.g. *Holton et al.*, 1995]. Stratosphere-Troposphere Exchange (STE) processes have important implications for the atmospheric chemistry and dynamics. For example, the transport of ozone depleting substances from the troposphere to the stratosphere plays a key role in the stratospheric ozone destruction chemistry. STE have direct influences on the vertical distribution of ozone, generally resulting in an enhancement in the upper tropospheric ozone and reduction in the lower

stratosphere. It is suggested that the STE event has a significant input into the tropospheric ozone budget. The STE process is shown to be the major contributor in the observed springtime maxima at a number of sites around the globe [e.g. *Oltmans*, 1981; *Levy et al.*, 1985; *Logan*, 1985]. For the northern hemisphere, the estimated ozone flux from the stratosphere to troposphere is reported to be $3\text{-}8 \times 10^{10}$ molecules $\text{cm}^{-2}\text{s}^{-1}$ [*Crutzen*, 1995], while, the flux in the southern hemisphere may be about half as large.

Generally, the intrusions of ozone rich stratospheric air enhances the ozone levels in the middle-upper troposphere, however, in some cases, it can deeply penetrate up to the lower troposphere as well, influencing the vertical distribution of ozone in the troposphere [e.g. *Levy et al.*, 1985; *Holton and Lelieveld*, 1996; *Marcy et al.*, 2004]. To identify and quantify the role of this process, the measurements of vertical distribution of ozone and meteorological parameters are essential. The contribution of STE can be significant even at the surface at both low and high altitude monitoring sites as reported in several studies [e.g. *Ludwig et al.*, 1977; *Haagenson et al.*, 1981; *Stohl et al.*, 2000; *Cooper et al.*, 2005; *Akriditis et al.*, 2010].

The thermal structures of the troposphere, sometimes discern stable layers with temperature inversions, which are often termed as the multiple tropopause or tropopause folds. These tropopause folding events are suggested to be one of the major mechanisms and conducive structures, responsible for the transport of ozone rich air from the lower stratosphere to the troposphere [e.g. *Reed*, 1955; *Shapiro*, 1980; *Lamarque and Hess*, 1994; *Lefohn et al.*, 2011]. The conditions conducive for

STE events are also associated with the upper tropospheric and lower stratospheric jet streams and the intrusions can be of synoptic scales [Reed, 1955; Danielson, 1968]. Moreover, the frequency of the occurrences of tropopause folds have been found to be maximum over the subtropical regions and is associated with the prevailing subtropical upper level jets [Schmidt *et al.*, 2005; Randel *et al.*, 2007].

Chen *et al.* [2011] have shown that the frequency of multiple tropopause events over the Tibetan plateau is as high as 80% sometimes during the winter. Over the Southern Himalayas, stratospheric intrusions are found to play key roles in the tropospheric ozone variations throughout the year except the summer-monsoon [Cristofanelli *et al.*, 2010]. These studies suggest that tropopause characteristics show significant variability and the associated dynamics is playing very important role in the tropospheric ozone variations over these regions. For an improved understanding of the STE processes, the study of the variability in the Upper Troposphere and Lower stratosphere (UTLS) structure is essential [Stohl *et al.*, 2003], however, at present the observational datasets of vertical profiles of ozone and temperature are severely lacking over the Indian region. This inhibits the quantification of the multiple tropopause events and associated influences on the ozone distribution over this region.

1.2.3. Surface Deposition

Ozone is little water-soluble and its deposition from the atmosphere to the earth surface is essentially a dry deposition. This depositional loss of ozone is an

important process in the budget of tropospheric ozone. The dry deposition flux (F) can be defined as the product of ozone concentration (C) and the deposition velocity (v_d) [Seinfeld and Pandis, 2006] as follows:

$$F = - v_d C$$

The deposition velocity depends on the level of atmospheric turbulence, the properties of the depositing species and on the nature of the surface. The typical value of ozone deposition velocity on the continental surfaces is about 0.4 cm s^{-1} or more, while, it is less than 0.1 cm s^{-1} on the marine or snow surface [Seinfeld and Pandis, 2006]. The ozone deposition velocity over a grass field showed a distinct diurnal variation with highest values (0.2 to 0.5 cm s^{-1}) during the daytime and lowest values ($\sim 0.1 \text{ cm s}^{-1}$) during the nighttimes [Pio *et al.*, 2000]. Similar diurnal patterns with median values of 0.32 cm s^{-1} during the daytime and 0.04 cm s^{-1} during the nighttime were reported from a tropical forest area in the northern Thailand [Matsuda *et al.*, 2005]. More information of the physical, chemical, dynamical and deposition processes influencing the ozone distribution are discussed in the Modeling section of Chapter 2.

1.2.4. Budget of Tropospheric Ozone

The magnitudes of the sources and sinks of ozone are not well quantified due to the availability of limited observations and large spatial and temporal variations in ozone. The chemical lifetime of tropospheric ozone varies typically from days to weeks similar to the dynamical timescales of transport and mixing. The lifetimes of ozone precursors span even on a wider range and thus global 3-D models coupling

the chemistry and transport are required to understand the budget of tropospheric ozone [e.g. *Stevenson et al.*, 2006; *Wu et al.*, 2007; *Wild et al.*, 2007].

The contributions of photochemical ozone production and stratospheric inputs are estimated to be 5060 ± 570 and 520 ± 200 Tg per year [*Stevenson et al.*, 2006]. However, it has been found that there are large differences between global ozone budgets from different models [*Wu et al.*, 2007; *Denman et al.*, *IPCC*, 2007]. The contributions of photochemical production and losses, stratospheric input and loss due to dry deposition in 21 global chemistry models are shown in the Figure 1.4.

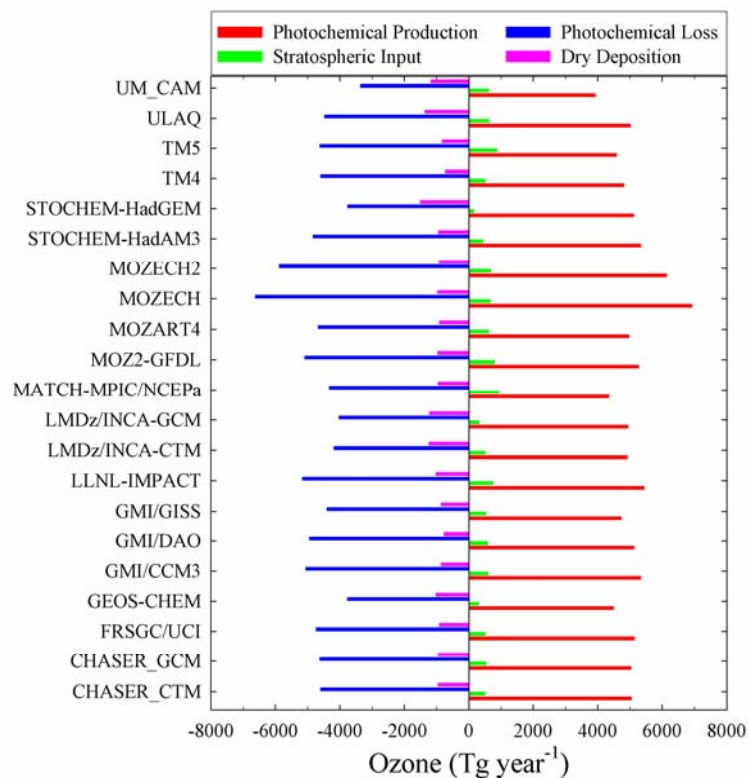


Figure 1.4: The global photochemical production and loss of ozone simulated by the present day 21 global chemistry transport models for the year 2000. For description of the models, please see *Stevenson et al.* [2006].

It is suggested that the global ozone budget is governed mainly by the photochemical production and losses, while, the stratospheric input and depositional losses have less contributions. The differences among different models could arise mainly due to the uncertainties in the emissions of ozone precursors, erroneous parameterization of various meteorological processes including photolysis, convection, and stratosphere-troposphere exchange etc. [Stevenson *et al.*, 2006; Wu *et al.*, 2007].

1.3. Long-Range Transport

Apart from the local and regional emissions, it is now widely recognized that long-range transport also plays an important role in the observed variations of air pollutants. It is well known that the hemispheric transport of pollutants could exacerbate the regional air quality problems and result in the exceedance of the air quality criteria [e.g. *HTAP*, 2010 and references therein]. The long-range transport of pollutants mainly depends upon three factors. First, the amount of the pollutant produced or emitted at the source, second is the meteorological conditions leading to the transport and finally the physical and chemical en-route transformations. It has been shown that baseline surface ozone levels have experienced widespread increase in the past few decades and the inflowing ozone levels in the west coasts of North America and Europe were observed to be as high as 75 to 94% of the WHO standards [Parrish *et al.*, 2009; *HTAP*, 2010]. The influence of baseline ozone is considerably higher even in the free troposphere/higher altitudes (3 to 8 km) and is

estimated to be as high as 85% of the U.S. air quality standards during the spring [Cooper *et al.*, 2010].

The magnitude of the influences of long-range transport is generally determined by the global distribution of the emissions and the major meteorological transport pathways. An analysis of the global distribution of tropospheric NO₂ indicates that NO_x emissions increased very rapidly over China during 1996 to 2005 (up to 29% per year) and other parts in Asia, while, in contrast the emissions over the USA and Europe decreased significantly [e.g. Richter *et al.*, 2005; Van der A *et al.*, 2008; HTAP, 2010]. In recent bottom-up emission inventories, South and East Asian NO_x emissions were shown to be increased by 44% with an increase of 55% in China [Zhang *et al.*, 2009]. NO_x emissions were decreased by about 30% over the Europe and by 37% over the USA [Royal Society, 2008; U.S. EPA, 2010]. As the polluted air masses uplift to the middle-upper tropospheric altitudes, a significant fraction of NO_x is converted into peroxyacetyl nitrate (PAN) and relatively less amount is available for ozone production [Li *et al.*, 2004; Miyazaki *et al.*, 2005]. Additionally, the relatively clear cold and drier conditions lead to considerably different chemistry in the middle-upper troposphere. During the descends, the air masses get warmer and allow for thermal decomposition of PAN into NO_x which can resume ozone production [Hudman *et al.*, 2004; Zhang *et al.*, 2008].

In the mid-latitudes, generally wind speeds increase with the altitude, therefore, the pollutants which are uplifted into the middle-upper troposphere can be transported rapidly, particularly in the regions near the influences of jet streams. Thus, the

processes, which can uplift the pollution, are considered to be the most conducive for the long-range transport. Wintertime westerly winds are very strong over the north Indian region and it is suggested that the pollution emitted from this region can be transported over the greater distances and on very faster timescales (few days). The transport in the mid-latitudes is generally dominated by the westerly winds bringing the pollution from East Asia to North America across the North Pacific ocean, from North America to Europe via North Atlantic ocean and from Europe to Arctic and central Asia. There are numerous studies on the impacts of Asian emissions on the global environment [e.g. *Liu et al.*, 2003; *Cooper et al.*, 2004], over the North America [*Jacob et al.*, 1999a; *Fiore et al.*, 2002; *Zhang et al.*, 2008] and over the Europe [*Stohl et al.*, 2007; *Fiedler et al.*, 2009].

The long-range transport from Asia to USA was shown to offset the benefits of 25% reductions in domestic emissions of ozone precursors over the western USA [*Jacob et al.*, 1999; *Jaffe et al.*, 1999]. Similarly, the North American anthropogenic pollution was found to be contributing substantially (about 11%) to the annual tropospheric ozone over the Europe [*Auray and Bey*, 2005]. However, the studies on the import of foreign pollution to the Asia has been limited [e.g. *Lin et al.*, 2010 and reference therein]. Few studies indicated that the impact of European export on Asian surface ozone is about 0.5 to 5 ppbv over different receptor areas [e.g. *Wild et al.*, 2004; *Fiore et al.*, 2009]. Further details on the pathways and timescales of long-range transport of air pollution can be seen elsewhere [e.g. *Stohl et al.*, 2002; *Lin et al.*, 2010]

1.4. Long-term Trends in Trace Gases

1.4.1. Ozone

The assessment of long-term changes in the tropospheric ozone levels has been difficult mainly due to the scarcity of observations over representative sites [Forster *et al.*, 2007]. However, available ground based and balloon-borne ozone measurements have been utilized to investigate the trends in ozone over the different regions such as USA [e.g. Logan, 1985; Logan, 1994; Fiore *et al.*, 1998; Jaffe *et al.*, 2003; Parrish *et al.*, 2004; Oltmans *et al.*, 2006; Cooper *et al.*, 2010], Canada [e.g. Tarasick *et al.*, 2005], Europe [e.g. Logan, 1994; Naja *et al.*, 2003; Lelieveld *et al.*, 2004; Simmonds *et al.*, 2004; Oltmans *et al.*, 2006], Japan [e.g. Naja and Akimoto, 2004; Tanimoto *et al.*, 2009] and New Zealand [Bodeker, 1998] etc. Estimated long-term trends in ozone were found to vary in both sign and magnitude along with the possible causes for these changes [Oltmans *et al.*, 2006]. A compilation of the available long-term datasets made recently (Figure 1.5) shows that the baseline tropospheric ozone levels have undergone significant increase over the North America, Europe and Asia in the last few decades [Parrish *et al.*, 2012].

Statistical analysis of long-term rural ozone observations shows either insignificant trends or a decreasing tendency over several U. S. surface sites [e.g. Oltmans *et al.*, 2006; Cooper *et al.*, 2012]. While, over the west coast of the North America, ozone levels are observed to be increasing during last 20 years [Parrish *et al.*, 2009; Cooper *et al.*, 2010]. A positive trend of 1.4% per year was observed in the surface ozone levels at Lassen N. P. site in USA during 1988 to 2003 [Jaffe *et al.*, 2003] in agreement with the aircraft observations [Parrish *et al.*, 2004]. Springtime ozone

levels over western North America have increased at a rate of 0.41 ± 0.27 ppbv yr⁻¹ during 1995 to 2011 [Cooper *et al.*, 2012]. It was found that the rate of ozone increase was highest, when the measurements are heavily influenced by direct transport from Asia [Cooper *et al.*, 2010]. Ozone levels over a marine site in the west coast of Ireland discern an increasing trend until late 1990s with no increase thereafter [Derwent *et al.*, 2007]. Unlike the European west coast Mace head, the ozone levels over the western North America do not show any indication of stabilization and are increasing continuously [Parrish *et al.*, 2009; Cooper *et al.*, 2010].

Over Europe, ozone levels increased from the 1950s to early 1990s [Stahelin *et al.*, 1994; Logan, 1994; Logan *et al.*, 1999] and since then ozone trends have levelled off or slightly decreasing. Ozone levels show a decrease since 1998 in the ozonesonde, MOZAIC and alpine site observations [Logan *et al.*, 2012]. The observed decreasing trend of -1.6 ± 0.2 ppbv/year in the photo-chemically aged boundary layer air is consistent with the reduction in NO_x emissions over the Europe [Naja *et al.*, 2003]. Ozonesonde observations over Canada show negative trends in tropospheric ozone during 1980 to 1990, while, the trend becomes positive during 1991 to 2001 [Tarasick *et al.*, 2005].

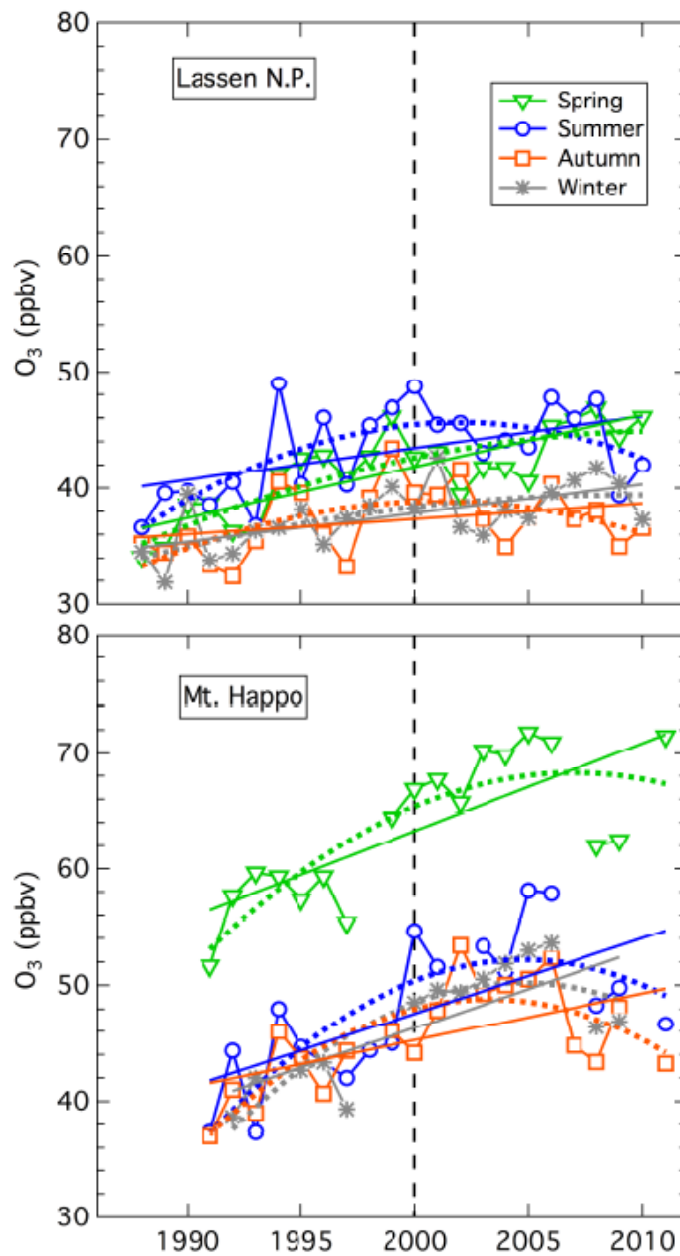


Figure 1.5: Long term trends in seasonally averaged ozone levels at high altitude sites (~1.9 km) Lassen N. P. in Western North America and Mt. Happo in Japan (adapted from Parrish et al., 2012).

Observations are much sparse over the Asia as compared with those over the North America and Europe. The trajectory-assisted analysis of ozonesonde observations shows that regionally polluted ozone levels have increased by 11 to 20% during 1970s to 1990s over Japan, which is attributed to the increase in the NO_x emissions over China in the 1990s [*Naja and Akimoto, 2004*]. Decadal ozone trends were observed to be insignificant at remote surface sites in Japan; however, the trend was significantly higher (1.25 ± 0.53 ppbv/year) over the mountain site Mt. Happo [*Tanimoto et al., 2009*]. The observed increase was shown to be mainly due to the increase in the anthropogenic emissions over the Asia using a chemistry transport model. Moreover, model and observations show disagreements after 2003 and it was suggested that either the actual growth of the emissions and/or the export of Asian pollution is underestimated. Tropospheric ozone column over Beijing, China obtained from ozonesonde observations also show a positive trend over the last decade [*Wang et al., 2012*].

Long-term ozone observations are very limited over the Indian region, however, a comparison of ozone levels during 1990s with those made during 1950s suggests a linear increase at 1.45% per year over Ahmedabad [*Naja and Lal, 1996*]. *Saraf and Beig* [2004] analyzed the ozonesonde observations carried out by the Indian Meteorological Department (IMD) statistically. In this analysis, it was found that ozone levels over Trivandrum did not show any statistically significant trend, however, a significant increasing trend was observed over Pune. Notably, in contrast to the southern India, significant increase in the ozone levels has been reported over the major urban centre Delhi in the northern India throughout the troposphere [*Saraf and Beig, 2004*].

1.4.2. CO₂ and CH₄

Long-lived greenhouse gases such as CO₂, CH₄ and N₂O have also increased significantly since pre-industrial era. The major sources of CO₂ include fossil fuel combustion in the transportation and industrial emissions. Deforestation also releases CO₂ and reduces its uptake by vegetations. CH₄ emissions are generally associated with the agricultural activities, biomass burning, distribution of natural gas and landfills. Wetlands are a natural source of methane. Living vegetations could also have a 10 to 30 % contribution in the global CH₄ budget as discovered by *Kepler et al.* [2006]. N₂O is also emitted by human activities such as use of fertilizers and fossil fuel burning. Natural processes in oceans and soils could also emit N₂O. Sulphur Hexafluoride (SF₆) is generally used as an electrical insulator in the power distribution equipments. It is also released as an inter tracer to study the transport processes in the atmosphere and oceans.

Figure 1.6 shows the long-term changes in CO₂, CH₄ and N₂O over the last 2000 years [*Forster et al.*, 2007]. The levels of greenhouse gases before 1950s are estimated by analyzing the air bubbles trapped in the polar ice cores and are used to extend the records up to AD 0 [*MacFarling Meure et al.*, 2006]. These measurements have confirmed that the CO₂ levels have increased globally by about 100 ppmv over the last 250 years [*Forster et al.*, 2007]. The average growth rate in CO₂ during 1960 to 2005 is estimated to be 1.4 ppmv per year. The growth rates are accelerated and CO₂ levels increased by about 19 ppmv during 1995 to 2005. Recently, it has been reported that CO₂ levels exceeded 400 ppmv for a single day for the first time over Mauna Loa Observatory, Hawaii

(<http://climate.nasa.gov/news/916>). The observed enhancements in the CO₂ levels are attributed mainly to the increasing emissions from fossil fuel combustion. Gas flaring, industrial sources (e.g. cement production); deforestation and biomass burning are the other contributors to this enhancement [e.g. *Houghton*, 2003; *Andreae and Merlet*, 2001; *van der Werf*, 2004]. Here it should be noted that this increase in CO₂ levels imposes the largest radiative forcing of any forcing agent on the climate. CO₂ measurements over Mauna Loa in the Northern Hemisphere (NH) and at Baring Head, New Zealand in the Southern Hemisphere (SH) form the longest continuous CO₂ data records [e.g. *Keeling et al.*, 1995; *Manning et al.*, 1997; *Keeling and Whorf*, 2005]. Remote sites were preferred for these measurements to avoid short-term variations due to local anthropogenic influences. Considering very long lifetimes of these gases, measurements over these remote locations are representative of large-scale variations/levels. However, to estimate the sources and sinks of CO₂, better spatial and temporal coverage of the measurements is required.

Methane is ranked second in terms of the radiative forcing by long-lived greenhouse gases (LLGHGs) after CO₂ [*Ramaswamy et al.*, 2001]. The average global CH₄ levels are estimated to be $1,774.62 \pm 1.22$ ppbv during 2005 [*Forster et al.*, 2007]. Global observations revealed that atmospheric abundances of CH₄ have increased by about 30% in the last 25 years; however, the growth rate has decreased significantly in the late 1990s, unlike that in CO₂ [*Blake and Rowland*, 1988; *Dlugokencky et al.*, 1998; *Simpson et al.*, 2002; *Cunnold et al.*, 2002; *Dlugokencky et al.*, 2003; *Lowe et al.*, 2004]. Currently, the observed reductions in the CH₄ growth rate and therefore the future changes in its levels are not well understood however are suggested to be linked with the imbalance between its sources and sinks. Insignificant trend in the

OH radical, which is the primary sink for CH₄, suggests that CH₄ emissions are not increasing and are more-or-less stabilized [e.g. Hansen *et al.*, 2000; Dlugokencky *et al.*, 1998; Francey *et al.*, 1999].

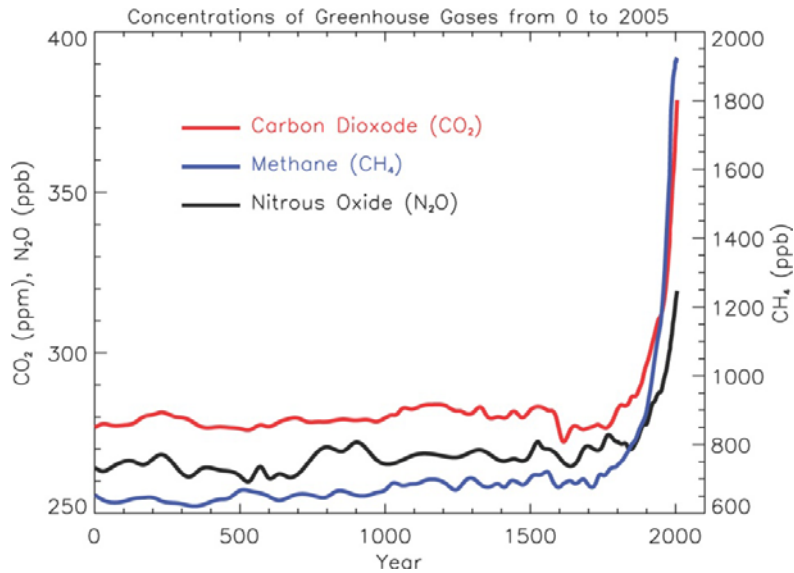


Figure 1.6: Long-term trends in the atmospheric concentrations of long-lived greenhouse gases over the last 2000 years. This figure is obtained from Forster *et al.*, IPCC, [2007].

N₂O is ranked fourth among the long-lived greenhouse gases (LLGHGs) in terms of the radiative forcing after CO₂, CH₄ and CFC-12. N₂O levels are observed to increase significantly from its pre-industrial levels of $\sim 270 \pm 7$ ppbv to 319 ± 0.12 ppbv in 2005 [Forster *et al.*, 2007]. N₂O levels are increasing almost linearly for the past few decades with the growth rate of $\sim 0.26\%$ per year. The main driver for the observed enhancements in the N₂O levels since pre-industrial era are suggested to be the increase in microbial production in fertilized agricultural activities. Considering the decreasing trend in CFC-12, it is suggested that N₂O can take over the third

place in terms of LLGHGs radiative forcing, if it keeps on increasing with the current trend. Sulphur Hexafluoride (SF₆) levels were about 4.2 pptv during 1998, which increased by about 20% during 2005 [Forster *et al.*, 2007]. A linear increase has been observed in its levels during the last decade and it is suggested that its emissions are not varying much. However, due to very long lifetimes (~1000 years or more), its emissions generally are accumulated in the atmosphere.

1.5. Present Scenario over the Indian region

The detailed measurements of ozone and other trace gases are very limited in the south Asia, where human population and the anthropogenic emissions of several key trace species have been increasing rapidly for the past few decades unlike the USA and Europe [e.g. Akimoto, 2003; Richter *et al.*, 2005; Ohara *et al.*, 2007]. South Asia is also home to five megacities (Delhi, Dhaka, Mumbai, Karachi, and Kolkata) and the Indo-Gangetic Plain (IGP) region, which is one of the most populated regions of the world. The pollutants emanating from South Asia are shown to have important implications not only for the people residing in this region but also for other parts of world. For example, convection associated with monsoonal circulation transport South Asian pollutants to the Mediterranean Sea [e.g. Lawrence *et al.*, 2003b; Park *et al.*, 2007]. Further, the chemical characteristics of South Asian emissions are different from those in other parts of the world because of their disproportionately large contribution from bio-fuel and biomass burning [e.g. Lawrence and Lelieveld, 2010].

Over the Indian region, observations of surface ozone were initiated in mid 1950s during pre-International Geophysical Year (IGY) followed by regular observations by India Meteorological Department (IMD) in 1960s using either electro-chemical or chemiluminescence methods. Realizing the importance of surface based observations of ozone and its precursors, extensive observations at a network of sites were initiated under the ISRO-GBP program in early 1990s. Under this program, observations were made covering the sites of different chemical environments including urban (Ahmedabad) [Lal *et al.*, 2000], rural (Gadanki) [Naja and Lal, 2002], coastal (Trivandrum) [Nair *et al.*, 2002] and high altitude mountain (Mt. Abu) [Naja *et al.*, 2003].

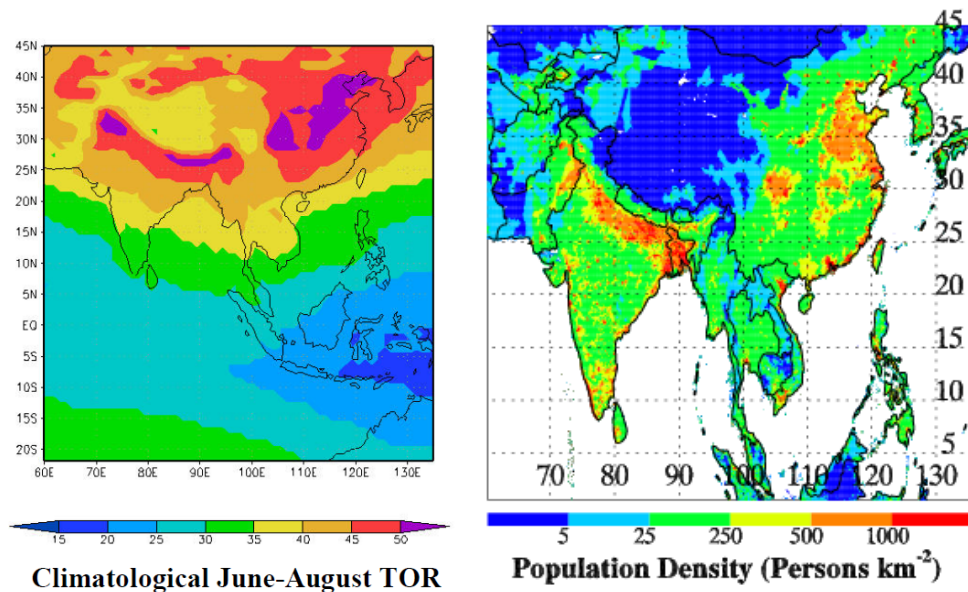


Figure 1.7: Climatological distribution of tropospheric ozone [Fishman *et al.*, 2003] over the India and Southeast Asia along with the distribution of population density.

In addition, campaign based observations over the marine regions surrounding India were also made [e.g. *Lal et al.*, 1998; *Naja et al.*, 2004; *Lal et al.*, 2007; *Srivastava et al.*, 2011]. Notably most of the studies were confined to the western and southern regions [e.g. *Lal et al.*, 2000; *Naja and Lal*, 2002; *Beig et al.*, 2007; *Reddy et al.*, 2008]. However, observations have been sparse in the Northern India [*Varshney and Aggarawal*, 1992; *Jain et al.*, 2005], where only two sites have observations with a complete ozone seasonal cycle. One site is a highly urbanized megacity (Delhi) [*Ghude et al.*, 2008a] and other one is a high altitude pristine site in the central Himalayan region (Nainital) [*Kumar et al.*, 2010]. Space-borne observations revealed that the pollution loadings, in the form of total tropospheric ozone (*Figure 1.7*), tropospheric column NO₂ and aerosol optical depth, are considerably elevated over the IGP region [*Fishman et al.*, 2003; *Jethva et al.*, 2005; *Ghude et al.*, 2008b]. Lack of in situ measurements of ozone and precursors over the northern Indian region inhibits the confirmation of the findings from satellite data. The underlying processes causing such spatial heterogeneity in the distribution of these gases over Indian region remain poorly understood. Apart from surface ozone observations, its vertical distribution is very useful. Historically vertical ozone distribution is measured by IMD at Delhi, Pune and Trivandrum. Apart from above these three sites, ozone vertical distribution was also measured at Ahmedabad during 2003-2007 [*Gupta et al.*, 2007; *Srivastava et al.*, 2010].

The measurements of surface ozone were initiated at a high altitude site Nainital located in the central Himalayas and it was found that seasonal variations and ozone levels over this region are different from the other parts of India [*Kumar et al.*, 2010]. Influences of open crop residue burning, downward transport from higher

altitudes and long-range transport from Africa and Europe were also observed over Nainital [Kumar *et al.*, 2011]. The influences of downward transport from stratosphere over the Himalayan region have also been documented using surface ozone observations over the Nepal Climate Observatory – Pyramid [Cristofanelli *et al.*, 2010]. However, there are no observations of vertical distribution of ozone over the central Himalayas so far. The in-situ measurements of ozone vertical distribution with a complete seasonal cycle are still very limited over this region and their information has relied mostly on MOZAIC (Measurements of Ozone and water vapour by Airbus In-Service Aircraft) observations [Sahu *et al.*, 2009] and balloon-borne observations by Indian Meteorological Department (IMD) [Saraf and Beig, 2004; Ganguly and Tzanis, 2011]. The limited observations have indicated significant increase in the tropospheric ozone levels over the Indian region [Naja and Lal, 1996; Saraf and Beig, 2004]. The long-term measurements of various long-lived greenhouse gases such as CO₂, N₂O and SF₆ are nearly non-existing over the Indian region so far.

1.6. Objectives and Outline of the Thesis

This thesis is aimed at investigating the variability in the spatial and temporal distribution of ozone and other trace gases in the lower atmosphere over the northern Indian region, primarily by conducting in situ ground-based and balloon-borne measurements. Northern India remains one of the least studied regions in South Asia despite of the fact that satellite-based observations [e.g. Fishman *et al.*, 2003, Ghude *et al.*, 2008b] and model results [e.g. Kumar *et al.*, 2012b] show much higher pollution loadings over this region as compared with the rest of the South Asia.

However, the lack of in situ measurements inhibited the validation of satellite observations and model results and the understanding of the underlying processes causing such spatial heterogeneity in the distribution of trace species. The observations made in this thesis would be invaluable for the verification of results obtained from satellite data and models.

Thesis objective can be divided broadly into following three parts.

- To investigate the vertical distribution of ozone over this region by conducting balloon-borne measurements from a high altitude site Nainital in the central Himalayas.
- To study the variability in surface ozone over the northern India using ground-based measurements at Pantnagar in the Indo-Gangetic Plain (IGP) region.
- To assess the variability and long-term trends in CO₂, CH₄ and CO at Nainital.

The one of the objective of this thesis is to investigate the various processes influencing the vertical distribution of ozone over the northern Indian region using balloon-borne measurements. Ozonesonde and radiosonde were launched from a high altitude site Nainital (29.37°N, 79.45°E, 1958 m amsl). The observed variations in the distribution of ozone and various meteorological parameters are analyzed for week to week and seasonal variations. Variations in the air temperature have been used to estimate the tropopause pressure and a comparison with the satellite and model results has been made. Ozonesonde profiles have been compared with the collocated satellite retrievals and biases in satellite retrievals over this region are

investigated. Ozonesonde profiles are further used to calculate the tropospheric columns and are compared with the satellite data. The role of variability in tropopause pressure in estimated tropospheric ozone columns have also been investigated. The variations in stratospheric tracers such as relative humidity and potential vorticity along with the simulations of chemical fields are used to study the stratospheric intrusion of ozone. Satellite derived fire counts data are used to classify the ozonesonde profiles in to high and low fire activity periods during the spring and the influences of northern Indian biomass burning on the ozone distribution are studied.

Continuous ground based measurements at a semi-urban site Pantnagar (79.5°E, 29.0°N, 231 m amsl) are used to study the physical, chemical and dynamical processes controlling the surface ozone variations in the Indo-Gangetic Plain (IGP) region. Analysis of the surface ozone observations at Pantnagar has been made using various meteorological parameters such as solar radiation, rainfall, mixing depth and simulations of back-air trajectories to understand the diurnal and seasonal variabilities in ozone. Satellite based observations are used to study the seasonal variations in ozone and precursors over the IGP. The observations at Pantnagar are compared with the available observations at other sites in India particularly with a nearby high altitude site Nainital in the central Himalayas to understand the transport of pollution from the IGP region to the Himalayas. The results from a global chemistry transport model (MATCH-MPIC) have been used to investigate the spatial and temporal variations in ozone over this region. This model has been further used to study the ozone production regime such as NO_x or hydrocarbon limited. Moreover, the observations at Pantnagar are used to drive a chemical box model (NCAR-MM) for a semi-urban environment in this region. The diurnal

variations in ozone are investigated and the sensitivity runs are made to understand the changes in the ozone levels due to those in the precursors and to estimate the ozone production and loss rates. The observations at Pantnagar along with another urban site Dehradun (78.1°E, 30.3°N, 640 m amsl) in the IGP are analyzed for the possible impacts of ozone pollution on the growth of vegetations by estimating the Accumulated Ozone above a Threshold of 40 ppbv (AOT40) index.

The measurements of greenhouse gases are made by collecting weekly air samples at Nainital and analyzing them using a Gas Chromatograph and IR based instrument to measure the concentrations greenhouse gases including CO₂ and CH₄. The analysis of long-term time series of these gases is made to study the seasonal variations and long-term trends in these gases over Nainital. A comparison of the observed seasonal variations and trends at Nainital with observations at other sites is also made.

This thesis contains seven chapters including the present **Chapter 1** which provides a brief background about the role of ozone and other trace gases in the atmosphere and the basic research work carried out. The detailed description of the instruments and measurement techniques, models and satellite data used in this study is provided in **Chapter 2**. The results of surface ozone measurements at Pantnagar site in the Indo-Gangetic Plain region are discussed in the **Chapter 3**. The analysis of balloon-borne measurements from Nainital is presented in the Chapter 4 and Chapter 5. In the **Chapter 4**, the seasonal variations in ozone and meteorological parameters have been discussed. **Chapter 5** includes the influences of various dynamical processes

and biomass burning on the ozone distribution. The analysis of long term observations of CO₂, CH₄ and CO has been discussed in the **Chapter 6** with emphasis on the seasonal variations and long-term trends. Finally in the **Chapter 7**, a brief summary and conclusions of the thesis are discussed with the future scope of this work.

Blank Page

Chapter 2

Methodology

In order to study the spatial and temporal variabilities in ozone and other trace gases, sensitive and accurate measurement techniques are essential. There have been significant improvements in various measurement techniques of trace gases in past few decades [e.g. *Heard, 2006*]. Among the chemical method, chemiluminescence and UV absorption method for surface ozone, UV absorption is the most popular method, while, the Gas Chromatography remains the preferred method for many hydrocarbons. Recently, CRDS based instruments are the most popular for trace gas measurements. These instruments are seen to have least interferences from other gases; however, these instruments are very costly. Balloon soundings using electrochemical sensors and LIDAR are the only techniques that can provide ozone profiles with good vertical resolution and accuracy throughout the troposphere and the lower stratosphere. Unlike LIDAR and many satellite observing systems, ozonesondes are not affected by clouds and are capable of resolving strong ozone gradients in the upper troposphere and lower stratosphere (UT/LS) [e.g. *Thompson et al., 2011*].

The different measurement techniques employed in the present thesis are discussed in the following sections:

2.1. Surface Ozone

Surface ozone measurements have been made using the online ozone analyzers (Teledyne M400E and Thermo Model-49i) operating on the principle of UV light absorption by ozone molecules at about 254 nm. These analyzers have a response time of about 20 seconds and a minimum detection limit of about one ppbv. The ambient air is drawn inside the analyzer through a Teflon tube from the rooftop of the second floor with a flow of about 1 L per min. The absolute accuracy of this system is reported to be about 5% [Kleinman *et al.*, 1994]. Average ozone values are stored over 15 min intervals and used for further analysis.

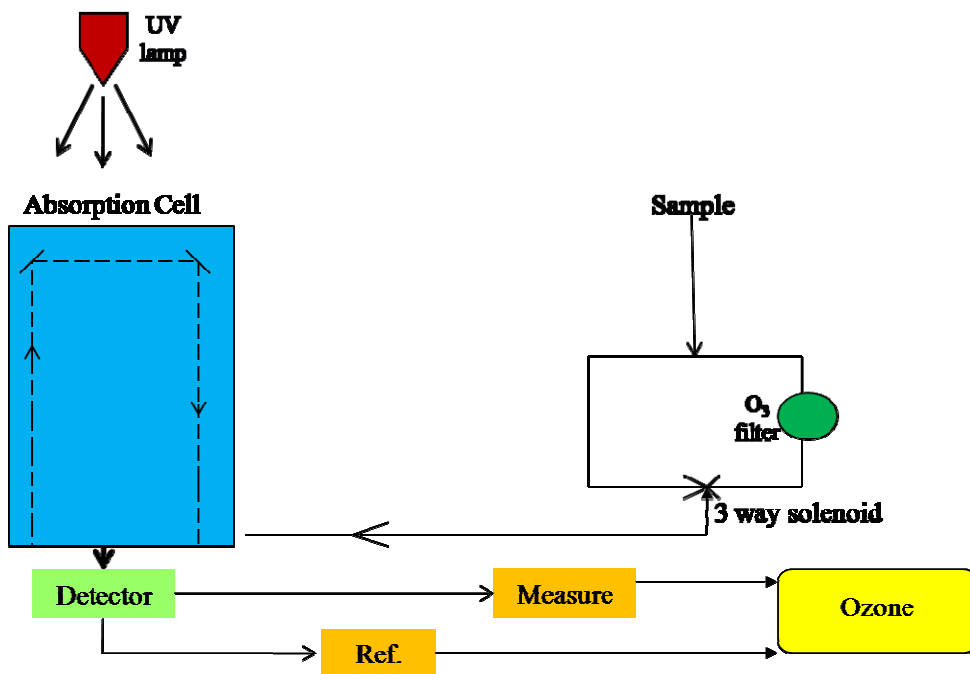


Figure 2.1: A simplified block diagram showing the operating principle of surface ozone measurements using the UV absorption technique.

Figure 2.1 shows a simplified block diagram of the ozone analyzer demonstrating its working principle. Air sample, after passing through a teflon filter, is divided into two air streams with one of them flowing directly through the absorption cell while other flows via an ozone scrubber (MnO_2). The two gas streams represent air with ozone and without ozone. These air streams are passed through an absorption cell for 5 to 10 seconds alternatively using a 3-way solenoid valve. In the absorption cell, these air samples are exposed to UV light (254 nm) to produce a reference (I_0) and measurement (I) signal. The measurement and reference signals represent the attenuation of UV light in the presence and absence of ozone in the air. I_0 and I are compared with each other using the Beer-Lambert's Law to estimate ozone concentration as follows:

$$I = I_0 e^{-\sigma LC} \quad [2.1]$$

Where σ is the molecular absorption coefficient of ozone at 254 nm (308 cm^{-1}), L is the effective length of the absorption cell, and C is the ozone concentration.

Some trace species can contribute to the detected attenuation by either absorption (gases) or scattering (aerosols), however any such contribution will be removed in this method due to the differential nature of equation 2.1. Other possible sources of error include the variations in the temperature and pressure of absorption cells, drifts in the UV lamp intensity and drift in the sensitivity of the detector. Both of the instruments are equipped with the temperature and pressure sensors for the possible corrections. The UV lamp used in these instruments is a low-pressure cold-cathode mercury vapour lamp with main emission line at 254 nm. The detector unit is a photodiode having built-in filters centered at around 254 nm. The accuracy of both

the analyzers is examined periodically by performing zero and span checks (Figure 2.2).

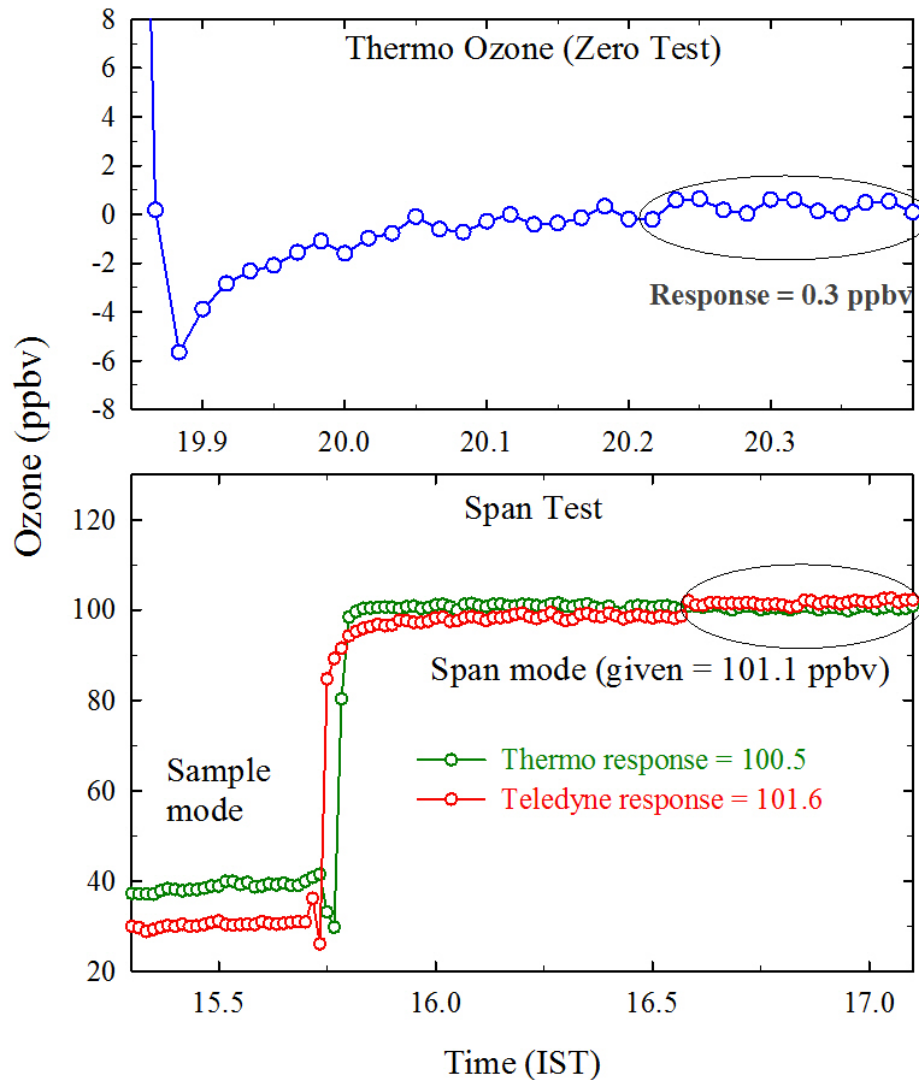


Figure 2.2: An example of responses of the ozone instrument during the zero and span tests carried out on 6 March 2011 at Nainital.

A zero air generator (Thermo model 1160) is employed to perform the zero tests. A typical example of a zero test is shown in the Figure 2.2. Span check is the test of

the instrument response when its inlet is connected to a known concentration of ozone (here 101.1 ppbv) produced by an in built ozone generator. The instruments, from Thermo and Teledyne both, responded well to the span tests with their average response in the range of 100.5 to 101.6 ppbv.

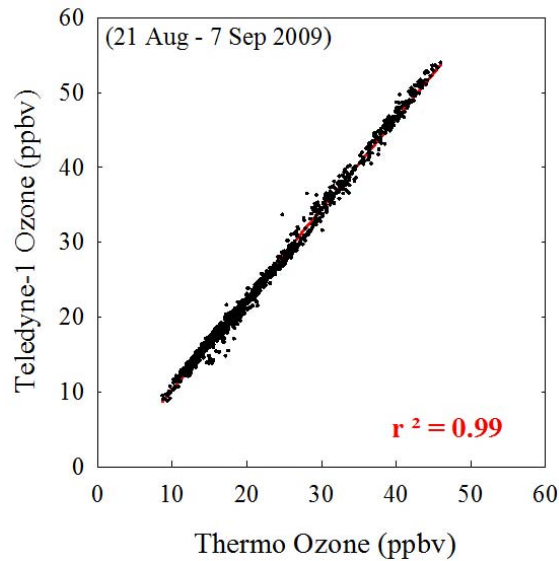


Figure 2.3: A strong positive correlation is observed between the simultaneous ozone observations from Thermo and Teledyne.

In addition to the zero and span tests, ozone observations from Thermo, USA and Teledyne, USA instruments have been inter-compared (Figure 2.3) by running them side by side using a common inlet system. The ozone observations from both the analyzers are seen to be in strong positive correlation ($r^2 = 0.99$) with each other. Further details of ozone observations by such instruments have been reported in *Lal et al.* [2000], *Naja and Lal* [2002], *Kumar et al.* [2010], and *Ojha et al.* [2012].

2.2. Balloon-borne Measurements

Measurements of ozone vertical distribution along with different meteorological parameters including air temperature, pressure, and relative humidity have been made by launching balloons carrying an “Ozonesonde” coupled with a conventional meteorological “Radiosonde” (meteorological sensors with GPS and transmitter) (Figure 2.4).

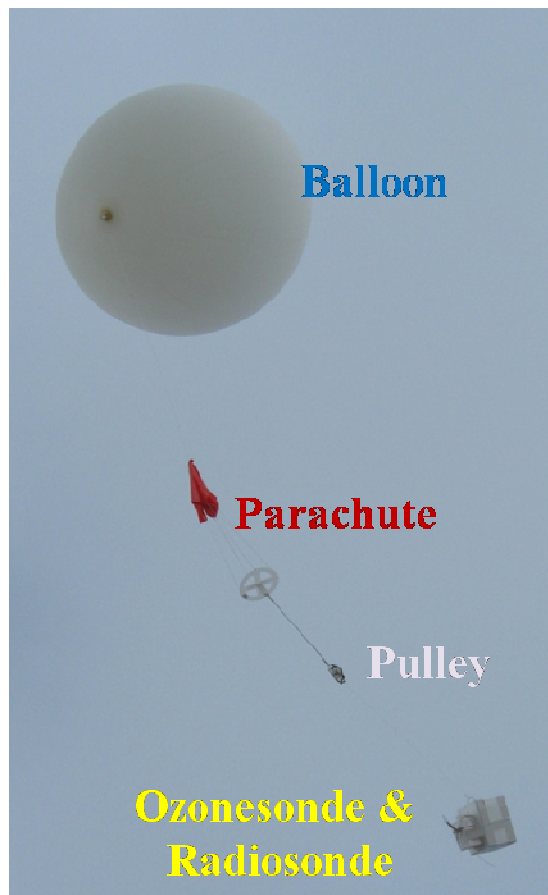


Figure 2.4: Balloon with ozonesonde and radiosonde during the ascent at ARIES, Nainital.

Ozonesondes have a long developmental history and these were introduced in the atmospheric science research during 1960s [e.g. *Komhyr*, 1969]. Ozonesondes have been the most popular/successful technique for providing ozone profiles from surface up to stratosphere depending upon the burst altitude of the balloons (generally ~30 to 35 km). Several inter-comparisons have been made among various ozonesondes over the last 4 decade [*Attmannspacher and Dutch*, 1970; *Barnes et al.*, 1985; *Kerr et al.*, 1994; *Komhyr et al.*, 1995; *Boyd et al.*, 1998; *Smit et al.*, 2007; *Deshler et al.*, 2008] and ozonesonde is now a proven technique. Three different types of ozonesondes have been employed at different stations around the globe, which are Electrochemical Concentration Cell (ECC), Brewer Mast (BM) and Japanese KC sonde. Out of these three, the ECC ozonesondes are most widely used and is being used in the present study which is described in the subsequent sections. The details of other types of ozonesondes can be seen elsewhere [e.g. *Brewer and Malford*, 1960; *Kobayashi and Toyama*, 1966; *Claude et al.*, 1987; *Fujimoto et al.*, 2004].

As the balloon ascends in the atmosphere, the information of ozone and meteorological parameters is transmitted to the receiving system at ground. Entire air segment consists of a balloon (1200 gm rubber), a parachute, a reel-pulley and instrument payload. The instrument payload includes an Ozonesonde (ECC sensor, Teflon pump, electronic interface card) and meteorological radiosonde (meteorological sensors and GPS). The ground segment includes an antenna, radio receiver, modem and a computer for receiving the data. Figure 2.5 shows the photographs of ozonesonde, radiosonde, antenna and receiver and Figure 2.6 shows an overview of the balloon sounding setup.

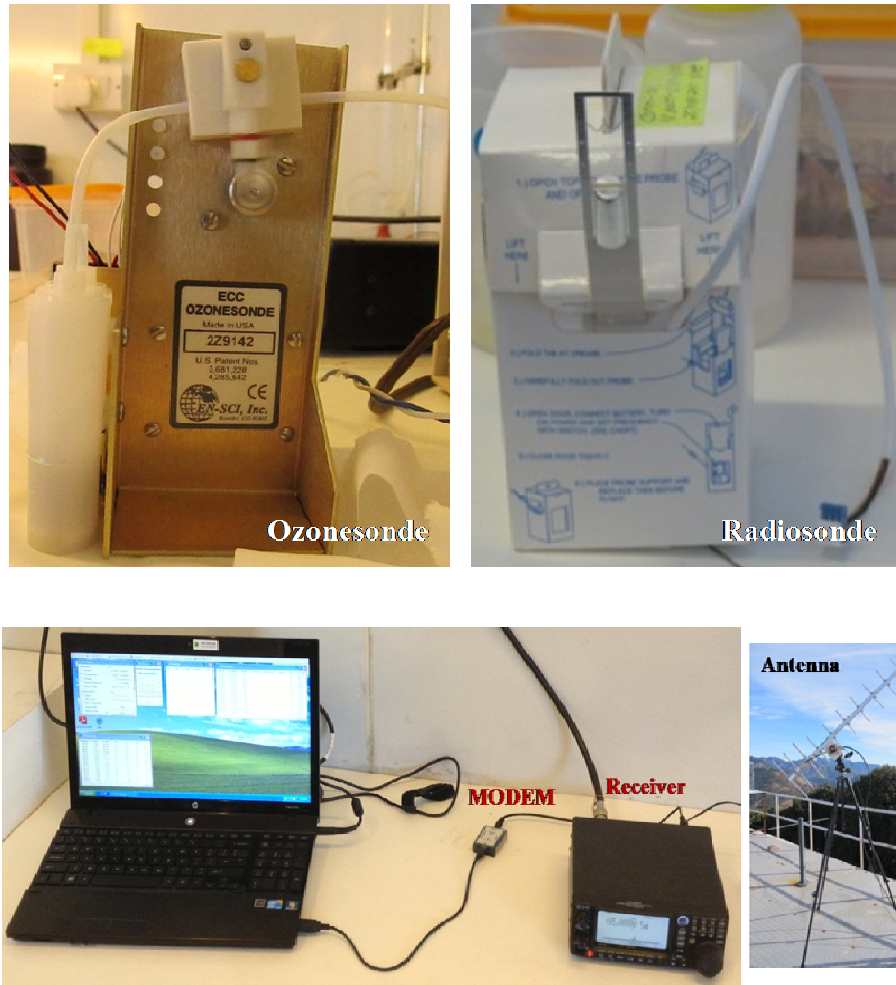


Figure 2.5: Ozonesonde, radiosonde, antenna and receiver coupled with the laptop via MODEM as used during the observations.

Before starting the regular observation, 7 test flights were conducted during September-October 2010 and regular observations were started during January 2011 with a frequency of 3 to 4 flights in each month. Generally, balloon flight is carried out on every Wednesday. Figure 2.6 shows an overview of the complete balloon sounding experiments. A portable tripod-mounted Yagi antenna with a built-in pre-amplifier coupled with a 403 MHz receiver has been used for data acquisition. Data

processing software supplied by the manufacturer is used to connect computer to the receiver via a 1200-baud rate modem. Balloons are filled with Helium gas with about 90 Kg/cm². In this study, all the sensors flown were new and used only once. The ascent rate of balloons was about 5 meter per second and generally balloon burst altitude is 30-32 km.

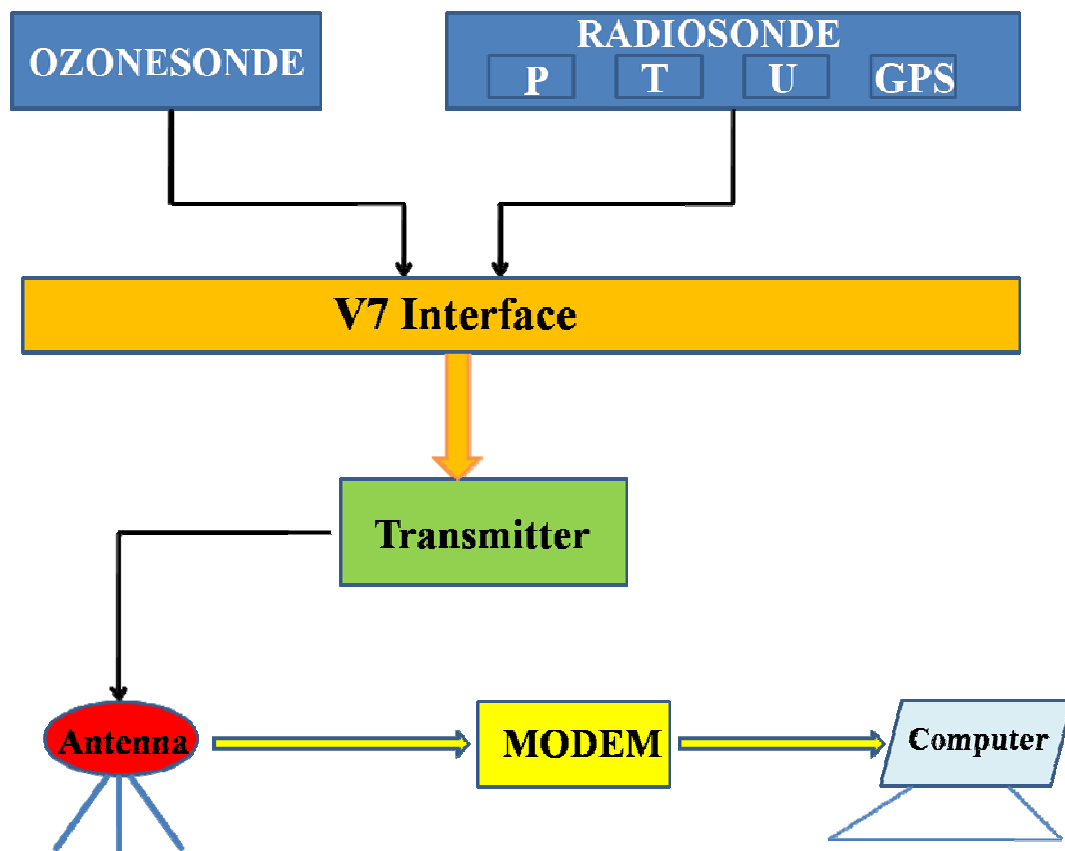


Figure 2.6: Layout of the balloon sounding experiments showing the measurement, data transmission and receiving system.

Duration of complete flight, comprising of ascend and descend, is 2 to 3 hours. Descend profiles have also been collected, however, are not used in the analysis as

measurements whose smaller size allows for the faster response. It is coated with the aluminum which minimizes the effects of solar and infrared heating. For the measurements of relative humidity, this radiosonde utilizes a variable capacitor having a polymer dielectric insulator. The permittivity of the insulator varies with the change in the relative humidity. The pressure is measured by a compensated peizo-resistive silicon pressure sensor. This radiosonde has a 12-channel GPS receiver and a 403 MHz data transmitter. The transmitter is a crystal-controlled oscillator that controls the opted channel frequency. It has a linearly polarized dipole antenna, which transmits FM modulated signal containing digital data for meteorological parameters (PTU) and GPS. In addition to the meteorological measurements made by the sensors of radiosonde it also transmits the GPS data and the ozone measurements if it is coupled with an ozonesonde.

The accuracies of pressure, temperature and humidity measurements are reported to be ± 1.8 hPa (surface to 400 hPa), ± 0.5 hPa (400 to 4 hPa), ± 0.3 °C and $\pm 5\%$ respectively. An in-built GPS is used to track the position of balloon and to calculate wind speed and wind direction. A detailed evaluation of the performance of Internet radiosonde and its comparison with Vaisala radiosonde (RS92) has been made recently [Hurst *et al.*, 2011].

2.2.2. Ozonesonde

Electrochemical concentration cell (ECC) ozonesondes (EN-SCI 2ZV7 ECC) [Komhyr *et al.*, 1969; Komhyr *et al.*, 1995] have been used to measure the vertical

distribution of ozone. ECC ozonesondes contains two half cells made of Teflon which serve as cathode and anode. Both of these cells contain platinum mesh acting as the electrodes which are immersed in the KI solutions of different concentrations.

ECC ozonesondes do not require any external electrical potential but get their driving electromotive force (0.13 V) from the differences in the concentrations of Potassium Iodide solutions in cathode and anode chambers. The electrolytes contain Potassium Bromide (KBr) and a buffer whose concentrations are same in each cell. The current generated by the oxidation of Potassium Iodide (KI) by ozone molecules is measured to derive the ozone concentration. This method is preferred for balloon flights due to its faster response time (1-2 seconds) and lightweight. A compact battery operated pump is used to draw air into the cell.

When ozone enters the sensor, it reacts with KI to form I₂ in the cathode



The cell converts I₂ into Iodide ions by flow of two electrons according to



In this way, for each ozone molecule entered the sensor, a flow of two electrons takes place in the external circuit of the cell. Measurement of this cell current (i_m) along with the flow rate of air into the sensor, ozone partial pressure is calculated as follows:

$$P_{O_3} = 4.307 \times 10^{-3} (i_m - i_b) T_{pt} \quad [2.4]$$

Where, i_b is the sensor background current (μA), T_p is the pump temperature (K) and t is time (seconds) taken by sonde pump to force 100 ml of air through the sensor.

Ozone mixing ratios are derived as follows:

$$O_3 \text{ (ppbv)} = 1000 P_{O_3}/P = 4.307 (i_m - i_b) T_p t / P \quad [2.5]$$

2.2.3. Preparation of the Ozonesonde For Flight

2.2.3.1. Advance Preparation

Advance preparation of the ozonesonde includes the testing of the overall performance of the instrument and charging of the sensor with the sensing solutions.

This preparation is done 3 to 7 days prior to the flight day to attain the low background current. This is done in the following steps:

- (a) The power leads of ozonesonde are first connected to the 12 VDC output from the ozonizer test unit and sonde is run with ozone free air for about 15 minutes. Sonde should generally draw less than 90 mA of current and develop at least 20 inches Hg pressure and 18 inch Hg vacuum. If it takes larger current or develops less pressure/vacuum then few ml of acetone are put into the pump inlet.
- (b) After achieving the proper pump performance, sonde air intake tube is connected to high ozone source in the tests unit and is conditioned with high ozone (few ppmv) for about 30 minutes followed by flushing it by ozone free air for about 5 minutes.
- (c) Cathode sensor is charged first by 3 ml of the solution by a teflon tipped syringe specially reserved for cathode. Then after 2 minutes, anode is charge by 1.5 ml solution. Now, sonde is run for ozone free air for about 10 minutes. Sonde is

then given a moderate input of ozone which produces about 5 μA sensors current. To check the sensitivity of the sensor, suddenly the ozone free air is passed and that should show the current less than 1.5 μA which indicates the satisfactory performance of the sensor.

- (d) Additional 2.5 ml of solution is filled in cathode cell and ECC sensor leads are short by a shorting plug or ordinary copper wire and sensor is kept in dark clean environment.

2.2.3.2. Preparation on the day of Balloon Launch

- (a) Cathode and anode solutions are removed completely and chambers are refilled by fresh solutions 3 ml cathode and 1.5 ml anode.
- (b) Ozone free air is passed for 10 minutes and sensor background current is recorded at the end of 10 minute. It should be less than 0.05 μA . sensor is then provided ozone rich air as to produce about 5 μA current for 10 minutes and after 10 minutes ozone free air is given and sensor currents for 1, 3, 5 and 10 minutes are recorded. The response of the sensor is satisfactory if

$$R = 100 \times (i_{t=0} - i_{t=1}) / i_{t=0} \geq 80\% \quad [2.6]$$

- (c) Ozonesonde is connected with the radiosonde and is checked for about 10 minutes for the performance of the whole instrument package. Fresh batteries are connected to the ozonesonde (16V) and radiosonde (6V). Pump flow rate and background current along with the serial numbers of ozonesonde and radiosonde are input to the software. The instrument package (ozonesonde and radiosonde) is tied with the balloon along with a parachute and a reel-pulley, as shown in the Figure 2.4 and launched.

Although there are different manufacturers for ozonesonde, however, laboratory and field inter-comparison experiments show that these are more-or-less in agreement with each other [Smit *et al.*, 2007; Deshler *et al.*, 2008]. The differences in ozone measurements are 5% or less below 20 km [Smit *et al.*, 2007]. The accuracy of this sensor is reported to be about \pm (5 to 10) % upto 30 km altitude [Smit *et al.*, 2007]. More details regarding Ozonesonde instruments can be seen elsewhere (e.g. <http://www.ndsc.ncep.noaa.gov/organize/protocols/appendix5/> and references therein).

2.3. Air Sampling for CO₂, CO and CH₄

Weekly air samples were collected at Nainital for the analysis of long-lived greenhouse gases and CO. Air samples were collected every Wednesday at 1400 hours at a cold trap (-30 °C) by a cooling unit using Glycol (Figure 2.8). Cooler air occupies less volume and thus sufficient air sample can be filled in the glass bottles. Moreover, water vapor gets condensed into the cold trap and is not sampled in the bottles. These sample bottles are then packed and sent to National Institute for Environmental Studies (NIES), Japan for analysis using a Gas Chromatograph and NDIR (Non Dispersive Infrared) analyzer.

The details on the analysis and calibrations have been reported in several studies [e.g. Nakazawa *et al.*, 1997; Tohjima *et al.*, 2002; Tohjima *et al.*, 2005; Tohjima *et al.*, 2010 and references therein].

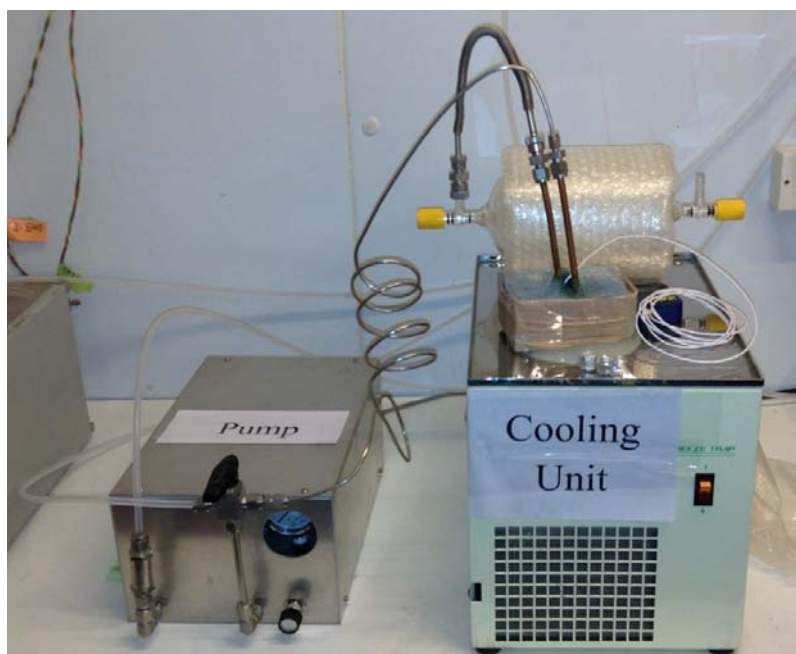


Figure 2.8: Picture showing the pump, cooling unit and glass bottle connected to it, as used for collecting air samples at -30°C .

2.4. Satellite Data

Along with the different in situ measurements, available datasets from the following satellite based sensors have also been used in the present study:

2.4.1. Tropospheric Emission Spectrometer (TES)

Tropospheric Emission Spectrometer (TES) is a satellite instrument onboard NASA's Aura satellite, part of the NASA's Earth Observing System (EOS) (<http://tes.jpl.nasa.gov/mission/>). TES is a Fourier Transfer infrared Spectrometer (FTIR) which measures the infrared radiance emitted from earth's surface and by atmospheric gases and aerosols. TES has the spectral coverage from 650 to 2250 cm^{-1} which is used to retrieve the vertically resolved profiles of ozone, CO, CH₄ and

water vapor. The spatial resolution of TES data is 0.5 x 0.5 km nadir. In global survey mode, TES conducts observations approximately every two days. In the present study, TES Level 2 data of ozone vertical profiles, tropospheric column ozone and tropopause pressure datasets obtained from <ftp://14ftl01.larc.nasa.gov/TES/TL2O3N.005/> have been used for the analysis of ozonesonde observations over Nainital. Moreover, the Level 3 datasets of tropospheric column ozone and CO at 681 hPa data from TES have been investigated over a semi-urban site in the Indo-Gangetic Plain. TES CO retrievals are used at 681 hPa because TES has higher sensitivity at this level [Rinsland *et al.*, 2006].

2.4.2. Moderate Resolution Imaging Spectroradiometer (MODIS)

This study utilizes the spatial and temporal variability in fire count data available from Moderate Resolution Imaging Spectroradiometer (MODIS) aboard Aqua and Terra satellites (<http://modis-land.gsfc.nasa.gov/fire.html>). The fire detection algorithm uses the variations in the brightness temperatures obtained from the MODIS measurements of 4 and 11 μm radiances. The fire detection strategy is based upon the absolute detection in the cases when fire strength is sufficiently high and on the detection relative to the background thermal emissions of the surrounding pixels [e.g. Justice *et al.*, 2002]. In this way the variations in the surface temperature and sunlight reflections are accounted for. Spatial resolution of MODIS is 1 km and it covers the global fire activity twice a day. MODIS provides the data for location of the fire, detection confidence, and fire radiative power. The fire data has also been available from another satellite based sensor Advanced Along Track Scanning

Radiometer (AATSR). However, this sensor operated only during the nighttime which could lead to an underestimation of the total fire activity [Arino and Rosaz, 1999].

2.4.3. Ozone Monitoring Instrument (OMI)

Ozone Monitoring Instrument (OMI) is a nadir-viewing imaging spectrometer onboard NASA's Aura satellite. OMI measures various key air pollutants including NO₂, SO₂, and aerosols with global daily coverage (<http://aura.gsfc.nasa.gov/instruments/omi.html>). OMI is a successor of TOMS with added capabilities to measure many more atmospheric constituents. OMI measurements of ozone profiles in the UV wavelengths complement the observations being made by TES in IR and MLS in microwave. OMI retrieved tropospheric column NO₂ (OMNO2e.003) version-3 and Level-3 daily data at 0.25°x 0.25° resolution have been used to study the temporal variations in NO₂ in the northern India.

2.4.4. Tropical Rainfall Measuring Mission (TRMM)

The Tropical Rainfall Measuring Mission (TRMM) is a collaborative mission between NASA, USA and JAXA, Japan (<http://pmm.nasa.gov/TRMM>). The main objectives of TRMM include the measurements of rainfall and energy of tropics and subtropics (<http://trmm.gsfc.nasa.gov/>). The main rainfall instruments are TRMM Microwave Imager (TMI), Precipitation Radar (PR), and Visible and IR Radio System (VIRS) [Kummerow *et al.*, 1998]. This study uses monthly rainfall data

TRMM 3B43 V6 at 0.25°x 0.25° spatial resolution to examine seasonal variations in rainfall over the northern India.

2.4.5. Atmospheric Infrared Sounder (AIRS)

Atmospheric Infrared Sounder (AIRS) instrument is onboard NASA's Aqua satellite and is also a part of its Earth Observing System. Aqua satellite covers the globe from pole to pole twice a day (<http://airs.jpl.nasa.gov/mission/description/>). The term “sounder” indicates that the temperature and water vapor are measured as a function of the altitude. AIRS also measures various trace components and clouds. AIRS measures the infrared brightness from the earth's surface and atmosphere. The instrument contains grating spectrometer which disperses the infrared energy across array of detectors (http://airs.jpl.nasa.gov/instrument/how_AIRS_works/). In the present study, the Level-3 data of tropopause pressure has been obtained from AIRS at 1°x1° resolution.

More details regarding the measurements and validations of TES [*Beer et al.*, 2001; *Rinsland et al.*, 2006; *Worden et al.*, 2007; *Nassar et al.*, 2008], MODIS [*Kaufman et al.*, 1998; *Justice et al.*, 2002], OMI [*Bucsela et al.*, 2006], TRMM [*Kummerow et al.*, 1998; *Adler et al.*, 2000; *Giglio et al.*, 2003] and AIRS [*Divakarla et al.*, 2006] can be seen elsewhere.

2.5. Modeling the Atmospheric Processes

The atmospheric models simulate the physical, chemical and dynamical processes and play vital roles in the interpretation of the field observations and in the

understanding of the key variables and processes [*Jacobson, 2005*]. A deviation of model simulations from the observations generally indicates insufficient understanding or omission of the processes. Moreover, models are also used to get the information on the future state of the atmosphere such as possible impacts of the changes in the anthropogenic emissions. Depending upon the spatial dimensions and complexity models are classified as zero or box model and one, two, and three dimension models. These models provide invaluable information on the spatial and temporal distribution of trace gases. The use of these models is essential over south Asian region where the in situ measurements are very sparse. Meteorological models have been used for simulating the weather and climate while air pollution is generally simulated using the photochemical models. Photochemical models are now being combined with the meteorology to simulate them as a whole to understand the role of emissions, chemistry and transport of pollution.

The zero dimensional (box) models do not incorporate any coupling between the chemistry and transport and are generally used to study the complex chemistry at a fixed location or to follow an air parcel along its trajectory [e.g. *Madronich, 2006*]. In the one-dimensional model, the atmosphere is treated as a single vertical column and variations with latitude and longitudes are not considered. These are generally used to understand the vertical distribution of the trace species [e.g. *Kasting and Singh, 1986*]. The two dimensional models, which consider the variability in latitude and altitude, are used to simulated chemistry and dynamics in the stratosphere and mesosphere which are more homogeneous as compared with troposphere [e.g. *Brasseur et al., 1999*]. The most realistic representation of the atmosphere is made using the three dimensional models having variations in longitude, latitude as well

as altitude [e.g. *Grell et al.*, 2005], however, these models need much more computational resources. The three dimensional models are generally classified into two types: global models and regional models. Global models have generally coarser spatial resolution i.e. 100 km or more while the resolution in regional models can be as fine as few hundred meters.

The physical, chemical and dynamical processes occurring in the atmosphere are coupled with each other and can be described using the continuity, momentum and energy equations. The time dependent processes are generally represented by ordinary differential equations while the space and time dependent processes are represented by partial differential equations.

2.5.1. Physical Processes

The incoming solar radiation and outgoing terrestrial radiations are affected by the gases and particles present in the atmosphere mainly via absorption and scattering processes. Ozone, carbon dioxide and water vapor are among the main constituents which contribute to the absorption of the terrestrial radiation in the lower atmosphere. These molecules reemit the radiation at different wavelengths. Scattering occurs when the particles or large gas molecules interact with the incident electromagnetic radiation and redirect it from its original path.

These processes are governed by physical laws including Beer-Lambert's law, Stefan-Boltzmann law, Wien's displacement law and Kirchoff's law. The Beer-

Lambert's law describes the logarithmic attenuation of the incident radiation in the atmosphere. Stefan-Boltzmann law states that the amount of the emitted radiation is directly proportional to the fourth power of the absolute temperature of the emitter. Wien's displacement law describes that the wavelength corresponding to the maximum emission is inversely proportional to the absolute temperature of the emitter. Further, Kirchoff's law adds that a good absorber of the radiation is also a good emitter of those wavelengths.

2.5.2. Chemical Processes

In the chemical processes, the reactant gases collide with each other and transform chemically into the products. A typical bi-molecular and tri-molecular reaction and their reaction rates can be represented as follows:

Bi-molecular: $R_1 + R_2 \rightarrow P_1 + P_2$ with reaction rate $d[P_1]/dt = k_1[R_1][R_2]$

Tri-molecular: $R_1 + R_2 + R_3 \rightarrow \text{products}$ with reaction rate $d[\text{prod}]/dt = k_2[R_1][R_2][R_3]$

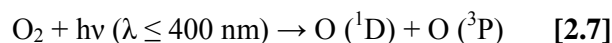
Here, the R_i and P_i are representing the reactants and products respectively and square brackets denote their concentrations, k_i represent the reaction rate coefficients.

In the photochemical processes, any species after absorbing a UV or visible photon can jump into an electronically excited state and can undergo one of the following four processes:

- (a) excited species reemit the photon and return to a lower electronic state (fluorescence or phosphorescence)
- (b) Collision with another molecule resulting in the transfer of energy (quenching)
- (c) Chemical reaction during its collision
- (d) Uni-molecular change such as its photo-dissociation

The probability of any of these processes is called as the quantum yield and thus the sum of the quantum yields for all the processes is unity.

For example, the photolysis of molecular oxygen which takes place as follows:



The rate of loss of O_2 can be written as $d[\text{O}_2]/dt = -J[\text{O}_2]$

Where, J is the rate constant for the O_2 photolysis and can be determined by the number of photons (solar flux q), the ability of the molecule to absorb these photons (absorption cross section σ_a) and the probability of the photo-dissociation. The product of these terms is integrated for all nonzero terms over all wavelengths as follows:

$$J = \int_{\lambda} \sigma_a (\lambda) \psi (\lambda) q(\lambda) d\lambda \quad [2.8]$$

The quantum yields and absorption cross sections are the fundamental properties of molecules which are generally estimated during laboratory experiments.

2.5.3. Dynamical Processes

The conservation of mass in an infinitesimally small volume of the fluid is expressed by the continuity equation. This equation is used to simulate the evolution

of an air parcel over time by taking the sources, sinks and transport into the account.

For a chemical species i with mass density ρ_i , this equation [Jacobson, 2005] can be written as:

$$\frac{\partial \rho_i}{\partial t} + \nabla \cdot (\rho_i \mathbf{v}) = S_i$$

Where $\mathbf{v} = (u, v, w)$ is the wind velocity vector, $\nabla \cdot (\rho_i \mathbf{v})$ is the flux divergence i.e. the flux out of the volume minus flux in and represents the transport term. S_i is the net local source term. The net source term include the contributions from the emissions, chemical processes and deposition. These processes will be discussed further in context of various models in the sections 2.6.2, 2.6.3 and 2.6.4. The continuity equation, along with the initial and boundary conditions, is used to investigate the spatial and temporal variability in the atmospheric species.

In the present study, different models have been used for simulations of air mass trajectories (HYSPLIT model), chemical evolution of air parcels (NCAR Master Mechanism Box model) and spatial and temporal variations in ozone and precursors (WRF-Chem and MATCH-MPIC) as discussed in the following subsections:

2.6. Models Used in the Study

2.6.1. Back-Air Trajectories (HYSPLIT)

Back-air trajectory simulations are an important tool to trace the sources of air pollution and to understand the role of local and regional influences, long-range transport etc. in the variabilities of ozone and other trace species. In the present study, Hybrid Single Particle Lagrangian Integrated Trajectory (HYSPLIT) model (http://www.arl.noaa.gov/HYSPLIT_info.php) has been used for simulating the back air trajectories of the air masses over the northern Indian region. This model has been developed by the collaborative work primarily among NOAA and Australia's Bureau of Meteorology and other institutions. HYSPLIT model can be driven by existing standard meteorological forecast fields obtained from regional or global models. Generally, the meteorological datasets such as NCEP/NCAR reanalysis available at the spatial resolution of $2.5^{\circ} \times 2.5^{\circ}$ at every 6 hours are used to run the HYSPLIT model. While in the present study, GDAS (Global Data Assimilation System) meteorological fields available at higher resolution ($1^{\circ} \times 1^{\circ}$) available at every three hours have been used.

These datasets include the gridded data of zonal, meridional and vertical wind components, temperature and other meteorological parameters at different pressure levels. The gridded data of topography and surface pressure are also provided as an input to the models. HYSPLIT model has also been configured to provide the variations in the meteorological parameters such as temperature, pressure, relative humidity, solar radiation and rainfall along the trajectories. More details of the back-air trajectory simulations using HYSPLIT model and obtaining meteorological

parameters along the trajectory can be seen elsewhere [Draxler and Rolph, 2012; Draxler et al., 2012].

2.6.2. Chemical Box Model (NCAR-MM)

The concentration of any chemical species X can be controlled by emissions, chemistry, transport and deposition as shown in the layout of an atmospheric box (Figure 2.9). The production and loss rates of X have contributions from the emission (E), chemical production (P), chemical loss (L) and deposition. In the box model, the spatial distribution of the species is not incorporated and the box is assumed to be well mixed.

The lifetime t of X in the box can be written in the terms of its mass (m in kg) and its removal rate ($F_{\text{out}} + L + D$ in kgs^{-1}) as follows:

$$t = m / (F_{\text{out}} + L + D)$$

The mass balance equation for the abundance of X can be written as follows:

$$dm/dt = \sum \text{sources} - \sum \text{sinks}$$

$$dm/dt = F_{\text{in}} + E + P - F_{\text{out}} - L - D$$

This equation can be solved for deriving the time evolution of the abundance i.e. $m(t)$ if all the terms on the right side are known. More details of box model can be seen elsewhere [e.g. Jacob, 1999b].

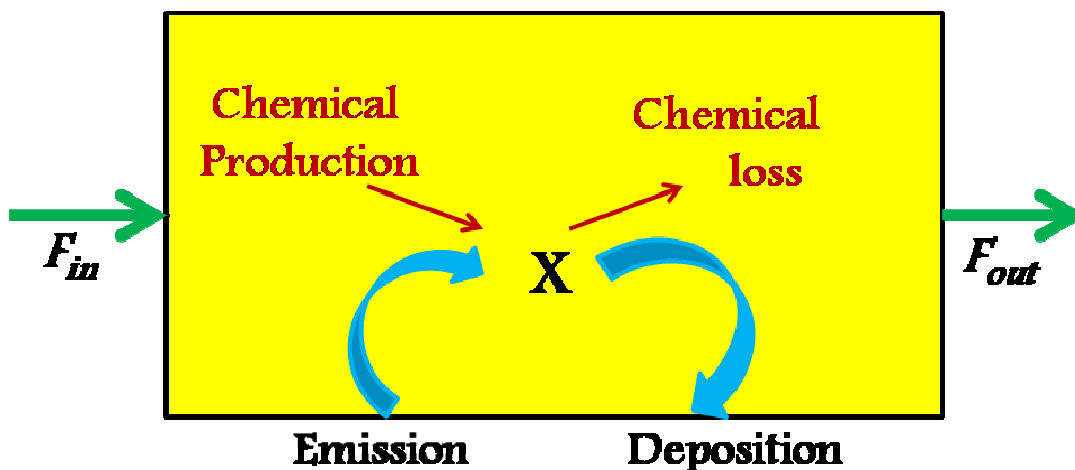


Figure 2.9: A Layout showing various processes influencing the concentration of a species X in an atmospheric box.

In the present study, the NCAR Master Mechanism (NCAR-MM) box model developed at National Center for Atmospheric Research, Boulder, USA, has been employed for simulating the diurnal variations in surface ozone and for investigating the sensitivity of ozone variations to changes in NO_x and NMHCs. This model consists of highly detailed gas phase chemistry with about 2000 species participating in about 5000 reactions and can simulate the time evolution of an air parcel initialized with known concentrations assuming no further dilution, emissions, and transport (<http://cprm.acd.ucar.edu/Models/MasterMech/index.shtml>).

In this study, the model is initialized with O_3 , H_2O , NO , NO_2 , CO , OH , HO_2 , CH_2O , CH_4 , i-butane, n-butane, Isoprene, Xylene, and Toluene while N_2 , O_2 , M and photons are hard-wired in the model. Photolysis rate coefficients i.e. j-values are estimated using the Tropospheric Ultraviolet Visible (TUV) radiative transfer model [Madronich and Flocke, 1999] with 4-stream discrete ordinates radiative transfer

solver [Stamnes *et al.*, 1988]. Further details of the NCAR-MM model can be seen elsewhere [Madronich, 2006].

2.6.3. Regional Chemistry Transport Model (WRF-Chem)

The WRF model is a fully compressible and non-hydrostatic model. This study uses the version 3.3.1 of the model. WRF-Chem model developed jointly by NOAA and some other research institutes (<http://ruc.fsl.noaa.gov.wrf/WG11>). Its vertical coordinate is a terrain-following hydrostatic pressure coordinate. The WRF-Chem model differs from most of the present day air quality models (e.g. SMAQ, CMAQ) in the sense that air quality and meteorological components are fully consistent with each other and thus it is termed as an “online” model [Grell *et al.*, 2005]. The other air quality models are called as “offline” as they treat the chemistry system independently of the meteorological model. However, the independent treatment of chemistry and meteorology in the offline models may lead to loss of important information about the processes occurring on time scales much smaller than output time of the meteorological model (e.g. wind speed and direction, rainfall and cloud formation). In contrast to the “offline” models, the chemistry and meteorology components of WRF-Chem use same transport scheme, same horizontal and vertical grids, same time steps and same physics schemes for the subgrid-scale transport. Additionally, WRF-Chem model may also include the feedbacks between the meteorology and chemistry. The major components of the WRF-Chem model are the (1) WRF Preprocessing System, (2) real data initialization and (3) the WRF solver (ARW or NMM) including the chemistry. These components are described in detail in the following subsections.

2.6.3.1. The WRF Pre-processing System (WPS)

The WRF Preprocessing System (WPS) is a set of three programs whose collective role is to prepare the input data for the real data initialization program by defining the simulation domain and interpolating the static terrestrial fields and the meteorological data to the model domain. The three programs are known as geogrid, ungrib and metgrid respectively. The geogrid defines the model domain and interpolates static geographical data to the grids; ungrib extracts meteorological data from the GRIB-formatted files; and metgrid program combines the outputs of the geogrid and ungrib programs and horizontally interpolates the meteorological data to the simulation domain. The work of vertically interpolating meteorological fields to WRF eta levels is performed within the *real* program. The WPS programs read the parameters from a common “namelist.wps” file. This namelist file has separate namelist records for each programs and a shared section containing the parameters to be used by more than one WPS program. The information about WRF model solver (ARW or NMM), the start and end time of the simulations for each domain, total number of domains to be used in the simulation, time resolution of input meteorological data and the input/output formats is declared under the shared section of namelist.wps. The parameters required for defining the simulation domains such as the number of grid points in the west-east and north-south direction, spatial resolution, map projection, reference latitude and longitude for the domain and the location of static terrestrial data are defined under the geogrid section. In this study, the simulation domain is defined on the Mercator projection with center at 25° N, 80° E. The domain covers nearly the entire South Asian region at 45 km spatial resolution with 90 grid points in both west-east and north-south directions. The terrain height, land-use/vegetation, soil properties and albedo are

interpolated from 10 min (approximately 19 km) U. S. Geological Survey to the model domain.

After defining the simulation domain, the next step is to extract the meteorological fields using the ungrid program. The ungrid program reads GRIB files and writes the data in a simple format, called the intermediate format. The GRIB files generally represent the output of other regional/global models. In this study, NCEP Final Analysis (FNL) data from Global Forecasting System (GFS) available at spatial resolution of 1° and temporal resolution of 6 hours (<http://dss.ucar.edu/datasets/ds083.2/data/>) has been used for initializing the meteorological fields in the model. The final step of the WPS system is to combine the output of geogrid and ungrid programs by using the metgrid program. The metgrid program horizontally interpolates the meteorological fields extracted by the ungrid program onto the simulation domain defined by the geogrid program. The interpolated metgrid output can then be used by the real data initialization program.

2.6.3.2. Types of Emissions Used

Anthropogenic emissions of CO, NO_x, SO₂, NMVOCs, PM₁₀, PM_{2.5}, BC and OC are obtained from INTEX-B emission inventory [Zhang *et al.*, 2009] and RETRO database as discussed in detail recently [Kumar *et al.*, 2012a; Kumar *et al.*, 2012b]. Biomass burning emissions are provided from NCAR Fire Inventory (FINNv1) [Wiedinmyer *et al.*, 2011]. Biogenic emissions are online calculated using MEGAN model [Guenther *et al.*, 2006]. Regional atmospheric Chemical Mechanism

(RACM) is the gas phase chemistry used which includes 237 reactions among 77 species [Stockwell *et al.*, 1997]. The initial and boundary conditions for chemical fields are updated every 6 hours from MOZART [Emmons *et al.*, 2010]. Model time step is set to 180 s and output at every one hour is obtained.

2.6.3.3. Model Physics

The different physics options used in the model configuration are the microphysics, cumulus parameterization, planetary boundary layer, land-surface model and radiation. The WRF-Chem model encompasses a variety of single and double moment schemes to explicitly resolve water vapor, clouds and precipitation processes. The single moment schemes predict only the number concentrations while double moment schemes predict not only the number concentration but also the mixing ratios of cloud, ice, snow, graupel and hail. The prediction of both number concentrations and mixing ratios allows for a more robust treatment of the particle size distributions, which are very important for calculating the microphysical process rates. Therefore, the double moment microphysical parameterization described by Thompson *et al.*, [2004] has been used for the present study. The Kain-Fritsch cumulus parameterization scheme that utilizes a simple cloud model with moist updrafts and downdrafts including the effects of entrainment and relatively simple microphysics [Kain, 2004] has been used in the present study. The radiation scheme provide atmospheric heating due to the radiative flux divergence and surface downward long-wave and shortwave radiation for the ground heat budget. Long-wave radiation includes infrared or thermal radiation absorbed and emitted by gases and surfaces. Shortwave radiation includes the visible and

surrounding wavelengths that make up the spectrum. Hence, the only source is the Sun, but the process includes absorption, reflection and scattering in the atmosphere and at the surface. In the present model configuration, the rapid radiative transfer model (RRTM) [Mlawer *et al.*, 1997] is used to simulate long-wave radiation. The shortwave radiation processes are simulated using the Goddard shortwave scheme [Chou and Suarez, 1994].

The Noah land-surface model, developed jointly by NCAR and NCEP, has been used in the model set-up for this study. The Planetary boundary layer (PBL) scheme determine the flux profiles within the well-mixed boundary layer and the stable layer and thus provide atmospheric tendencies of temperature, moisture (including clouds) and horizontal momentum in the entire atmospheric column. Here, the Mellor-Yamada-Janjic (MYJ) scheme is used for the parameterization of the turbulence in the PBL and free atmosphere [Janjic, 2002]. The setup and detailed evaluation of WRF-Chem model over South Asia has been provided recently [Kumar *et al.*, 2012a; Kumar *et al.*, 2012b].

2.6.4. Global Chemistry Transport Model (MATCH-MPIC)

Spatial and temporal variations in ozone and related species are also obtained from the offline global chemistry transport model MATCH-MPIC (Model of Atmospheric Transport and CHemistry – Max Planck Institute for Chemistry version 3.0). MATCH-MPIC was developed at the National Center for Atmospheric Research and the Max Planck Institute for Chemistry

(http://cwf.mpic.de/~cwf/match/match_overview.html). The version from *Lawrence et al.* [2003a] developed for chemical weather forecasts is used here, with a few updates, most importantly at a higher resolution (T106 vs. T42), and with updated emissions. The simulations here are driven by NCEP/NCAR reanalysis meteorology data at T106 horizontal resolution ($\sim 0.9^\circ \times 0.9^\circ$) with 42 vertical levels (from the surface to ~ 2 hPa) available every 3 hours. A time step of 10 minutes is used in the simulations.

The meteorology component of MATCH uses the NCEP data to simulate advective transport [*Rasch and Lawrence*, 1998], and also to diagnose convection [*Zhang and McFarlane*, 1995; *Hack et al.*, 1994], vertical diffusion [*Holtslag and Boville*, 1993], cloud fractions [*Slingo*, 1987], and cloud microphysics [*Rasch and Kristjansson*, 1998]. Surface emissions of CO, NO_x, and non-methane hydrocarbons for industrial sources are taken from EDGAR inventory [*Olivier et al.*, 1999]. Biomass burning emissions are based on climatological emissions from GFEDv2 [*Van der Werf et al.*, 2006]. Soil NO_x emissions are taken from *Yienger and Levy* [1995]. Lightning NO_x emissions are calculated online based on convective mass flux, with the global lightning NO_x emissions scaled to 2 Tg(N)/yr. Aircraft emissions are taken from *Schmitt and Brunner* [1997]. Photolysis rates are computed using online actinic flux calculations at eight representative wavelengths, and the modeled cloud fractions and ozone profiles. Based on the technique of *Landgraf and Crutzen* [1998], including consideration of modeled cloud and O₃ profiles. Dry deposition is from *Ganzeveld and Lelieveld* [1995], and heterogeneous loss of N₂O₅ on aerosols is based on *Dentener and Crutzen* [1993]. Cloud scavenging by precipitation and gravitational settling processes in non-precipitating clouds are

computed based on the modeled precipitation production rates in each grid cell, as described in *Lawrence and Crutzen* [1998] and *Crutzen and Lawrence* [2000].

Over the Asian region, this model is shown to reproduce the NO_x variability well including the enhanced abundances of NO₂ over China and northeast India, in addition to the higher levels during the biomass burning periods, however, the absolute levels were somewhat underestimated [*Kunhikrishnan et al.*, 2004]. Further details of MATCH-MPIC description as well as evaluation can be found elsewhere [*Rasch et al.*, 1997; *Lawrence et al.*, 1999; *Von Kuhlmann*, 2001; *Von Kuhlmann et al.*, 2003; *Lawrence et al.*, 2003a].

2.6.5. Global Chemistry Transport Model (MOZART)

The Model for Ozone and Related chemical Tracers (MOZART) is an offline global chemistry transport model developed collaboratively by National Center for Atmospheric Research (NCAR) and the Max Planck Institute for Meteorology and NOAA/GFDL (<http://www.acd.ucar.edu/gctm/>). In the present study the results from version 4 of the MOZART model has been obtained from the model website (<http://www.acd.ucar.edu/wrf-chem/mozart.shtml>). In this setup, the input meteorological fields are used from NASA GMAO GEOS-5 model. The anthropogenic emission data is taken from the ARCTAS inventory (<http://www.cgrer.uiowa.edu/arctas/emission.html>) and fire emissions are taken from FINN-v1 [*Wiedinmyer et al.*, 2011]. The spatial resolution of the model output is 1.9x2.5 degree with 56 pressure levels. More detailed description of this model and evaluation can be seen in *Emmons et al.* [2010].

Chapter 3

Surface Ozone Variations at Pantnagar in the Indo- Gangetic Plain

The Indo-Gangetic Plain (IGP) region is one of the most densely populated regions in the world, however, ground based measurements of air pollutants are very limited here. IGP region stretches from the Indus river system in Pakistan to the delta of Ganges River in Bangladesh in the west-east direction. The high altitude Himalayan range is its northern border while plateau of Deccan is located in its south. IGP region in the northern India encompasses a variety of emission sources such as coal-based thermal power plants, industries, vehicular emissions, bio-fuel burning, mining and crop-residue burning. Analysis of INTEX-B emission inventory data shows that the emissions of CO, NO_x and NMVOCs are significantly higher over the IGP region than those over the rest of India [Zhang *et al.*, 2009]. Pollutants emitted

from this region get trapped in the complex hilly terrain leading to the elevated levels of trace gases and aerosols. This spatial heterogeneity in the distribution of trace species have been reported using satellite based observations of tropospheric ozone, CO, NO₂ and aerosol properties [Fishman *et al.*, 2003; Di Girolamo *et al.*, 2004; Jethva *et al.*, 2005; Gautam *et al.*, 2009; Kar *et al.*, 2010; Giles *et al.*, 2011]. The outflow of the pollutants from the IGP region further influences the pristine oceanic regions surrounding India [Lelieveld *et al.*, 2001; Lal *et al.*, 2007; Srivastava *et al.*, 2011].

Despite such importance, the observations of trace gases are highly sparse in the IGP region in the northern India while previous studies were mostly confined to the western and southern parts of India [e.g. Lal *et al.*, 2000; Naja and Lal, 2002; Beig *et al.*, 2007; Reddy *et al.*, 2008]. However, surface ozone observations with a complete seasonal cycle have been made only at two sites, in the northern India. One site is a highly urbanized megacity (Delhi) [Ghude *et al.*, 2008a] and the other one is a high altitude clean site in the central Himalayas (Nainital) [Kumar *et al.*, 2010]. In light of these conditions, continuous surface ozone observations have been initiated at a semi-urban site Pantnagar in the IGP region since March 2009.

3.1. Observation Site

Surface ozone measurements are made at the College of Basic Sciences and Humanities (CBSH) in the G. B. Pant University of Agriculture and Technology (GBPUAT), Pantnagar (29.0°N, 79.5°E, 231m amsl) during March 2009 to June

2011. The geographical location of this site overlaid on the topographical and population density (CIESIN) maps is shown in the Figure 3.1.

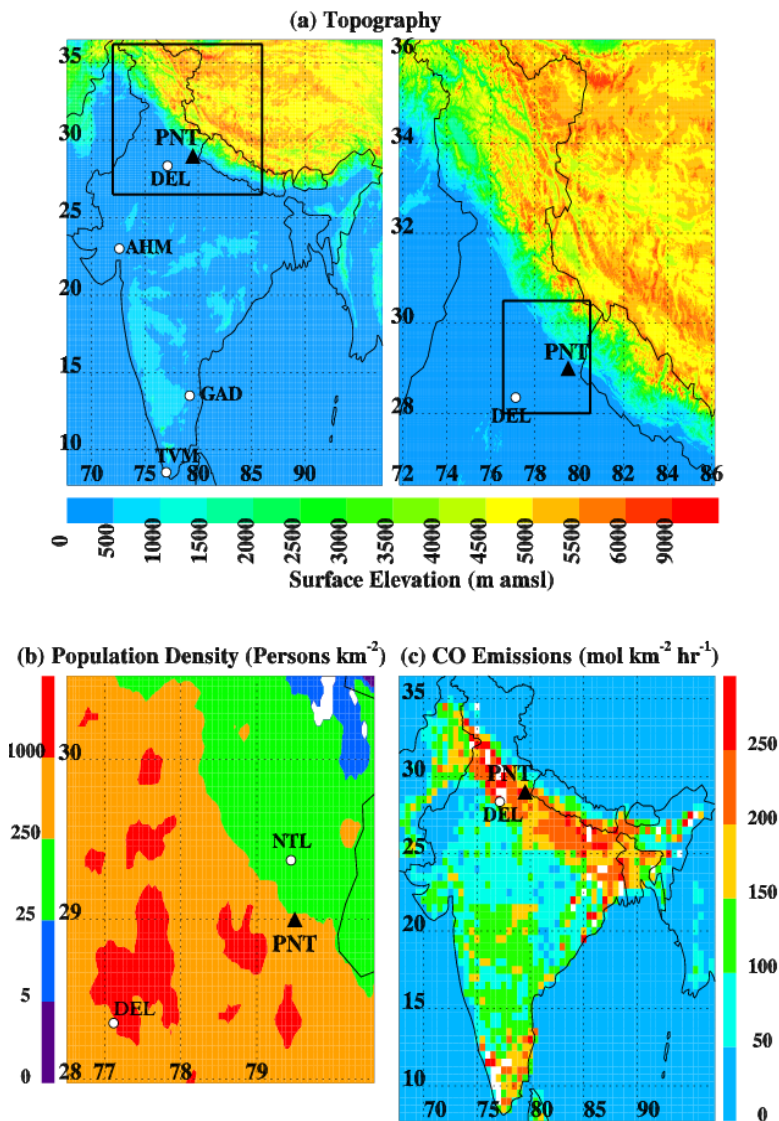


Figure 3.1: (a) Topographical map of India with zoomed map of the northern India, (b) population density around the observation site, and (c) annual average CO emissions (INTEX-B) over India are shown. A belt of higher CO emissions, from the northern India to the eastern side, is the IGP region. Observation site, Pantnagar (PNT) is marked with a black filled triangle, other sites used for comparison namely

Delhi (DEL), Ahmedabad (AHM), Gadanki (GAD), Trivandrum (TVM) and Nainital (NTL) are marked with white filled circles.

Here it is evident that the topography in this region is very complex as high altitude Himalayan Mountains are in the north while low altitude plains are located in the south and west of this site. Mountains of 1500 to 2000 m altitude are about 50 km away, while, the mountains of 4000 to 5000 m altitude are about 130 km away from the site. The population density around the site is about 250 to 1000 persons per km² while it is significantly less (25 to 250 persons per km²) in the northern region. The university campus encompasses a large area with a perimeter of about 30 km, which is used primarily for the agricultural research. There are no major anthropogenic emissions except the local vehicular movement inside the university campus. Some small-scale industries are located in the nearby towns such as Rudrapur and Haldwani (12-25 km away). The nearest megacity Delhi is about 225 km away in the southwest of Pantnagar. Annual average anthropogenic emissions of CO (INTEX-B) are shown in the Figure 3.1(c), in which the higher emission belt from north to east largely represents the IGP region. The measurements of surface ozone have been made using online ozone analyzers (Teledyne M400 E and Thermo 49i) based on the UV light absorption technique. The ambient air inside the analyzer is drawn through a teflon tube from the rooftop of the second floor. In addition, air samples have been collected from Pantnagar and Haldwani in pre-evacuated glass bottles for the analysis of CO and CH₄ using Gas chromatography. These measurement techniques are discussed in Chapter 2 (section 2.1) and more details can be seen elsewhere [Lal *et al.*, 2000; Naja and Lal, 2002; Lal *et al.*, 2007; Kumar *et al.*, 2010].

3.1.1. General Meteorology

Three day back air trajectories are simulated at Pantnagar at an altitude of 1000 m above ground level (AGL) for January, April, July and October representing winter, spring, summer-monsoon and autumn seasons (Figure 3.2.) using the HYSPLIT model. The trajectories are color coded according to the atmospheric pressure to depict the altitude ranges attained by the air masses before reaching to the site. Wind patterns are generally northerly-north westerly during winter while air masses circulate over the continental Indian region including polluted IGP during spring and autumn. Cleaner marine air masses arrive to the site during the summer-monsoon. Such seasonal changes in the synoptic winds are generally seen every year over this region [Asnani, 2005; Kumar *et al.*, 2010]. Moreover the analysis of the back air trajectories indicate that air masses are mostly within the boundary layer during spring when the average mixing depth is higher (~2500 m).

In situ measurements of meteorological parameters are not available at the site during the study period and therefore GDAS data available every 6 hours at a spatial resolution of $1^{\circ} \times 1^{\circ}$ have been used to obtain the solar radiation, temperature and mixing depth using HYSPLIT model [Draxler and Rolph, 2012]. Rainfall data has been taken from TRMM satellite as discussed in chapter 2. HYSPLIT simulated solar radiation is observed to be in good agreement with another meteorological dataset NCEP ($r^2 = 0.98$). The mixing depth is estimated using the Turbulent Kinetic Energy (TKE) profile method in which mixing depth is assigned to the height at which TKE either decreases by a factor of two or to value less than 0.21. More

details of this model and meteorological datasets are available elsewhere [e.g. Draxler *et al.*, 2012].

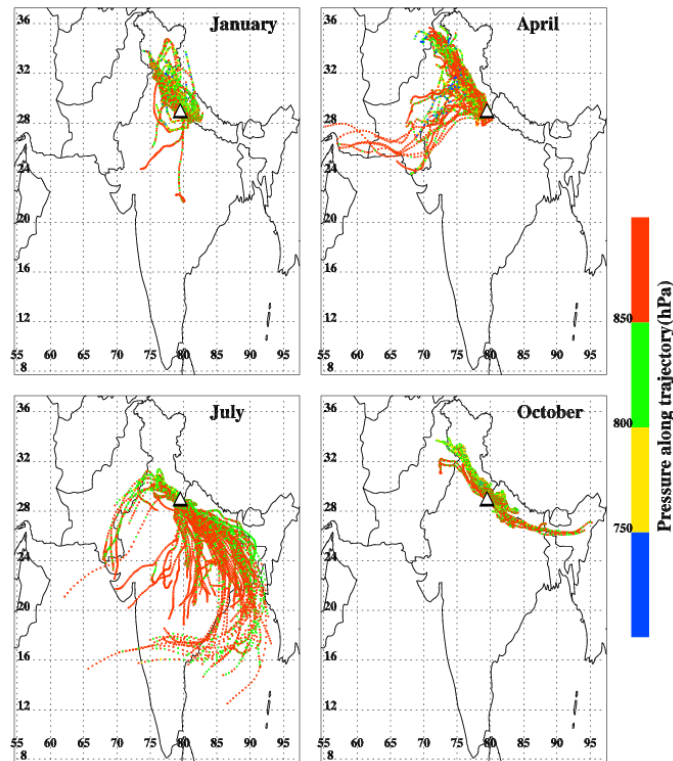


Figure 3.2: Three days backward(1000 AGL) trajectories at Pantnagar for all days in January, April, July and October 2010 are shown. The trajectories are color coded, according to the atmospheric pressure along the trajectories, to portray the altitude range attained by the air masses before arriving at the observation site.

The seasonal variations in the solar radiation, temperature and rainfall over Pantnagar are shown in the Figure 3.3. Noontime solar radiation is lower during winter generally associated with the prevailing foggy conditions. Solar radiation undergoes a systematic increase from January to June and is most intense during

spring. A dramatic reduction in the solar radiation is observed during July to September coinciding with the maximum rainfall associated with the arrival of monsoon. During autumn solar radiation shows a recovery with a secondary maximum. The seasonal variation in temperature is more-or-less similar to that in the solar radiation and it shows maximum during spring (~26°C) and minimum during winter (~12°C).

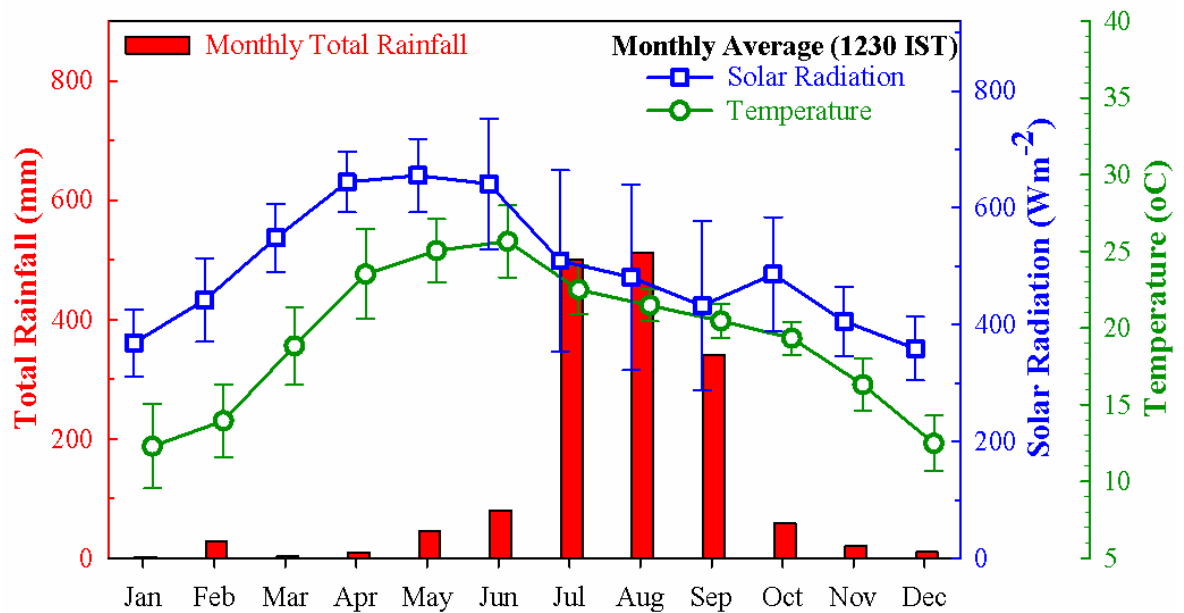


Figure 3.3: Seasonal variations in monthly total rainfall from TRMM (2009-2010), solar radiation (Wm^{-2}) and temperature from GDAS data (2009-2011) over Pantnagar.

3.2. Diurnal Variations in Ozone

Monthly average ozone diurnal variations from January to December during March 2009-June 2011 period at Pantnagar are shown in Figure 3.4. These diurnal variations are characterized by higher values during daytime and lower values during nighttime. Daytime build up is observed throughout the year, except some cloudy/rainy days during July to September. Such diurnal variations are common at urban and rural sites and are attributed mainly to the daytime in situ photochemical production of ozone from its precursors including NO_x , CO, and VOCs [e.g. Kleinman *et al.*, 1994; Naja and Lal, 2002].

However, the dependence of ozone production on the concentrations of its precursors is complex and non-linear [e.g. Lin *et al.*, 1988], and will be discussed later in detail using a chemical box model (see section 3.6). Lower ozone levels during the nighttime are largely associated with the titration of ozone by NO and deposition of ozone. During March to June, ozone mixing ratios attain the lowest value during early morning (just after sunrise). This could be due to ozone losses through reactions with NO and NO_2 , which maybe produced by photo dissociation of NO_3 and N_2O_5 accumulated overnight. Such minimum in the ozone levels just after sunrise has also been reported from another urban site in India [Lal *et al.*, 2000]. In addition to photochemistry, the evolution of the boundary layer during daytime, has also been suggested to contribute to the ozone variations through mixing of near surface air having lower ozone levels with the ozone rich air aloft [Zhang and Rao, 1999; Rao *et al.*, 2003].

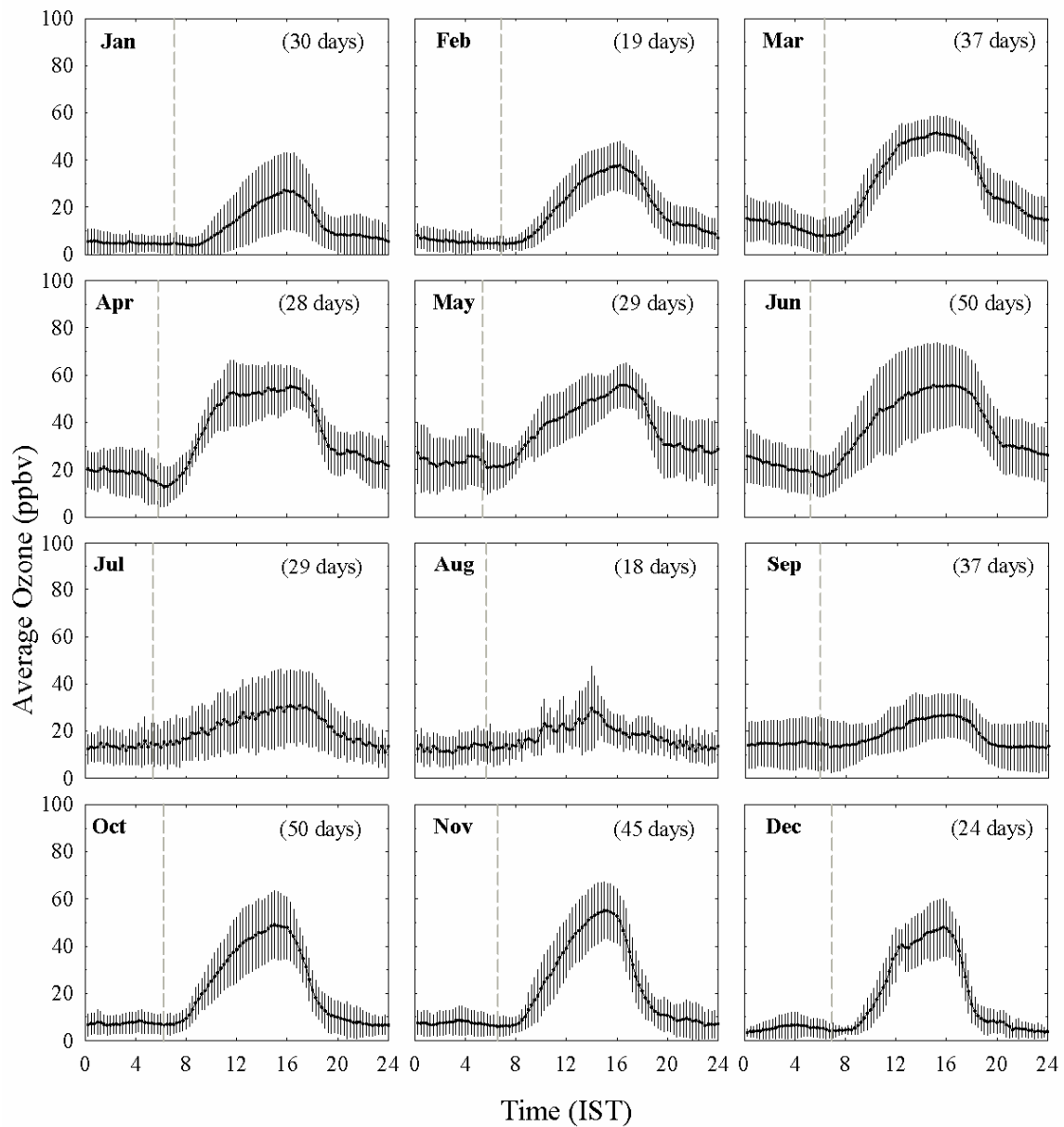


Figure 3.4: Monthly average diurnal variation in ozone at Pantnagar from January to December during March 2009 to June 2011 period. Sunrise times in these months are also shown as dotted lines and total numbers of days for which observations are available in each month are mentioned in the upper right corner in each month plot.

3.2.1. Rate of change in ozone

The morning and evening time rates of change of ozone can be used as an indicator of the chemical environment (i.e. urban or rural) prevailing over a site [e.g. *Naja and Lal*, 2002]. Urban sites generally show symmetric diurnal patterns, i.e. rates of change in ozone during morning and evening hours are similar, while rural sites are characterized by lower loss rates during evening hours. Morning time rate of increase of ozone i.e. ozone formation process strongly depends upon the available amount of precursors, while evening time loss rate i.e. ozone titration process would mainly depend upon the NO levels.

Generally, over the Indian region, NO levels are observed to be lower at rural sites in comparison with those at urban sites, which lead to slower ozone titration by NO during evening hours at a rural site [e.g. *Naja and Lal*, 2002]. In view of this, diurnal variations in average ozone mixing ratios at Pantnagar are compared with those observed at other urban (Delhi and Ahmedabad) and rural (Gadanki) sites in India (Figure 3.5a). The diurnal variations in the rates of change in ozone (ppbv/hour) are also calculated at these four sites (Figure 3.5b). The ozone decrease during evening time at Pantnagar is comparable to those at Ahmedabad and Delhi, while the decrease in ozone is slower at Gadanki.

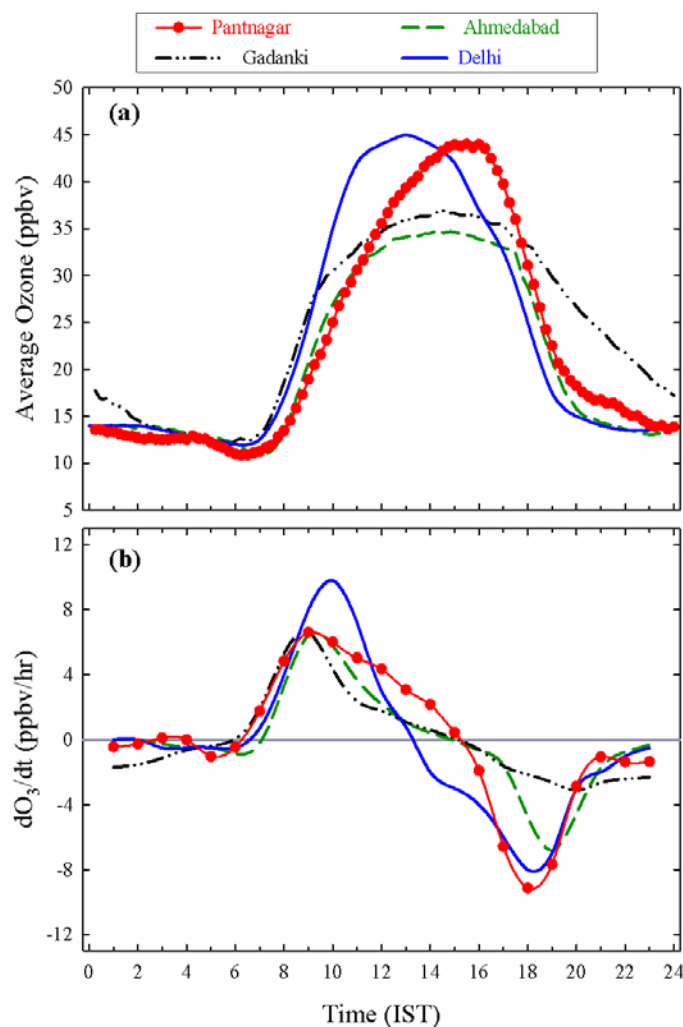


Figure 3.5: (a) Average diurnal variations in ozone and (b) diurnal variation in rate of change of ozone (ppbv/hour) at Pantnagar along with those at Delhi [Ghude et al., 2008a], Ahmedabad [Lal et al., 2000] and Gadanki [Naja and Lal, 2002].

Morning (0800-1100 hours) and evening (1700-1900 hours) time rates of change in ozone are compared among these four sites for annual dataset (Table 3.1). For Pantnagar site, the morning and evening time rate of change of ozone are also estimated for different seasons. Urban sites (Delhi and Ahmedabad) show nearly similar magnitude of morning and evening rates of change whereas the evening rate

of change at the rural site (Gadanki) is lower than that during morning hours. In contrast, morning and evening rates are not similar at Pantnagar; in addition, the evening rate of change (8.5 ppbv hr^{-1}) is higher than morning rate of change (5.6 ppbv hr^{-1}). This suggests that the ozone loss process via NO titration could be stronger at Pantnagar than that at Gadanki indicating that NO_x emissions could be higher over this region (IGP) when compared with those over the Southern region (e.g. Gadanki). The difference in ozone rate of change between daytime and nighttime is much greater during winter and autumn when compared with spring and summer at Pantnagar (Table 3.1).

Table 3.1: Comparison of rate of change in ozone at Pantnagar with those at other sites in India. Positive rate is for increase in ozone while negative is indication for decrease in ozone.

Sites	Rate of change during 0800-1100 hours IST (ppbv/hr)	Rate of change during 1700-1900 hours IST (ppbv/hr)	Reference
Delhi	+8.3	-7.5	<i>Ghude et al., 2008a</i>
Ahmedabad	+5.9	-6.4	<i>Lal et al., 2000</i>
Gadanki	+4.6	-2.6	<i>Naja and Lal, 2002</i>
Pantnagar	All data: $+5.6 \pm 2.9$	All data: -8.5 ± 4.4	<i>Present study</i>
	Winter(DJF): $+4.6 \pm 2.0$	Winter(DJF): -10.3 ± 4.0	
	Spring(MAM): $+8.4 \pm 2.4$	Spring(MAM): -10.6 ± 0.5	
	Summer(JJA): $+3.6 \pm 2.1$	Summer(JJA): -3.0 ± 2.8	
	Autumn(SON): $+5.6 \pm 3.5$	Autumn(SON): -10.0 ± 4.6	

3.3. Seasonal Variation in Ozone

The seasonal variation in monthly average ozone mixing ratios at Pantnagar is depicted in Figure 3.6 along with variations in daily (24-hour) average and daytime (1130-1630 hours) hourly average ozone. The daily and monthly average ozone mixing ratios at Pantnagar show a systematic increase from January to May, decrease sharply in mid June to attain very low levels (10-30 ppbv) that endure until September, and a slight increase during October-November. The seasonal variations in daytime and nighttime average ozone levels (Figure 3.6) are similar to all data monthly average except during October-December, when daytime levels show a sharp increase and thus a secondary maximum that is not seen in all data monthly average. Nighttime data show lower values during October-December. The monthly statistics of surface ozone mixing ratios at Pantnagar is shown in Table 3.2. Average ozone levels are observed to be highest (39.3 ± 18.9 ppbv) in May, while these are lower in January (10.8 ± 12.1 ppbv) and summer-monsoon (16.8 ± 8.9 ppbv in August). Although monthly average ozone levels remain below 40 ppbv throughout the year but hourly average ozone levels in excess of 80 ppbv are observed occasionally particularly during spring. Average CO values, derived from whole air samples at Pantnagar, are moderately high (188-484 ppbv) while average CH₄ values range from 1.81 to 2.11 ppmv.

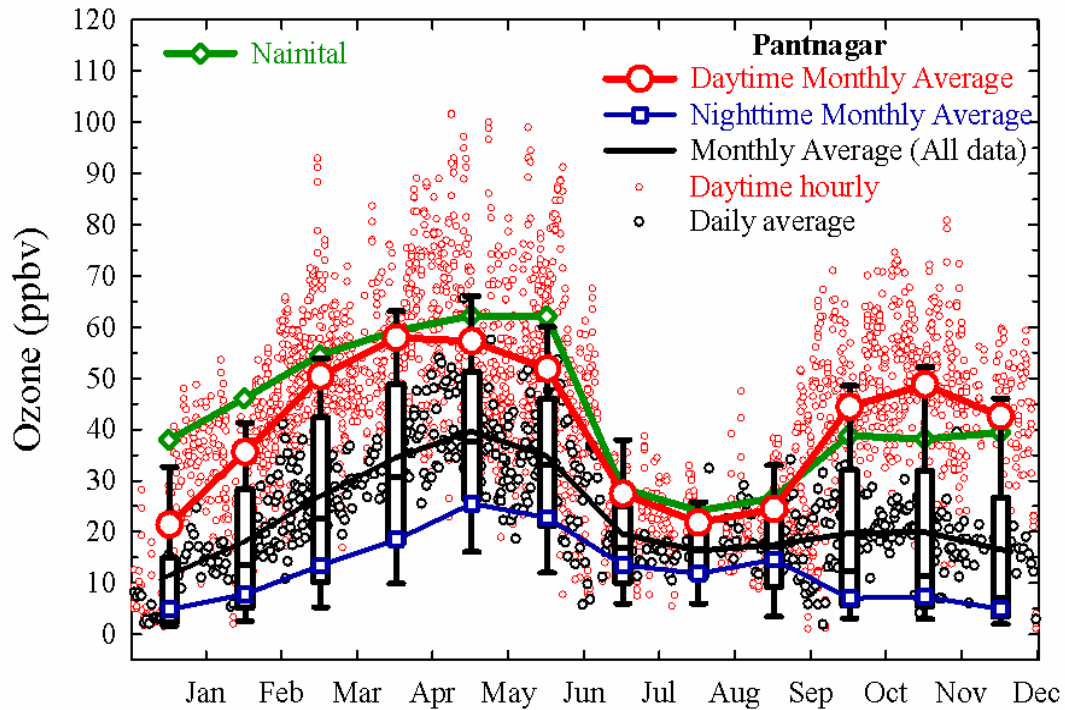


Figure 3.6: Seasonal variations in monthly (24 hours), daily (24 hours), daytime (1130-1630 hours) and nighttime (0100-0300 hours) average ozone at Pantnagar. Monthly average ozone mixing ratios at a nearby high altitude site (Nainital) are also shown.

Since in situ observations of CO and NO₂ are not available with sufficient temporal resolution at Pantnagar, data from space-borne sensors are used to examine seasonal variations in CO and NO₂. TES CO (at 681 hPa), OMI tropospheric column NO₂ and TES tropospheric column ozone are obtained over a 1° x 1° grid box centered at Pantnagar. The seasonal variations in OMI tropospheric column NO₂, TES CO and TES tropospheric column ozone are similar with highest values during spring and lower during summer/monsoon (Figure 3.7). A secondary maximum in these space-

borne observations of ozone, NO₂ and CO during autumn is also seen similar to the daytime average surface ozone observed at Pantnagar (Figure 3.6).

Table 3.2: Monthly average mixing depth, ozone with one sigma deviation, maximum ozone, number of ozone data counts (15 minutes average), average CO, average CH₄ and number of samples during study period at Pantnagar.

Month	Mixing depth (m AGL)	Ozone (ppbv)	Maximum	Ozone Count	CO (ppbv)	CH ₄ (ppmv)	Count
Jan	597 ± 335	10.8 ± 12.1	50	2918	400.7 ± 274.2	2.11 ± 0.22	5
Feb	855 ± 429	18.1 ± 14.7	67	4020	-	-	-
Mar	1476 ± 664	27.0 ± 18.8	97	6376	484.4 ± 114.8	1.94 ± 0.17	5
Apr	2621 ± 749	34.5 ± 20.3	95	4009	292.3 ± 188.6	1.82 ± 0.03	12
May	2556 ± 722	39.3 ± 18.9	105	5777	399.2 ± 204.4	1.82 ± 0.03	12
Jun	2399 ± 849	34.8 ± 18.4	103	6343	187.6 ± 14.9	1.81 ± 0.03	2
Jul	1256 ± 573	19.6 ± 12.7	69	2819	277.1 ± 100.3	1.85 ± 0.05	8
Aug	884 ± 290	16.8 ± 8.9	81	1693	291.2 ± 124.9	1.86 ± 0.11	6
Sep	627 ± 271	17.4 ± 10.8	56	3581	425.4 ± 148.9	2.11 ± 0.18	3
Oct	614 ± 361	19.7 ± 17.7	78	4760	339.8 ± 106.6	2.11 ± 0.08	4
Nov	616 ± 317	20.0 ± 19.1	83	4449	409.9 ± 199.7	2.09 ± 0.19	5
Dec	610 ± 299	16.1 ± 17.2	62	2453	205.1	1.81	1
Average	1358 ± 982	25.0 ± 19.2	105	49198	348.5 ± 176.7	1.91 ± 0.16	63

The seasonal variations in ozone are generally in good agreement with the variations in solar radiation (Figure 3.3) and satellite retrieved lower tropospheric CO and tropospheric column NO₂ (Figure 3.7). Like ozone, all these parameters show an increasing tendency from January to May, decrease to lower levels during June-

September and increase again during October-December. These variations suggest that the coupling of higher solar radiation with higher levels of precursor gases lead to enhanced daytime photochemical ozone production and thus higher ozone levels are observed during spring and autumn. Lower levels of all the species observed during July-September are largely due to Asian monsoonal circulation, which leads to inflow of pristine marine air masses in this region and also suppresses the photochemical activity through widespread cloudy/rainy conditions. The arrival of marine air masses over this region is evident from the back-air trajectory analysis (Figure 3.2) and occurrence of highest rainfall at Pantnagar (Figure 3.3) during these months. During January, this region is generally covered by thick fog and lowest ozone levels observed during this month could be due to fog-induced suppression of photochemical activity as also indicated by ozone diurnal variation for January (Figure 3.4).

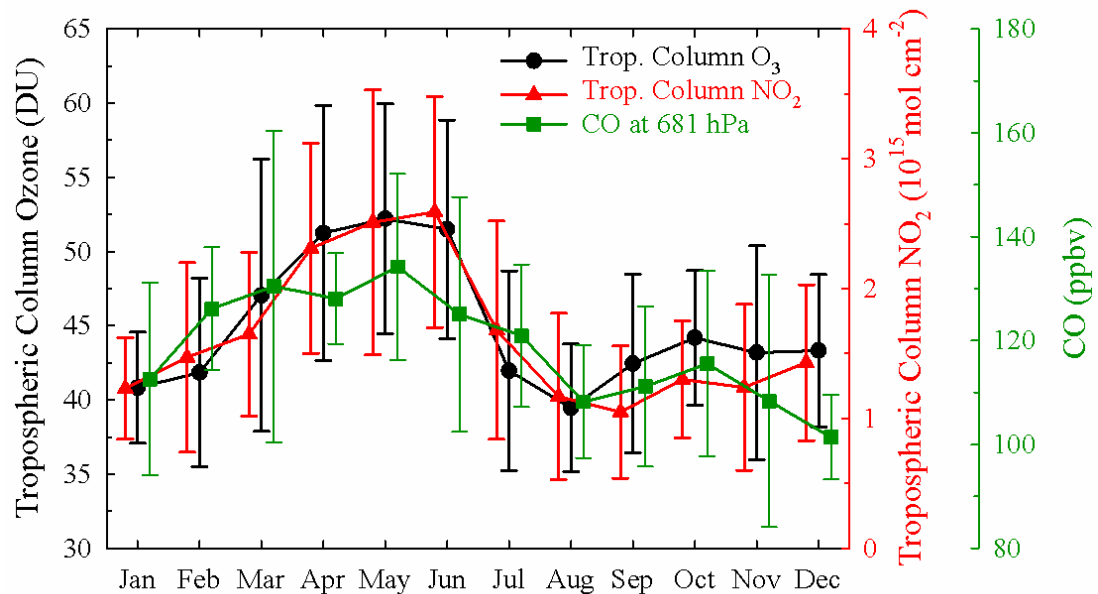


Figure 3.7: Seasonal variations in the tropospheric column ozone, tropospheric column NO₂ and CO at 681 hPa over Pantnagar.

The increase in nighttime levels during spring months suggest for an overall increase in the regional background ozone. This could be due to higher ozone production on the regional scale of northern India [Kumar *et al.*, 2010] and occurrence of significantly higher biomass burning activity during spring [Kumar *et al.*, 2011] in this region. The difference between daytime and nighttime monthly average ozone levels can be termed as photochemical build-up at this site and shows large variability with values as low as 9-14 ppbv during August-September and as high as 32-41 ppbv during spring and autumn months.

Here it can be noted that during spring and autumn seasons, when ozone levels (and precursors) show primary and secondary peaks respectively, air masses mostly circulate over the continental Indian region including polluted IGP region before reaching (within 1-2 days) at the observation site (Figure 3.2). Thus, the air masses, being well exposed to the regional emissions of this region, could be rich in ozone and precursors. However, the secondary ozone peak observed during autumn is not as high as that during spring. Notably, the solar radiation is less intense during autumn as compared to spring. In addition, biomass burning activities are highest during spring over this region, when compared with the biomass burning during autumn [Kumar *et al.*, 2011].

3.3.1. Correlation between Ozone and Mixing depth

The diurnal and seasonal variations in the mixing depth over Pantnagar are shown in Figure 3.8. As expected, mixing depth starts growing gradually after the sunrise, it evolves rapidly during 0800-1200 hours to attain maximum values during noontime

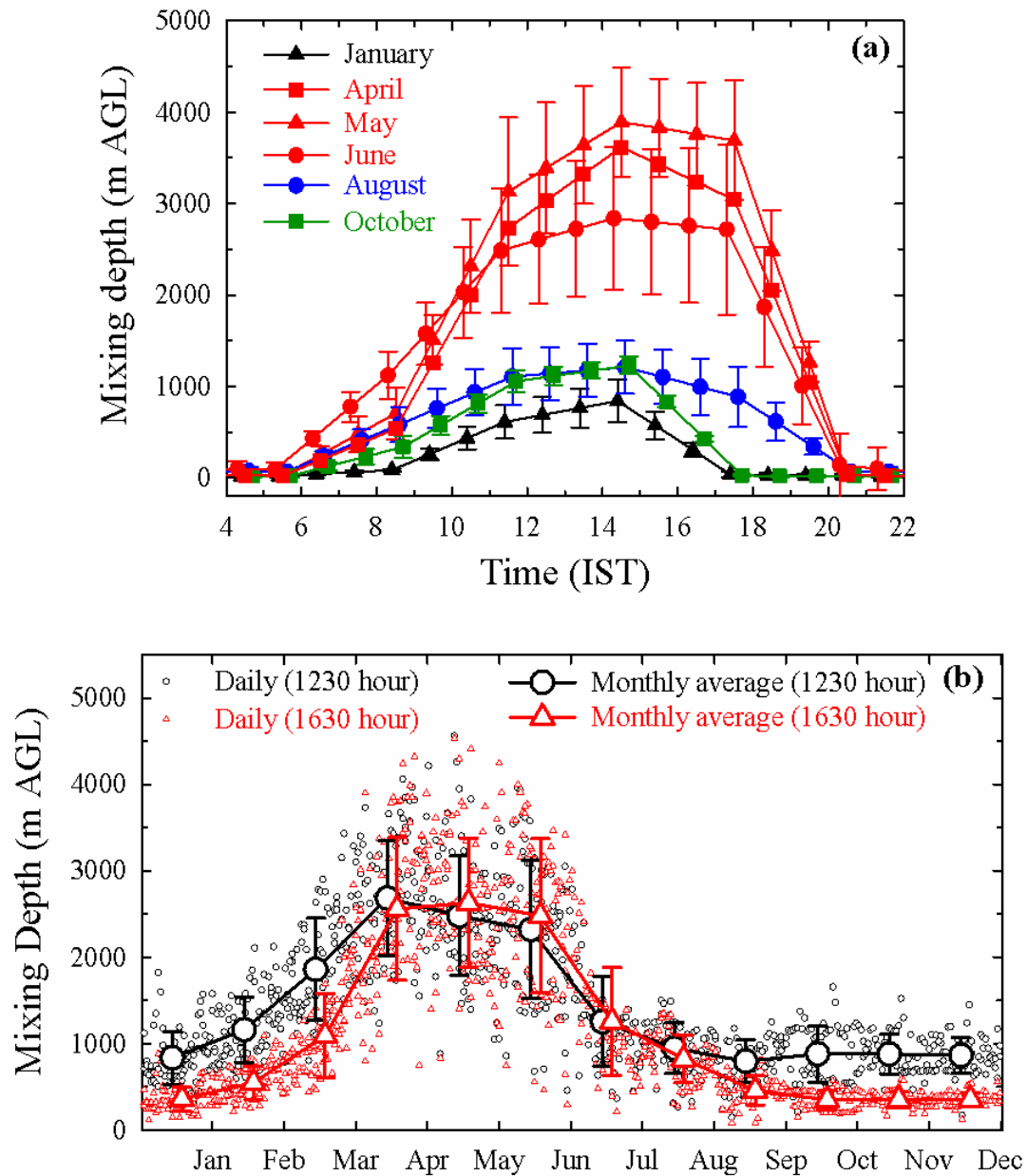


Figure 3.8: (a) Average diurnal variations in mixing depth at Pantnagar during four different months (January, April, August and October) representing four seasons. Two additional months (May and June) are also shown. (b) Seasonal variations in the daily and monthly average mixing depth at Pantnagar. Mixing depth is obtained from GDAS data.

and decreases thereafter. Mixing depth is as high as about 4 km during noontime of May while it is only about 0.9 km during January. Mixing depth is also lower during August and October. Mixing depth remains very low (50-100 meters) during nighttime and unlike daytime, nighttime mixing depth remains nearly similar in all the months. The monthly average mixing depth is highest (about 2500 m) during April and May while it is less than 1500 m during rest of months (Figure 3.8b and Table 3.2).

The highest daytime mixing depth during spring is in agreement with the seasonal variation in solar radiation and temperature at this site. The mixing depth during the 1630 hour is somewhat lower than the mixing depth during the 1230 hour in autumn and winter. This is mainly due to a lower temperature and hence reduced boundary layer mixing during the afternoon period in autumn and winter.

Higher ozone levels during spring and autumn are mainly attributed to the photochemical ozone production, however, boundary layer mixing processes could also contribute to the observed ozone variabilities. Boundary layer mixing can lead to some enhancements in near surface ozone levels by mixing it with the ozone-rich air aloft [Zhang and Rao, 1999; Rao *et al.*, 2003]. In general, ozone seasonal variations are in good agreement with those in the mixing depth until the end of the monsoon period. Ozone and the mixing depth both show a systematic increase from winter to spring. A decreasing tendency in their values begins in mid June and remains low during monsoon period. Diurnal amplitude in ozone and mixing depth also follow similar trend (Figure 3.4 and 3.8a). After September, ozone level increases, particularly in daytime but the mixing depth remains almost steady.

Therefore, despite a lower mixing depth during October, November and December, there is a significant increase in the ozone value suggesting minimal role of boundary layer processes in ozone enhancement during autumn.

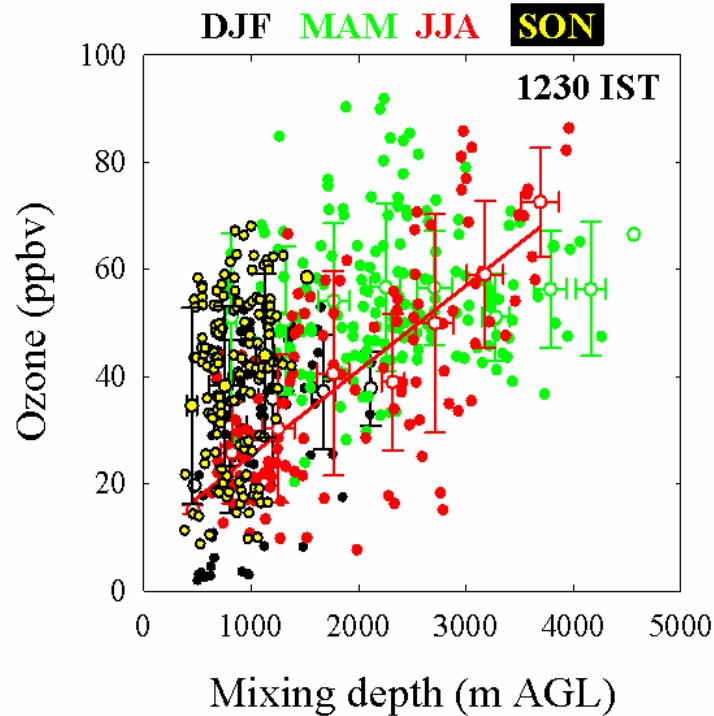


Figure 3.9: Correlation between daytime average ozone and the mixing depth at 1230 hour IST in different seasons at Pantnagar. Filled symbols are daytime average data and open symbols are binned average data for the respective season. The r^2 has been estimated for the binned average data points. In the binned average data points, one sigma horizontally spread is in the bins of 500 m mixing depth and one sigma vertical spread is in the associated ozone data.

Figure 3.9 shows the correlation between daytime average ozone and the mixing depth over four seasons. The ozone data has been binned corresponding to bins of

500 m mixing depth to calculate coefficient of determination (r^2). The calculation of binned average allows for smoothing the random variations in observations. The r^2 value is 0.90 for annual data and it is highest (0.96) during the summer-monsoon (June-July-August). Among June, July and August, higher ozone levels and higher mixing depths belong to June when dry weather conditions prevail around the observing site. Lower levels occur in July and August when both the boundary layer mixing and photochemical ozone production are suppressed by cloudy-rainy conditions due to arrival of south-west monsoon at the site.

Depending upon the relative ozone abundances in the near surface air and the air present at higher altitudes, the variability in boundary layer height can influence the surface ozone levels. Here, average ozone levels are observed to be significantly higher at a nearby high altitude site Nainital (~ 2 km amsl) as compared with average surface ozone at Pantnagar (Figure 3.6). Thus, the deeper boundary layer can enhance the ozone levels at the surface by mixing near surface air with the ozone rich air aloft. This enhancement in surface ozone, due to daytime convective mixing, would supplement the ongoing ozone production at Pantnagar. On the other hand, a shallower boundary layer would prevent such mixing and also lead to trapping of the ozone in a smaller volume, which is followed by an increase in the depositional loss of ozone. A group of data with a large spread in ozone but very limited mixing depth range is seen in autumn and somewhat in winter too. This comparative analysis suggests that boundary layer mixing also plays a role in the observed ozone variabilities apart from that of photochemistry.

3.4. Comparison with observations at other sites in India

Seasonal variation in surface ozone observed at Pantnagar are compared with those at other sites namely Delhi (28.35°N, 77.12°E) [Ghude *et al.*, 2008a], Gadanki (13.5°N, 79.2°E) [Naja and Lal, 2002], Nainital (29.37°N, 79.45°E) [Kumar *et al.*, 2010] and Trivandrum (8.55°N, 77°E) [David and Nair, 2011] in India (Figure 3.10). Delhi, Gadanki and Trivandrum are representative of urban, rural and coastal environments respectively. Nainital is a high altitude (1958 m amsl) site in the central Himalayas. Generally, sites in the Northern Indian region and having proximity to the IGP region (Pantnagar, Nainital and Delhi) show higher ozone levels during spring whereas sites in Southern India (Gadanki and Trivandrum) show higher ozone levels during winter. Additionally, seasonal amplitudes are rather higher over the sites in the Northern region, when compared with amplitudes at sites in the Southern region. Thus, the processes controlling ozone levels over the northern Indian region including IGP are different from those over the southern India.

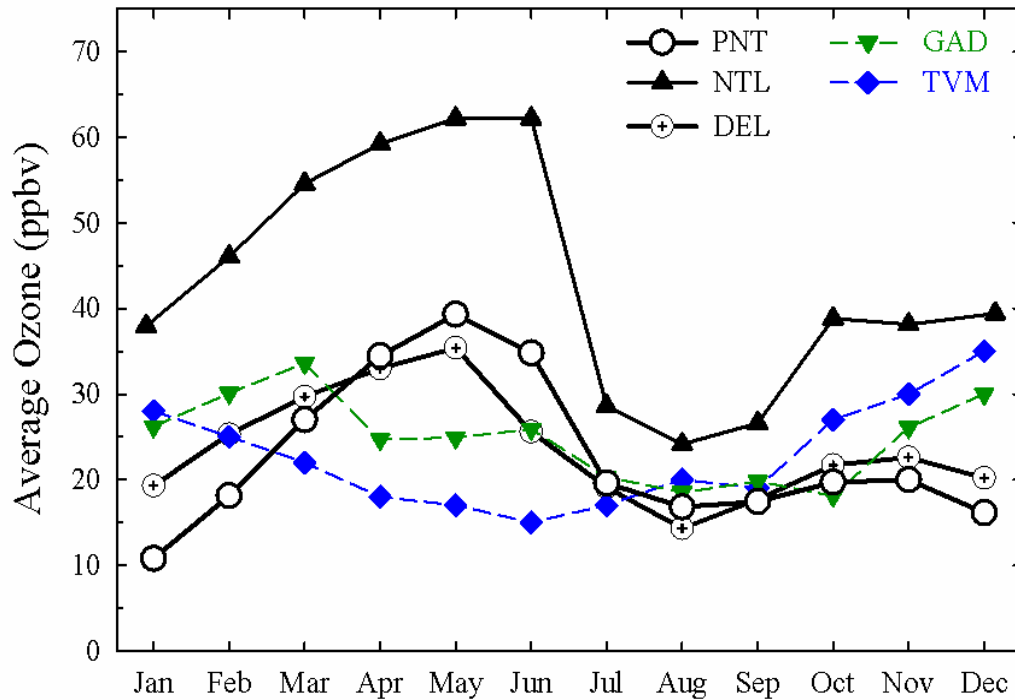


Figure 3.10: Comparison of the observed monthly average ozone seasonal variations at Pantnagar (PNT) with the observations at other sites Nainital (NTL), Delhi (DEL), Gadanki (GAD) and Trivandrum (TVM) in India.

3.4.1. Ozone at Pantnagar and Nainital

The seasonal variation in monthly average ozone at Pantnagar is similar to that observed at Nainital, a high altitude site (29.37°N, 79.45°E, 1958 m amsl) in the central Himalayas, except during autumn when a secondary maximum discerned at Nainital (Figure 3.6). Further, monthly average ozone levels are significantly higher (8 to 28 ppbv) at Nainital, when compared with those at Pantnagar.

Nainital is a high altitude site and relatively longer lifetime of ozone could be a major factor in displaying higher levels at Nainital. Unlike the all data average ozone, daytime average ozone at Pantnagar shows a secondary maximum during

autumn that is similar to the observation at Nainital. Since, in-situ photochemical ozone production is little at Nainital [Kumar *et al.*, 2010]; the similarity between the ozone data at Pantnagar and Nainital indicates a possible role of convective mixing in transporting ozone and precursors from the IGP to the central Himalayas. Particularly, daytime average ozone is higher (3-10 ppbv) at Pantnagar than the average ozone at Nainital during October-December.

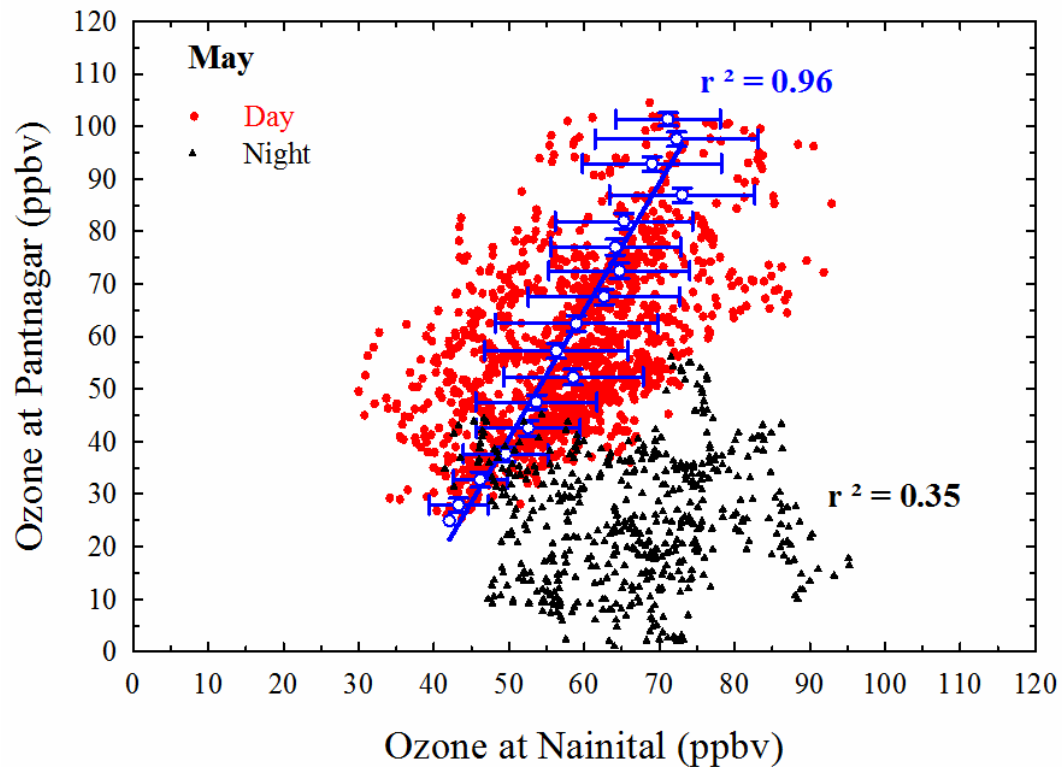


Figure 3.11: Correlation between ozone mixing ratios at Nainital and Pantnagar during afternoon hours (1130-1630 hours) and nighttime (01-03 hours) in May. Open symbols are binned average in 5 ppbv bins and error bars represent one-sigma spread in the binned data.

The boundary layer evolves fully during afternoon hours and the mixing depth at Pantnagar is even higher than the altitude of Nainital during spring (Figure 3.8a).

The daytime mixing depth is as high as 3890 m in May. Additionally, daytime (1130-1630 hours) ozone levels observed at Pantnagar and Nainital are seen to have strong positive correlation ($r^2 = 0.96$) during May, while no clear relationship is seen during the nighttime (Figure 3.11). r^2 value is estimated using 5-ppbv binned ozone data. Horizontal and vertical error bars show 1 sigma spread in the bins of 5-ppbv. Since Nainital and Pantnagar are separated by only about 30 km, air masses over Pantnagar and Nainital could be well mixed during daytime and show a strong positive correlation. During the nighttime, the shallower boundary layer at Pantnagar decouples its atmosphere from that of Nainital and there is no clear relationship between them. The above analysis suggests that emissions and photochemical processes occurring in the IGP can influence the air quality of the Himalayan region, particularly during spring mid-day, when the convective mixing is the strongest in this region.

3.5. Results from a Global Chemistry Transport Model

(MATCH-MPIC)

The spatial distributions of MATCH-MPIC simulated monthly mean surface ozone over the South Asian region for January, April, July and October, representing the winter, spring, summer-monsoon and autumn seasons respectively, are shown in Figure 3.12. During January, ozone levels are lower (20-40 ppbv) over northern India while levels are higher (40-50 ppbv) over central India and much higher (above 60 ppbv) over the coastal Arabian Sea and the northern part of Bay of Bengal.

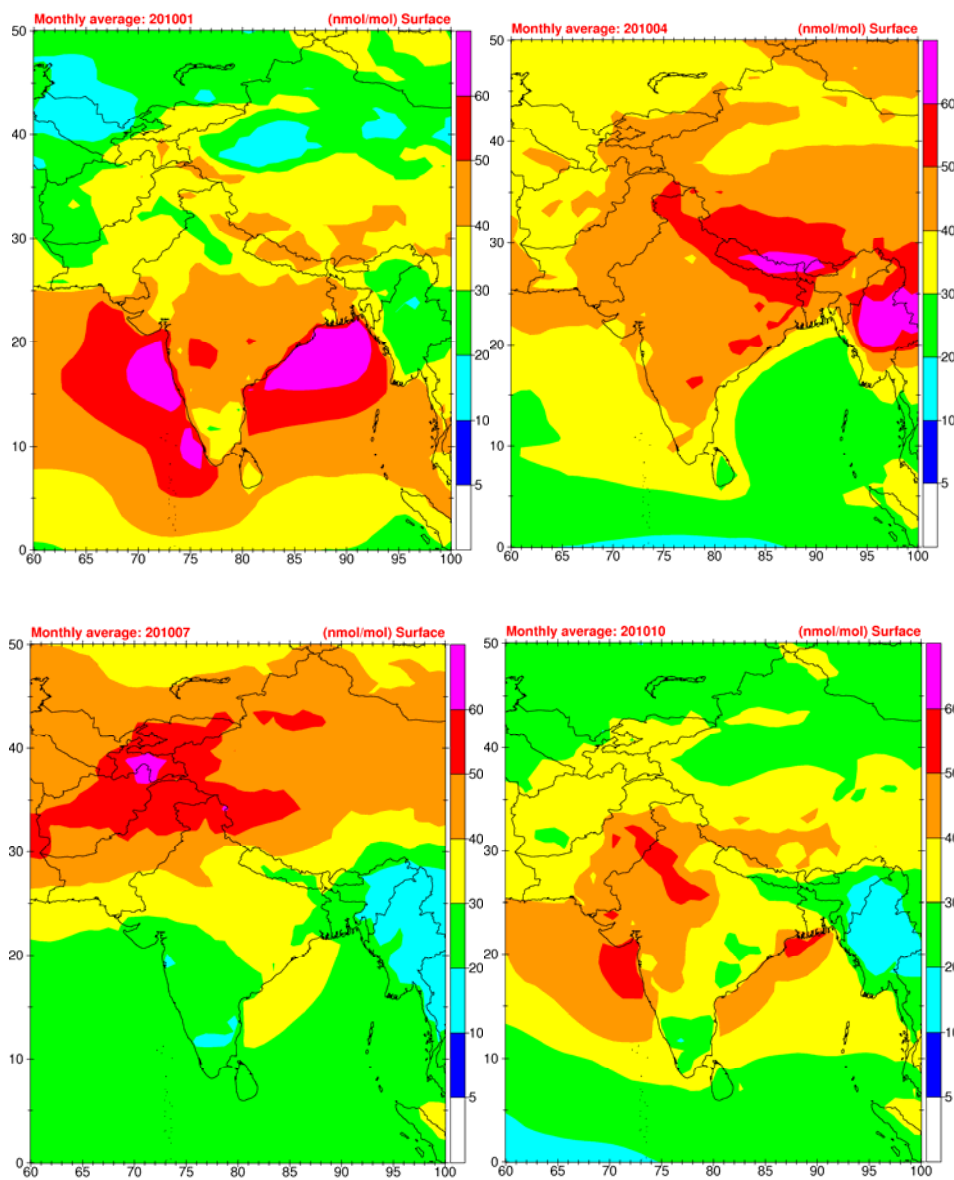


Figure 3.12: MATCH-MPIC simulated spatial distribution of surface ozone over the South Asian region, during four different months January, April, July and October representing four seasons, of the year 2010.

Such higher ozone levels over the oceans (50-60 ppbv and higher) were also noticed during the INDOEX (Indian Ocean Experiment) observations [Lal and Lawrence, 2001] and other campaigns [Naja et al., 2004; Srivastava et al., 2011], and is mainly

explained by en-route photochemical ozone production in the continental outflow. In absence of NO_x sources in the marine boundary layer, chemical losses of ozone are minimal in the transported plumes, in contrast with the nearby coastal cities, where ongoing NO_x emissions would lead to significant chemical losses of ozone. Occasionally, there could be some contribution from the downward transport of ozone rich air from the free troposphere in producing such high levels of surface ozone as suggested by *Lal and Lawrence, 2001* and reported observationally over Bay of Bengal by *Sahu and Lal, 2006*. Similar feature was also seen over the Mediterranean Sea versus the nearby European polluted continental regions [*Lawrence et al., 2003b*].

From winter to spring, ozone levels increase over most of South Asia and elevated levels are seen over the IGP (50-60 ppbv and more) and parts of Nepal and Burma while they decrease over the oceanic regions (20-40 ppbv). During the summer/monsoon, the arrival of cleaner marine air mass results in the lowest ozone levels (20-40 ppbv) over most of the Indian region but higher ozone levels can still be seen in northern part of South Asia and China, indicating that these regions are not much influenced by the monsoonal circulation. During autumn, ozone levels again show a recovery over most of the Indian region with the recovery of solar radiation and pollution loadings, including ozone precursors. Model simulated spatial distributions in CO and NO_x were also seen to be more-or-less similar to the ozone spatial distribution, except that the CO levels are higher in winter. Model simulations also show elevated levels of CO and NO_x over the IGP region; however, their highest levels are observed during winter and autumn.

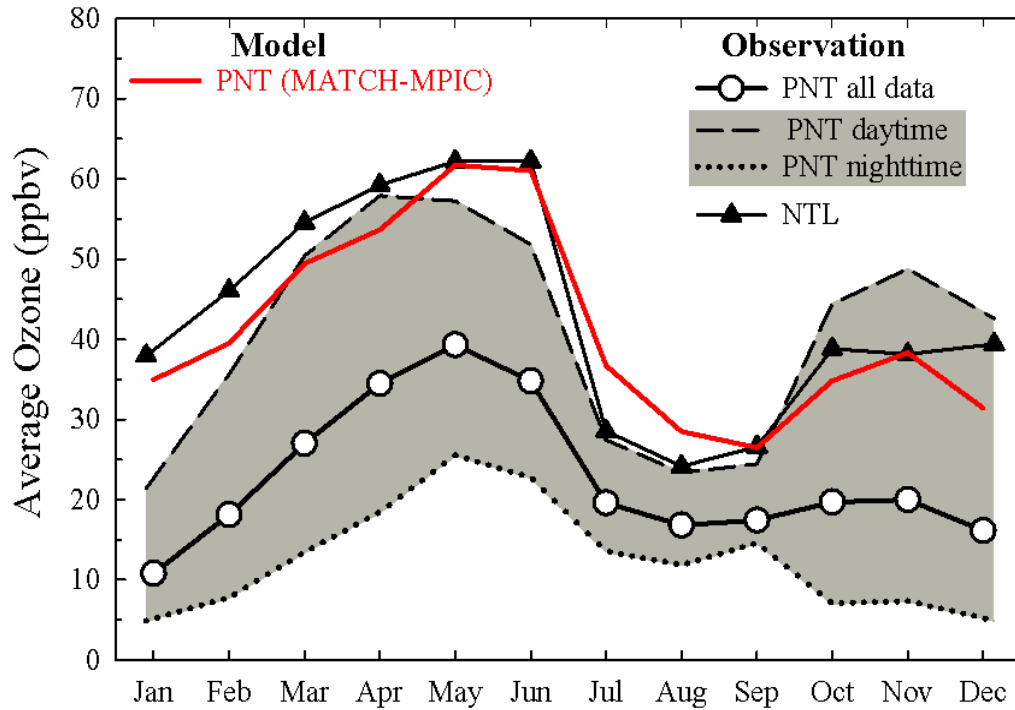


Figure 3.13: Comparison of the observed ozone seasonal variation at Pantnagar (PNT) with the results from MATCH-MPIC model. Seasonal variation in ozone, at a nearby high altitude site Nainital, is also shown. Upper range and lower range in grey shaded region is daytime and nighttime ozone data at Pantnagar, respectively.

The variability of modeled surface ozone around Pantnagar in the model results is qualitatively similar to the observed variations at Pantnagar with lower values in January (winter) and July (summer/monsoon), but higher values during April (spring) and October (autumn) (Figure 3.13). This figure also shows the variations in daytime and nighttime monthly average ozone at Pantnagar along with monthly average surface ozone at Nainital. Apart from agreement in the seasonal variabilities, the model overestimates the observed values during all the months (e.g. by ~22 ppbv in May and by ~12 ppbv in August). Ozone diurnal variations from the model results were also compared with the observations during few months to

investigate the cause of higher ozone levels in the model results. The nighttime model values are found to be significantly higher (e.g. by ~20 ppbv in May) than the observed levels. Thus, it appears that higher model values during nighttime are likely leading to the overestimation of average ozone. Higher ozone levels during the nighttime could be due to the underestimation of model NO_x emissions over this region, leading to less titration of ozone by NO during nighttime. As mentioned earlier (Section 3.1.1), based on the observed ozone decrease rate, NO levels are expected to be high over the IGP region; further observations would be needed to confirm this possibility. The model result is, however, in good agreement with daytime ozone at Pantnagar and the average ozone at Nainital. This may be due to the coarse spatial resolution of the model, which means it is not able to adequately resolve the urban environment of the IGP from the nearby cleaner mountains. Topography is very complex in this region and surface altitude increases by about 1700 m within a short span of about 10 km. Additionally, the October-November secondary maximum is more prominent in the model than in the observations at Pantnagar. The seasonal variations in the model (MATCH-MPIC) simulated CO from fossil fuel and biomass burning over Pantnagar are shown in the Figure 3.14. This analysis shows higher levels of biomass burning and fossil fuel CO during autumn over this region.

Summarizing, though the model seems broadly representative of the ozone observations, there are differences between the model and observations, due to several factors, especially uncertainties in magnitude and ratios of emissions, the relatively coarse spatial resolution (despite being high resolution for a global model) which leads to errors in the treatment of the complex regional meteorology.

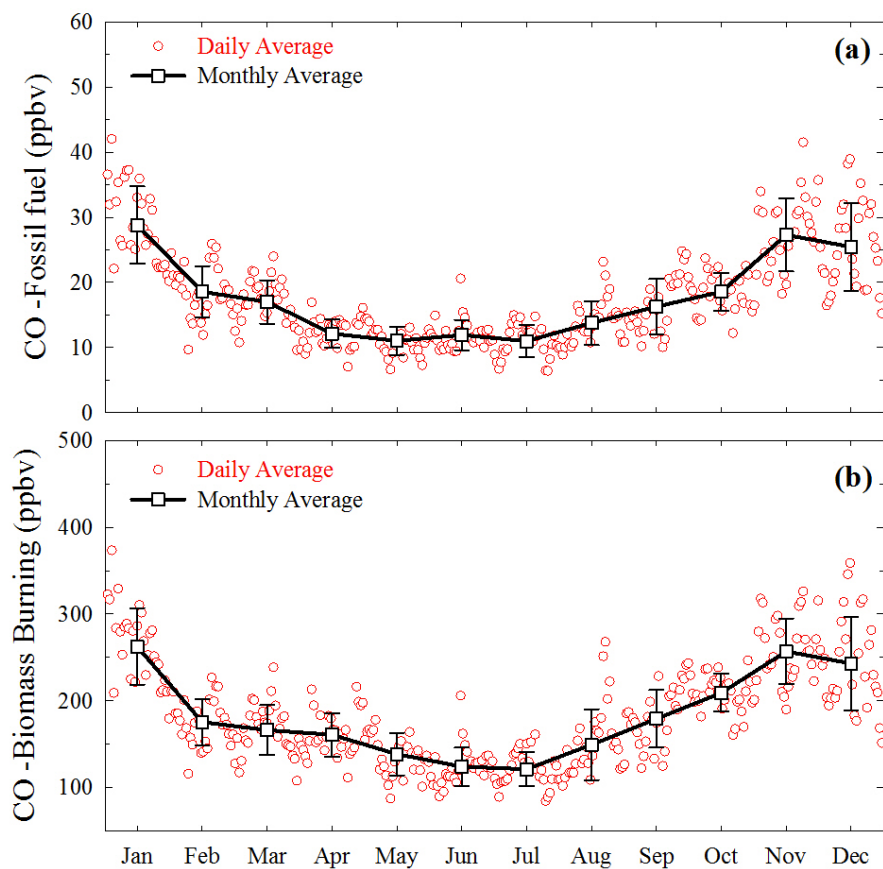


Figure 3.14: Seasonal variations in CO from fossil fuel and biomass burning over Pantnagar simulated from MATCH-MPIC model.

3.5.1. Variations in H₂O₂ and HNO₃ from MATCH-MPIC

The variations in H₂O₂ and HNO₃ can be used as indicators of the sensitivity of ozone production to NO_x and hydrocarbons [Sillman, 1995]. In the urban environments, major sources of odd hydrogen species, i.e., the sum of OH, HO₂ and RO₂ [Kleinman, 1986, Sillman et al., 1990, Sillman, 1991] are ozone photolysis followed by reaction of O(¹D) with water vapor and the photolysis of aldehydes and

other intermediate reactive organic compounds. Major sink reactions for odd hydrogen are the following -



In addition to the reactions from R3.1 to R3.3, formation of PAN (Peroxyacetylnitrate) could also be a significant sink for the odd hydrogen. The nature of ozone chemistry as NO_x-sensitive or hydrocarbon-sensitive would be determined by the relative rates of formation of peroxides (R3.1 and R3.2) and nitric acid (R3.3) and to their contribution as sinks for odd hydrogen. Generally, noontime values of H₂O₂ to HNO₃ ratios less than 0.4 are found to be associated with the hydrocarbon-sensitive ozone chemistry, while values higher than 0.4 are associated with the NO_x-sensitive chemistry [Sillman, 1995].

Seasonal variations in MATCH-MPIC simulated daytime (1130-1630 hours) daily and monthly average values of H₂O₂, HNO₃ and H₂O₂/HNO₃ ratio at Pantnagar for the year 2010 are shown in the Figure 3.15. H₂O₂ shows nearly similar seasonality to that of ozone with higher values during spring (2.7 ± 0.9 ppbv in May) and autumn (2.0 ± 0.7 ppbv in October) and lower values during winter (0.5 ± 0.3 to 0.9 ± 0.4 ppbv) and summer/monsoon (1.1 ± 0.5 ppbv in August). The variations in HNO₃ values are more-or-less similar to those in ozone except in winter. HNO₃ values are higher during spring (1.4 ± 0.5 ppbv in May) and autumn (1.5 ± 0.7 ppbv in November) and lowest during summer/monsoon (0.1 ± 0.1 ppbv in August). Most of

the time, daytime daily average values of H_2O_2/HNO_3 ratios are more than one except during early winter and late autumn.

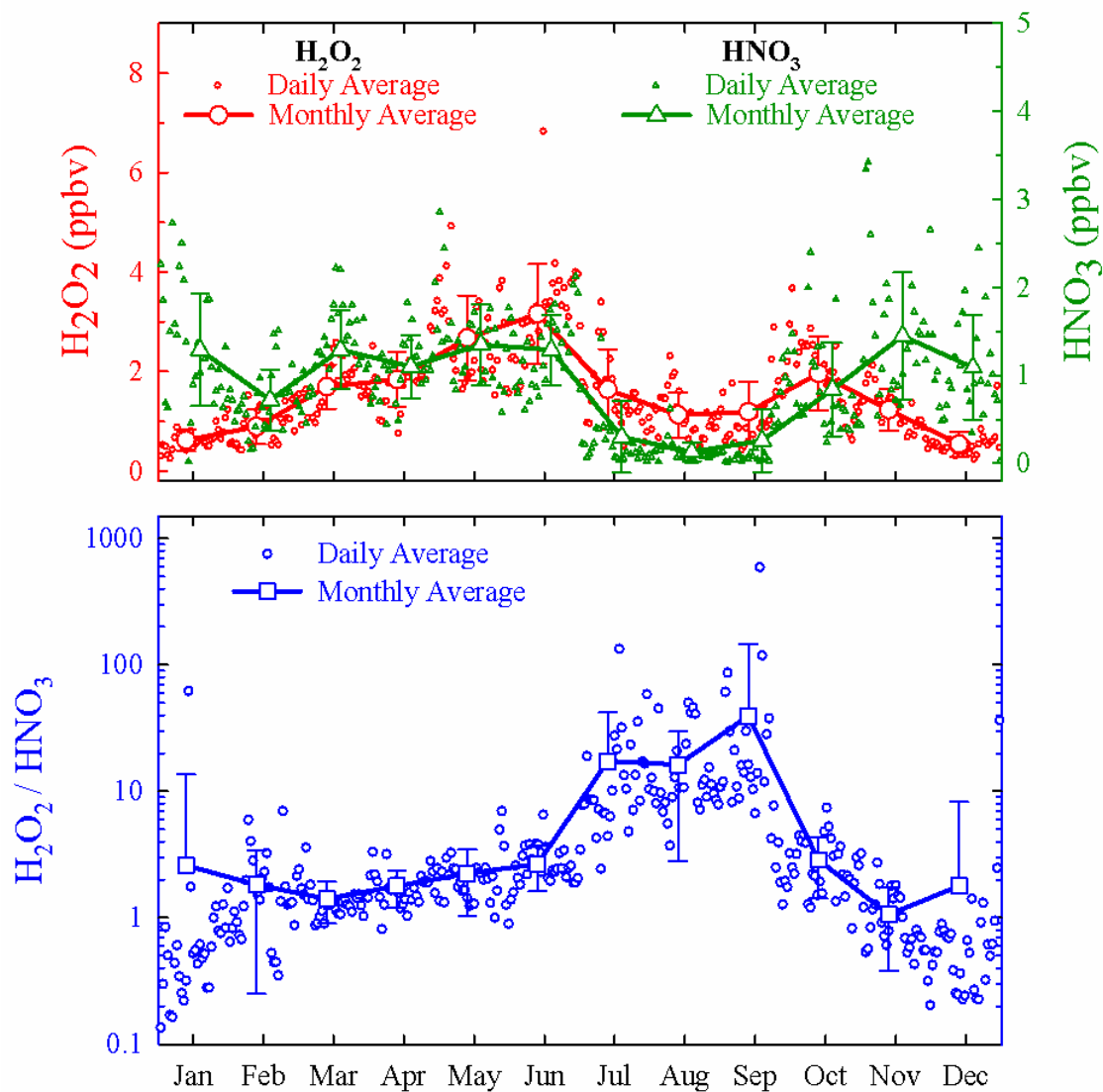


Figure 3.15: MATCH-MPIC simulated variations in daytime (1130-1630 hours) H_2O_2 , HNO_3 and H_2O_2/HNO_3 ratios at Pantnagar during January to December 2010.

Generally, average $\text{H}_2\text{O}_2/\text{HNO}_3$ values range from 1.1 ± 0.7 to 2.9 ± 1.5 , except during summer-monsoon, and are well above the critical limit of 0.4 [Sillman, 1995] indicating that ozone chemistry over this region is NO_x -limited. Higher ratios during summer-monsoon (16.3 ± 13.4 to 39.5 ± 108.0) are mainly due to very low values of HNO_3 associated with long range transport of cleaner marine air masses and possibility of enhanced wet depositional losses of HNO_3 in the heavy rainfall (Figure 3.2 and 3.3) during the summer-monsoon. The sensitivity of ozone chemistry to NO_x at Pantnagar will further be shown using sensitivity simulations from a chemical box model in the next section.

3.6. Photochemical Ozone Production Rate and Sensitivity to

NMHCs and NO_x

Ozone levels depend non-linearly on the concentrations of its precursors including hydrocarbons, CO and NO_x [Lin *et al.*, 1988; Chameides *et al.*, 1992; Sillman, 1999] and thus ozone control policies in urban and rural regions are region specific and difficult to design. Here, we attempt to characterize the dependence of surface ozone on NMHCs and NO_x by combining the available observations, emissions over this region and using a chemical box model. A chemical box-model is set-up to simulate the diurnal variation of ozone at Pantnagar to lend confidence into the use of model for the aforementioned sensitivity study.

The environmental conditions of typical spring (April) are selected for the box model simulations at Pantnagar (Table 3.3). The overhead total column ozone is set to the value obtained from OMI. The model is initialized with the observed

concentrations of CO, NO_x, CH₄ and few light non-methane hydrocarbons (C₂-C₅) at this site while other species are assumed and set to the typical values of a semi-urban environment.

Table 3.3: *Environmental conditions, representing spring, opted for the chemical box model simulations.*

Temperature	298 K
Relative Humidity	50%
Surface albedo	0.10
Parcel elevation	500 m
Overhead O ₃ column	262 DU (OMI)
Aerosol optical depth at 550 nm (vertical, total)	0.235 (for continental aerosol)
Aerosol Angstrom coefficient	1
Aerosol single scattering albedo	0.99

Anthropogenic emissions of CO, NO_x and hydrocarbons from Intercontinental Chemical Transport Experiment–Phase B (INTEX-B) emission inventory [Zhang *et al.*, 2009] are used. Since INTEX-B emissions are representative of the year 2006 and analysis of historic emissions (1980-2003) from Regional Emission Inventory for Asia (REAS) [Ohara *et al.*, 2007] indicates an increase of about 8% per year in NO_x emissions over India, therefore NO_x emissions are increased by 40% for this study. Figure 3.16 shows chemical box model simulated diurnal ozone variation. The modeled (base run) diurnal variation is in good agreement with the observations. However, model values are lower during mid-night. This model run is

shown as “base run” in Figure 3.16. The instantaneous production (P), loss (L) and net production (P-L) rates of ozone [Duderstadt et al., 1998; Kanaya et al., 2009] are also calculated for this base run as follows and shown in Figure 3.17.

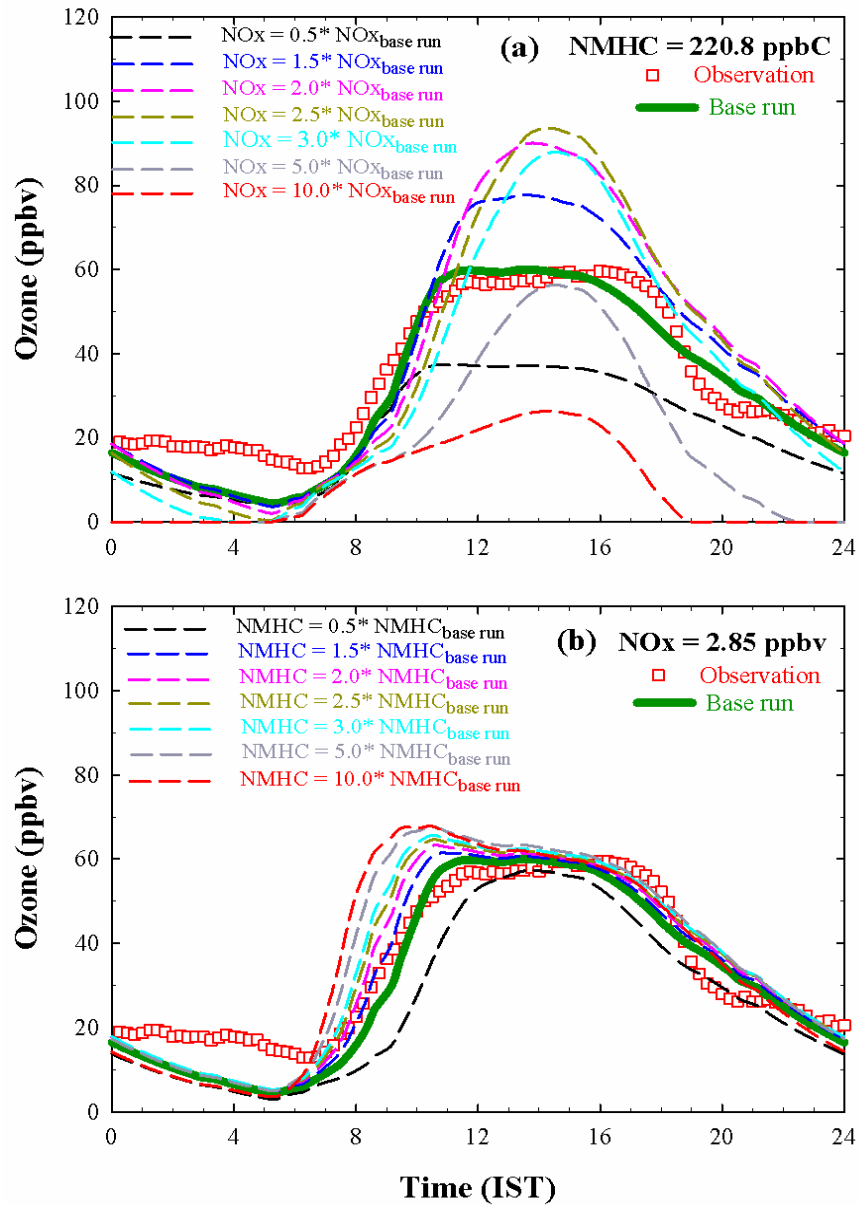


Figure 3.16: Box model simulated diurnal variations in surface ozone. Apart from the base run, diurnal variations in ozone for (a) different levels of NO_x and constant level of NMHCs and (b) different levels of NMHCs and constant level of NO_x are also shown.

$$P(O_3) = k_1 [HO_2] [NO] + \sum k_{2i} [RO_2]_i [NO] \quad [3.4]$$

$$L(O_3) = k_3 [O^1(D)] [H_2O] + k_4 [OH] [O_3] + k_5 [HO_2] [O_3] \quad [3.5]$$

$$P - L(O_3) = P(O_3) - L(O_3) \quad [3.6]$$

Where k_1 to k_5 are the rate coefficients of the $HO_2 + NO$, $RO_2 + NO$, $O^1(D) + H_2O$, $OH + O_3$ and $HO_2 + O_3$ reactions, respectively.

The ozone production rate $P(O_3)$ starts increasing rapidly after sunrise to about 1000 hours and thereafter it decreases. Highest values of $P(O_3)$ are observed to be 14.5 ppbv h^{-1} during 0900-1000 hours. Total ozone produced during daytime (0800 – 1600 hours) is estimated by converting these instantaneous $P(O_3)$ values to hourly averages and then integrating from 0800 to 1600 hours. This way, the total ozone produced in the daytime is 81.2 ppbv. The ozone loss rate $L(O_3)$ shows an increasing tendency slightly later than $P(O_3)$ and shows a symmetric decreasing trend unlike $P(O_3)$. The total ozone loss per day is 8.3 ppbv. The rate of net ozone production i.e. $P-L(O_3)$ follows similar variations as that in the $P(O_3)$ with highest values of $P-L(O_3)$ of 13.9 ppbv h^{-1} during 0900-1000 hours. Integrated net ozone production in a day is 72.9 ppbv. Accumulated ozone calculated from the observed rate of change of ozone (Figure 3.5b) during 0800-1600 hours is 45.4 ppbv. The difference in these two quantities, integrated ozone from box model and observations, (~27.5ppbv) can be attributed to the physical and dynamical processes, which are not considered in the chemical box model simulations.

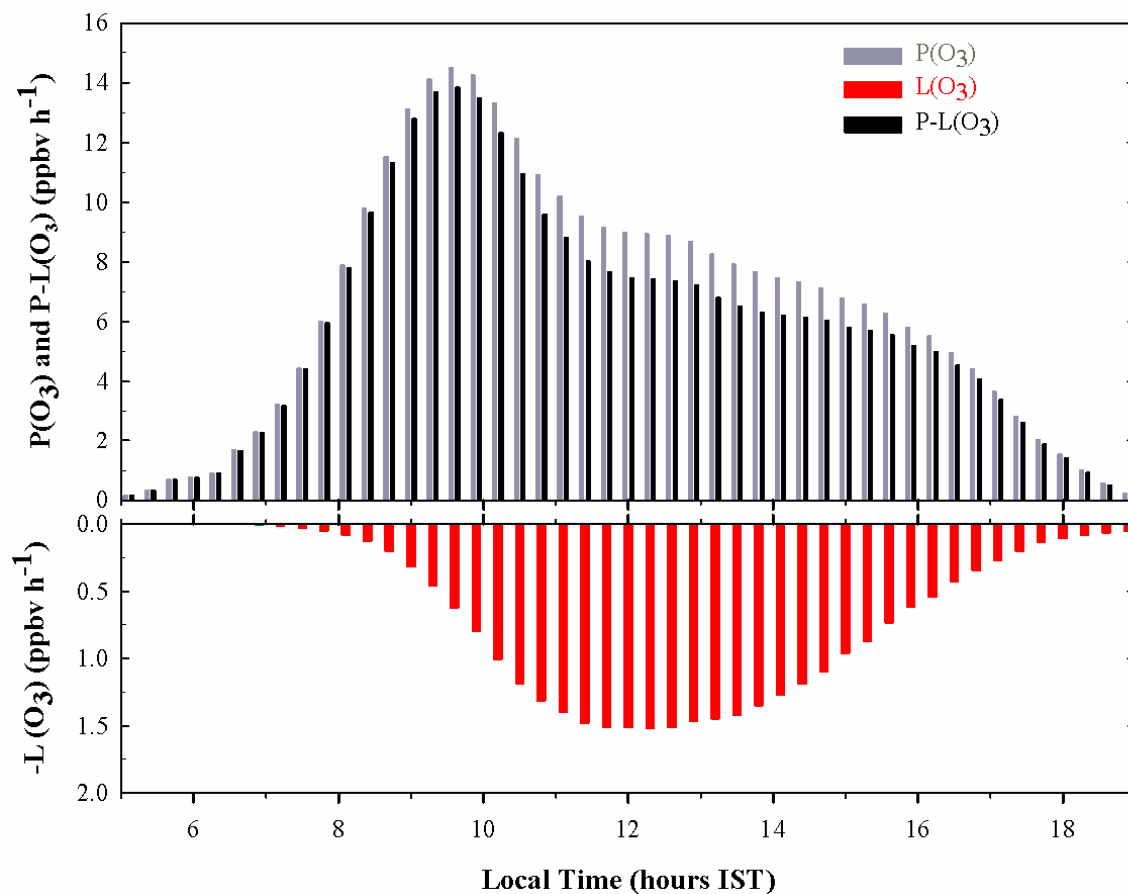


Figure 3.17: Diurnal variations in ozone production rate $P(O_3)$, ozone loss rate $L(O_3)$ and net ozone production rate $P-L(O_3)$ estimated from box model simulations for the base run.

Apart from the base run, two sets of sensitivity simulations are also conducted. One set of runs is made by keeping NMHCs constant at the values of the base run (220.8 ppbC) with varied NO_x levels between 0.5 to 10 times of the base run NO_x value (2.85 ppbv). A second set of runs was made by keeping NO_x value constant at its base run value (2.85 ppbv) with varied NMHCs levels between 0.5 to 10 times of the base run value of NMHCs. These two sets of simulations along with the base run are shown in Figure 3.16.

Model simulated ozone diurnal variations for varying NO_x levels shows rapid increase in the daytime ozone levels from ~ 37 ppbv (for $0.5 \cdot \text{NO}_x$ base run case) to ~ 93.5 ppbv ($2.5 \cdot \text{NO}_x$ base run) (Figure 3.16a). In contrast, when NO_x levels are increased further, ozone levels start decreasing from ~ 88 ppbv (for $3 \cdot \text{NO}_x$ base run) to ~ 26 ppbv ($10 \cdot \text{NO}_x$ base run). Apart from changes in ozone levels, daytime variations also change from a broad pattern to a peak type of pattern, when increasing NO_x levels. In contrast to the sensitivity tests for varying NO_x levels, ozone diurnal variations and its levels do not show significant changes for varying the levels of NMHCs (Figure 3.16b). Ozone levels show only a small increase (~ 5 ppbv) from ~ 57 ppbv (for $0.5 \cdot \text{NMHC}$ base run) to ~ 62.5 ppbv (for $10 \cdot \text{NMHC}$ base run) for whole range of NMHCs. The above analysis indicates that ozone production chemistry is NO_x limited in this region, while variations in the levels of hydrocarbons play a minor role in affecting ozone levels.

3.7. Impact of Ozone Pollution on the vegetations in IGP:

Estimation of AOT40 index

An attempt is being made to understand the possible impacts of ozone pollution on the vegetations in the IGP region. Surface ozone observations from Pantnagar and another urban site in this region Dehradun (78.1°E , 30.3°N , 640 m amsl) are used to estimate the Accumulated Ozone exposure above a Threshold of 40 ppbv (AOT40 index). AOT40 values are calculated only for the months having more than 80% of the days of the data in that month. For more than a year data, average of different years for the month is taken.

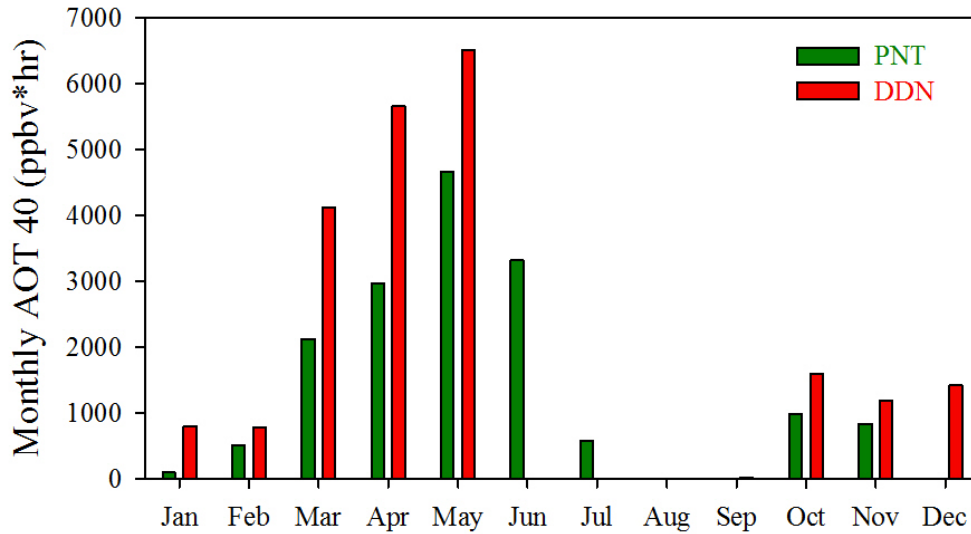


Figure 3.18: Seasonal variations in monthly AOT40 over two sites Pantnagar (PNT) and Dehradun (DDN) in the IGP.

AOT40 estimated from the hourly average daytime (during 0700-1900 hours period) ozone data as the sum of enhancements in hourly ozone concentrations above 40 ppbv [Mills *et al.*, 2007]. AOT 40 expressed as:

$$\text{AOT40 (ppbv * hr)} = \sum_{i=1}^n ([O_3]_i - 40) \quad \text{for } [O_3]_i \geq 40 \text{ ppbv}$$

Where $[O_3]_i$ is the hourly mean ozone mixing ratio during 0700-1900 hours and n is the number of hours in the 3-month growing season. Monthly AOT40 values are observed to be highest during May (4661.4 ppbv*hr), intermediate in July (578 ppbv*hr) and lowest during January (98.6 ppbv*hr) (Figure 3.18). The critical level of three-monthly AOT40 values is suggested to be 3000 ppbv*hr, which represents a 5% reduction in yield [Mills *et al.*, 2007]. AOT40 value of above 3000 ppbv*hr will lead to further reduction in crop yield.

Three-monthly AOT40 values have also been estimated by summing up three consecutive months in moving manner (e.g. Jan-Feb-Mar, Feb-Mar-Apr etc.). In this manner, three-monthly AOT40 values are highest during late winter and spring, ranging from 5600.4 ppbv*hr (Feb-Mar-Apr) to 10948.5 ppbv*hr (Apr-May-Jun). Clearly, these three-monthly AOT40 values are much higher than the critical levels of 3000 ppbv*hr. These estimated three-monthly AOT 40 value at Pantnagar for February-March-April (5600 ppbv*hr) is at the lower end when compared with another model [Roy *et al.*, 2009] simulated value in this region (5000-12500 ppbv*hr).

3.8. Summary and Conclusions

The observations of surface ozone at a semi-urban site Pantnagar (29.0°N, 79.5°E, 231 m amsl) in the IGP during March 2009 – June 2011 are analyzed using meteorological parameters including the boundary layer data, backward trajectories, satellite data, simulations from a global chemistry transport model and a photochemical box model. Ozone mixing ratios at Pantnagar discern daytime photochemical build up. Higher rate of change of ozone during evening time (-8.5 ppbv hr^{-1}) suggests stronger ozone loss chemistry over the IGP due to higher NO_x emissions. The ozone seasonal variation is characterized by highest levels during spring and lower levels during summer/monsoon and winter. Monthly average ozone levels are generally less than 40 ppbv; however, hourly average ozone levels are in the range of 80-100 ppbv particularly during spring. Moreover, the daytime ozone shows a secondary peak during autumn which is not observed in the all data. The ozone photochemical buildup is estimated to be 32-41 ppbv in spring and

autumn and 9-14 ppbv during August-September. CO levels are moderately high (188-484 ppbv) while CH₄ values range from 1.81 to 2.11 ppmv.

Observed ozone seasonality is in good agreement with the solar radiation and satellite retrieved lower tropospheric CO and tropospheric NO₂. During spring and autumn, air masses mostly circulate over the continental Indian region, including the IGP, before reaching to the observation site and thus could be rich in ozone and precursors. The northern Indian biomass burning acts as an additional source of ozone precursors during spring. In addition to photochemistry, boundary layer dynamics is also shown to a key role in the ozone variations. The lower levels of all the gases during July-September are mainly attributed to the arrival of southwest monsoon bringing cleaner marine air. A correlation analysis between the surface ozone observations at Pantnagar and those at the nearby high altitude site Nainital indicates strong positive correlation ($r^2 = 0.96$) in the springtime noon hours (1130-1630 hours). It is suggested that the emissions and photochemical processes in the IGP region can influence the air quality of the Himalayas via boundary layer mixing processes. A comparison of these observations sites in India shows that ozone levels over the northern India are highest during spring, while, sites located in the southern part of India show maximum ozone levels during winter. This comparison highlights the diversity of emissions as well as processes controlling ozone levels over different parts of Indian region.

A global chemistry transport model (MATCH-MPIC) reproduces the overall springtime elevated ozone levels over the IGP, lower ozone during the

summer/monsoon and winter, and a recovery phase during autumn. However, the model overestimates the ozone levels over Pantnagar, particularly during the nighttime, which could be due to underestimation of NO_x emissions resulting in less ozone titration. The model simulated H_2O_2 and HNO_3 variations are used as an indicator of ozone sensitivity to hydrocarbons and NO_x . Average $\text{H}_2\text{O}_2/\text{HNO}_3$ values vary from 1.1 ± 0.7 to 2.9 ± 1.5 suggesting that ozone chemistry over this region is NO_x -limited. This is further corroborated with the simulations using a chemical box model (NCARMM) and ozone production and loss rates at Pantnagar are estimated. Integrated net ozone production, from the box model, in a day, is estimated to be 72.9 ppbv.

Chapter 4

Vertical Distribution of Ozone and Meteorological Parameters over the central Himalayas

The ground-based and balloon-borne observations of ozone distribution are very limited over the Indian region particularly over the northern India including the highly populated and polluted Indo-Gangetic plain (IGP) region. Space-borne observations have revealed large spatial heterogeneity in the distribution of tropospheric ozone over the Indian region with highest levels over IGP [Fishman *et al.*, 2003]. Earlier, measurements of vertical ozone distribution were initiated by Indian Meteorological Department (IMD) in 1960s using Indian ozonesondes

[Sreedharan, 1968]. There have been some concerns related with the data quality of Indian ozonesonde measurements [e.g. Logan, 1999]; nevertheless, these observations from IMD have been used for trend estimation [Saraf and Beig, 2004]. Since, ozone sensor from Environmental Scientific (EN-SCI) have been used globally [Komhyr, 1969], these sensors are used for the measurements of ozone vertical distribution over the western India [Srivastava *et al.*, 2012]. Few measurements of ozone vertical profiles were also carried out over the Indian Ocean [Srivastava *et al.*, 2011] and IGP [Gupta *et al.*, 2007].

Except a campaign based observation [Gupta *et al.*, 2007], balloon-borne ozone observations are not existing in the IGP and Himalayan region. Topography is also very complex in the Himalayas; therefore, different processes controlling the ozone distribution are not well studied in this region. Simultaneous measurements of the vertical profiles of ozone and meteorological parameters would be invaluable to understand the different processes controlling the ozone distribution over this region. Additionally, findings from the space-borne sensors needs confirmation from ground based sensors.

In light of this, the balloon soundings have been initiated from a mountain top called Manora Peak near Nainital (79.45°E, 29.37°N, 1958 m amsl) located in the central Himalayas, hereafter mentioned as Nainital (Figure 4.1). This site is reasonably away from any kind of direct influences of anthropogenic emissions and is considered as a better regional representative site in the northern Indian region [e.g. Kumar *et al.*, 2010; Kumar *et al.*, 2011]. Sharply peaking mountains are situated in

the northern and eastern directions of the site while mountains of altitudes less than 1000 m are located in the south and west. The Nainital city is located about 2 km away from the site toward the north. There are no major industrial activities in the Nainital and the population is about 0.4 million. The nearby cities, Haldwani and Rudrapur are about 20 to 40 km away from the site and have some small-scale industries.

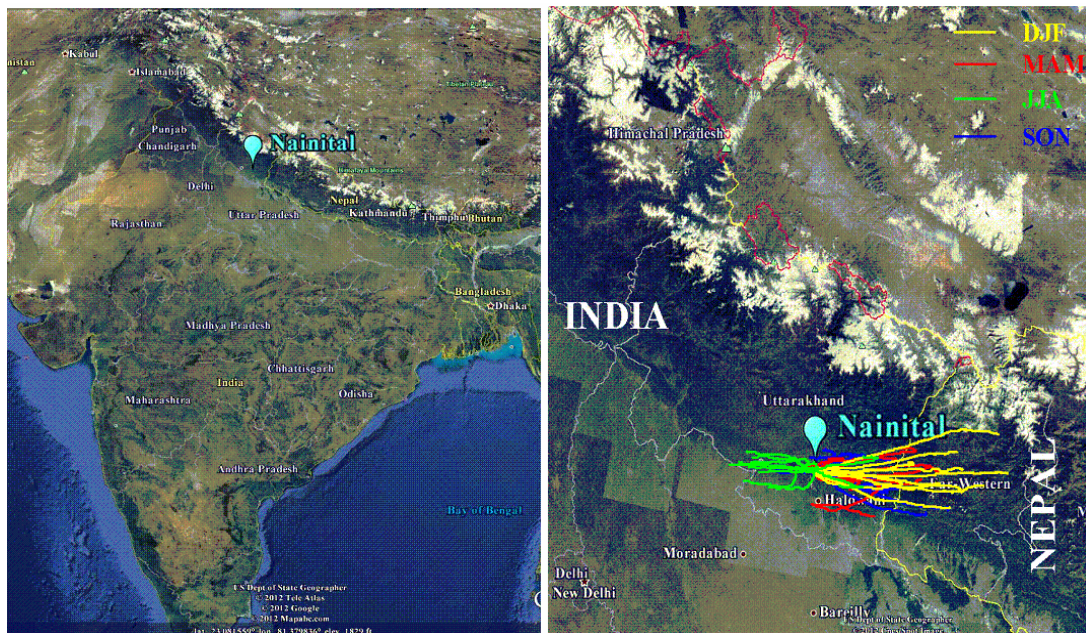


Figure 4.1: Location of the observation site Nainital, in the map of India, shown by a cyan color balloon. Drift of balloons during flights are shown for different seasons namely winter (DJF), spring (MAM), summer-monsoon (JJA) and autumn (SON).

Moreover, the Nainital site is located just north of the Indo-Gangetic Plain (IGP) region, which is the most densely populated and polluted region in India [e.g. Fishman et al., 2003]. Several test flights have been conducted during September-October 2010 before starting the regular weekly observations during January 2011.

Since then balloon soundings were made every week resulting in a collection of total 48 profiles during the year 2011. The details of soundings conducted in each month are given in the Table 4.1.

Table 4.1: Total number of balloon soundings with serial numbers of the radiosonde and ozonesonde launched during different months of year 2011.

Day of Observation	Radiosonde	Ozonesonde	Total Profiles
January: 7th, 19th, 28th	S12542, S12553, S12174	2Z9172, 2Z9180, 2Z9173	3
February: 2nd, 11th, 17th	S12551, S12162, S12550	2Z9188, 2Z9174, 2Z9176	3
March: 7th, 10th, 30th	S6671, S12549, S9274	2Z9141, 2Z9177, 2Z9171	3
April: 6th, 13th, 20th, 29th	S12540, S12539, S12534, S8760	2Z9186, 2Z9194, 2Z9179, 2Z9178	4
May: 4th, 9th, 12th, 16th, 18th, 25th	S12176, S12170, S4093, S2533, S4033, S3137	2Z9182, 2Z9181, 2Z9175, 2Z9193, 2Z9185, 2Z9169	6
June: 2nd, 7th, 15th, 29th	S6660, S4323, S7127, S6284	2Z9135, 2Z9187, 2Z9138, 2Z9190	4
July: 6th, 22nd, 27th	S6582, S7211, S3326	2Z9140, 2Z9170, 2Z9191	3
August: 3rd, 11th, 18th, 24th, 31st	S6641, S12536, S12546, S12545, S16154	2Z9189, 2Z9192, 2Z9139, 2Z9184, 2Z9183	5
September: 7th, 16th, 21st, 25th	S16375, S16391, S16371, S16167	2Z9166, 2Z9164, 2Z9195, 2Z9142	4
October: 5th, 12th, 19th, 25th	S16166, S16374, S16367, S7062	2Z10267, 2Z10265, 2Z10273, 2Z10271	4
November: 2nd, 9th, 16th, 23rd, 30th	S12535, S16366, S14641, S16361, S16365	2Z10272, 2Z10278, 2Z10269, 2Z10268, 2Z10259	5
December: 7th, 14th, 21st, 28th	S16368, S16395, S16178, S16364	2Z10262, 2Z10263, 2Z10260, 2Z10257	4
Total profiles during Jan-Dec 2011 = 48			

Efforts were made to keep the launch time more-or-less fixed on different days; however, launch time has to be varied (Figure 2.7) due to the unavailability of the required permissions from the navigation controllers. However, it can be seen that general launch time has been within a time window of two hours around 1200 hours IST, except few cases.

Details on entire setup used for balloon flights including the ozone sensor and radiosonde have been described in the Chapter 2. The raw data has been averaged into the vertical bins of 100 meter. All the data points were checked for 2-sigma filter from the mean value of that bin and the data points exceeding the mean by more than 2-sigma were filtered. Then this filtered data has been used in the further analysis. The results are discussed in the following sections:

4.1. Variations in the Meteorological Parameters

The synoptic winds over this region commonly show the seasonal changes every year [Asnani, 2005]. Air masses circulate over the continental Indian region including the IGP during the spring and autumn before reaching to the observation site. While, cleaner marine air masses are received during the summer-monsoon. During winter months, mostly westerly and northwesterly winds prevail over this region. Solar radiation is generally most intense during the spring and significantly lower during the summer-monsoon and winter. Highest values of relative humidity and maximum rainfall over this region are observed during the summer-monsoon. Further details of general meteorology and the synoptic winds over this region can

be seen elsewhere [e.g. *Sagar et al.*, 2004; *Asnani*, 2005; *Kumar et al.*, 2010]. The maiden observations of the vertical profiles of the meteorological parameters over the central Himalayas discern significant variations as discussed in the following subsections:

4.1.1. Air Temperature and Relative Humidity

The vertical profiles of air temperature obtained from the radiosonde observations for all the flights during twelve months of the year 2011 are shown in the Figure 4.2. Average temperature near the surface (2500 m amsl) is found to be highest during the summer-monsoon ($15.0 \pm 1.0^\circ\text{C}$) and lowest during the winter ($6.3 \pm 3.2^\circ\text{C}$). Moreover, the variability (one sigma value in percentage) in near surface temperature during summer-monsoon is much lower (6.4%) in comparison with the other seasons (23.6 to 51.2%). The seasonal variation in the temperature in the lower troposphere and middle troposphere is observed to be similar to that near the surface. However, the variations are different in the upper troposphere (e.g. at ~ 15000 m amsl), where in contrast the maximum temperature ($-63.8 \pm 2.8^\circ\text{C}$) is in winter and minimum temperature ($-67.7 \pm 2.9^\circ\text{C}$) is seen during the autumn.

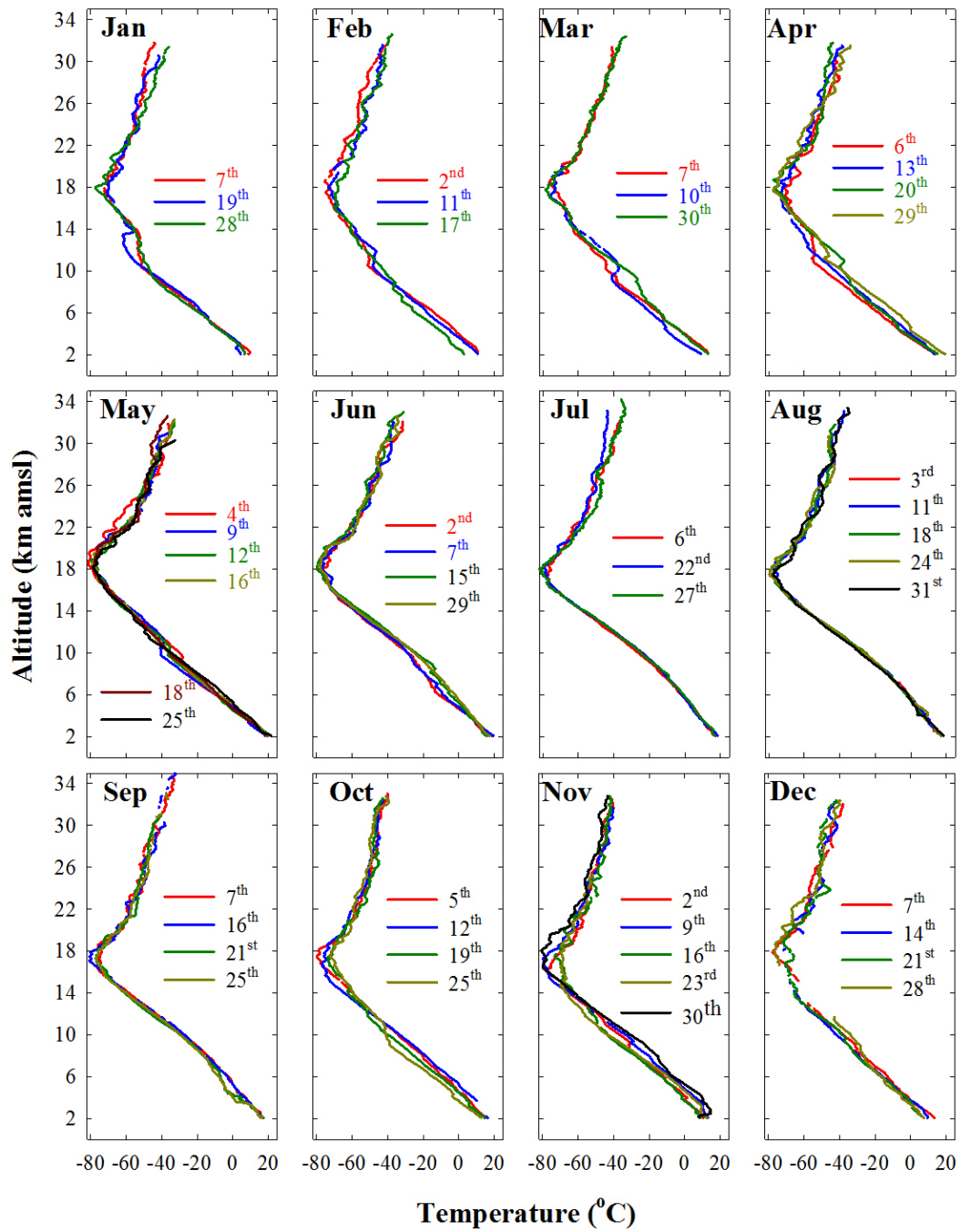


Figure 4.2: The vertical profiles of air temperature during twelve months of the year 2011 obtained from the radiosonde observations at Nainital in the central Himalayas.

Temperature profiles are observed to have inversions in the middle troposphere on several occasions during winter and spring. These inversions could be associated with the presence of the multiple tropopauses as well as the intrusions of ozone rich air into the troposphere. These features are investigated in more detail in the section 4.2 of this chapter and section 5.1 in the Chapter 5. These kinds of temperature inversions are not observed during most of the summer-monsoon period.

The vertical profiles of relative humidity during January-December of the year 2011 obtained from the radiosonde observations are shown in the Figure 4.3. The vertical profiles of relative humidity show very large week-to-week and seasonal variabilities over this region. Near surface values of relative humidity are maximum during the summer-monsoon period ($89.5 \pm 10.3\%$) and minimum during the winter ($27.3 \pm 31.5\%$). Such higher one-sigma value (31.5) in the relative humidity indicates that week-to-week variability over this region is very high near surface during winter. Moreover, maximum in the near-surface relative humidity during the summer-monsoon is indicating the prevalence of the cloudy and rainy conditions over this region. Here it can be noted that such conditions could suppress the ozone photochemistry by reducing the solar radiation and lead to the wet removal of some of the ozone precursors as well.

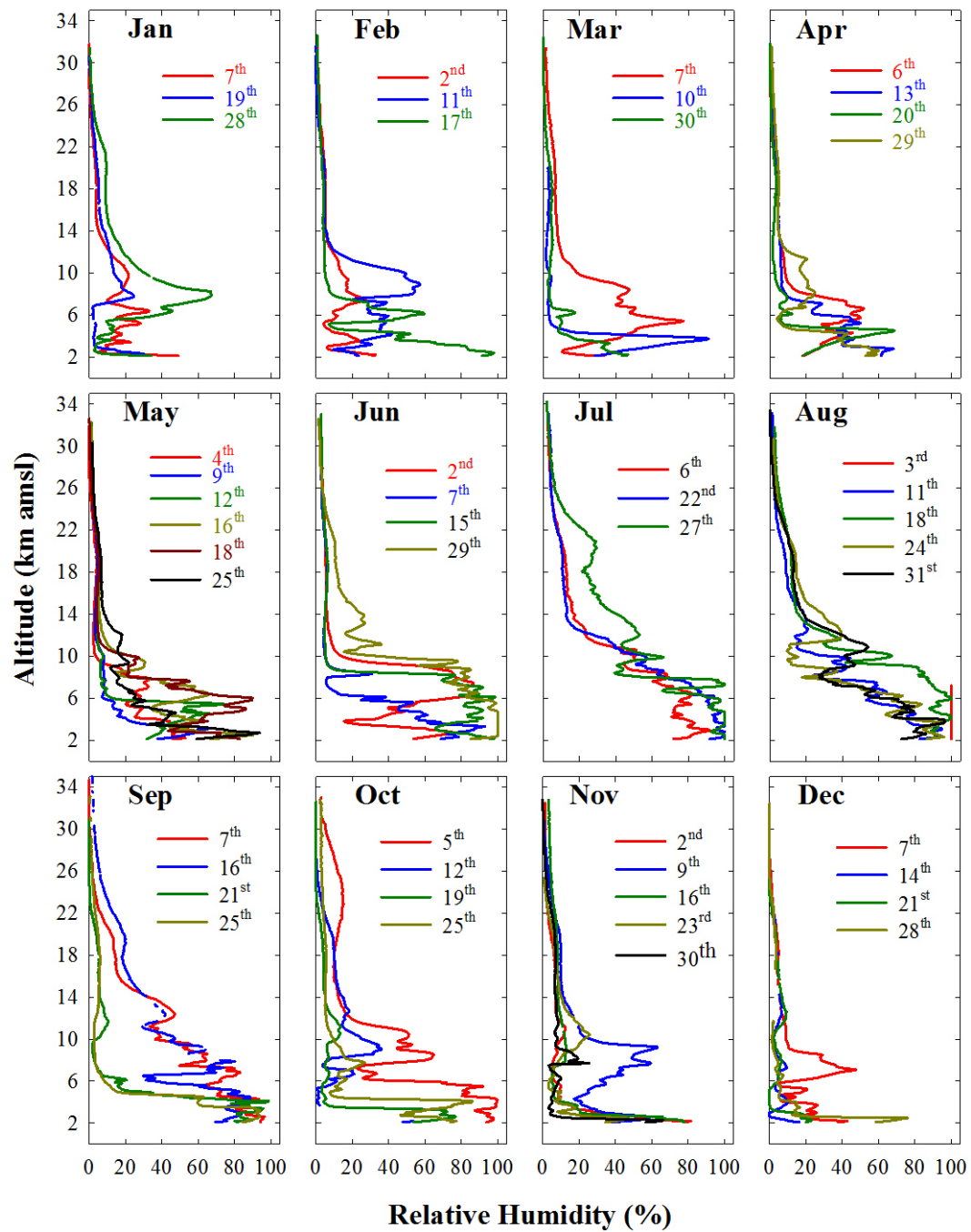


Figure 4.3: The vertical profiles of relative humidity during twelve months of the year 2011 obtained from the radiosonde observations at Nainital in the central Himalayas.

4.1.2. Wind Speed and Wind Direction

The vertical profiles of wind speed during January-December of the year 2011 obtained from the radiosonde observations over the central Himalayas are shown in the Figure 4.4. Wind speed shows a prominent vertical profile with strongest winds in the middle troposphere in all the seasons except during the summer-monsoon. Wind data could not be collected during the 19th January flight due to a technical problem in the communication. Near surface wind speeds are observed to be the strongest during the spring (6.8 ± 2.7 m/s) and the weakest during the winter (4.0 ± 1.7 m/s). While, in contrast with the variations in wind speeds near the surface, the variability is different in the higher altitudes. In the lower to upper tropospheric altitudes, the wind speeds are strongest during the winter and weakest during the summer-monsoon.

Moreover, the peak wind speeds in the seasonally averaged profiles were strongest (68.2 ± 14.8 m/s at 11.5 km) during winter and moderately higher during the spring (36.3 ± 15.3 m/s at 11.9 km) and autumn (36.0 ± 19.5 m/s at 12.1 km). During the summer-monsoon, the wind speed does not show a clear maximum in the profile and winds were observed to be moderately stronger in the middle-upper troposphere (~ 14 m/s) and strongest in the stratosphere (18.1 ± 5.2 m/s at 30.4 km amsl).

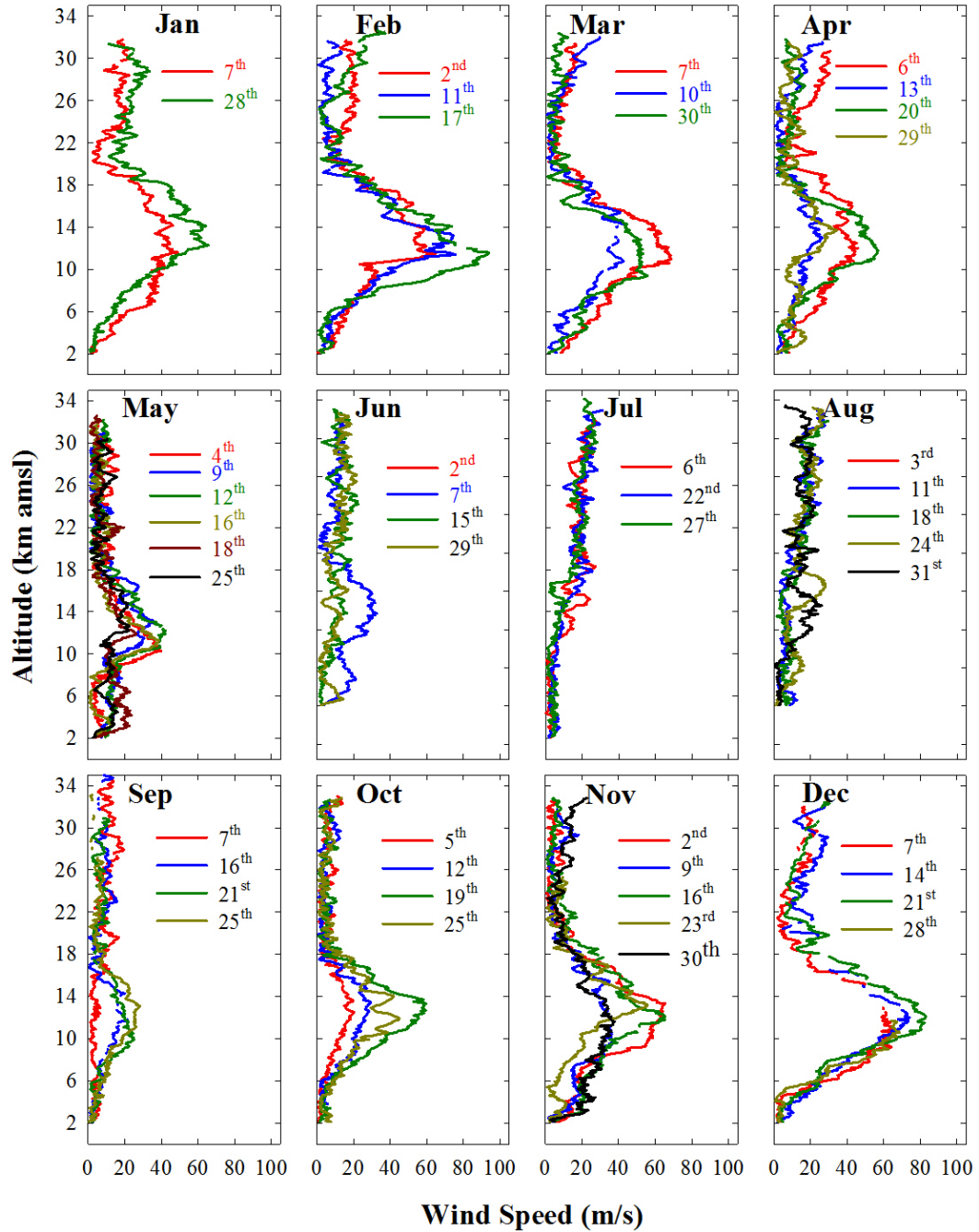


Figure 4.4: The vertical profiles of wind speed during twelve months of the year 2011 obtained from the radiosonde observations at Nainital in the central Himalayas.

The presence of very strong winds (40 to 80 m/s) in the middle-upper tropospheric altitudes over this region, observed more frequently during the winter and occasionally during spring and autumn too, is suggested to be associated with the prevailing subtropical jets. These stronger winds in the middle troposphere could bring pollution from the upwind regions to above the central Himalayas. While, the emissions uplifted from this region could be transported to the downwind regions on the faster timescales. Moreover, this also indicates the presence of intense dynamical processes in the middle-upper tropospheric altitudes particularly during winter, which is consistent with the suggested possibility of the wintertime multiple tropopauses/tropopause fold processes over this region.

The seasonal variations in the wind direction at different altitudes over the central Himalayas are shown (Figure 4.5) in the form of percentage occurrences in the four quadrants 0-90, 90-180, 180-270 and 270-360 degrees. The dominance of northwesterly winds is clearly visible (50-89% in the 2-4 km) during winter and spring in the lower troposphere. While, in contrast, the maximum contribution during summer-monsoon is from the southeasterly winds (28-68%) in the 2 to 4 km range. Southwesterly winds also contribute significantly during summer-monsoon in 4 to 6 km (13-39%). The variations in the wind directions are observed to be different in the higher altitudes (e.g. 8 to 12 km), where, during January-February, the occurrences of southwesterly winds are very less (7-15%) as compared with the lower altitudes.

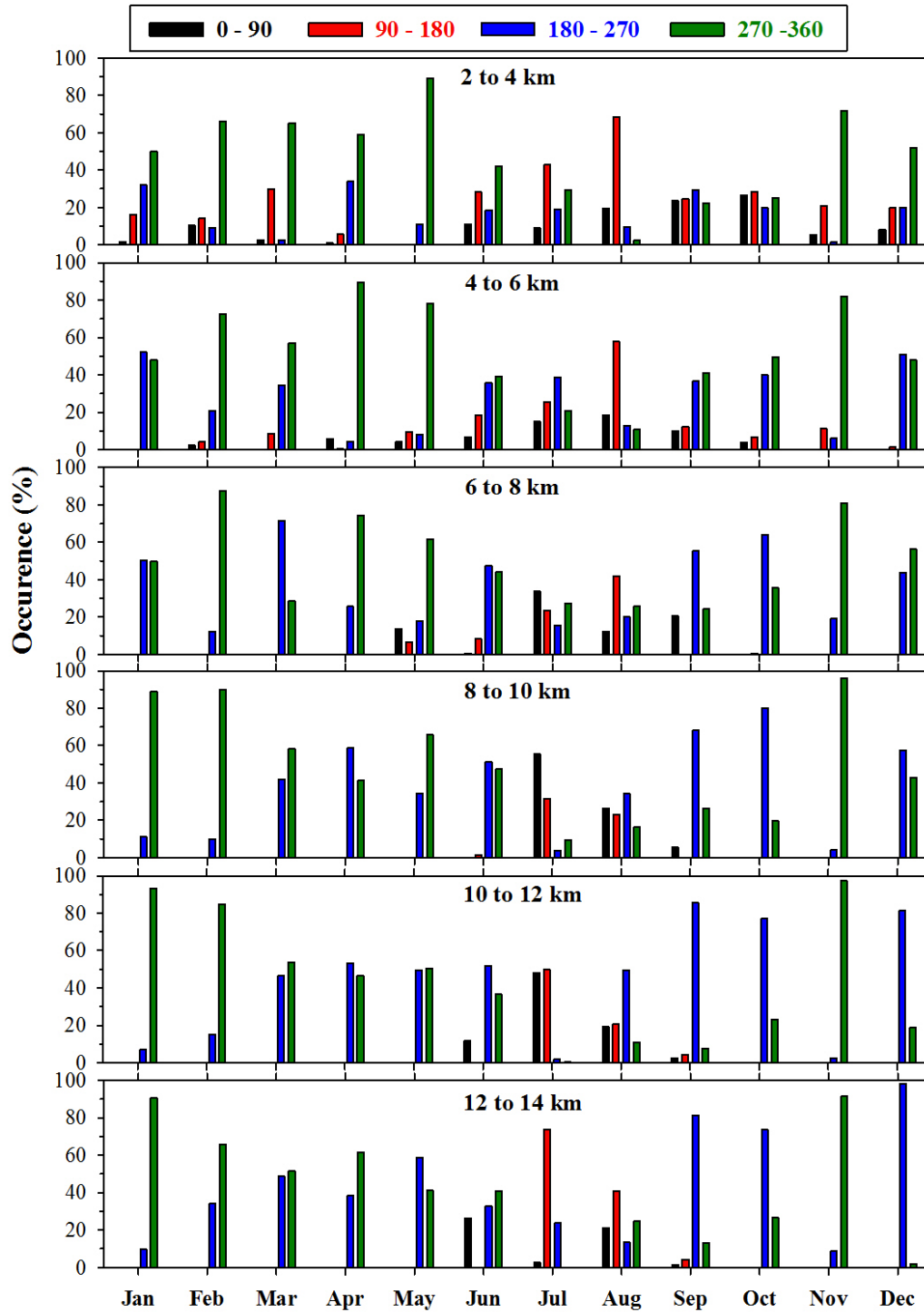


Figure 4.5: The seasonal variations in the wind direction at different altitudes, as the percentage occurrences in four quadrants (0-90, 90-180, 180-270 and 270-360 degrees).

4.2. Estimation of Tropopause Pressure

The observed temperature profiles have been used to investigate the variability in tropopause pressure. The tropopause definition is defined using the lapse rate criteria of WMO, which states it as the lowest altitude at which the lapse rate decreases to 2°C/km or less and the average lapse rate between this altitude and all higher altitudes within 2 km does not exceed 2°C/km [WMO, 1957]. The calculations of lapse rates from radiosonde data have been made using the following method described in Reichler *et al.* [2003]:

$$\Gamma(p) = -\frac{\partial T}{\partial z} = -\frac{\partial T}{\partial p} \frac{\partial p}{\partial z} = -\frac{\partial T}{\partial p^k} \frac{\partial p^k}{\partial p} \frac{\partial p}{\partial z}$$

Here, T is the temperature, p is pressure, z is the height and $k = R/c_p$ where R is the gas constant for the dry air and c_p is the specific heat capacity of air at constant pressure. Using the hydrostatic approximation, the above equation transforms as:

$$\Gamma(p) = \frac{\partial T}{\partial p^k} \frac{p^k}{T} \frac{kg}{R}$$

Using this lapse rate profiles and the WMO criteria, tropopause pressure defined as Lapse Rate Tropopause (LRT) has been calculated for the days of balloon flight. In addition, the tropopause pressure data has also been obtained from two satellite-based instruments (AIRS and TES). Tropopause pressure has also been estimated using the meteorology from WRF model output. The seasonal variations in the

tropopause pressure from the radiosonde, satellites and model results are shown in the Figure 4.6a.

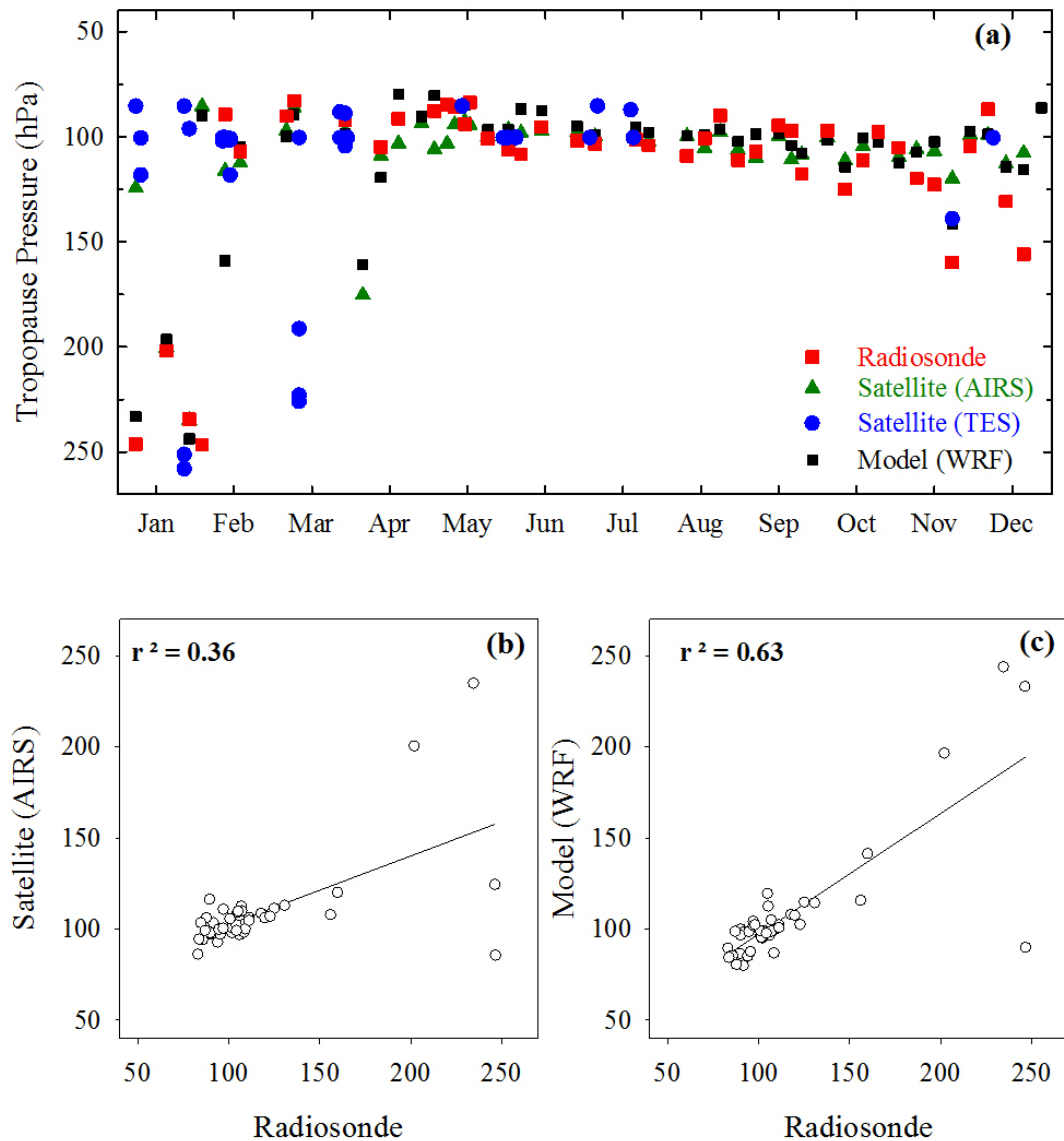


Figure 4.6: (a) The seasonal variation in lapse rate tropopause (LRT) over Nainital estimated from radiosonde measurements for year 2011. Lapse rate tropopause (LRT) data obtained from satellite (AIRS) and model results (WRF) are also shown for the comparison. (b) Correlations between LRT from radiosonde and satellite and (c) radiosonde and model are shown.

Clearly, the tropopause pressure from all the datasets show significant variability over this region. Tropopause pressure does not show a clear seasonal cycle over this region and all the three datasets show similar tropopause pressure values from April to October. While, it discerns a dramatic variability during winter and somewhat in early spring too. The seasonally and annual average tropopause pressure from radiosonde, satellites and WRF model are tabulated in the Table 4.2.

Table 4.2: Tropopause pressure (hPa) in four seasons from the radiosonde observations, AIRS and TES satellites and WRF model.

	Radiosonde	AIRS	TES	WRF
Winter (DJF)	166.6 ± 66.9	132.6 ± 50.2	116.2 ± 51.3	136.9 ± 62.4
Spring (MAM)	90.7 ± 7.1	104.1 ± 22.3	128.1 ± 55.8	96.6 ± 22.1
Summer (JJA)	102.9 ± 6.2	100.2 ± 3.3	96.9 ± 6.5	96.0 ± 4.8
Autumn (SON)	112.3 ± 17.6	107.3 ± 5.9	139.1*	106.9 ± 11.6
Annual Average	115.6 ± 41.1	109.7 ± 27.3	116.8 ± 46.4	107.9 ± 34.4

* indicates only one data point.

The annual average tropopause pressure from the radiosonde (115.6 ± 41.1 hPa) is seen to be in reasonable agreement with the AIRS and TES satellites (109.7 ± 27.3 and 116.8 ± 46.4 hPa respectively) and model results (107.9 ± 34.4 hPa). As indicated by the standard deviations in different seasons, the variability in radiosonde tropopause is found to be highest during winter ($\sigma = 66.9$ hPa) as

compared with the other seasons. The differences between the radiosonde data (166.6 ± 66.9 hPa) with satellites (116.2 ± 51.3 and 132.6 ± 50.2 hPa) and model (136.9 ± 62.4 hPa) are also significantly higher during the winter. The correlation analysis of the radiosonde data with satellite (AIRS) and model (WRF) results have been shown in the Figures 4.6b and 4.6c respectively. It is found that the radiosonde data bears better correlation with the model results ($r^2 = 0.63$) as compared with its correlation with the satellite data ($r^2 = 0.36$).

Large variability in the tropopause pressure during winter and early-spring could be associated with the occurrences of tropopause folds or multiple-tropopause as also reported over the Tibetan Plateau during winter [Chen *et al.*, 2011]. It has been shown that tropopause dynamics could in turn lead to the stratosphere-troposphere exchange of the air-masses which would influence the tropospheric ozone distribution. Moreover, the differences in the tropopause calculations from observations, satellite data and models could lead to the differences in the tropospheric column of pollutants. These implications of tropopause variability will be discussed in more detail in the section 4.4.

4.3. Vertical Distribution of Ozone

The vertical profiles of ozone obtained from the ozonesonde observations over the central Himalayas during twelve months of the year 2011 are shown in the Figure 4.7.

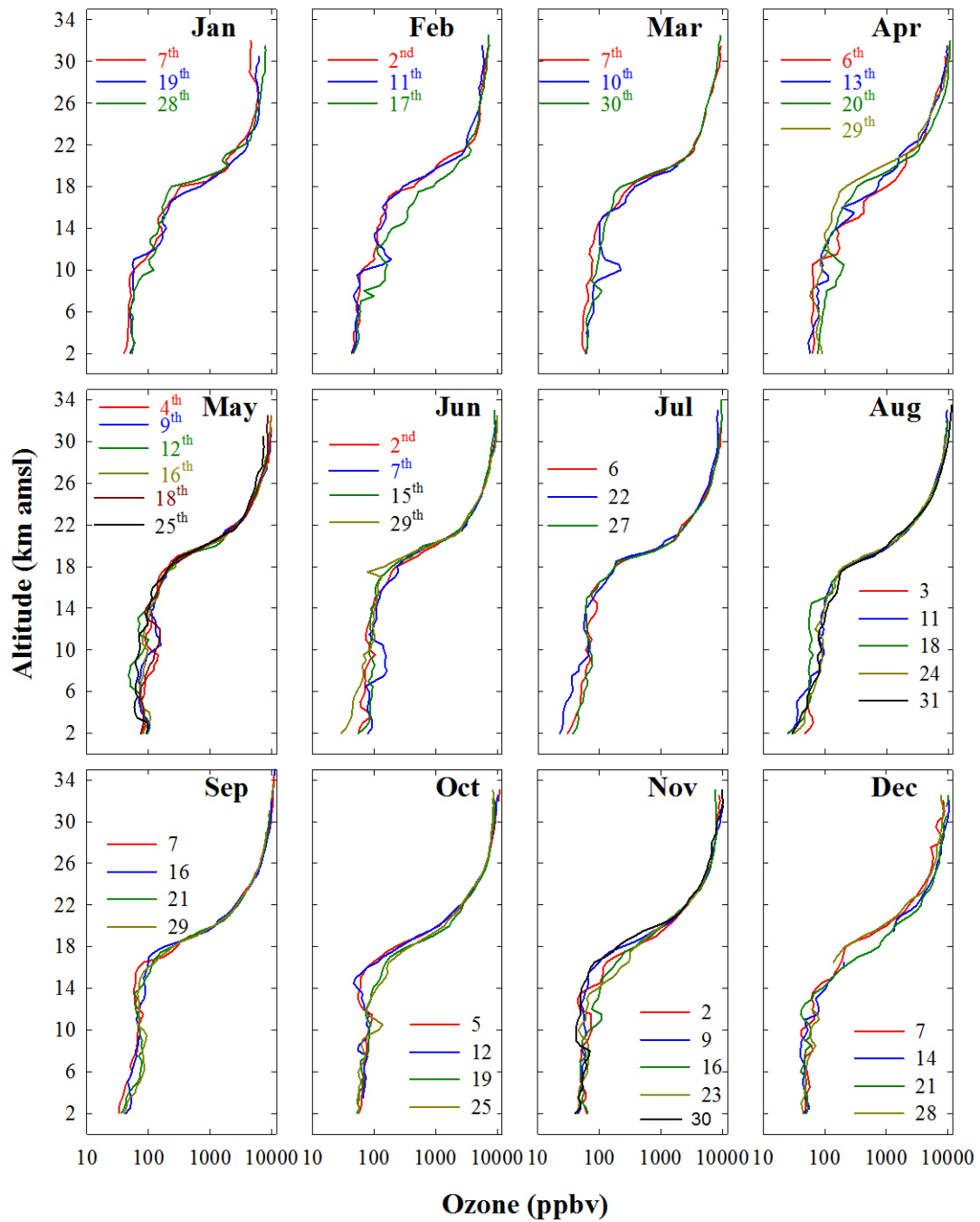


Figure 4.7: The vertical profiles of ozone during twelve months of the year 2011 obtained from the ozonesonde observations at Nainital in the central Himalayas.

The observations reveal large week-to-week and seasonal variabilities in the vertical distribution of ozone over this region. Variability (1σ in percentage) in the near surface (2500 m amsl) ozone is highest during the summer-monsoon (43.4%), moderate during the spring and autumn (21.6 and 17.8%) and lowest during the winter (9.6%).

This seasonality in the ozone variations is consistent in the lower troposphere (5000 m amsl). While, in the middle troposphere (10 km amsl), the ozone variability is maximum during the winter (46.9%) and minimum during the autumn (27.1%) in contrast with the lower troposphere. This is again different in the in the upper troposphere (15 km amsl), where, the ozone variability is maximum during the spring (43.1%) and minimum during the summer-monsoon (21.9%). The difference in the variabilities in the lower, middle and upper troposphere suggests that the processes influencing ozone variations are different in different altitude regions. The observed maximum ozone variability in the lower troposphere during the summer-monsoon is attributed to the dramatic variability in the meteorological conditions consisting of cloudy-rainy conditions. Wind direction also changes drastically mainly from northwesterly to southeasterly. Lower tropospheric ozone also shows moderately high variability during spring and autumn and it is suggested to be associated with the local photochemical and dynamical processes. As mentioned earlier that solar radiations is maximum during spring followed by autumn over this region. While, minimum variability during winter indicates minimal role of local photochemical and dynamical processes in the lower atmosphere. The observed maximum ozone variability in the middle troposphere during the winter coincides

with the strongest winds at this altitude and presence of multiple tropopauses. This indicates that middle-tropospheric ozone during winter is mainly controlled by dynamical processes. In the upper troposphere, highest variations during spring again indicate the role of dynamics including stratosphere-troposphere-exchange. Minimum variations in the summertime upper troposphere suggest that the influences of monsoonal circulations are minimal in the UT.

Apart from the above, few notable features include the observations of stratospheric intrusions and secondary ozone maxima in the ozone profiles. On 17th February, significantly higher ozone levels can be clearly seen from the lower stratosphere up to about 6-7 km amsl (Figure 4.7). This event seems to be a deep stratospheric intrusion. Additionally, on many occasions, secondary ozone peaks are observed in the middle troposphere more frequently during spring. These events will be discussed in more detail in the chapter 5. All the observations have been averaged for four seasons up to an altitude of 18 km to show the tropospheric variabilities more clearly (Figure 4.8).

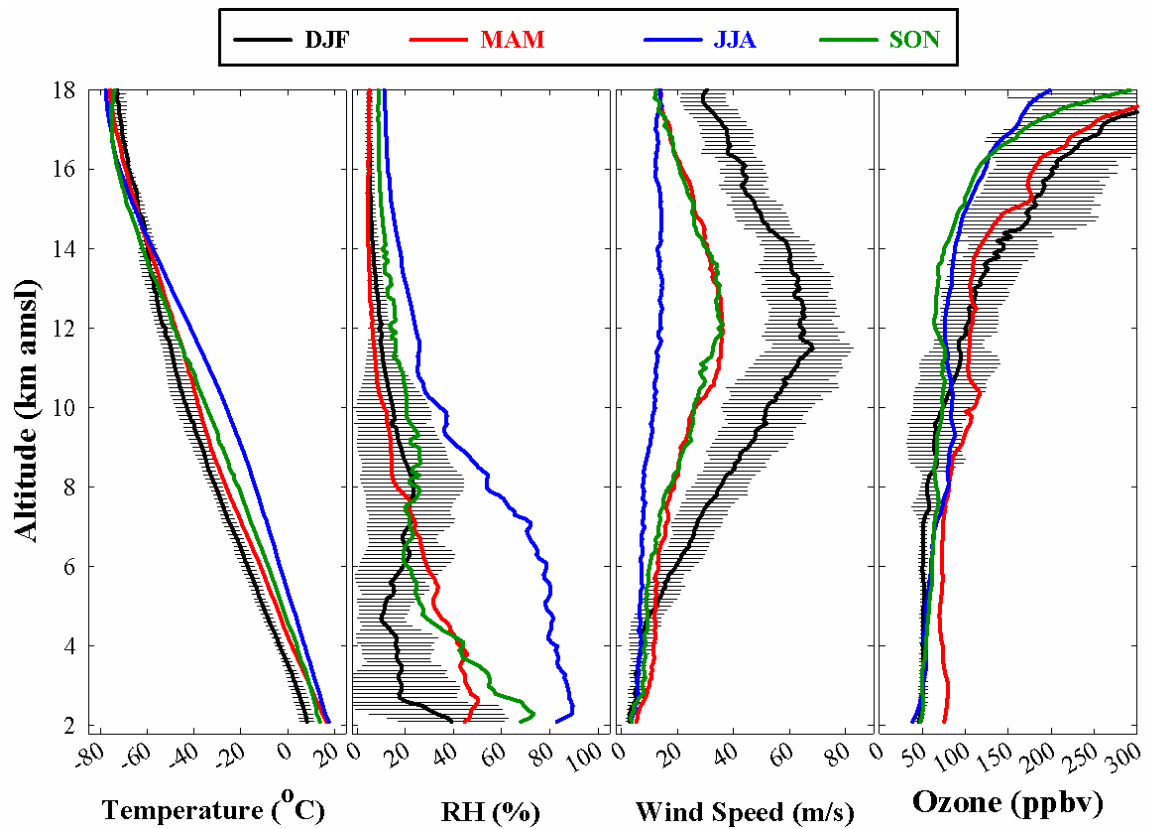


Figure 4.8: The seasonal variations in the seasonally averaged vertical profiles of temperature, relative humidity, wind speed and ozone over Nainital during the year 2011.

Temperature and relative humidity profiles show maximum values during the summer-monsoon (JJA). Presence of a subtropical jet is clearly seen with highest wind speed during winter in the middle-troposphere. Average ozone mixing ratios in the lower troposphere are highest (70 to 80 ppbv) during spring. To investigate the ozone seasonal variability in different altitudes, ozone data are divided into layers of 2 km starting from surface up to 14 km as shown in the Figure 4.9.

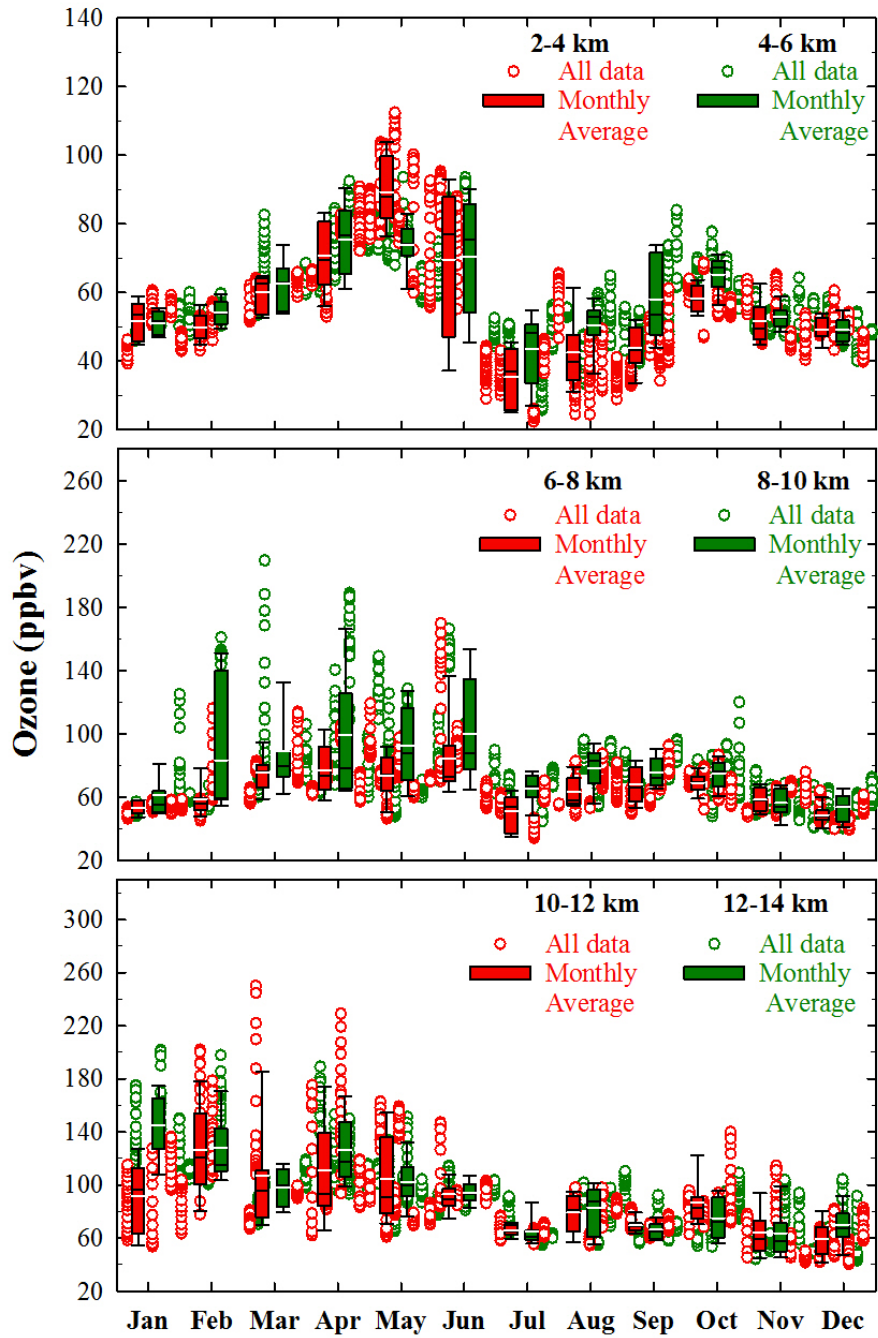


Figure 4.9: The seasonal variations in the layers of 2-2 km thickness (a) 2 to 4 and 4 to 6 km (b) 6 to 8 and 8 to 10 km (c) 10 to 12 and 12 to 14 km over Nainital during 2011. Monthly mean values are shown by white lines on the boxes while median values are shown by black lines.

Lower troposphere (2 to 6 km) shows a very prominent seasonal cycle with highest levels (more than 100 ppbv in May) during spring and lowest levels during the summer-monsoon. Ozone levels are also lower during winter and there is a secondary peak during autumn. This variability in the 2 to 6 km is observed to be consistent with the variability in meteorological parameters and surface ozone observations over this region [Kumar *et al.*, 2010; Ojha *et al.*, 2012]. Ozone seasonality is less pronounced in the higher altitudes (6 to 10 km and 10 to 14 km) as compared with the lower troposphere. However, in the higher altitudes also the ozone levels show a tendency of higher levels during spring and lower levels during the summer-monsoon.

It has been shown that photochemical production of ozone from the local and regional emissions of precursors in favorable meteorological conditions is the main driver of springtime ozone maxima over this region [Ojha *et al.*, 2012]. The northern Indian biomass burning is suggested to provide an additional supply of ozone precursors during the spring [Kumar *et al.*, 2011]. The quantitative contribution of biomass burning in the ozone enhancements will be discussed more in the Chapter 5. Lower ozone levels during summer-monsoon are mainly associated with the arrival of cleaner marine air masses over this region. Along with the arrival of the ozone and precursors depleted air masses, prevailing cloudy and rainy conditions further suppress the ozone photochemistry. The influence of regional emissions and photochemistry decreases with the altitude and observed seasonality is not that much pronounced at higher altitudes. While, dynamical processes including advection and

intrusions from stratosphere play the key roles in controlling the ozone variabilities in middle-upper troposphere.

4.4. Comparison With the Satellite Data

The satellite retrievals constitute an important dataset to study the distributions and long-term changes in tropospheric ozone at regional and global scales but validation of these retrievals is essential to lend confidence in their use for such scientific studies. Tropospheric Emission Spectrometer (TES) provides the global distribution of tropospheric ozone every other day and TES ozone retrievals have been validated over the USA [*Worden et al., 2007; Nassar et al., 2008*]. However, such a validation exercise has not been conducted for the Indian region using ECC sonde. In view of this, present ozonesonde observations at Nainital provide a very good opportunity for a comparison with TES satellite retrieved ozone profiles over the northern Indian region. This comparison becomes more important due to complex topography over the central Himalayan region, where altitude varies from less than 0.5 km to 5-6 km within 3-4° latitude-longitude region. In this direction, TES ozone retrievals are compared with spatially and temporally co-located in situ ozonesonde profiles for the first time to identify errors and biases in satellite retrievals as explained in the following sections.

4.4.1. Collocation Criteria and Application of TES operator

All the satellite retrievals falling within ± 48 hours of ozonesonde observations and within a $5^\circ \times 5^\circ$ box centered at Nainital are considered as collocated.

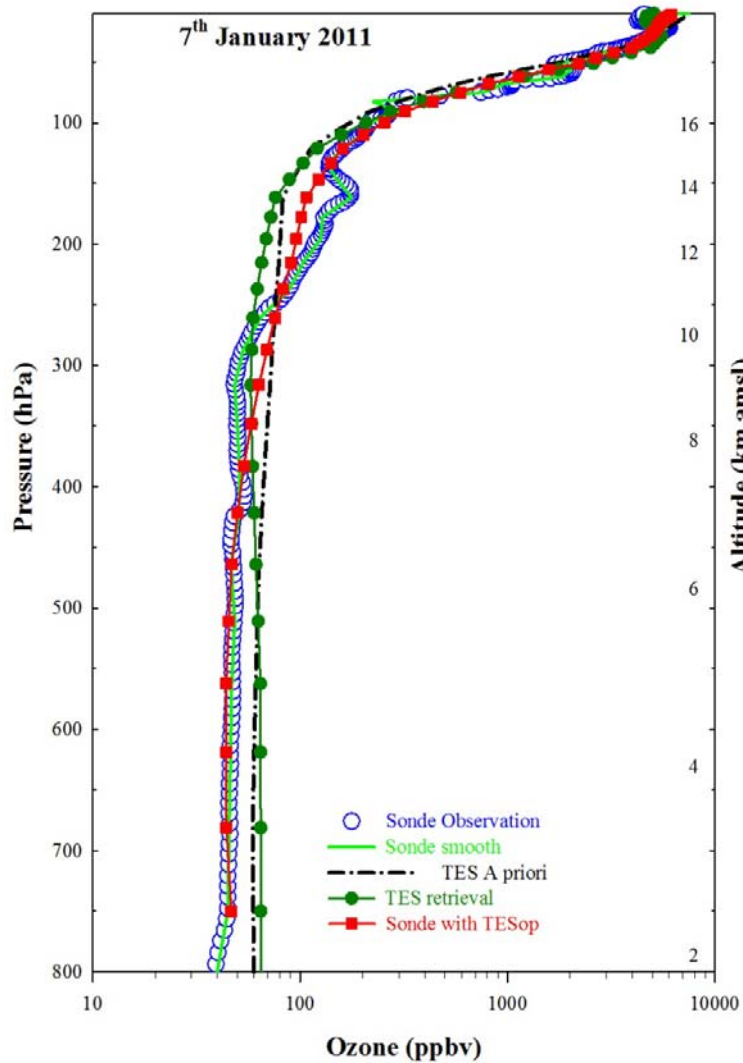


Figure 4.10: A comparison of the original ozonesonde profile, sonde data smoothed using the TES a priori, TES a priori, TES retrieval and TES operated sonde profile for one day observation on 7th January 2011.

For comparing TES and ozonesonde datasets [e.g. *Worden et al.*, 2007; *Nassar et al.*, 2008], it is essential to take into account the vertical resolution and sensitivity of TES. This is done by applying the TES-averaging kernel and a-priori profile to the ozonesonde profile. The resulting vertical profile is referred to as Sonde profile with TES operator (Sonde with TESop) and it represents the profile which TES would have estimated for the given atmospheric state in absence of other errors. The vertical grid of ozonesonde data and TES retrievals is also different as ozonesonde profiles generally do not go above 10 hPa and TES profiles are available from surface to 0.046 hPa. The unmeasured part of stratosphere in ozonesonde profiles is approximated by appending the ozonesonde profile with TES a priori above 10hPa. Further, the ozonesonde data has been interpolated and extrapolated to a fine levels pressure grid of 800 pressure levels from surface to 0.046 hPa to homogenize the original irregular and variable ozonesonde data with the TES. Thus obtained ozonesonde profile is then applied by the TES averaging kernel. Figure 4.10 shows the original ozonesonde profile, sonde data smoothed using the TES a priori, TES a priori, TES retrieval and TES operated sonde profile for one observation (7th January 2011). The validation methodology, adopted here, has been discussed in detail by *Worden et al.* [2007].

4.4.2. Comparison of the Vertical Profiles

The seasonally averaged ozone profiles from the ozonesonde observations, collocated TES satellite retrievals and ozonesonde with TES operator are shown for the four seasons in the Figure 4.11. In general, the three datasets show similar vertical distribution and agree with each other within the 1-sigma spread. The ozonesonde profiles operated by the TES operator are observed to be in better

agreement with the TES data. In the lower troposphere, the differences between TES and sonde data with TESop are mostly less than 10 ppbv except in the summer-monsoon. The differences are higher in the middle tropospheric and upper tropospheric altitudes (~15 and 20 ppbv).

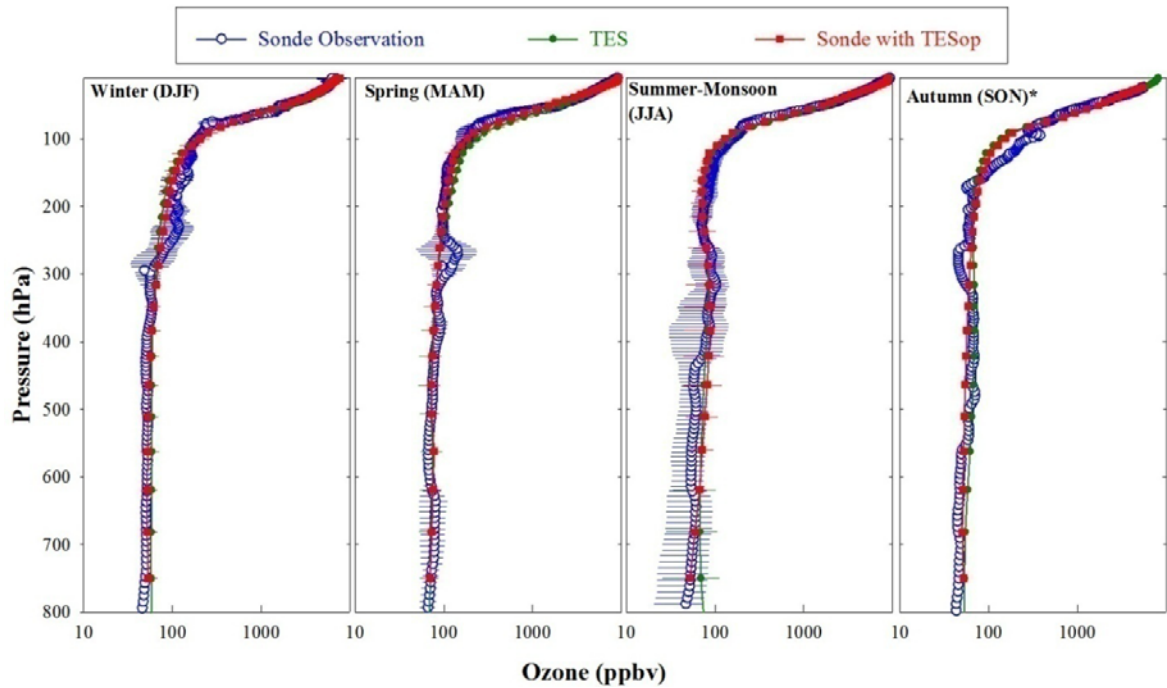


Figure 4.11: Comparison of seasonally averaged collocated observations from ozonesonde and TES satellite during winter, spring, summer-monsoon and autumn.

Here it can be noted that the secondary ozone peak features observed in the ozonesonde profiles between 300 hPa and 200 hPa pressure levels during winter and spring are not seen in the satellite retrievals. Similarly, the ozone depleted layer which can be seen during the autumn at about 300 hPa pressure in the ozonesonde profile, is not seen in the satellite retrieved ozone profile. This suggests that the satellite is generally able to detect the variations in the ozone distribution but has

limitations particularly in capturing small features/events of high or low ozone in the ozone distribution that is likely due to limited sensitivity. To quantify the differences between satellite retrievals and ozonesonde data, the vertical profiles of the percentage bias has been calculated.

$$\text{Percentage Bias} = \frac{(\text{TES ozone} - \text{Sonde ozone with TESop}) \times 100}{\text{Sonde ozone with TESop}}$$

Figure 4.12 shows the vertical profiles of the percentage biases during the four seasons over this region. It is observed that there is significant variability in the vertical profile of percentage bias during different seasons.

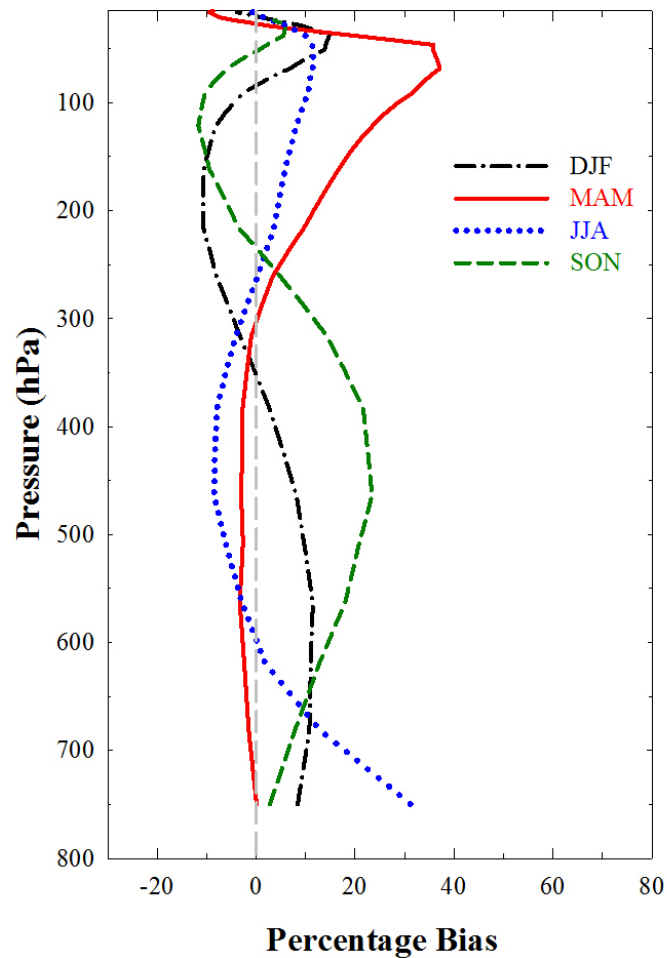


*Figure 4.12: The vertical profiles of the percentage bias in the TES retrievals during different seasons. Autumn season includes only one day profile and denoted by *.*

TES overestimates the ozone levels near the surface (~749 hPa) in all the seasons, except in spring, by 3 to 31.2%. The maximum bias in the near surface ozone is observed to be 31.2% during the summer-monsoon. The summer-monsoon season is characterized by thick cloud cover around Nainital and highest bias during this season might be due to limited ability of TES through the clouds. TES overestimates the ozone levels in the lower and middle troposphere (up to 400 hPa) by 5 to 22.5% during winter and autumn. While, during the summer-monsoon, ozone levels are underestimated by about 8% above 600 hPa in contrast with the near surface ozone. In contrast with other seasons, the TES ozone is in very good agreement with the ozonesonde data during spring and the bias is only 2-3% up to 400 hPa. However, near the tropopause, the bias is very high (more than 30%) during spring.

4.4.3. Tropospheric Column Ozone (TCO)

In this section, we compare the observed tropospheric column ozone (TCO) with available TES retrievals of TCO. The observed TCO is estimated by integrating the observed ozone profiles from surface to the tropopause pressure estimated from the radiosonde temperature profiles as discussed in the section 4.2. The tropopause pressure retrievals from TES are also used to identify the uncertainty in the calculation of TCO due to differences in TES retrieved and radiosonde observed tropopause pressure. The number of spatially and temporally co-located satellite and observed profiles was too small ($N = 12$) for such a comparison and thus we have

relaxed our co-location criterion. For this comparison, we select all the TES retrievals falling within 2 hours of sonde launch time and in a $5^{\circ}\times 5^{\circ}$ box around Nainital, and do not smooth sonde data with TES operator. Since there are small differences in the original ozonesonde profiles and those smoothed with TES operator (as shown in the previous section), this relaxation is anticipated to have relatively small influence on the conclusion from this comparison.

The seasonal variations in daily and monthly average TCO values from the sonde and TES are shown in Figure 4.13. The observed seasonality in TCO is detected well by the TES satellite, in general, however some differences are observed particularly during the winter and autumn. Satellite retrievals are not available during the complete summer-monsoon (JJA) period, however, the drastic decreases during June-July are observed in the TES data. TCO data from the ozonesonde observations show a typical seasonality comprising of spring maxima (47.2 ± 9.8 DU) and winter minima (30.4 ± 10.1 DU).

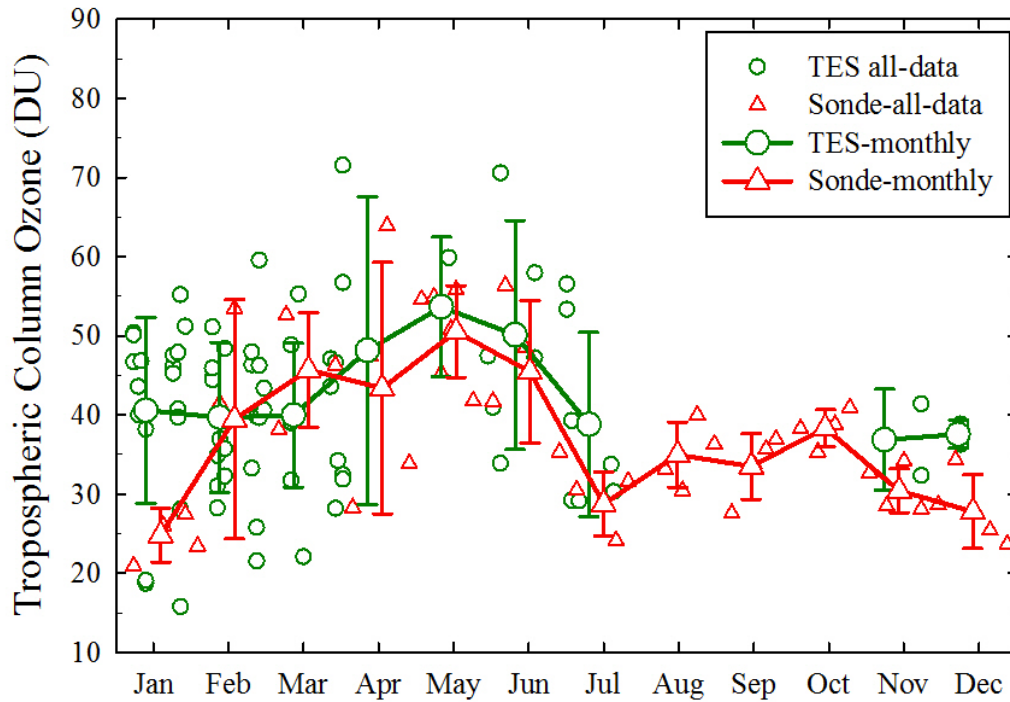


Figure 4.13: The seasonal variation in the daily and monthly values of TCO from the sonde and TES all observations are shown.

This seasonality in the ozonesonde-TCO is consistent with the surface ozone observations over this region [Kumar *et al.*, 2010; Ojha *et al.*, 2012]. However, the secondary ozone peak in autumn [Kumar *et al.*, 2010] is not very prominent in the TCO data. Further, the summer-monsoon TCO values are moderately higher (37.1 ± 9.5 DU) as compared with the autumn (33.8 ± 4.2 DU). The annual average TCO value from ozonesonde observations is estimated to be 37.5 ± 10.5 DU and average TCO from TES data is 41.3 ± 11.2 DU.

4.4.4. Correlation Analysis

The ability of TES to detect TCO variabilities is further examined by performing a correlation analysis using the spatially and temporally collocated observations (Figure 4.14). Here, the TCO from sonde is calculated using the ozonesonde profiles operated by the TES operator as discussed in the section 4.1.1 and is denoted by Sonde-TCO-TE Sop.

Considering the observed differences between the TES tropopause and sonde tropopause pressure (section 4.2), an attempt is further made to investigate the influence the variations in tropopause on the TCO values. For this, the tropopause pressure from the TES data has been applied on the TES operated sonde TCO values and is denoted by Sonde-TCO-TE Sop-TE S-Trop. The correlations of TES TCO with Sonde-TCO-TE Sop and Sonde-TCO-TE Sop-TE S-Trop are shown in the Figure 4.14. A linear regression fit has been made to estimate the coefficient of the determination (r^2) between the satellite and sonde datasets.

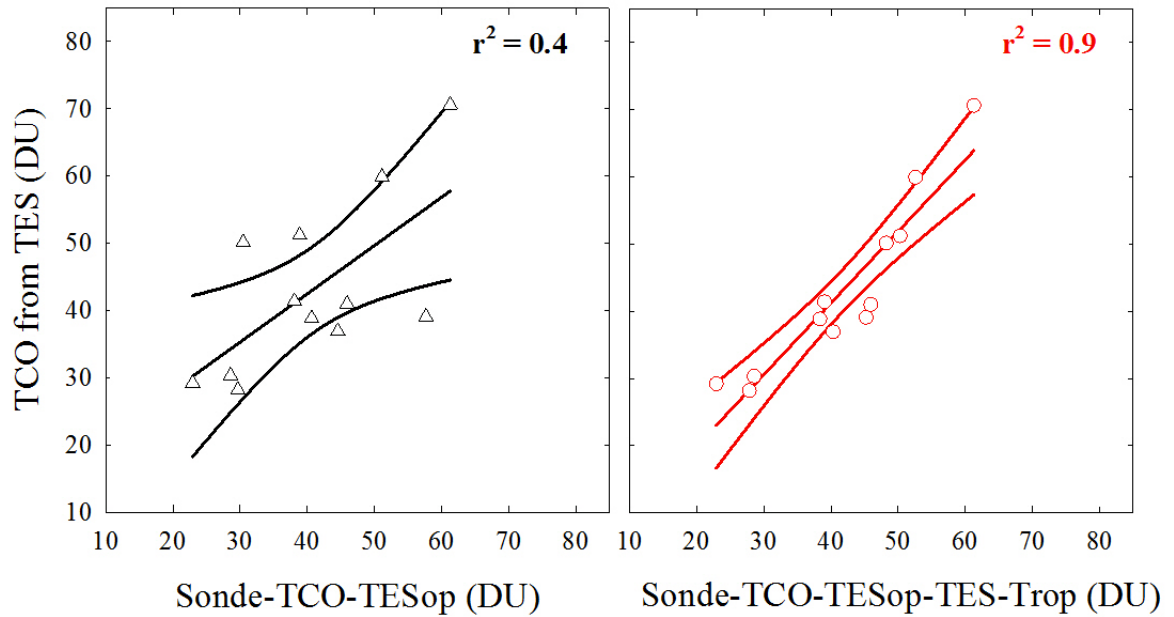


Figure 4.14: The correlations of TES TCO with Sonde-TCO-TE Sop and Sonde-TCO-TE Sop-TE S-Trop are shown. A linear regression fit has been made to estimate the coefficient of the determination (r^2) between the satellite and sonde datasets. The 95% confidence interval for the fit is also shown.

Here, it can be seen that collocated satellite data and sonde observations bear a general agreement with each other ($r^2 = 0.4$). However, this correlation improves drastically ($r^2 = 0.9$), when the same tropopause is used for the two datasets. This is mainly associated with the integration of smaller or larger columns of the atmosphere in the different datasets. It is concluded that uncertainties in the location of the tropopause can cause significant uncertainty in the tropospheric columns of the pollution. Moreover such influences could be more important for ozone as there are large gradients in the ozone concentration across the tropopause. This study highlights that since this region discerns large variability in the tropopause, the satellite based observations can have uncertainties in providing the tropospheric

columns of pollution. Here it can be noted that the tropopause dynamics is one of the processes which can cause such differences, however, the inherent biases in the satellite retrievals could also have the contribution in the observed differences.

4.5. Summary and Conclusions

Balloon-borne observations of ozone and meteorological parameters, during January to December 2011 from Nainital in the central Himalayas, are analyzed. Tropopause pressure calculated from the radiosonde data shows similar variations to those from satellite data and WRF model. Dramatic variations in the tropopause pressure during winter and spring are suggested to be associated with the tropopause folds or multiple-tropopause events. Tropopause pressure from radiosonde is in better agreement with the model ($r^2 = 0.63$) as compared with the satellite data ($r^2 = 0.36$). Very strong winds (40 to 80 m/s) observed in the middle-upper troposphere are suggested to be associated with the subtropical jets. The lower tropospheric relative humidity shows large variations in the distribution with maximum values during summer-monsoon and minimum during winter.

Ozone levels in the lower troposphere shows prominent seasonality with highest levels (~100 ppbv in May) during spring and lowest levels during summer-monsoon. Ozone levels also show a secondary peak during autumn. This seasonality is consistent with the surface-based ozone observations over this region. However, the ozone seasonality is less pronounced in the middle-upper troposphere and it is

suggested that the controlling processes are different in different layers of the troposphere.

Ozonesonde profiles are compared with the co-located satellite (TES) retrievals and generally two datasets bear reasonable agreement with each other. The differences between ozonesonde data and satellite retrievals are generally lesser (10 ppbv) in lower troposphere as compared with middle-upper troposphere (15-20 ppbv). It is found that TES overestimates the lower tropospheric ozone in all the seasons except during spring. TES underestimates the ozone levels by about 8% above 600 hPa during summer-monsoon, while, during winter and autumn it overestimates the ozone levels in the lower-middle troposphere by 5 to 22.5%. The biases are observed to be highest during summer-monsoon which could be due to limited ability of TES through the clouds.

Tropospheric column ozone (TCO) estimated from the ozonesonde observations show a spring maxima (47.2 ± 9.8 DU) and winter minima (30.4 ± 10.1 DU), which is detected reasonably well by the TES satellite. However TCO values show significant variations during winter and autumn similar to those in the tropopause pressure values. To investigate this, when the TES tropopause pressure is used with the ozonesonde profiles to estimate the TCO values the correlations is improved drastically ($r^2 = 0.9$). This suggests that satellite-based observations of the tropospheric columns of pollution can have limitations associated with the variability in tropopause pressure.

Blank Page

Chapter 5

Influences of Dynamical Processes and Biomass Burning on Ozone Distribution

The dynamical processes such as stratospheric intrusions [e.g. *Levy et al.*, 1985; *Holton and Lelieveld*, 1996; *Cristofanelli et al.*, 2003; *Marcy et al.*, 2004] and advection [e.g. *HTAP*, 2010 and references therein; *Cooper et al.*, 2010] are shown to play key roles in influencing the vertical distribution of ozone. As described in the previous chapter, elevated ozone layers were observed in the middle-upper tropospheric altitudes on many occasions. A possible event of stratospheric intrusion was also noticed during winter. Thus, it is suggested that various dynamical processes strongly influence the ozone vertical distribution over this region and therefore should be investigated in detail. In addition, the analysis of surface observations and satellite data [*Kumar et al.*, 2011] have shown that the biomass burning activities over the northern Indian region are maximum in spring, which

could influence the levels of ozone-precursors and amplify the regional ozone production. However, the possible contribution of biomass burning activities in influencing ozone vertical distribution has not been studied so far.

In this chapter, the role of dynamical processes and the role of biomass burning in influencing the ozone distribution over this region are studied using the ozonesonde and radiosonde observations, model simulations of meteorological and chemical fields, satellite data of tracers and fire counts.

5.1. Stratosphere-Troposphere Exchange (STE)

The uncertainty in the tropospheric ozone budget is largely associated with the limited knowledge of contributions from the Stratosphere-Troposphere Exchange (STE). To identify these events and their input to the tropospheric ozone, measurements of ozone and meteorological parameters are essential in the Upper-Troposphere and the Lower-Stratosphere (UTLS). These studies on STE are very sparse over the Indian region [*Mandal et al.*, 1998; *Ganguly and Tzanis*, 2011] and its role is not well understood. Tropopause folding events and influences of STEs over this region are more frequent during winter and early spring [*Cristofanelli et al.*, 2010; *Chen et al.*, 2011]. One of such event observed during February 2011 has been discussed in the section 5.1.2.

In order to detect the STE events, the temporal variations in the specific stratospheric tracers are analyzed. Potential vorticity (PV) has been used as a tracer of stratospheric air masses in the troposphere [e.g. *Cristofanelli et al.*, 2006] and can be calculated as follows:

$$P_{\Theta} = -g \partial\Theta/\partial p (\xi_{\Theta} + f)$$

Where P_{Θ} is potential vorticity, g is the acceleration due to gravity, Θ is the potential temperature, p is the atmospheric pressure, ξ_{Θ} is the component of the curl of wind vector normal to an isentropic surface and f is the Coriolis parameter. Due to highly stable stratification, i.e. strong positive vertical gradient in the potential temperature, caused by ozone layer PV is very high in the stratosphere as compared with troposphere [Beekmann *et al.*, 1994]. Cristofanelli *et al.* [2006] suggested that air masses characterized by PV value of greater than 1.6 pvu, where 1 pvu = $10^{-6} \text{ m}^2 \text{ K kg}^{-1} \text{ s}^{-1}$, are associated with stratospheric air. In the atmosphere above 350 hPa, PV values increase rapidly with the altitude and reaches typically above 1.0 pvu near the tropopause [Danielsen, 1968]. Along with the high levels of ozone and PV values, stratospheric air masses are generally characterized by lower water vapor and lower concentrations of one of the anthropogenic tracers such as CO. The identification of STE events have mostly relied upon the observations of cleaner and drier air masses [e.g. Stohl *et al.*, 2000; Trickl *et al.*, 2010].

5.1.1. Seasonal Variations in PV over Nainital

The meteorological fields from a regional chemistry transport model (WRF-Chem) have been used to estimate the PV values at different pressure levels over the Nainital for all the days of ozonesonde flights during January-December 2011 (Figure 5.1). The seasonal average values of PV at 200, 300 and 400 hPa are also given in the Table 5.1.

Table 5.1: The seasonal average values of PV at different pressure levels over Nainital using the data of flight days obtained from WRF-Chem simulated meteorology.

	DJF	MAM	JJA	SON	Annual
400 hPa	0.4±0.4	0.5±0.3	0.5±0.3	0.4±0.2	0.5±0.3
300 hPa	0.9±0.9	1.1±0.8	0.5±0.4	0.5±0.3	0.8±0.7
200 hPa	2.3±1.6	1.8±0.9	0.5±0.6	0.9±1.0	1.3±1.2

The seasonal variations in PV at 400 hPa are less pronounced and the average PV values range from 0.4 to 0.5 in all the seasons (Table 5.1). In-contrast, PV variations at 300 and 200 hPa pressure levels show the highest values during spring and winter, respectively. Here, it can be noted that near the tropopause, the highest PV values are observed during winter (2.3±1.6 pvu) indicating the more intrusion directly from the stratosphere. The minimum PV values at 200 hPa are noticed during the summer-monsoon (0.5±0.6). In general, the PV values show large variability during winter and spring and somewhat in autumn, particularly above the 300 hPa. This suggests that the influences of stratospheric intrusions are more likely during winter and spring with least probably during the summer-monsoon.

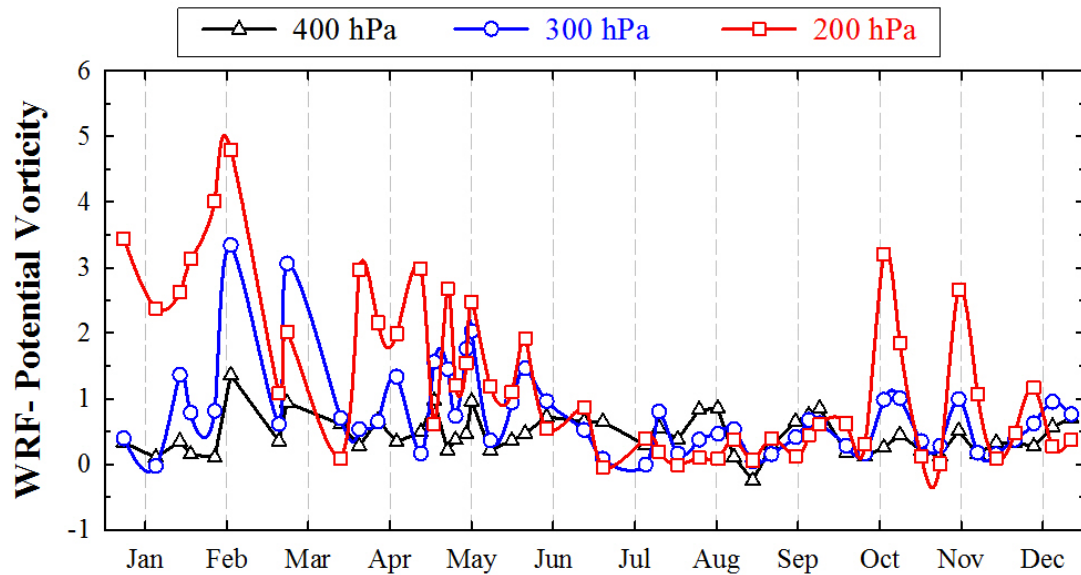


Figure 5.1: Seasonal variations in potential vorticity at three pressure levels over Nainital, on the flight days, obtained using the WRF-Chem simulated meteorology.

The winter time higher PV values and variabilities over Nainital are in agreement with the more intense observations of tropopause folding events over this region (Tibetan Plateau) [Chen *et al.*, 2011]. Moreover, minimum influences of STE during summer-monsoon and higher influences in other seasons are also consistent with the previous studies over the Nepal Climate Observatory (5079 m amsl) in the Himalayas [Cristofanelli *et al.*, 2010]. The maximum values of PV at all the three pressure levels are observed to be on 17th February and indicate strong STE influence on this day which is analyzed further in the next section.

5.1.2. STE Event on 17th February 2011

An event of significantly elevated ozone levels in the middle to upper troposphere is observed on 17th February as compared with the average ozone vertical distribution during the winter. Figure 5.2 shows the ozone distribution on the event day along with all the profiles of the winter season and the seasonal average ozone profile. Clearly, during the event day, ozone levels in the middle troposphere (e.g. 140-150 ppbv at ~10 km) and upper troposphere (e.g. 350-360 ppbv at ~16 km) are very high as compared with the wintertime average ozone profile (70-75 ppbv at 10 km and ~200 ppbv at 16 km) over Nainital.

Thus, the ozone levels during the event are about 1.7 to 2 times higher in the middle-upper troposphere as compared with the average distribution. In contrast, ozone levels in the lower troposphere do not show any significant enhancement during the event days and are observed to be mostly within the variability of the average wintertime ozone distribution.

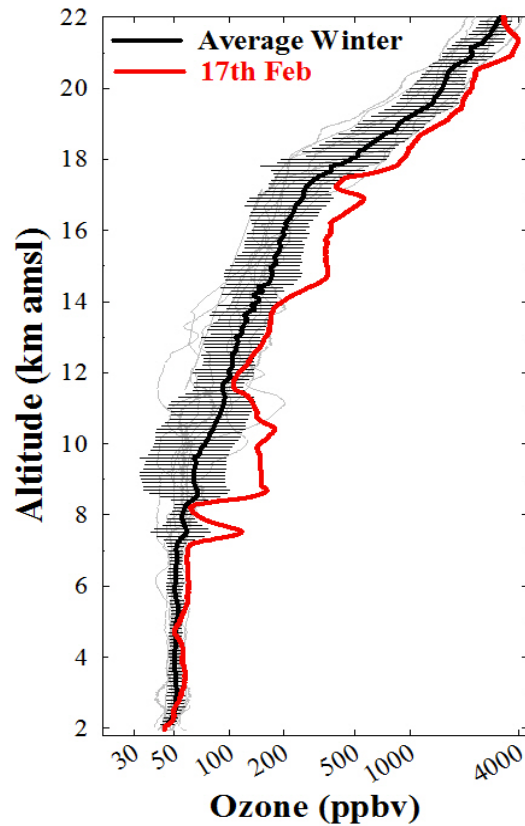


Figure 5.2: Ozone vertical distribution during the high ozone event on 17th February 2011 along with all the ozone profiles and seasonally averaged profile in winter.

5.1.2.1. Change in the Potential Vorticity

Considering the absence of any significant ozone enhancement in the lower troposphere, it is very unlikely that the ozone rich air could have been uplifted from the boundary layer to the middle-upper troposphere. Therefore, it is possible that these enhancements in ozone could be mainly associated with the intrusion of the air from the higher altitude. This argument is supported by the fact that ozone enhancements are associated with the significant increase in the PV values, which

are observed to be highest on this day among all the observations (Figure 5.1). To see the horizontal extent of this intrusion, a contour map of WRF-Chem potential vorticity at 300 hPa during the event on 17th February is compared with the observations during the previous flight on 11th February (Figure 5.3).

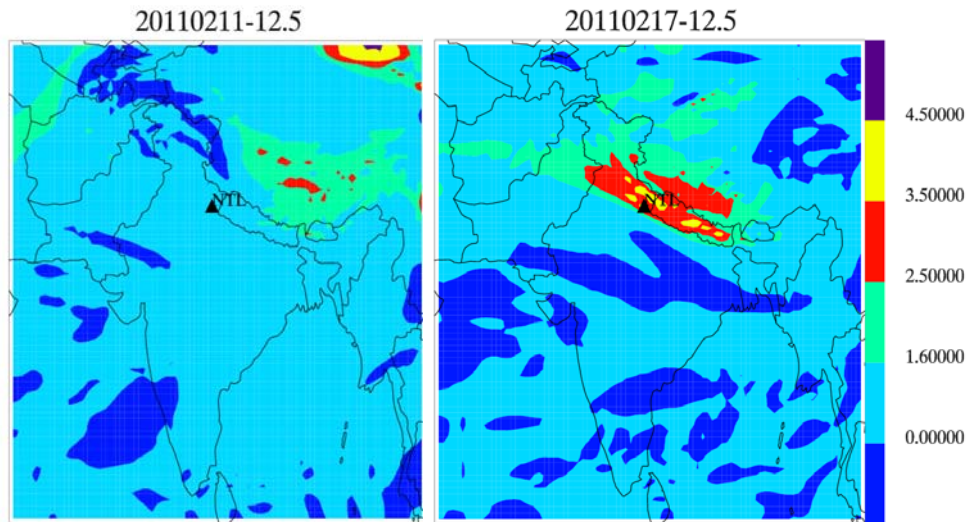


Figure 5.3: Contour maps of potential vorticity at 300 hPa pressure level over the South Asian region on 11th February and 17th February 2011 obtained from WRF-Chem meteorology simulation. The location of the balloon launching site Nainital (NTL) is shown as a triangle.

PV value is less than 1.6 pvu around Nainital on 11th February are, while, it shows very high PV values (2.5 pvu and more) on the 17th February. Such a large enhancement in the PV values is noticed to be extended over a larger region around the site covering most of the Indo-Gangetic Plain region, the Himalayan Mountains and over the some parts of Nepal.

5.1.2.2. Change in the Relative Humidity

The temporal changes in the relative humidity are another key tracer to identify the stratospheric intrusion events. It is shown that the air masses originated from the stratosphere are much drier than those originated from the troposphere and thus their mixing in the troposphere should lead to significant reduction in the relative humidity values [e.g. *Bithell et al.*, 1999]. To diagnose this possibility, the relative humidity (RH) profiles obtained from the radiosonde observations are analyzed. Figure 5.4 shows the RH profiles on 17th February, two nearest observations on 2nd and 11th February along with the seasonally averaged RH profile with 1-sigma variations for winter.

The relative humidity on 17th February decreases sharply above ~7 km amsl and remains very low in the higher altitudes. RH values in the 8 to 12 km altitude range were 50 to 57% on 11th February which show drastic decrease on 17th February and are observed to be ~10% or less. Additionally the RH values in this altitude range are seen to be lower as compared with the seasonal average values (10-23 %).

In addition, the satellite data from AIRS is used to investigate the changes in the distribution of relative humidity during the event and before the event periods over the northern Indian subcontinent. The Figure 5.5 shows the RH distribution during 10 to 12 February and on 17 February 2011 at 400, 300 and 200 hPa.

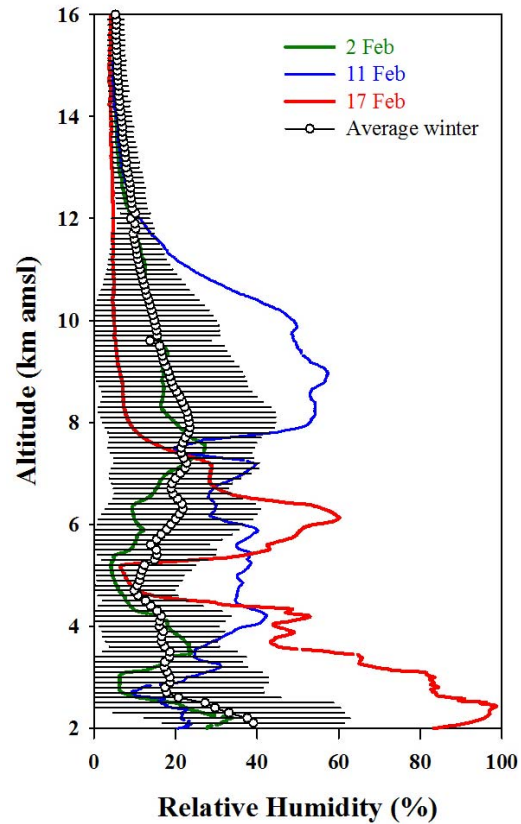


Figure 5.4: Relative humidity profiles during the event day (17th February) and two closest observations on 11th and 2nd February. Seasonally Averaged RH profile during winter (DJF) is also shown for the comparison.

The distribution of relative humidity shows clear reductions over the northern Indian region at all the pressure levels. At 400 hPa, the RH values are 50% to 70% during 10-12 February which is reduced to about 20% to 30% on 17 February. At 300 and 200 hPa pressure levels, clear patches of significantly reduced RH values i.e. 0-10% and 0-5% respectively are visible surrounding the Nainital site. This is consistent with the radiosonde observations and confirms the presence of drier air over the north India during the high ozone period.

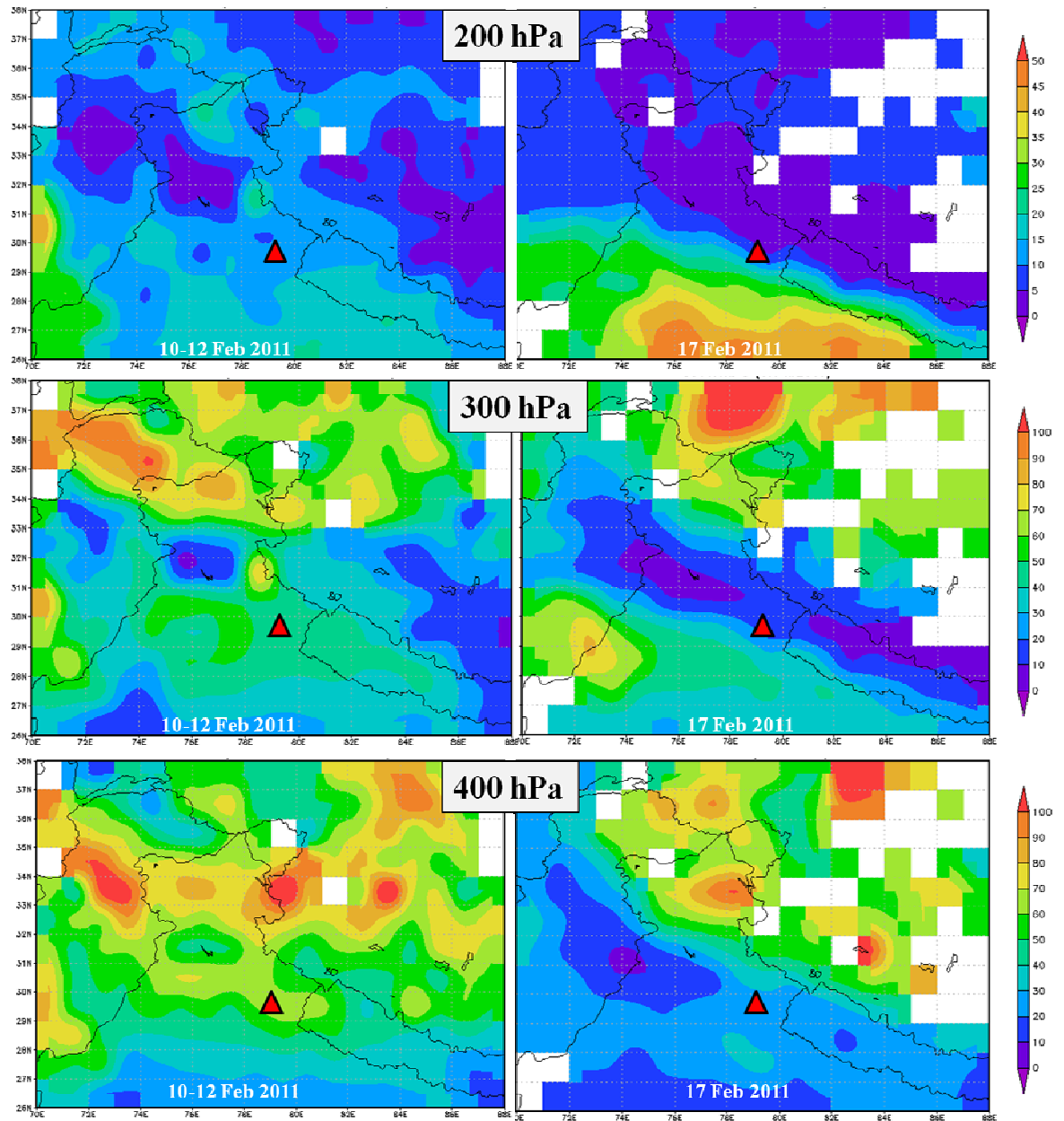


Figure 5.5: The distribution in relative humidity from AIRS satellite during 10-12 February, 2011 and on 17 February, 2011 at 400, 300 and 200 hPa over the northern Indian subcontinent. The location of the observation site Nainital is shown by a red filled triangle.

5.1.2.3. Back Air Trajectory

To investigate the role of advection, 5-days back air trajectories have been simulated over Nainital using the HYSPLIT model at altitudes of 6, 9, 15, 16, 18 and 20 km above ground level (AGL) (Figure 5.6). Figure 5.6a and 5.6b are for 11 February 2011 while Figure 5.6c and 5.6d are showing the trajectories for 17 February 2011. The HYSPLIT model has been driven by GDAS meteorological data and has been used to estimate the along-trajectory values of relative humidity also.

It is seen that back air trajectories at 9 km AGL and higher altitudes do not show any clear change in the transport pattern between 11 February and 17 February. While, the back air trajectory at 6 km AGL (~8 km amsl) are from different sources on these days and air masses are originated from higher latitudes during the event day. Earlier, near 8 km amsl, an ozone enhancement was noticed on 17 February and it is suggested that it was due to transport of ozone rich air from the higher latitude regions.

In contrast to the 6 km AGL, the advection patterns are found to be more-or-less similar between 11 and 17 February. Thus, the differences in the upper-troposphere are not likely associated with the advection and as suggested could be the influences of downward transport from higher altitude region. Further, the observed reductions in relative humidity from radiosonde and satellite data are again seen in the HYSPLIT model output. At 6 km AGL, the relative humidity values at the site are

observed to be nearly similar on 11 and 17 February (about 30%). While, in contrast, at 9 km RH values reduced from 70-90% on 11 February to 20% on 17 February.

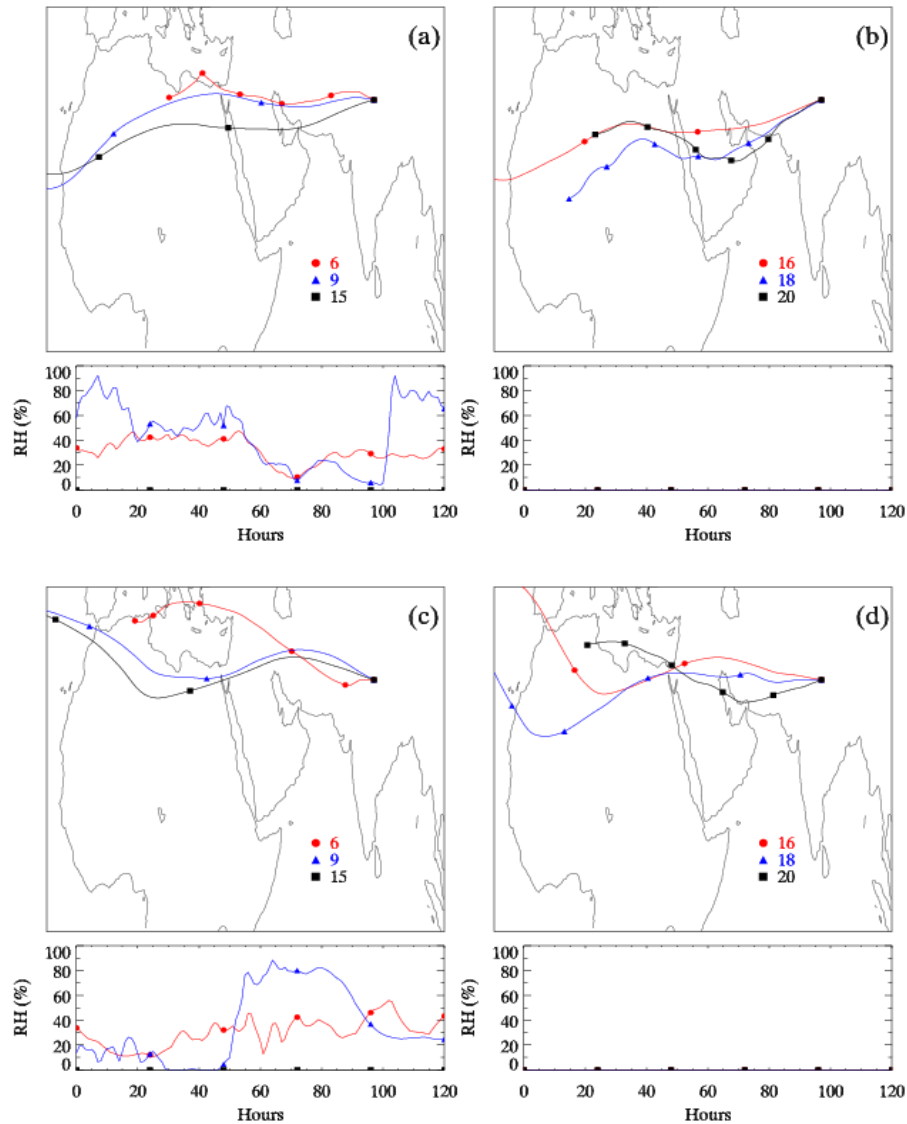


Figure 5.6: 5-day back air trajectories have been simulated over Nainital using the HYSPLIT model at different altitudes 6, 9, 15, 16, 18 and 20 km above ground level (AGL). Figures a and b are for 11 February 2011 while c and d are showing the trajectories for 17 February 2011.

Absence of a significant changes in the transport patterns indicate minimal role of the advection processes in the observed ozone enhancements in the upper troposphere, except near 6 km AGL. In contrast, the observed reductions in the relative humidity and the enhancement in the potential vorticity suggest the major role of stratospheric intrusion in the ozone enhancement. The observed reductions in RH indicate the presence of drier air and it is concluded that air masses could have been transported from the higher altitudes, which are poor in water vapor but rich in ozone.

5.1.2.4. Model Simulations

In addition to analyzing the temporal variations in meteorological tracers (potential vorticity and relative humidity) of STE, a global model (MOZART) and a regional chemistry-transport model (WRF-Chem) simulated chemical fields are studied. Figure 5.7 shows the vertical distribution of ozone from ozonesonde observations, WRF-Chem and MOZART for 11 February and 17 February.

Model simulated ozone distributions from both the models (WRF-Chem and MOZART) discern elevated ozone layers on 17 February as compared with 11 February. However, there are two main differences in the observation and model simulated ozone distributions. First is the model estimated ozone enhancement is less as compared with the observations and secondly the maximum enhancement is at a lower altitude i.e. higher pressure level. The observations show the maximum enhancement in ozone near 300 hPa pressure level from about 52.9 ppbv on 11

February to 148.7 ppbv on 17 February with the enhancement of about 181.1%. The ozone enhancement is slightly lower in the higher pressure levels e.g. ozone enhancement at 400 hPa is about 114.7%. The WRF-Chem model shows the maximum enhancement of 58.1% near 430 hPa while at 300 hPa the model simulated ozone show very small change (7%). The MOZART simulated ozone enhancement at 430 hPa is about 82.2%, however its peak enhancement is 91.4% at 400 hPa. In contrast to the observations, ozone enhancement is not seen at 300 hPa.

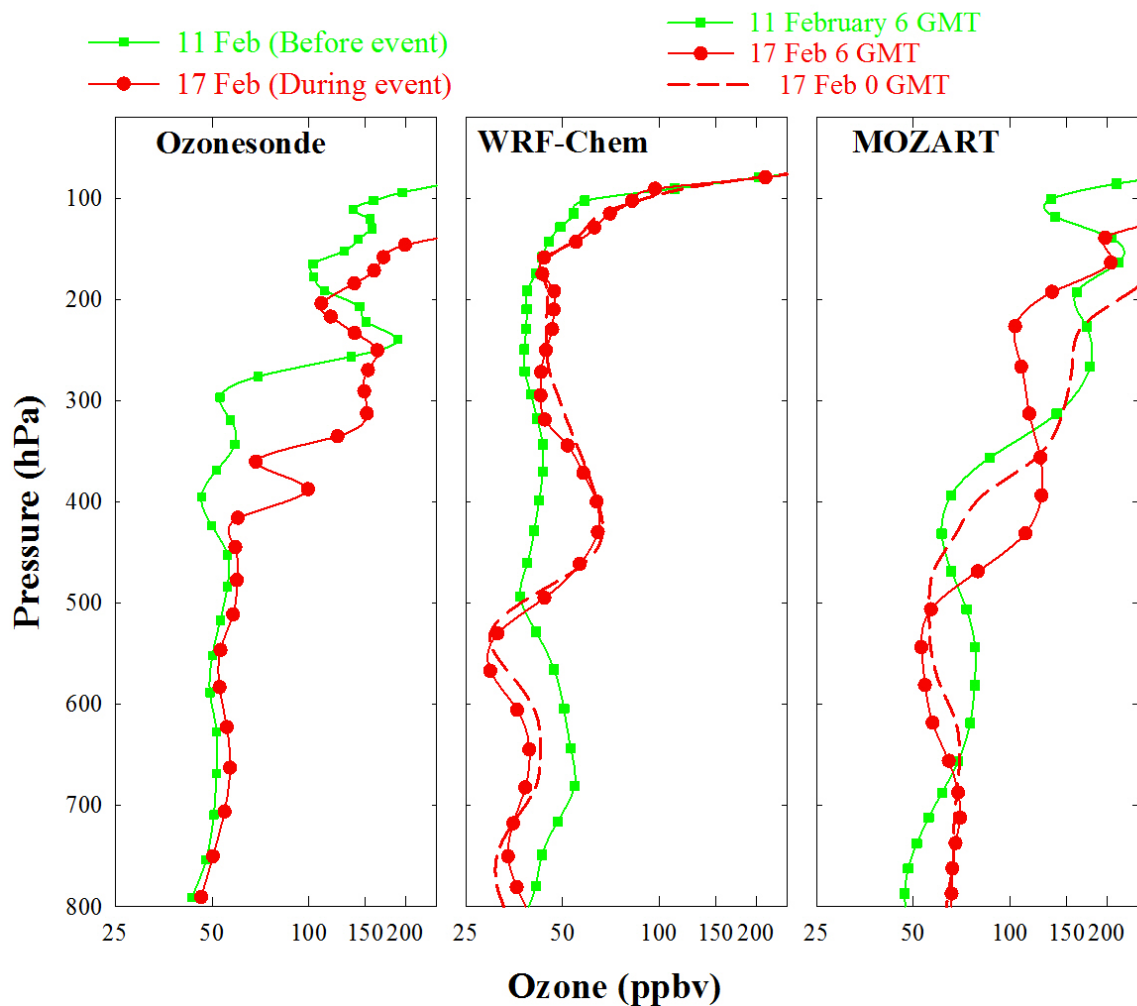


Figure 5.7: A comparison of ozone profiles on 11 and 17 February 2011 obtained from ozonesonde observations, WRF-Chem model and MOZART model simulations.

Models do show significant enhancements in the ozone levels but at lower altitudes (400 to 430 hPa) region as compared with the observations (300 hPa). Moreover, the maximum ozone enhancement in the model simulations is lesser as compared with the enhancement in the observations. A comparison between the two models indicates that MOZART is capturing the peak slightly better in terms of the peak altitude and the magnitude of the enhancements. Therefore, MOZART simulated chemical fields are further investigated. Since, the MOZART shows the maximum ozone enhancements at 400 hPa therefore the distributions of the chemical fields at 400 hPa are plotted as contour maps over the South Asian region (Figure 5.8).

Ozone mixing ratios are observed to be varying from 60 ppbv to maximum about 100 ppbv around the site on 11 February. During 17 February a patch of significantly high ozone (100-120 ppbv and higher) appears over this region. Clearly this intrusion of high ozone is observed to be over a large spatial area of about $10^{\circ} \times 10^{\circ}$ around the site. This event was indicated to be associated with the stratospheric influence by the temporal variations in the meteorological tracers in the previous subsections. Here, we further analyze a chemical tracer CO to investigate this event (Figure 5.8). It is suggested that the air masses of stratospheric origin should be generally depleted in the species having mainly an anthropogenic source (such as CO).

CO levels were varying in the range of 80 to 100 ppbv at 400 hPa pressure levels over most of the Indian region during 11 February while a patch of CO depleted air (60 to 80 ppbv) is visible from south west to the north east of the Nainital site. The

spatial distribution of CO changes drastically and on 17 February the CO depleted air mass is observed over the site and the surrounding region. Notably, this reduction in the CO surrounding the Nainital is located just over the region having enhanced ozone. Further, the spatial size of this CO reduction is almost similar to that of ozone enhancement.

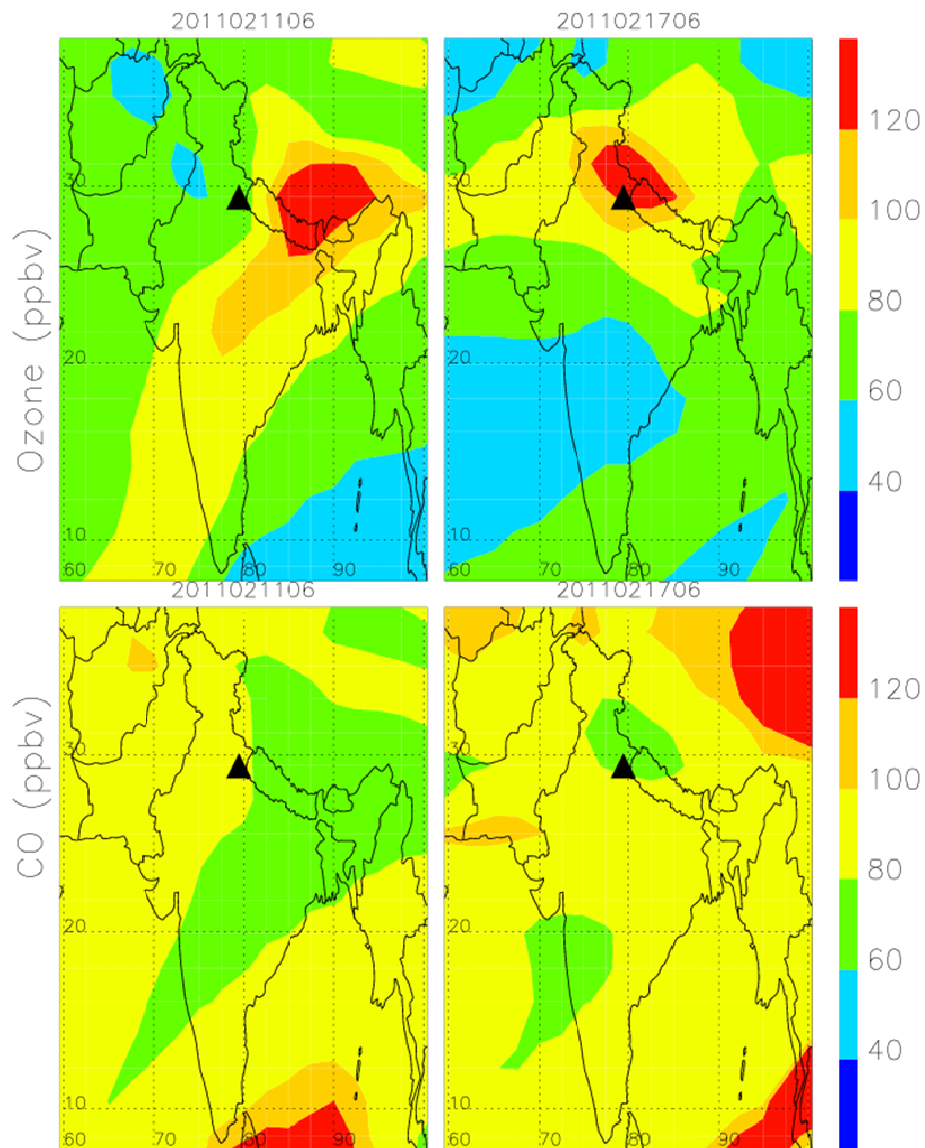


Figure 5.8: MOZART simulated spatial distributions in the ozone and CO at 400 hPa on 11th and 17th February over the South Asian region.

Figure 5.9 shows the contour maps of MOZART simulated ozone and CO as the functions of pressure and latitude at the fixed longitude of the Nainital site during 11 and 17 February 2011. This figure clearly shows that the ozone rich air masses are descending up to about 400 hPa, however, this influence is more on the lower latitudes during 11 February. While, on 17 February the ozone rich air is observed to be descending just above the 30°N at the latitude of the measurement site.

The ozone rich air mass (120 ppbv and more) is seen to be influencing the 400 hPa to 200 hPa pressure range over this region. Moreover, the distribution of CO shows the intrusion of relatively CO-poor (60-80 ppbv) air masses coinciding with the patch of high ozone as compared with the 80-100 ppbv levels on 11 February. The air masses from the stratosphere, which are ozone rich but poor in CO, have been transported into the middle-upper tropospheric altitudes and resulted into the observed ozone enhancement on 17 February.

Meteorological as well as the chemical fields confirm the intrusion of the stratospheric air masses into the troposphere which resulted in large enhancement in the middle-upper tropospheric ozone levels. It is suggested that such events could perturb the contribution of STE processes into the budget of tropospheric ozone particularly during the winter months over this region. More detailed measurements of ozone distribution and meteorological parameters and model simulations are highly desirable to improve our understanding of STE process in the tropospheric ozone budget quantitatively.

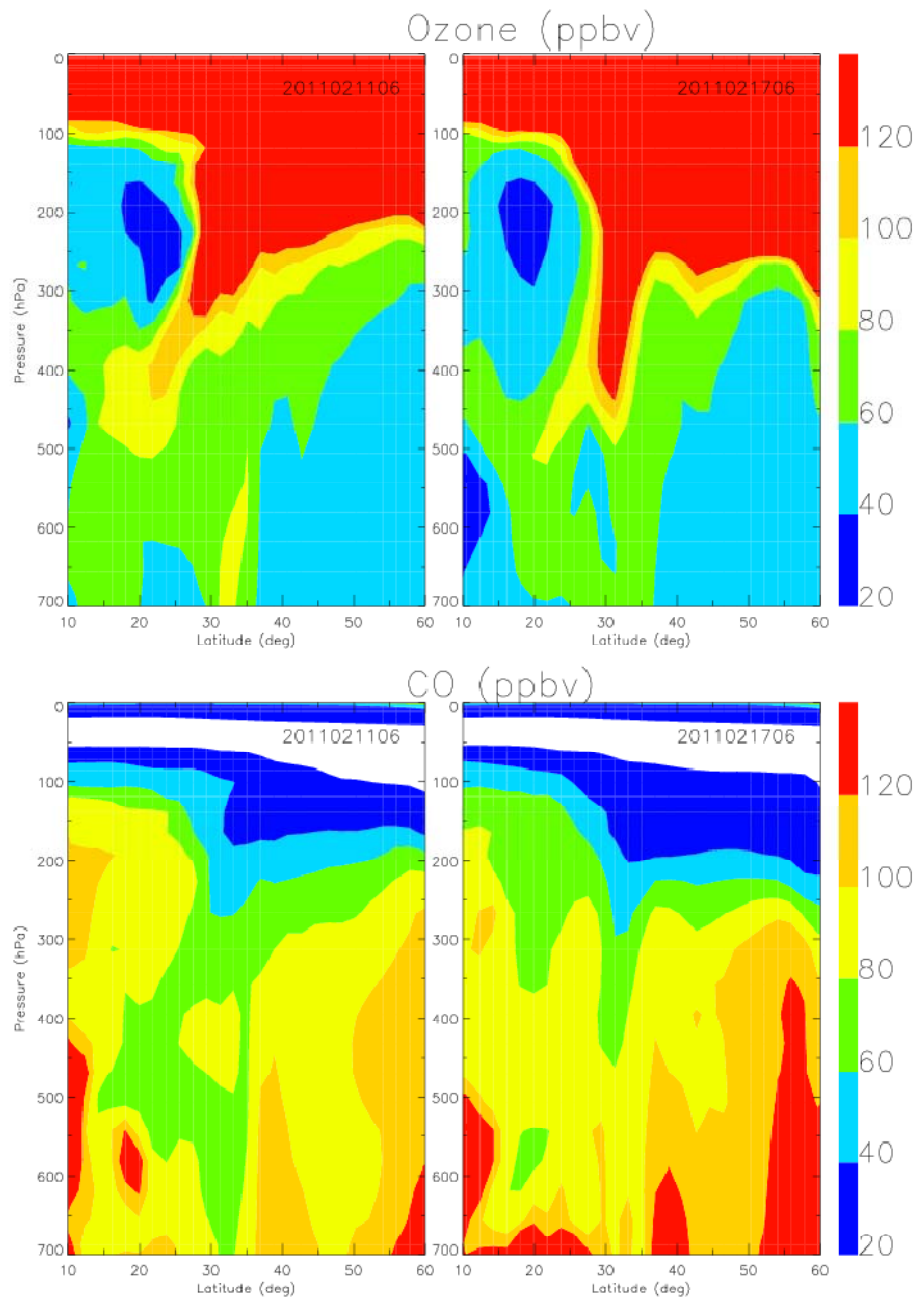


Figure 5.9: The contour maps of MOZART simulated ozone and CO as the functions of pressure and latitude at the fixed longitude of the Nainital on 11th and 17th February, 2011.

5.2. Secondary Ozone Peaks

The elevated ozone layers are generally observed in the troposphere and sometimes in the lower stratosphere and are defined as secondary ozone peaks (SOPs). These SOPs have been observed in different parts of the world and were attributed to the complex dynamical and chemical processes which are still poorly understood [e.g. Lemoine, 2004; Hwang *et al.*, 2007; Trickl *et al.*, 2011]. Hwang *et al.* [2007] attributed the occurrences of SOPs to be associated with the stratosphere-troposphere exchange. Trickl *et al.* [2011] found elevated ozone layers in the middle and upper troposphere over the central Europe and attributed them to the transport from the stratosphere along the subtropical jet streams.

The ozonesonde observations over Nainital also show the presence of SOPs over this region. SOPs are observed over this region in all the seasons and a comparison of the profiles on the days of SOPs with the seasonally average ozone distribution are shown in the Figure 5.10. Ozone profiles are observed to have layered structures of elevated ozone levels (~140 to 250 ppbv) in the middle troposphere (~8 to 12 km). The frequency of such events is higher (3 events) during spring as compared with the other seasons (1 event in each season). In contrast to the middle troposphere, ozone levels in the lower troposphere are within the seasonal variabilities (1-sigma), except on 7th June. Moreover, these SOPs events do not show feature of higher ozone levels at the higher altitudes than the altitude of SOPs, like the event of 17th February, 2011 (section 5.1.2) and hence lacks the signature of the direct downward transport from the stratosphere.

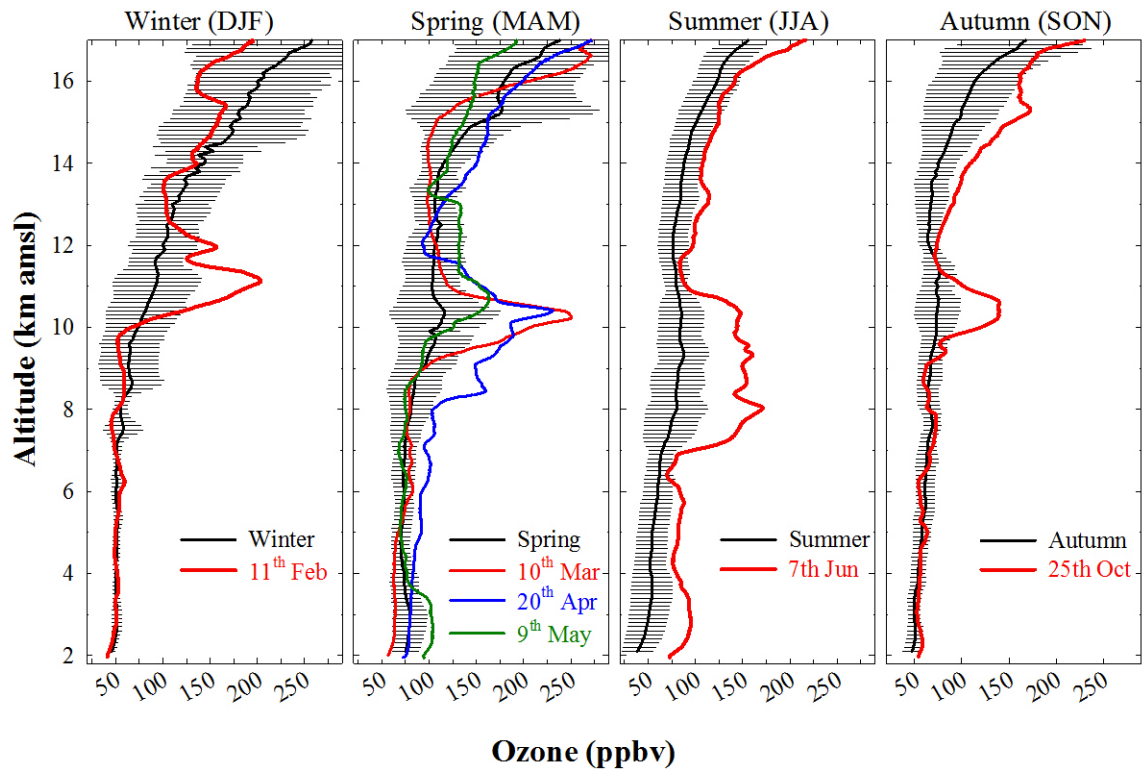


Figure 5.10: The presence of secondary ozone peak in the middle troposphere during different flights. Seasonally average ozone profiles are also shown for the comparison.

Thus, the other possibility for such SOPs events is the advection of ozone rich air in form of long range transport. It can be noted that during winter, spring and somewhat in autumn, the wind speeds are very strong in the middle troposphere and occasionally influenced by the subtropical jets. These strong winds could bring ozone rich air masses from distant sources within a short time. Sometimes the observed enhancements are very high such as on 10th March, when the ozone levels are about 250 ppbv and could have influence of stratosphere-troposphere exchange also.

Here, we report the occurrences of secondary ozone peaks for the first time over this northern Indian region. However, the one year data is not sufficient (only 6 occurrences) for calculating the frequencies and detailed comparison with other parts of the world. Nevertheless, these observations will be filling a gap over the south Asian region and will be invaluable for the adequate understanding of the underlying meteorological, chemical and dynamical processes and making better model evolutions.

5.3. Influences of Biomass Burning

Biomass burning activities play key roles in the tropospheric ozone chemistry through the emissions of various ozone precursors. The biomass burning activities over the northern Indian region could thus influence the distribution of ozone. Biomass burning activities are shown to enhance the levels of ozone and precursors over this region significantly using the ground based and space borne measurements [Kumar *et al.*, 2011]. In this section, an attempt is made to understand the role of the biomass burning activities in the tropospheric ozone vertical distribution over the northern Indian region combining the ozonesonde observations with satellite retrieved fire counts data.

5.3.1. Seasonal Variation in Biomass Burning

The fire counts data from MODIS satellite has been used to investigate the seasonal variations in the biomass burning activity over the northern Indian region (60 to

95°E and 20 to 38°N). Figure 5.11 shows the seasonal variations in the daily total and monthly total fire counts over the northern Indian region during 2011.

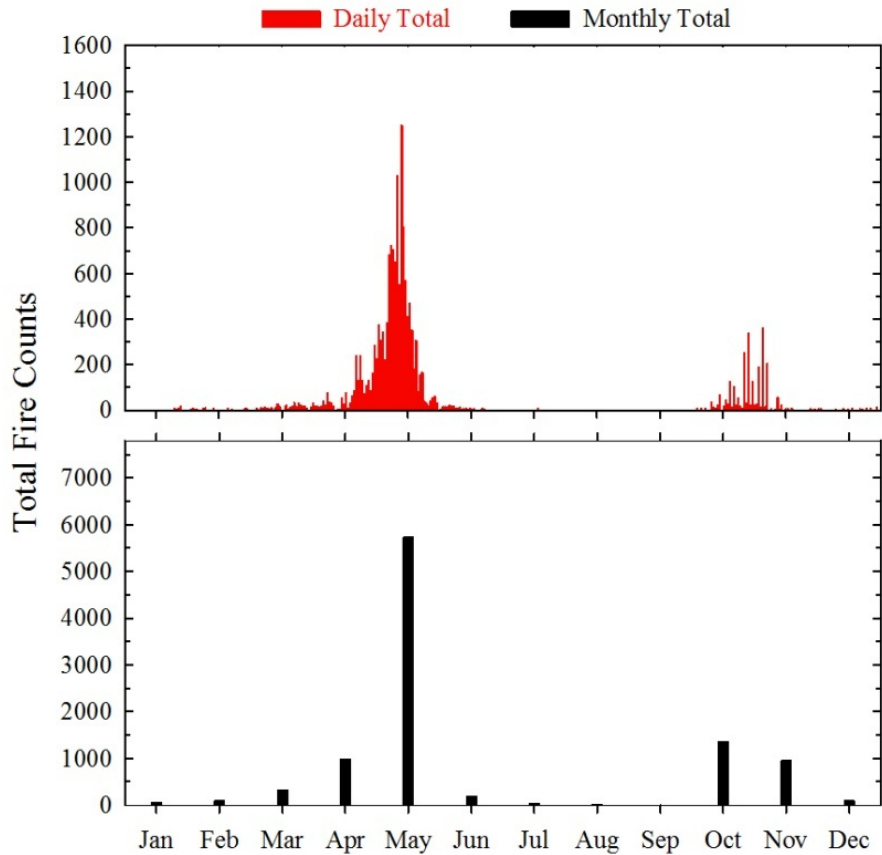


Figure 5.11: Seasonal variations in the daily total and monthly total fire counts obtained from MODIS satellite over the northern Indian region during 2011.

Biomass burning activities are observed to show a major peak during spring and a secondary enhancement during the autumn season. Monthly total fire counts are highest during May (5723 counts) over this region. Fire activity during autumn is also moderately high (1337 counts during October). The maximum daily total fire counts were observed to be as high as 1248 counts on 14 May 2011. The observed

seasonal variations in daily and monthly total fire counts over the northern Indian region during 2011 are found to be similar as reported for previous years [*Kumar et al.*, 2010]. Most of the biomass burning activities over the northern Indian region are associated with the crop residual burning in the agricultural areas supplemented with some contributions from forest fires [*Kumar et al.*, 2010]. In order to investigate the influence of biomass burning activities on the ozone distribution, more frequent balloon flights were conducted during intense fire period (May) and just prior to it (late April).

5.3.2. Classification of High and Low Fire Activity Periods

The time series of daily total fire counts during spring over the northern Indian region obtained from the MODIS sensors onboard Aqua and Terra are shown in the Figure 5.12. This time series is used to classify the Low Fire Activity Period (LFAP) as 30th March to 29th April and High Fire Activity Period (HFAP) as 4th May to 25th May. Ozone sonde flights during these periods are classified accordingly and in this way, a total of 5 profiles are averaged to represent the low fire activity period while a total of 6 profiles are averaged to represent the high fire activity period.

A comparison is made between the average ozone vertical distributions during HFAP and LFAP (Figure 5.13). Ozone levels show a clear enhancement during the HFAP as compared with the ozone levels during the LFAP, mainly from the near-surface to about 4 km amsl. Above an altitude of about 4.5 km amsl ozone levels are observed to be nearly similar during HFAP and LFAP. This suggests that the

influences of biomass burning activities are observed up to about 4.5 km. It is shown that the mixing depth during May generally varies up to 3 to 4 km amsl and the associated mixing might be inducing the distribution of the near surface fire emissions in the lower troposphere.

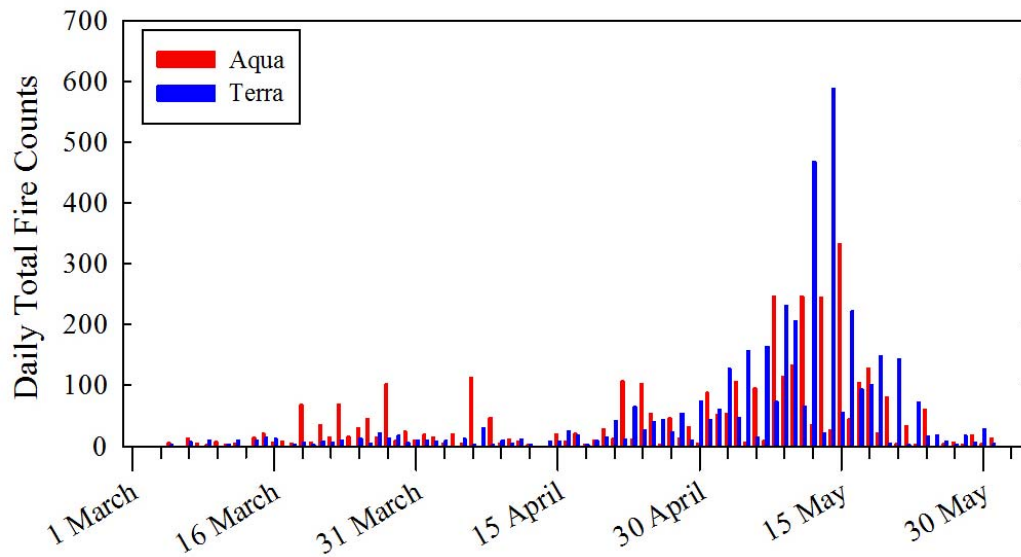


Figure 5.12: The time series of daily total fire counts during spring over the northern Indian region obtained from the MODIS sensors onboard Aqua and Terra.

The maximum enhancement in the ozone levels is observed at about 2.9 km amsl with HFAP ozone levels of 96.0 ± 8.1 ppbv as compared with the LFAP ozone levels of 70 ± 13.7 ppbv. The mean enhancement in 2 to 4 km altitude range is estimated to be 19.9 ± 4.6 ppbv, which is found to be statistically significant (paired t-test). The 95% confidence interval for the observed ozone enhancement in this altitude range is estimated to be from 17.7 to 22.1 ppbv. This analysis suggests that the northern Indian biomass burning during spring leads to the significantly

enhancement in the lower tropospheric ozone and influences the vertical distribution of ozone.

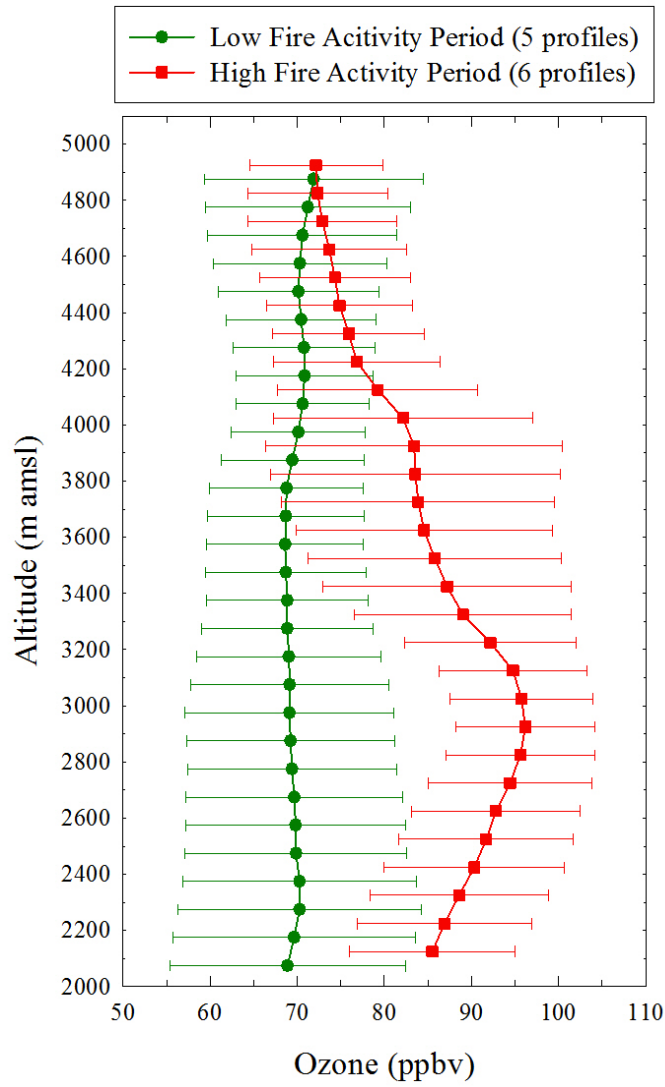


Figure 5.13: Average vertical distribution of ozone over Nainital obtained from ozonesonde observations during low fire activity period (LFAP) and high fire activity period (HFAP).

5.4. Summary and Conclusions

The ozonesonde observations are analyzed using the meteorological parameters, model simulations and satellite data to investigate the role of dynamical processes and biomass burning in influencing the ozone distribution. The variations in potential vorticity (PV) indicate that the stratospheric intrusions influence ozone distribution during winter, spring and autumn, while, these are not observed during the summer-monsoon. PV values are highest on 17th February along with the elevated ozone levels in middle-upper troposphere, however any such ozone enhancement is not seen in the lower troposphere. On this event, the relative humidity, from the radiosonde, satellite as well as GDAS datasets shows large reduction, which is again indicating that ozone rich air could have been transported from the higher altitudes.

Model simulated ozone enhancement is seen at a lower altitude as compared with the observations and moreover the models underestimated the ozone enhancement. MOZART model results are in slightly better agreement with the observations in terms of the altitude and the magnitude of the enhancements. Analysis of MOZART shows a patch of significantly high ozone (100-120 ppbv and higher) and reduced CO at 400 hPa surrounding the measurement site. This analysis confirms the stratospheric intrusion into the troposphere leading to large enhancement in the middle-upper tropospheric ozone levels. Simulations from these two models (WRF-Chem and MOZART) discern some limitations in reproducing this event and further improvements are needed in the models. Ozone profiles over Nainital are observed to show secondary ozone peaks (SOPs) in the middle troposphere (~8 to 12 km)

more frequently during spring. SOPs are attributed to the advection of ozone rich air masses via strong winds in middle-troposphere; however, occasionally stratosphere-troposphere exchange could also have some contribution to these events, which needs further analysis.

More balloon soundings were conducted during spring 2011, to investigate the role of northern Indian biomass burning in influencing ozone distribution over this region. Ozone profiles are classified into Low Fire Activity Period (LFAP) and High Fire Activity Period (HFAP) using MODIS fire count data. The ozone levels during the HFAP show significant enhancement as compared with the ozone levels in LFAP. The 95% confidence interval for the observed ozone enhancement in the 2-4 km altitude range is estimated to be 17.7-22.1 ppbv. This analysis shows that the northern Indian biomass burning contributes significantly in the spring time higher ozone over this region.

Chapter 6

Variations in CO₂, CH₄ and CO over the central Himalayas

Most of the observed global warming has been attributed to the enhancements in the Long-Lived Greenhouse Gases (LLGHG) since the pre-industrial era. The important Long-lived greenhouse gases are Carbon dioxide (CO₂), Methane (CH₄), Nitrous Oxide (N₂O) and Sulfur Hexafluoride (SF₆). CO₂ and CH₄ are ranked first and second respectively in terms of the radiative forcings imposed by LLGHGs on the climate [Forster *et al.*, 2007]. Globally CO₂ levels have been observed to be increasing [e.g. Keeling *et al.*, 1976; Thoning *et al.*, 1989; Keeling *et al.*, 1995] from 316 ppm in 1960 to 393 ppm in 2012, at an average rate of about 1.22 ppm per year at Mauna Loa, Hawaii (<http://scrippsco2.ucsd.edu/home/index.php>). CH₄ levels have also increased significantly however growth rate has decreased since late 1990s in contrast with that for CO₂ [Dlugokencky *et al.*, 2009]. Due to very long lifetimes of these gases, the observations over remote locations are suggested to be the

representative of large-scale variations. However, the monitoring over a network of sites is needed for the estimation of sources and sinks of these gases. CO is not a direct greenhouse gas, however, as a precursor of an effective greenhouse gas ozone, it also contributes to the climate change indirectly upon conversion to CO₂ through reaction with OH. Moreover, CO has been employed as a tracer of anthropogenic influences in the variabilities of CO₂ and CH₄ using the correlation analysis.

In order to investigate the contributions of the greenhouse gases in climate change, their long-term systematic measurements are required. Considering this, monitoring of various greenhouse gases are being made globally under different networks, such as surface measurements [*Keeling et al.*, 1976; *Dlugokencky et al.*, 2009; *Prinn et al.*, 2000], tall tower network [*Andrews et al.*, 2013], aircraft measurements [*Machida et al.*, 2008], and network of CO₂ flux towers [e.g. *Saigusa et al.*, 2005].

However, the measurement sites of the greenhouse gases for sources and sinks estimation are generally located in the developed countries and do not provide necessary data coverage worldwide for estimating GHGs fluxes using inverse modelling [e.g., *Bousquet et al.* 2000; *Gurney et al.*, 2002; *Enting*, 2002, *Patra et al.* 2006]. In addition to the surface CO₂ measurements, campaign based aircraft observations are increasing and satellite observations are being made as an aid to constrain flux estimations and to better understand the transport of greenhouse gases [e.g. *Patra et al.*, 2011; *Umezawa et al.*, 2012].

Column CO₂ data using space-borne sensors would complement the in-situ measurements by wider spatial and temporal coverage. However, understanding the differences between surface, profiles, and column observations of atmospheric CO₂ and its variability at all temporal (e.g. seasonal and synoptic) and spatial scales is necessary for combined data usage. Another major challenge in space-borne CO₂ observations is the stringent requirement of measurement precision [e.g., *Rayner and O'Brien, 2001; Patra et al., 2003*]. Space-borne observations need to have 1% precision for the similar flux uncertainty reduction by inverse models as the in-situ measurements.

Realizing the limitations in global coverage of surface observations, specific satellite missions (e.g. OCO and GOSAT) are in progress for measurements of GHGs from space-borne platforms. These sensors are based on observations of light emitted from the atmosphere and the earth surface in near infrared and thus measurements are possible only in clear-sky conditions [*Crisp et al., 2004*]. Sampling only in clear-sky conditions would introduce biases as CO₂ uptake is stronger under clear-sky condition in most ecosystems and thus lower column CO₂ values than adjacent days. Apart from plant physiology driven differences, cloudy conditions are generally associated with low-pressure systems accompanied by enhanced upward transport of air across the planetary boundary layer (PBL), while clear-sky conditions are associated with high-pressure systems. The former would produce lower column CO₂ while the latter biased towards higher values under identical ecosystem activity.

Unlike global observations, long-term systematic datasets of greenhouse gases are very limited over the Indian region. Longest and only CO₂ observations from Cape Rama, Goa was reported recently in open literature [Bhattacharya *et al.*, 2009], while the knowledge on the variabilities and trends in other greenhouse gases are nearly non-existing over the Indian region. The Cape Rama site observe GHGs flux signals during the northeast monsoon season, when the winds are from the continental India to the Arabian Sea, and during the southwest monsoon season this site samples air that is representative of the southern hemisphere [Bhattacharya *et al.*, 2009]. Another observation site in northern India is at Hanle (78.96 °E, 32.77 °N, 4517 m amsl), where, detailed analysis with publication is not available. For better understanding of the regional GHG cycling within India, weekly air samples have been collected from a high altitude site Nainital (79.45 °E, 29.37 °N, 1958 m amsl) located in the central Himalayas since September 2006. These samples have been analyzed for some of the greenhouse gases in collaboration with the National Institute for Environmental Studies (NIES), Japan as discussed in the Chapter 2. The long-term measurements of CO₂, CH₄ and CO are investigated here from September 2006 to December 2011.

6.1. Seasonal Variations

6.1.1. Seasonal Variation in CO₂

The seasonal variation in CO₂ levels at Nainital averaged over the period from September 2006 to December 2011 are shown in the Figure 6.1 in the form of a box plot. The average CO₂ levels show a prominent seasonal cycle over Nainital with the maximum levels during spring (395.9±5.9 ppm in May) and minimum levels during

the post-monsoon/autumn (374.4 ± 5.8 ppm in October). The monthly average values of CO₂ during twelve months along with the maximum and minimum values and counts are given in the Table 6.1.

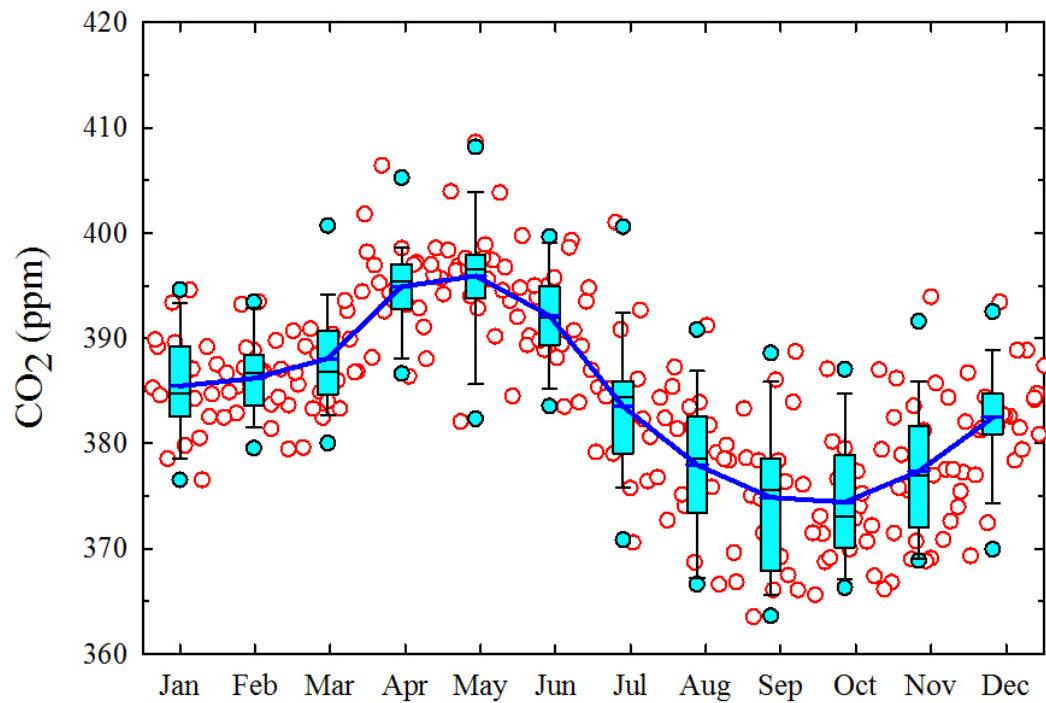


Figure 6.1: The seasonal variation in CO₂ levels at Nainital during September 2006-December 2011 are shown as a box plot. Average monthly values are shown by a thick blue line. All observations are also shown in open red circles to show the week to week variations.

The average CO₂ value during the measurement period is estimated to be 384.3 ± 9.0 ppm with maximum value of 408.6 ppm and minimum value of 363.5 ppm at Nainital. The seasonal amplitude i.e. the difference between maximum and minimum monthly average CO₂ levels is calculated to be 21.5 ppm. The variability

in the CO₂ levels over Nainital, as seen from the standard deviation values, is highest during the autumn (5.8 to 7.2 ppm) and lowest during the winter (3.6 to 5.2 ppm).

Table 6.1: *The monthly average values of CO₂ (ppm) during twelve months as well as in the annual dataset along with the maximum and minimum values and counts.*

Month	Average CO₂ (ppm)	Maximum	Minimum	Counts
Jan	385.5±4.8	394.6	376.5	19
Feb	386.2±3.6	393.5	379.5	20
Mar	388.1±4.9	401.8	379.6	22
Apr	394.9±4.3	406.4	386.4	22
May	395.9±5.9	408.6	382.1	21
Jun	392.2±4.4	399.7	383.5	22
Jul	383.5±6.7	401.0	370.6	20
Aug	378.0±6.7	391.2	366.6	21
Sep	374.9±7.2	388.7	363.5	20
Oct	374.4±5.8	387.1	366.1	24
Nov	377.4± 6.2	393.9	368.8	25
Dec	382.5±5.2	393.4	369.3	23
Annual	384.3±9.0	408.6	363.5	259

The terrestrial ecosystem, during their growth, act as a major sink of atmospheric CO₂ by absorbing it from the air for conducting photosynthesis. When plants die and undergo decomposition they return CO₂ back to the atmosphere and act as a source

of CO₂. This phenomenon creates the observed seasonal cycle in the time series of CO₂. Over the northern Indian region, crop growing season (Kharif) starting from arrival of summer-monsoon (June) leads to a reduction in the CO₂ levels until October when it reaches its minimum. Due the crop harvesting during November-December (Kharif) CO₂ again rises. CO₂ levels peak during April-May coinciding with the major crop-harvesting season (Rabi) over the northern India. Further, maximum biomass burning activities, associated mainly with the burning of crop residues, over the northern India is also suggested to contribute to the observed springtime maxima in CO₂.

6.1.1.1. Comparison with the Mauna Loa and Global Marine Observations

Figure 6.2 shows the comparison of seasonal variation in CO₂ levels over Nainital with the Mauna Loa and average global marine observations (from NOAA) during the study period [Conway *et al.*, 1994]. Seasonal cycle phase at Nainital is found to be similar to that over the Mauna Loa (MLO) as CO₂ levels over MLO are also highest during May (390.5±3.2 ppm) and lowest during October (384.0±3.7 ppm). However, the seasonal amplitude at Nainital is much larger (21.5 ppm) as compared with the Mauna Loa (~6.5 ppm). The average global marine CO₂ levels are observed to be highest during April (388.0±3.0 ppm) and lowest during August (384.0±3.0 ppm), which is somewhat different than at Nainital and MLO. Further, the seasonal amplitude of marine CO₂ levels is even smaller (4.0 ppm). This suggest the cycling of CO₂ is strong over the northern India in annual scale.

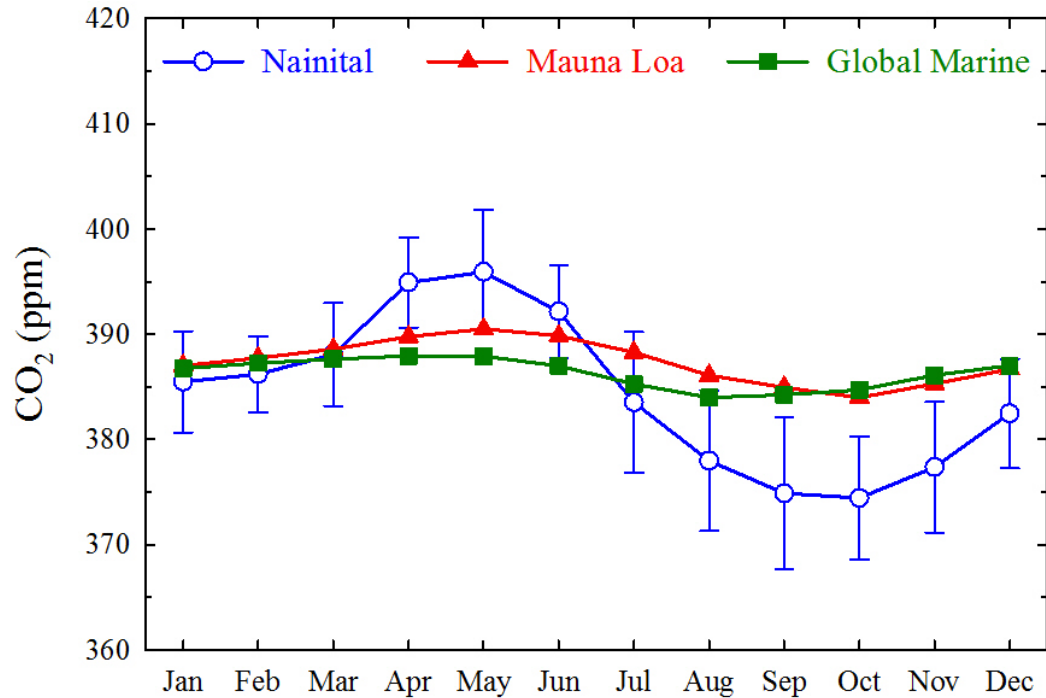


Figure 6.2: The comparison of seasonal variation in CO₂ levels over Nainital with the Mauna Loa and global marine observations (obtained from NOAA; <http://www.esrl.noaa.gov/gmd/ccgg/trends/>) during the study period.

6.1.2. Seasonal Variation in CH₄

The seasonal variation in CH₄ levels at Nainital during September 2006-December 2011 are shown in the Figure 6.3 in the form of a box plot. The average CH₄ levels show a clear seasonal cycle over Nainital with peak during autumn (2.0±0.08 ppm in September). The average CH₄ levels are lowest during June, however, during most of the spring and winter months, average CH₄ does not show much variability (1.91-1.92 ppm). The monthly average values of CH₄ during twelve months along with the maximum and minimum values and counts are given in the Table 6.2. The average CH₄ values over Nainital during the measurement period obtained from all the data

points has been estimated to be 1.93 ± 0.07 ppm with maximum value of 2.15 ppm and minimum value of 1.82 ppm. These average CH_4 levels are somewhat higher than the global averaged CH_4 value of 1.813 ± 0.002 ppm in 2011 [WMO, 2012]. The seasonal amplitude in the monthly average CH_4 levels is estimated to be 0.11 ppm over Nainital. The variability in the CH_4 levels over Nainital, as seen from the standard deviation values, is highest during the autumn (0.06 to 0.08 ppm) and lowest during June (0.04 ppm).

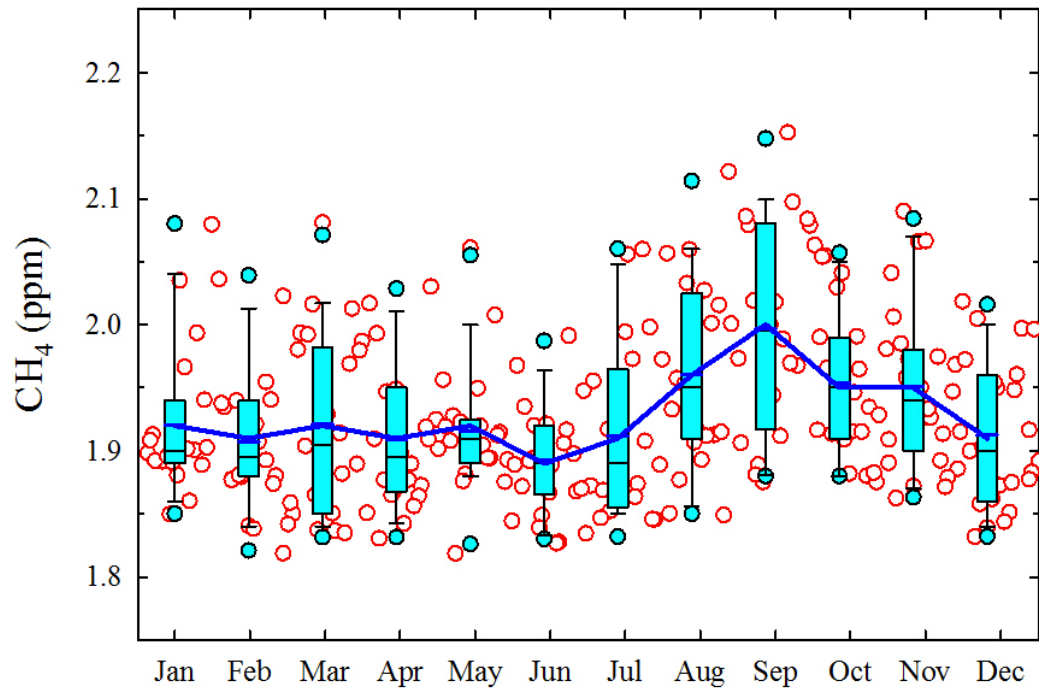


Figure 6.3: The seasonal variation in CH_4 levels at Nainital during September 2006-December 2011 are shown as a box plot. Average monthly values are shown by a thick blue line. All observations are also shown in open red circles to show the week to week variations.

Table 6.2: The monthly average values of CH₄ (ppm) during twelve months as well as in the annual dataset along with the maximum and minimum values and counts.

Month	Average CH₄ (ppm)	Maximum	Minimum	Counts
Jan	1.92±0.06	2.08	1.85	19
Feb	1.91±0.06	2.04	1.82	20
Mar	1.92±0.07	2.08	1.83	22
Apr	1.91±0.06	2.03	1.83	22
May	1.92±0.05	2.06	1.82	21
Jun	1.89±0.04	1.99	1.83	22
Jul	1.91±0.07	2.06	1.83	21
Aug	1.96±0.07	2.12	1.85	21
Sep	2.00±0.08	2.15	1.88	20
Oct	1.95±0.06	2.06	1.88	25
Nov	1.95±0.06	2.09	1.86	25
Dec	1.91±0.06	2.02	1.83	23
Annual	1.93±0.07	2.15	1.82	261

Regional enhancements in the methane emissions over the Indo-Gangetic Plain [Frankenberg *et al.*, 2005] in the northern Indian region have been suggested to be associated mainly with the rice cultivation and to somewhat lesser extent with the domestic cattle [Goroshi *et al.*, 2011]. The observed seasonal maxima of CH₄ during September (Kharif season) over Nainital is in agreement with the previous study based on satellite data and is attributed to the rice cultivation [Goroshi *et al.*, 2011]. However, the concentrations of CH₄ during summer season are also dominated by loss due to the reaction with OH [Patra *et al.*, 2009]. Thus, CH₄ seasonal cycle over

Nainital, India should not be linked to emissions alone, and further analysis using 3-dimensional chemistry-transport modelling is required for elucidating seasonal variations of CH₄ at this location.

6.1.3. Seasonal Variation in CO

The seasonal variation in CO levels at Nainital during September 2006-December 2011 are shown in the Figure 6.4 in the form of a box plot. The average CO levels show two peaks in the seasonal cycle over Nainital with the more prominent peak during the spring (291.2±137.3 ppb in April), secondary peak during the autumn (269.4±89.1 ppb during November) and minimum levels during the summer-monsoon (142.4±26.8 ppb in August).

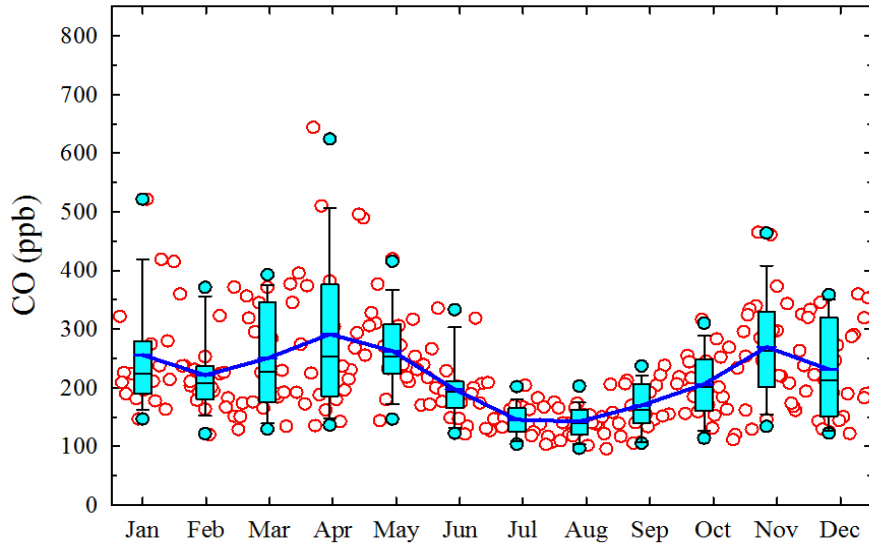


Figure 6.4: The seasonal variation in CO levels at Nainital during September 2006-December 2011 are shown as a box plot. Average monthly values are shown by a thick blue line. All observations are also shown in open red circles to show the week to week variations.

Table 6.3: *The monthly average values of CO (ppb) during twelve months as well as in the annual dataset along with the maximum and minimum values and counts.*

Month	Average CO (ppb)	Maximum	Minimum	Counts
Jan	255.9±98.9	521.2	146.5	19
Feb	221.3±65.3	371.4	119.8	20
Mar	250.2±88.0	395.3	128.6	22
Apr	291.2±137.3	644.0	135.1	22
May	262.6±66.7	419.7	143.7	21
Jun	197.1±54.2	335.5	120.9	22
Jul	145.6±25.4	203.8	103.0	21
Aug	142.4±26.8	205.6	95.8	21
Sep	170.2±40.8	237.8	105.2	20
Oct	206.0±56.0	316.4	111.3	25
Nov	269.4±89.1	464.9	129.0	25
Dec	231.4±80.9	359.8	121.8	23
Annual	221.1±87.7	644.0	95.8	261

The monthly average values of CO during twelve months along with the maximum and minimum values and counts are given in the Table 6.3. The average CO values over Nainital during the measurement period obtained from all the data points has been estimated to be 221.1±87.7 ppb with maximum value of 644.0 ppb and minimum value of 95.8 ppb. The seasonal amplitude in the monthly average CO levels is estimated to be 148.8 ppb over Nainital. The variability in the CO levels over Nainital, as seen from the standard deviation values, is highest during the

spring (66.7 to 137.3 ppb) and lowest during the summer-monsoon (25.4 to 54.2 ppb).

This seasonal cycle of CO over Nainital is observed to be similar to those in surface ozone over this region [Kumar *et al.*, 2010; Ojha *et al.*, 2012]. It is suggested that the CO seasonality is mainly controlled by the influences of regional pollution supplemented with a significant contribution from the biomass burning activities.

6.2. Long-Term Trends

The long-term measurements of CO₂, CH₄ and CO are being used here to investigate possible trends in these gases over this region, for the first time. Figure 6.5 shows the time series of CO₂, CH₄ and CO from all the observations along with the monthly average values with 1-sigma from September 2006 to December 2011 over Nainital. These time series show a trend modulated with a seasonal cycle more clearly in the case of CO₂ while there is more variability in the cases of CH₄ and CO. In order to estimate the long-term trends in these gases, data has to be first deseasonalized i.e. the seasonal cycle is to be removed from the time series.

The data has been deseasonalized [e.g. Logan, 1985] by subtracting the monthly mean data of entire period $\bar{Y}(\text{month})$, from the monthly means of a specific year $Y(\text{month, year})$ as follows:

$$Z(\text{month, year}) = Y(\text{month, year}) - \bar{Y}(\text{month}) \quad [6.1]$$

Here, $Z(\text{month, year})$ denote the deseasonalized time series. The deseasonalized time series of CO_2 , CH_4 and CO over Nainital along with a linear regression fit for the 2006-2011 period are shown in the Figure 6.6.

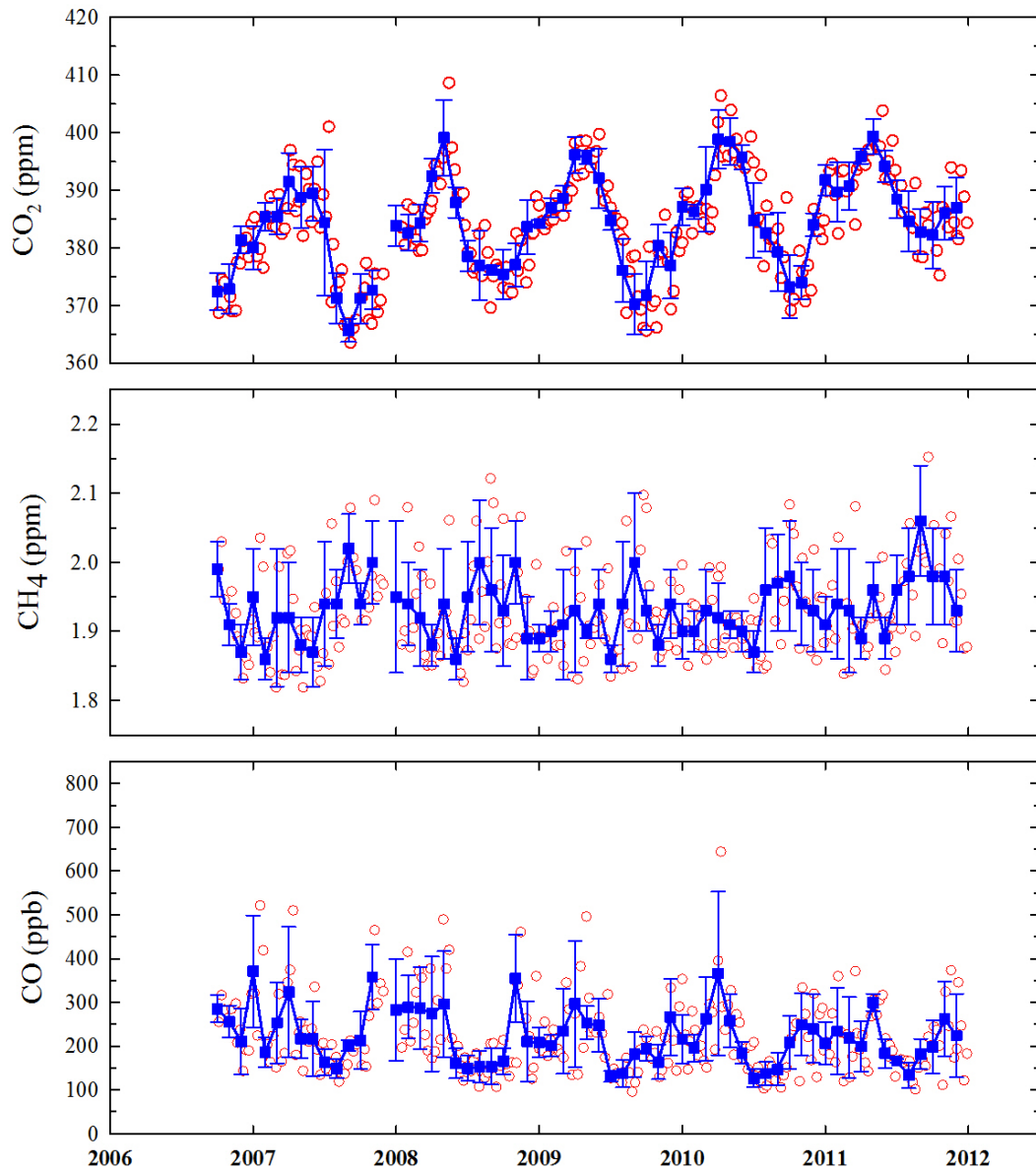


Figure 6.5: The time series of CO_2 , CH_4 and CO along with the monthly average values with 1-sigma from September 2006 to December 2011 over Nainital.

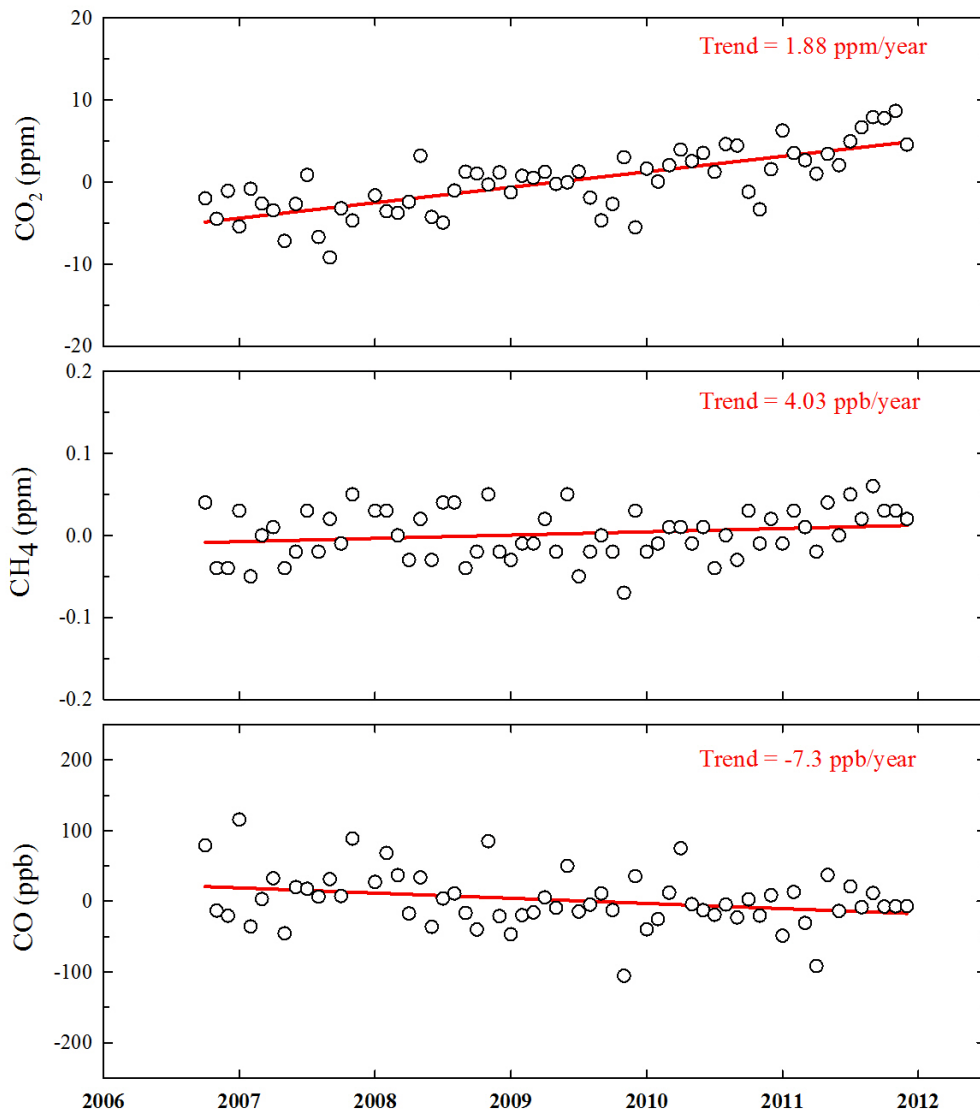


Figure 6.6: The deseasonalized time series of CO₂, CH₄ and CO over Nainital along with a linear regression fit for the 2006-2011 period.

The CO₂ data shows a clear positive trend over Nainital during 2006-2011 period. The trend using the linear regression fit is estimated to be about 1.88 ppm per year. This trend in the CO₂ levels over Nainital is found to be in good agreement with the observed trends during the study period over the Mauna Loa (1.60 to 2.43 ppm per

year) as well as over the average global marine observations (1.64 to 2.40 ppm per year) [<http://www.esrl.noaa.gov/gmd/ccgg/trends/>].

The current CO₂ levels, i.e., the annual average CO₂ during 2011 at Nainital is estimated to be 389.6±6.3 ppm, which is found to be similar to the Mauna Loa and average global marine CO₂ levels (390.5 to 391.6 ppm). The observed enhancements in the CO₂ levels are mainly attributed to the increased emissions from fossil fuel combustion, gas flaring and cement production, since the preindustrial era [Forster *et al.*, 2007]. Biomass burning and deforestations are the other sources which contribute to the increasing trends in CO₂ levels [Andreae and Merlet, 2001; Houghton, 2003; Van der Werf, 2004; Forster *et al.*, 2007].

In contrast to CO₂, which shows a clear positive trend in the levels over Nainital, CH₄ and CO levels do not show a clear trend (Figure 6.6). CH₄ levels show a very small positive trend of 4 ppb per year, while, CO levels show a slight negative trend of 7.3 ppb per year. It has been reported that CH₄ levels have substantially increased since the pre-industrial era, however, its growth rate has reduced to nearly zero during last 25 years [Dlugokencky *et al.*, 1998; Simpson *et al.*, 2002; Forster *et al.*, 2007]. However, since 2007, atmospheric CH₄ has been increasing again [WMO, 2012]. Thus, the observed trend in CH₄ over Nainital is found to be in reasonable agreement with the reported global trends.

The previous years (prior to the year 2007) slowdown in the global growth rates of CH₄ are not well understood [e.g. *Prather et al.*, 2001; *Forster et al.*, 2007]. However, a wide range of hypotheses have been put forward to explain this slowdown of CH₄ growth rate, which includes reduction [*Hansen et al.*, 2000] or stabilisation of CH₄ emissions [*Francey et al.*, 1999]. In a recent study, *Kai et al.* [2011] attributed the CH₄ trends to the decreased microbial sources in the northern hemisphere.

CO levels over Nainital show a slight decreasing values (7.3 ppb per year) during the study period which is consistent with the global trends. However, the observed negative trend is slightly higher (~3.3% per year) as compared with the global observations. The trends in CO over the northern hemisphere have been observed to change from an increase of 1% during 1980s to a decrease of 1 to 1.5% during 1990s and 2000s [e.g. *Khalil and Rasmussen*, 1988; *Khalil and Rasmussen*, 1994; *Novelli et al.*, 2003; *Angelbratt et al.*, 2011].

6.3. Inter-Species Correlation Analysis

In this section, the inter-species correlations among CO, CO₂ and CH₄ over Nainital have been analyzed for different seasons to investigate the relationships among their variabilities and to identify their possible common sources and transport.

6.3.1. CO-CH₄ Correlations

A scatter plot analysis has been performed between CH₄ and CO as shown in the Figure 6.7. Individual data points of CH₄ are binned into 50 ppb bins of CO to smooth the random variations and the coefficient of determination is estimated using a linear regression fit in the binned average data. CH₄ shows strong positive correlations with CO in all the seasons over Nainital with r^2 values varying from 0.56 to 0.93. This indicates that CH₄ and CO over Nainital are generally controlled by common processes during all the seasons.

Further, the CH₄ and CO ratios can be used to identify the source types by comparing them with the emission ratios from different sources such as fossil fuel, biofuel or biomass burning [Xiao *et al.*, 2004]. The global and East Asian (including India) CH₄/CO emission estimated [Xiao *et al.*, 2004] during the Transport and Chemical Evolution over the Pacific (TRACE-P) are given in the Table 6.4.

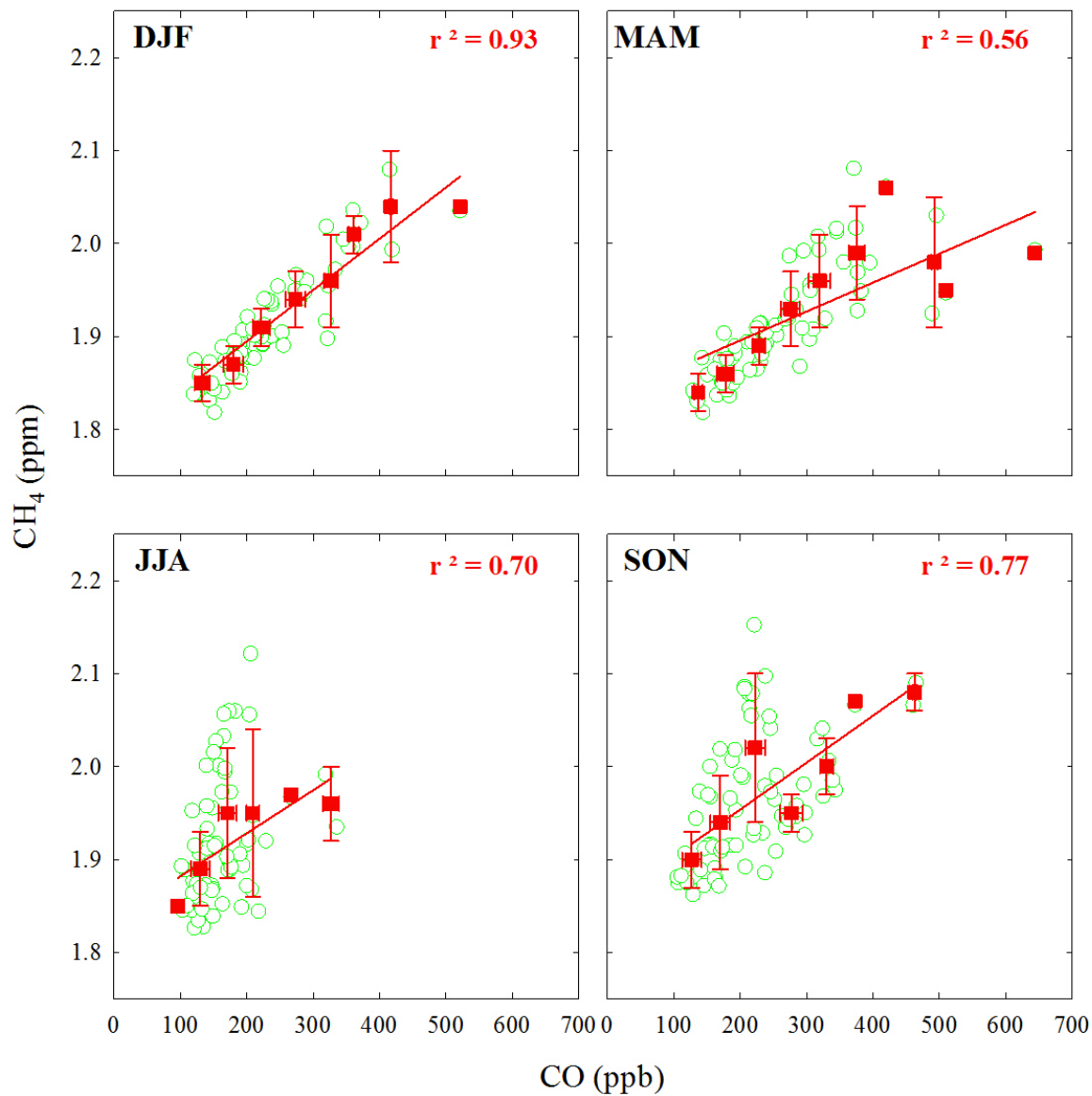


Figure 6.7: Scatter plots showing the correlations between CH₄ and CO over Nainital during four seasons. All the data points are shown by open green circles. Coefficient of determination (r^2) have been estimated using the binned data (red filled squares).

Table 6.4: Estimates of Global and East Asian CH₄/CO emission during TRACE-P period as obtained from Xiao et al. [2004].

	Global CH₄/CO	East Asian CH₄/CO
Fossil Fuel	0.46	0.30
Biofuel	0.10	0.10
Biomass Burning	0.11	0.12

The observational CH₄/CO value over Nainital are represented by the slope values of the scatter plot between CH₄ and CO. The estimated CH₄/CO value vary from 0.31 (during spring) to 0.55 (during winter) over Nainital. A comparison of these estimates with the emission ratios from different sources (Table 6.4) indicate that CH₄ and CO variations are more influenced by the fossil fuel combustion over this region.

6.3.2. CO-CO₂ Correlations

CO₂ shares the common sources with some of the other trace gases particularly with CO and the emission ratio CO₂ and CO strongly varies with different combustion types and efficiencies versus the terrestrial biosphere. Thus, the correlation analysis between CO₂ and CO can be a useful tracer of different source types [e.g. *Andreae and Merlet, 2001; Suntharalingam et al., 2004; Wang et al., 2010*]. The emission estimates of CO₂ and CO along with the emission ratio CO₂/CO for different source types over Indian region as obtained from *Suntharalingam et al. [2004]* are given in the Table 6.5. In order to investigate the sources of CO₂ over Nainital, a correlation

analysis has been performed between CO₂ and CO for different seasons as shown in the Figure 6.8.

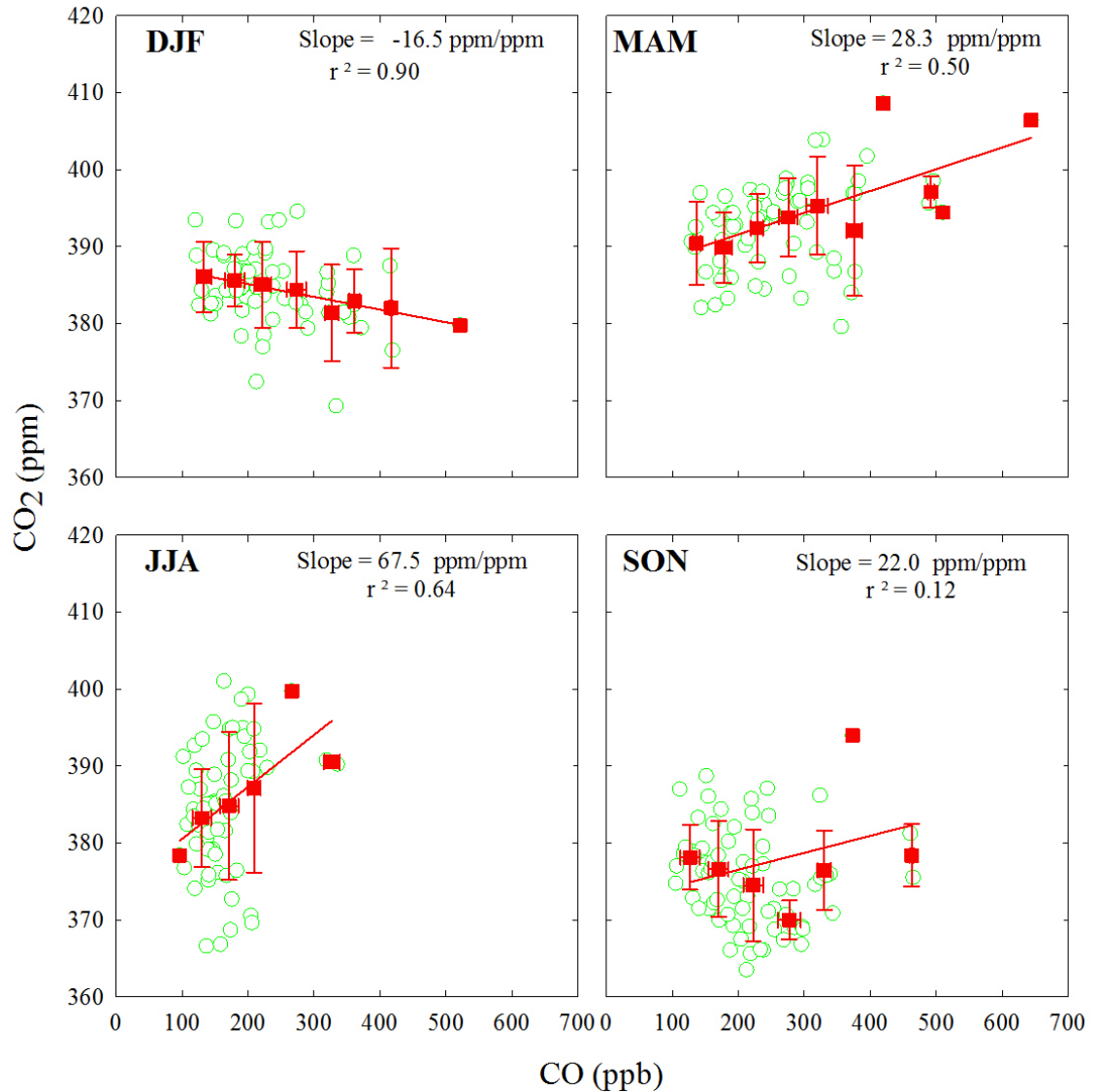


Figure 6.8: Scatter plots showing the correlations between CO₂ and CO over Nainital during four seasons. All the data points are shown by open green circles. Coefficient of determination (r^2) have been estimated using the binned data (red filled squares).

The CO₂ data has been first binned into 50 ppb bins of CO and the coefficient of determination (r^2) and slope values have been estimated using the correlation plot of binned average data. The variations in CO₂ and CO are observed to positively correlated during the spring and summer-monsoon. The relationship is observed to be negative during the winter, while, CO₂ and CO do not show any significant correlation during the autumn ($r^2 = 0.12$). In contrast with the winter and autumn, common sources and processes are suggested to control the variations of CO₂ and CO during spring and summer-monsoon as indicated by the observed strong positive relationships between the two species.

Table 6.5: Estimates of CO₂ and CO emissions and CO₂/CO emission over India for TRACE-P period obtained from Suntharalingam et al. [2004].

	CO₂ Emissions (Gg C/d)	CO Emissions (Gg C/d)	CO₂/CO Emission ratio
Fossil Fuel	484	20	24
Biofuel	496	34	15
Biomass Burning	552	46	12
Biosphere	1080	11	98

In order to further understand the controlling processes, the estimated slope values from the observed CO and CO₂ are compared with the emission ratios for the different sources as given in the Table 6.5. The slope values are 28.3 ppm/ppm

during the spring while it is much higher (67.5 ppm/ppm) during the summer-monsoon. Thus the springtime variabilities are mainly attributed to the emissions related to fossil fuel while the monsoontime variations would be more controlled by the biosphere.

6.4. Summary and Conclusions

Weekly air samples collected at Nainital in the central Himalayas have been analyzed for CO₂, CH₄ and CO during September 2006-December 2011. CO₂ levels show a prominent seasonal cycle over Nainital with a spring maximum (395.9±5.9 ppm in May) and a post-monsoon/autumn minimum (374.4±5.8 ppm in October) which is attributed to the growth and decomposition of the vegetations with some influences of biomass burning activities over this region. The observed CO₂ seasonal cycle at Nainital is similar to the variations at Mauna Loa (MLO), however, the seasonal amplitude is much larger at Nainital (~21.5 ppm) than that at the Mauna Loa (~6.5 ppm). CH₄ levels over Nainital show a peak during autumn (2.0±0.08 ppm in September) while these are lowest in June. The seasonal maxima of CH₄ during September is attributed to the rice cultivation and is in agreement with satellite based studies. CO levels over Nainital show a seasonal cycle similar to that in surface ozone over this region and is associated with the regional pollution supplemented with biomass burning.

The long-term time series of CO₂, CH₄ and CO over Nainital are deseasonalized and fitted with a linear regression to estimate the trends. CO₂ shows an increasing trend

of about 1.88 ppm per year over Nainital which is similar to Mauna Loa and global marine observations. The positive trends in CO₂ is mainly due to the increased fossil fuel combustion, gas flaring, cement production, biomass burning and deforestation. CH₄ shows a small positive trend (about 4 ppb/ year), while, CO shows a negative trend (about 7.3 ppb/year). The reduction in CH₄ growth is suggested to be due to reduction or stabilisation of its emissions and decreased microbial sources in the northern hemisphere.

The observed positive correlations between CO and CH₄ over Nainital indicate that these gases are generally controlled by common processes. Estimated CH₄/CO values over Nainital are compared with the emission ratios from different sources which shows that CH₄ and CO levels are more influenced by fossil fuel combustion. CO₂ bears a positive correlation with CO suggesting the role of common processes controlling the variations in these gases particularly during spring and summer-monsoon. CO₂/CO values are estimated to be 28.3 ppm/ppm during spring and 67.5 ppm/ppm during the summer-monsoon. Comparative analysis of CO₂/CO values suggest that springtime variations are mainly governed by fossil fuel emissions, while, biosphere influences these gases during summer-monsoon.

Chapter 7

Summary and Future Scope

The present thesis work has been aimed to understand the spatial and temporal variations on the distribution of trace gases over the northern Indian region with main emphasis on ozone. Space borne studies have shown that the pollution loading is considerably higher over this region, however, the understanding of the underlying processes has been very limited until now. In this thesis, an attempt has been made to fill this gap by conducting the ground-based and balloon-borne observations in this region. Apart from the observations, data from space-borne sensors and model simulations are also employed for extensive studies over this region. The detailed analysis of the observations made has been presented in the Chapters 3, 4, 5 and 6. Here, a summary of the main conclusions is given in the following subsections:

7.1. Variations in Surface Ozone at Pantnagar in the Indo-Gangetic Plain (IGP) region

The Indo-Gangetic Plain (IGP) region, in the northern India, is one of the most densely populated regions in the world, which encompasses a variety of emissions including those from thermal power plants, industries, automobiles, bio-fuel

burning, mining, crop-residue burning etc. Moreover due to the complex topography, the emissions from this region get trapped and lead to the elevated levels of trace gases and aerosols. The spatial heterogeneity in the distribution of pollutants have been reported using satellite observations [*Fishman et al.*, 2003; *Di Girolamo et al.*, 2004]. However, the ground based measurements of air pollutants are very limited over this region. Observations of surface ozone with a complete seasonal cycle are only available at a highly urbanized megacity (Delhi) [*Ghude et al.*, 2008a] and a pristine mountain site Nainital in the central Himalayas [*Kumar et al.*, 2010]. In view of this, observations of surface ozone were made at a semi-urban site Pantnagar (29.0°N, 79.5°E, 231m amsl) in the IGP during March 2009–June 2011 and these data were analyzed using meteorological parameters, the boundary layer evolution, backward trajectories, space-borne observations, results from a global chemistry transport model and a photochemical box model.

Ozone diurnal variations are characterized by daytime photochemical build up. The rate of change of ozone during morning (+5.6 ppbv hr⁻¹) and evening time (-8.5 ppbv hr⁻¹) are dissimilar and a higher ozone loss rate in the evening suggests that ozone loss processes could be stronger over the IGP due to high NO_x emissions. The seasonal variations in daily and monthly average ozone at Pantnagar show a systematic increase from January to May, decrease sharply to lower levels during June-September then a slight increase during October-November. Notably, daytime average ozone shows prominent secondary maxima during October-November which is not seen in the all data. Ozone levels are observed to be highest during the spring months (39.3±18.9 ppbv in May) and lower during the summer/monsoon (16.8±8.9 in August) and winter (10.8±12.1 ppbv in January). Similarly, the

seasonal ozone photochemical buildup is 32-41 ppbv in spring and autumn and 9-14 ppbv during August-September. Monthly average values are mostly below 40 ppbv; however, occasionally hourly average ozone levels are in the range of 80-100 ppbv, particularly during spring. CO levels are observed to be moderately high (188-484 ppbv) while CH₄ values range from 1.81 to 2.11 ppmv.

Observed ozone seasonality is in good agreement with the solar radiation and satellite derived lower tropospheric CO and tropospheric column NO₂. Lower levels of all the gases during July-September are mainly attributed to the arrival of southwest monsoon bringing cleaner marine air to this region. During spring and autumn, air masses mostly circulate over the continental Indian region, including the IGP, before reaching to the observation site and thus could be rich in ozone and precursors. However, the spring peak is higher than the autumn peak that could be due to the presence of additional ozone precursors from biomass burning and intense solar radiation during spring when compared with those during autumn. In addition to the photochemistry, the boundary layer dynamics could also play a role in the observed ozone variabilities. It is shown that the lower mixing depth during autumn could led to have a minimal role of the boundary layer processes in ozone enhancement during autumn, unlike in spring when the boundary layer height is also higher.

A comparison of ozone observations at Pantnagar, with a nearby high altitude site Nainital, located in the central Himalayas, were also made. Ozone mixing ratios at Pantnagar and Nainital show strong positive correlation ($r^2 = 0.96$) in the daytime

(1130-1630 hours), during spring when mixing depth over Pantnagar is also higher. While the nighttime (0100-0300 hours) ozone mixing ratios do not show a clear relationship. This indicates that emissions and photochemical processes in the IGP region can influence the air quality over the cleaner Himalayan region via the boundary layer mixing processes, mainly during daytime. Comparison of the ozone seasonal variation at Pantnagar with other sites in India shows that sites in the northern Indian region, having proximity to the IGP region, have maximum ozone levels during spring, while sites located in the southern part of India show maximum ozone levels during winter. This comparison highlights the diversity of emissions as well as processes controlling ozone levels over different parts of Indian region.

A global chemistry transport model (MATCH-MPIC) has been used to simulate the spatial and temporal variabilities in ozone and related species over this region. The model reproduces the overall springtime elevated ozone levels over the IGP, lower ozone during the summer/monsoon and winter, and a recovery phase during autumn. However, the model overestimates the ozone levels during all the months, which is attributed to the higher ozone levels in the model during the nighttime. This could be due to a possible underestimation of NO_x emissions resulting in less ozone titration. In addition, model ozone shows a more pronounced secondary maximum during autumn. CO-tracer based analysis suggests that this overestimation in the model could be associated with the biomass burning. The MATCH-MPIC output is further used to assess the variabilities in H_2O_2 and HNO_3 as an indicator of ozone sensitivity to hydrocarbons and NO_x . Average values of $\text{H}_2\text{O}_2/\text{HNO}_3$ ratios range from 1.1 ± 0.7 to 2.9 ± 1.5 , which suggests that ozone chemistry over this region is NO_x -limited. Further, simulations from a chemical box model are used to estimate ozone

production and loss rates at Pantnagar and to study the ozone sensitivity with changes in NO_x and NMHCs. Integrated net ozone production, from model, in a day, is estimated to be 72.9 ppbv.

7.2. Vertical Distribution of Ozone and Meteorological Parameters over the Central Himalayas

The systematic balloon-borne ozone observations are non-existing in the central Himalayan region and there are few observations over the Indo-Gangetic plain, at an urban site Kanpur, [Gupta *et al.*, 2007]. In view of this, balloon-borne measurements have been initiated from a mountain top called Manora Peak near Nainital (79.45°E, 29.37°N, 1958 m amsl) in the central Himalayas. Weekly balloon-borne observations of ozone and meteorological parameters have been carried out during Jan-Dec 2011 and total 48 profiles are collected and data are analyzed. Average temperature near the surface (2500 m amsl) is highest during the summer-monsoon ($15.0 \pm 1.0^\circ\text{C}$) and lowest during the winter ($6.3 \pm 3.2^\circ\text{C}$), however, the variability during summer-monsoon is much lower (6.4%) as compared with other seasons (23.6 to 51.2%). Relative humidity discerns large variabilities in the distribution with maximum near-surface values during summer-monsoon ($89.5 \pm 10.3\%$) and minimum during winter ($27.3 \pm 31.5\%$).

Wind speed shows a prominent vertical profile with maximum speeds in middle-troposphere in all the seasons except during the summer-monsoon. Near surface wind speeds are observed to be the strongest during the spring (6.8 ± 2.7 m/s) and the

weakest during the winter (4.0 ± 1.7 m/s). The very strong winds (40 to 80 m/s) observed in the middle-upper tropospheric altitudes over this region and are suggested to be associated with the prevailing subtropical jets. The seasonal variations in the wind direction at different altitudes over the central Himalayas shows the dominance of northwesterly winds (50-89%) during winter and spring in the lower troposphere, while, lesser contribution is from the southwesterly (2-34%) and southeasterly (0-30%) regime. On the contrary, southeasterly winds contribute maximum in the 2-4 km (28-68%) and 4-6 km (13-39%) during the summer-monsoon period.

The seasonal variations in the tropopause pressure calculated from the radiosonde measurements are compared with tropopause data from satellite observations and WRF simulations over this region. All the three datasets show similar tropopause pressure values from April to October, while, it shows dramatic variations during winter and early spring. Radiosonde data shows better correlation with the model results ($r^2 = 0.63$) in comparison with the satellite data ($r^2 = 0.36$). Observed variability in the tropopause during winter and spring is suggested to be associated with the tropopause folds or multiple-tropopause events, which is a dominant atmospheric phenomenon at the junction of tropics and mid-latitude.

Ozone distribution shows large variabilities over this region. Variability (1σ in percentage) in the near surface (2500 m amsl) ozone is highest during the summer-monsoon (43.4%), moderate during the spring and autumn (21.6 and 17.8%) and

lowest during the winter (9.6%). In contrast, the ozone variability is maximum during the spring (43.1%) and minimum during the summer-monsoon (21.9%) in the upper troposphere (15 km amsl). These differences suggest that the processes controlling ozone variations are different in different layers of the troposphere. Ozone levels in the lower troposphere (2 to 6 km) show a prominent seasonal cycle with highest levels (~100 ppbv in May) during spring and lowest levels during the summer-monsoon. A secondary peak is observed during autumn and the ozone levels are also lower during winter. This seasonality in the lower troposphere is in agreement with the ground based ozone observations over this region. The seasonality in ozone is less pronounced in the higher altitudes (6-10 km & 10-14 km).

Further, ozonesonde profiles are compared with the spatially and temporally co-located satellite (TES) retrieved ozone data for the first time to identify errors and biases in satellite retrievals. The seasonally averaged ozone profiles from the ozonesonde observations agree with the collocated TES retrievals and are generally observed to be within the 1-sigma spread. The differences between ozonesonde data and satellite retrievals with TES operator are less (< 10 ppbv) in lower troposphere as compared with the middle-upper troposphere (15 and 20 ppbv). The percentage biases in the satellite retrievals show significant variability and satellite overestimates the ozone levels near the surface (~749 hPa) in all the seasons except during spring by 3 to 31.2%. TES underestimates the ozone levels by about 8% above 600 hPa during summer-monsoon, while, during winter and autumn it overestimates the ozone levels in the lower and middle troposphere (up to 400 hPa)

by 5 to 22.5%. The biases are highest during summer-monsoon which is attributed to limited ability of TES through the clouds. Notably, the satellite retrieved ozone profiles do not show the observed features of secondary peaks which indicates that it has limitations in capturing small features in the ozone distribution.

Ozonesondes profiles are used to estimate the tropospheric column ozone (TCO) and are compared with TES TCO data. TCO data from the ozonesonde observations show a typical seasonality comprising of spring maxima (47.2 ± 9.8 DU) and winter minima (30.4 ± 10.1 DU). The observed seasonality in TCO is detected well by the TES satellite, however some differences are observed particularly during the winter and autumn. Satellite data shows a general agreement with sonde observations ($r^2 = 0.4$), while, the correlation is improved drastically ($r^2 = 0.9$) when the same tropopause levels is used for the two datasets. It is concluded that the satellite based observations can have uncertainties in providing the tropospheric columns of pollution due to the variability in tropopause pressure.

7.3. Influences of Dynamical Processes and Biomass Burning on Ozone Distribution

The role of various dynamical processes and biomass burning in influencing the ozone distribution over this region are investigated using the ozonesonde and radiosonde observations, model simulations of meteorological and chemical fields, satellite data of tracers and fire counts. The potential vorticity (PV) values at different pressure levels over Nainital for all the observation days during January-

December 2011 are estimated using a regional model (WRF-Chem) simulated meteorological fields. The variations in PV values particularly above the 300 hPa indicate that the influences of stratospheric intrusions are more likely during winter and spring while these are not seen during the summer-monsoon. This result is consistent with the previous studies over the Nepal Climate Observatory (5079 m amsl) in the Himalayas [*Cristofanelli et al.*, 2010].

PV values are observed to be highest on 17th February along with the observation of significantly elevated (about 1.7 to 2 times higher) ozone levels in the middle-upper troposphere. Since, ozone levels in the lower troposphere do not show any significant change on this day, thus this event is investigated for the possibility of a stratospheric intrusion. This possibility is supported by a significant increase in potential vorticity (PV) (2.5 pvu and more) values during the event. Further, the relative humidity also decreases sharply above ~7 km amsl and remains very low in the higher altitudes during the event. The reduction in the humidity has also been confirmed using the satellite data (AIRS). HYSPLIT simulated back air trajectories do not show any appreciable change in the transport pattern indicating minimal role of the advection. Presence of drier air suggests that the air masses could have been transported from the higher altitudes, which are poor in water vapor but rich in ozone.

An analysis of data from two chemistry transport model (WRF-Chem and MOZART) results shows that the global as well as regional chemistry transport models had some limitations in reproducing the STE event over this region. It is found that model estimated ozone enhancement is less as compared with the

observations and the maximum enhancement is at a lower altitude. It is seen that MOZART results are in better agreement with the observations in terms of the peak altitude and the magnitude of the enhancements. Further analysis of MOZART output at 400 hPa pressure level displays a patch of significantly high ozone (100-120 ppbv and higher) over an area of about $10^{\circ}\times 10^{\circ}$ around the site. Moreover, model simulated CO at 400 hPa also shows large reduction around the site during the event. Thus, meteorological and chemical fields confirm the intrusion of the stratospheric ozone into the troposphere leading to large enhancement in the middle-upper tropospheric ozone levels. Such events can perturb the budget of tropospheric ozone particularly during the winter months over this region.

Several ozone profiles over Nainital also show the presence of secondary ozone peaks (SOPs). Ozone profiles discern the layers of elevated ozone levels (~140 to 250 ppbv) in the middle troposphere (~8 to 12 km). The SOPs are observed more frequently during spring (3 events). During the occasions of SOPs, ozone levels in the lower troposphere are within the 1-sigma variabilities suggesting that the regional pollution is unlikely the governing process. Moreover, the ozone levels above these layers also do not show any clear signature of the stratospheric influence. Considering the presence of strong winds in these altitude ranges, ozone rich air masses can be transported from distant sources. However, occasionally stratosphere-troposphere exchange could also have some contribution to these layers which needs further investigation.

It has been shown that biomass burning activities in the northern Indian region are maximum during the spring months and thus can influence the distribution of ozone by supplementing the emissions of ozone precursors. In this direction, more number of balloon soundings (2-3 soundings in a week) has been conducted during spring to investigate the possible influence of the biomass burning activities on the ozone vertical distribution over Nainital. Ozone profiles during these periods are classified into Low Fire Activity Period (LFAP) (30th March to 29th April) and High Fire Activity Period (HFAP) (4th May to 25th May) using MODIS fire count data. The ozone levels during the HFAP show significant enhancement in comparison with the ozone levels during the LFAP. The maximum enhancement is noticed at about 3 km amsl with HFAP ozone levels of 96.0 ± 8.1 ppbv as compared with LFAP ozone levels of 70 ± 13.7 ppbv. The 95% confidence interval for the observed ozone enhancement in the 2 to 4 km altitude range is 18-22 ppbv. This analysis shows that the northern Indian biomass burning plays a key role in the observed spring time ozone maxima in the lower troposphere over this region.

7.4. Variations in CO₂, CH₄ and CO over the central Himalayas

Most of the observed global warming has been attributed to the enhancements in the Long-Lived Greenhouse Gases (LLGHG) such as Carbon dioxide (CO₂), Methane (CH₄), Nitrous Oxide (N₂O) and Sulfur Hexafluoride (SF₆). CO₂ and CH₄ are ranked first and second respectively in terms of the radiative forcings imposed by LLGHGs on the climate. Due to very long lifetimes of these gases, the observations over remote locations are suggested to be the representative of large-scale variations. CO is not itself a greenhouse gas, however, being the precursor of ozone it also

contributes to the global warming indirectly. CO has also been used as a tracer of anthropogenic influences in the variations of CO₂ and CH₄. Despite of the vital roles of LLGHGs in the climate change, their long-term systematic measurements are very limited over the Indian region. In this direction, weekly air samples collected from a high altitude site Nainital (79.45 °E, 29.37 °N, 1958 m amsl) in the central Himalayas have been analyzed in collaboration with NIES, Japan since September 2006. The long-term data of CO₂, CH₄ and CO during September 2006-December 2011 has been analyzed for the seasonal variations and long-term trends.

CO₂ shows a prominent seasonality over Nainital with the spring maximum (395.9±5.9 ppm in May) and post-monsoon/autumn minimum (374.4±5.8 ppm in October). The observed seasonality is governed by the growth and decomposition of the vegetations. Over the northern Indian region, CO₂ levels peak during April-May coinciding with the major crop-harvesting season (Rabi) over the northern India. Further, maximum biomass burning activities associated with the crop residue burning also contribute to the observed springtime maxima. CO₂ seasonal cycle at Nainital is similar to that at Mauna Loa (MLO), however, the seasonal amplitude in CO₂ is much larger at Nainital (~21.5 ppm) as compared with the Mauna Loa (~6.5 ppm).

The average CH₄ levels show a clear seasonal cycle over Nainital with peak during autumn (2.0±0.08 ppm in September). The average CH₄ levels are lowest during June; however, CH₄ does not show much variability (1.91-1.92 ppm) during winter and spring. The observed seasonal maxima of CH₄ during September (Kharif

season) over Nainital is attributed to the rice cultivation and is consistent with satellite based study [Goroshi *et al.*, 2011]. CO levels discern prominent peak during the spring (291.2 ± 137.3 ppb in April), secondary peak during the autumn (269.4 ± 89.1 ppb during November) and minimum levels during the summer-monsoon (142.4 ± 26.8 ppb in August). The observed seasonality in CO over Nainital is similar to that in surface ozone over this region and attributed to the influences of regional pollution supplemented with the biomass burning.

In order to investigate the long-term trends in CO₂, CH₄ and CO over Nainital during 2006-2011 period, the data has been deseasonalized and fitted with a linear regression. CO₂ levels show a clear increasing trend of about 1.88 ppm per year over Nainital which is consistent with the trends over Mauna Loa (1.60 to 2.43 ppm per year) and global marine observations (1.64 to 2.40 ppm per year). The positive trends in CO₂ is attributed to the increased fossil fuel combustion, gas flaring, cement production, biomass burning and deforestation.

CH₄ levels discern a small positive trend of 4 ppb per year, while, CO levels show negative trend of 7.3 ppb per year. CH₄ levels have increased since the pre-industrial era considerably, however, its growth rate has reduced to nearly zero in last about 25 years [Dlugokencky *et al.*, 1998; Simpson *et al.*, 2002; Forster *et al.*, 2007]. However, since 2007, atmospheric CH₄ has been increasing again [WMO, 2012]. The reduction in CH₄ growth is attributed to the reduction [Hansen *et al.*, 2000] or stabilisation of CH₄ emissions [Francey *et al.*, 1999], and decreased microbial sources in the northern hemisphere [Kai *et al.*, 2011]. The observed negative trend in

CO is slightly higher (~3.3% per year) as compared with the global observations which vary from an increase of 1% during 1980s to a decrease of 1 to 1.5% during 1990s and 2000s.

CH₄ shows strong positive correlations with CO in all the seasons over Nainital with r^2 values varying from 0.56 to 0.93. This indicates that CH₄ and CO over Nainital are generally controlled by common processes in all the seasons. A comparison of the estimated CH₄/CO ratios over Nainital varying from 0.31 (during spring) to 0.55 (during winter) with the emission ratios from different sources indicate that CH₄ and CO variations are more influenced by fossil fuel combustion. Observed positive correlations between CO₂ and CO suggest that common processes control the variations during spring and summer-monsoon. The estimated CO₂/CO values are 28.3 ppm/ppm during the spring and much higher (67.5 ppm/ppm) during the summer-monsoon which indicate that the springtime variations are mainly influenced by the fossil fuel emissions while the monsoontime variations are more influenced by the biosphere.

7.5. Future Scope

During the present thesis work, balloon-borne observations of ozone distribution along with meteorological parameters were started over the central Himalayas. Moreover, surface ozone measurements were also initiated at a semi-urban site in the Indo-Gangetic Plain region and sample based measurements of greenhouse gases have also been started in the central Himalayan region. The analysis of these

observations suggests that complex chemical and dynamical processes influence the distribution of ozone and other trace gases and more detailed investigation would be highly desirable.

- During this thesis work, systematic weekly balloon-borne observations have been initiated in the northern Indian region which resulted into about 4 profiles in each month. These observations should be continued in future so that data of more years can be used to understand different processes and inter-annual variations. This will also help in better quantitative estimates of contributions from the regional pollution and long-range transport. Moreover, for the validation of satellite observations, more number of collocated profiles will improve the statistics and lead to better estimations of errors and biases. These measurements will also be used to identify the stratosphere-troposphere exchange events and their quantitative contribution to the tropospheric ozone budget over this region. Additionally, these observations will be the invaluable datasets to evaluate the performances of various global and regional chemistry transport models. Finally, the long-term trends of the vertical ozone profiles will be invaluable in the assessment of its contribution to the climate change and atmospheric warming/cooling.

- Surface ozone measurements have been started in the IGP region however, only ozone measurements are insufficient to fully understand the ozone chemistry in this region. There is a need to measure all the precursors such as CO, NO_x and hydrocarbons to better characterize the ozone photochemical processes.

Observations of radicals and other nitrogen compounds such as HNO_3 , HNO_2 , N_2O_5 , PAN etc. would be highly desirable. It would be better to have these observations simultaneously at IGP and the central Himalayas. Our understanding of the tropospheric chemistry over this region can be significantly improved by additional observations of hydrocarbons, hydroxyl and peroxy radicals. Better information of NO_x and VOCs limited regimes will help in air quality control. The continuous surface observations of ozone in the IGP region would be further used to estimate their impacts on the living beings and vegetations.

- In this thesis, it has been concluded that chemistry transport models have limitations in simulating the observed variations in ozone over this region. It is further inferred that these limitations are mainly associated with the emission data and complex topography of this region. Hence taking this into an account, higher resolution modeling is needed and at least 10 km x10 km resolution should be planned. This would enable to better simulate the processes such as the boundary layer variations and upslope-downslope mountain valley flows etc. The emission datasets could be improved by assimilating the satellite based observations and chemistry transport models will be used for the evaluation. High resolution modeling using improved emissions will improve the performance of the models and these models would be used to quantify the role of different processes. In particular, the models would be used to improve our understanding of the tropospheric ozone budget over this region. With the improved emissions and evaluated model, contributions from different local and

regional emission sources (anthropogenic, biomass burning, biogenic) and photochemistry could be estimated using various tracers in the model.

Blank Page

Bibliography

Adams, R. M., J. D. Glycer, S. L. Johnson, and B. A. McCarl (1989), A reassessment of the economic effects of ozone on U. S. agriculture, *JAPCA*, 39, 960-968.

Adams, R. M., Brian H. Hurd, Stephanie Lenhart, and Neil Leary (1998), Effects of global climate change on agriculture: an interpretative review, *Clim. Res.*, Vol-11:19-30.

Adler, R. F., D. T. Bolvin, S. Curtis, and E. J. Nelkin (2000): Tropical rainfall distributions determined using TRMM combined with other satellite and rain gauge information. *J. Appl. Meteor.*, 39, 2007–2023.

Akimoto, H. (2003), Global air quality and pollution, *Science*, 302, 1716-1719, doi: 10.1126/science.1092666.

Akriditis, D., P. Zanis, I. Pytharoulis, A. Mavrakis, Th. Karacostas (2010), A deep stratospheric intrusion event down to the earth's surface of the megacity of Athens. *Meteorol. Atmos. Phys.* 109, 9-18.

Arino, O. and J.M. Rosaz (1999), The ATSR World Fire Atlas and a Synergy with POLDER Aerosol Products. Proceedings of the International Workshop on the Applications of the ERS Along Track Scanning Radiometer, ESRIN, Frascati, 23-25 June 1999.

Andreae, M.O., and P. Merlet (2001), Emission of trace gases and aerosols from biomass burning, *Global Biogeochem. Cycles*, 15 (4), 955–966, doi:10.1029/2000GB001382.

- Andrews, A. E. et al. (2013), CO₂, CO and CH₄ measurements from the NOAA Earth System Research Laboratory's Tall Tower Greenhouse Gas Observing Network: instrumentation, uncertainty analysis and recommendations for future high-accuracy greenhouse gas monitoring efforts, *Atmos. Meas. Tech. Discuss.*, *6*, 1461-1553.
- Angelbratt, J. et al. (2011), Carbon monoxide (CO) and ethane (C₂H₆) trends from ground-based solar FTIR measurements at six European stations, comparison and sensitivity analysis with the EMEP model, *Atmos. Chem. Phys.*, *11*, 9253–9269.
- Ashmore, M. R (2005), Assessing the future global impacts of ozone on vegetation, *Plant Cell Environ.*, *28*, 949– 964.
- Asnani, G. C. (2005), Climatology of the tropics, in *Tropical Meteorology*, vol. 1, pp. 100-204, Pune, India.
- Attmannspacher, W., and H. Dütsch (1970), International Ozone Sonde Intercomparison at the Observatory of Hohenpeissenberg, *Rep. 120*, *Dtsch. Wetterdienstes*, Offenbach, Germany.
- Auvray, M., and I. Bey (2005), Long-range transport to Europe: Seasonal variations and implications for the European ozone budget, *J. Geophys. Res.*, *110*, D11303, doi: 10.1029/2004JD005503.
- Avnery, S., Denise L. Mauzerall, Junfeng Liu, Larry W. Horowitz (2011), Global crop yield reductions due to surface ozone exposure: 1. Year 2000 crop production losses and economic damage, *Atmos. Environ.*, *45*, 2284-2296.

- Baldocchi D. et al. (2001), FLUXNET: A new tool to study the temporal and spatial variability of ecosystem-scale carbon dioxide, water vapor and energy flux densities, *B. Am. Meteorol. Soc.* 82:2415-2434.
- Barnes, R. A., A. R. Bandy, and A. L. Torres (1985), Electrochemical concentration cell ozonesonde accuracy and precision, *J. Geophys. Res.*, 90, 7881– 7887.
- Beekmann, M., G. Ancellet, and G. Megie (1994), Climatology of tropospheric ozone in southern Europe and its relation with potential vorticity, *J. Geophys. Res.*, 99, 12,841–12,853.
- Beer, R., T. A. Glavich, and D. M. Rider (2001), Tropospheric emission spectrometer for the Earth Observing System's Aura satellite, *Appl. Opt.*, 40 (15), 2356-2367.
- Beig G., S. Gunthe, and D. B. Jadhav (2007), Simultaneous measurements of ozone and its precursors on a diurnal scale at a semi urban site in India, *J. Atmos. Chem.*, doi:10.1007/s10874-007-9068-8.
- Bhattacharya, S. K. et al. (2009), Trace gases and CO₂ isotope records from Cabo de Rama, India, *Curr. Sci.*, 97, 1336–1344.
- Bindoff, N.L., J. Willebrand, V. Artale, A. Cazenave, J. Gregory, S. Gulev, K. Hanawa, C. Le Quéré, S. Levitus, Y. Nojiri, C.K. Shum, L.D. Talley and A. Unnikrishnan, (2007), Observations: Oceanic Climate Change and Sea Level, In *Climate Change 2007: The Physical Science Basis, Contribution of Working Group I to the Fourth Assessment Report of the Intergovernmental Panel on Climate Change* [Solomon, S., D. Qin, M. Manning, Z. Chen, M. Marquis, K.B. Averyt, M. Tignor and H.L. Miller (eds.)], Cambridge University Press, Cambridge, United Kingdom and New York, NY, USA.

- Bithell, M., L. J. Gray, and B. D. Cox (1999), A three-dimensional view of the evolution of mid-latitude stratospheric intrusions, *J. Atmos. Sci.*, *56*, 673–687.
- Blake, D., and F. Rowland (1988), Continuing worldwide increase in tropospheric methane, 1978 to 1987, *Science*, *239*, 1129–1131.
- Brasseur, G. P., J. J. Orlando and G. S. Tyndall (1999), Atmospheric Chemistry and Global Change, pp. 209-234, *Oxford University Press*, New York.
- Brewer, A.W., & Milford, J.R. (1960), The Oxford-Kew Ozone Sonde, *Proc. Roy. Soc. London*, Ser. A, 470–495.
- Bodeker, G. E., I. S. Boyd, W. A. Matthews (1998), Trends and variability in vertical ozone and temperature profiles measured by ozonesondes at Lauder, New Zealand: 1986–1996, *J. Geophys. Res.*, *103*, 28661–28681.
- Bousquet, P., et al. (2000), Regional changes in carbon dioxide fluxes of land and oceans since 1980, *Science*, *290*, 1342–1346.
- Boyd, I. S., G. E. Bodeker, B. J. Connor, D. P. J. Swart, and E. J. Brinksma (1998), An assessment of ECC ozonesondes operated using 1% and 0.5% KI cathode solutions at Lauder, New Zealand, *Geophys. Res. Lett.*, *25*, 2409–2412.
- Bucsela, E. J., E. A. Celarier, M. O. Wenig, J. F. Gleason, J. P. Veefkind, K. F. Boersma, and E. J. Brinksma (2006), Algorithm for NO₂ vertical column retrieval from the Ozone Monitoring Instrument, *IEEE Trans. Geosci. Remote Sens.*, *44*, 1245–1258.
- Chameides, W. L., and J. C. G. Walker (1973), A photochemical theory of tropospheric ozone, *J. Geophys. Res.*, *78*, 8751-8760.

- Chameides, W. L., et al. (1992), Ozone precursor relationships in the ambient atmosphere, *J. Geophys. Res.*, *97*, 6037-6056.
- Chameides, W. L., Li Xingsheng, Tang Xiaoyan, Zhou Xiuji, Chao Luo, C. S. Kiang, J. St. John, R. D. Saylor, S. C. Liu, K. S. Lam, T. Wang, F. Giorgi (1999), Is ozone pollution affecting crop yields in China?, *Geophys. Res. Lett.*, *Vol. 26*, Issue 7, pages 867–870, doi: 10.1029/1999GL900068.
- Chen, X. L., Y. M. Ma, H. Kelder, Z. Su, and K. Yang (2011), On the behavior of the tropopause folding events over the Tibetan Plateau, *Atmos. Chem. Phys.*, *11*, 5113–5122.
- Chou, M. D., and M. J. Suarez (1994): An efficient infrared radiation parametrization for use in general circulation models, *NASA Tech Memo.* 104606, 3, 85 pp.
- Claude, H., R. Hartmannsgruber, and U. Köhler (1987), Measurement of atmospheric profiles using the Brewer-Mast sonde, *WMO Rep. 17, Global Ozone Res. and Monit. Proj.*, World Meteorol. Org., Geneva.
- Conway, T.J., et al. (1994), Evidence for interannual variability of the carbon cycle from the NOAA/CMDL sampling network. *J. Geophys. Res.*, *99(D11)*, 22831–22855.
- Cooper, O. R., C. Forster, D. D. Parrish, M. Trainer, E. Dunlea, T. Ryerson, G. Hübler, F. Fehsenfeld, D. Nicks, J. Holloway, J. deGouw, C. Warneke, J. M. Roberts, F. Flocke, and J. Moody (2004), A case study of transpacific warm conveyor belt transport: Influence of merging airstreams on trace gas import to North America, *J. Geophys. Res.*, *109*, D23S08, doi:10.1029/2003JD003624.

- Cooper, O.R., A. Stohl, G. Hübler, E. Y. Hsie, D. D. Parrish, A. F. Tuck, G. N. Kiladis, S. J. Oltmans, B. J. Johnson, M. Shapiro, J. L. Moody, and A. S. Lefohn (2005), Direct transport of mid-latitude stratospheric ozone into the lower troposphere and marine boundary layer of the tropical Pacific Ocean. *J. Geophys. Res.* *110*, D23310, doi: 10.1029/2005JD005783.
- Cooper, O. R., D. D. Parrish, A. Stohl, M. Trainer, P. Nédélec, V. Thouret, J. P. Cammas, S. J. Oltmans, B. J. Johnson, D. Tarasick, T. Leblanc, I. S. McDermid, D. Jaffe, D., R. Gao, J. Stith, T. Ryerson, K. Aikin, K., T. Campos, A. Weinheimer., and A. Avery (2010), Increasing springtime ozone mixing ratios in the free troposphere over western North America, *Nature* *463*, 344-348, doi: 10.1038/nature08708.
- Cooper, O. R., R.S. Gao, D. Tarasick, T. Leblanc, and C. Sweeney (2012), Long-term ozone trends at rural ozone monitoring sites across the United States, 1990–2010, *J. Geophys. Res.*, *117*, D22307, doi:10.1029/2012JD018261.
- Crisp, D., et al. (2004), The Orbiting Carbon Observatory (OCO) Mission. *Advances in Space Research*, *34*(4), 700-709.
- Cristofanelli, P., et al. (2003), Stratosphere-to-troposphere transport: A model and method evaluation, *J. Geophys. Res.*, *108*, 8525, doi:10.1029/2002JD002600, D12.
- Cristofanelli, P., P. Bonasoni, L. Tositti, U. Bonafe`, F. Calzolari, F. Evangelisti, S. Sandrini, and A. Stohl (2006), A 6-year analysis of stratospheric intrusions and their influence on ozone at Mt. Cimone (2165 m above sea level), *J. Geophys. Res.*, *111*, D03306, doi:10.1029/2005JD006553.

- Cristofanelli, P., et al., (2010), Tropospheric ozone variations at the Nepal Climate Observatory-Pyramid (Himalayas, 5079 m a.s.l.) and influence of deep stratospheric intrusion events, *Atmos. Chem. & Phys.*, 10, 6537-6549.
- Crutzen, P. J. (1973), A discussion of the chemistry of some minor constituents in the stratosphere and troposphere, *Pure Appl. Geo-Phys.*, 106-108, 1385-1399.
- Crutzen, P. J. (1995), Ozone in the troposphere, in composition, Chemistry and Climate of the Atmosphere, edited by H. B. Singh, pp. 349-393.
- Crutzen, P. J. and M. G. Lawrence (2000): The impact of precipitation scavenging on the transport of trace gases: A 3-dimensional model sensitivity study, *J. Atmos. Chem.*, 37, 81–112.
- Cunnold, D.M., et al. (2002), In situ measurements of atmospheric methane at GAGE/AGAGE sites during 1985-2000 and resulting source inferences. *J. Geophys. Res.*, 107 (D14), doi:10.1029/2001JD001226.
- Danielsen, E.F. (1968), Stratospheric-tropospheric exchange based on radioactivity, ozone and potential vorticity. *J. Atmos. Sci.* 25, 502-518.
- Davies, T.D., E. Schuepbach (1994), Episodes of high ozone concentrations at the earth's surface resulting from transport down from the upper troposphere/lower stratosphere: a review and case studies. *Atmos. Environ.* 28, 53-68.
- David L. M., and P. R. Nair (2011), Diurnal and seasonal variability of surface ozone and NO_x at a tropical coastal site: Association with mesoscale and

synoptic meteorological conditions, *J. Geophys. Res.*, *116*, D10303, doi: 10.1029/2010JD015076.

Denman, K.L., G. Brasseur, A. Chidthaisong, P. Ciais, P.M. Cox, R.E. Dickinson, D. Hauglustaine, C. Heinze, E. Holland, D. Jacob, U. Lohmann, S. Ramachandran, P.L. da Silva Dias, S.C. Wofsy and X. Zhang (2007): Couplings Between Changes in the Climate System and Biogeochemistry. In: *Climate Change 2007: The Physical Science Basis. Contribution of Working Group I to the Fourth Assessment Report of the Intergovernmental Panel on Climate Change* [Solomon, S., D. Qin, M. Manning, Z. Chen, M. Marquis, K.B. Averyt, M. Tignor and H.L. Miller (eds.)]. Cambridge University Press, Cambridge, United Kingdom and New York, NY, USA.

Dentener, F. J. and P. J. Crutzen (1993): Reaction of N₂O₅ on tropospheric aerosols: Impact on the global distributions of NO_x, O₃, and OH, *J. Geophys. Res.*, *98*, 7149–7163.

Derwent, R. G., P. G. Simmonds, A. J. Manning, and T. G. Spain (2007), Trends over a 20-year period from 1987 to 2007 in surface ozone at the atmospheric research station, Mace Head, Ireland, *Atmos. Environ.*, *41*, 9091–9098.

Deshler, T., et al. (2008), Atmospheric comparison of electrochemical cell ozonesondes from different manufacturers, and with different cathode solution strengths: The Balloon Experiment on Standards for Ozonesondes, *J. Geophys. Res.*, *113*, D04307, doi:10.1029/2007JD008975.

Desqueyroux, H., J. C. Pujet, M. Prosper, F. Squinazi, and I. Momas (2002), Short-term Effects of low-level air pollution on respiratory health of adults suffering from moderate to severe asthma, *Environ. Res.* *89*, 29-37.

- Di Girolamo, L. et al. (2004), Analysis of Multi-angle Imaging Spectro-Radiometer (MISR) aerosol optical depths over greater India during winter 2001-2004, *Geophys. Res. Lett.*, *31*, L231115, doi: 10.1029/2004GL021273.
- Divakarla, M. G., C. D. Barnet, M. D. Goldberg, L. M. McMillin, E. Maddy, W. Wolf, L. Zhou, and X. Liu (2006), Validation of Atmospheric Infrared Sounder temperature and water vapor retrievals with matched radiosonde measurements and forecasts, *J. Geophys. Res.*, *111(D10)*, D09S15, doi:10.1029/2005JD006116.
- Dlugokencky, E.J., K.A. Masarie, P.M. Lang, and P.P. Tans (1998), Continuing decline in the growth rate of atmospheric methane, *Nature*, *393*, 447–450.
- Dlugokencky, E.J., et al. (2003), Atmospheric methane levels off: Temporary pause or a new steady-state? *Geophys. Res. Lett.*, *30(19)*, doi:10.1029/2003GL018126.
- Dlugokencky, E. J., L. M. P. Bruhwiler, J. W. C. White, L. K. Emmons, Paul C. Novelli, Stephen A. Montzka, Kenneth A. Masarie, Patricia M. Lang, A. M. Crowell, John B. Miller and L. V. Gatti, (2009), Observational constraints on recent increases in the atmospheric CH₄ burden, *Geophys. Res. Lett.*, *36*, L18803, 10.1029/2009GL039.
- Draxler, R.R. and G.D. Rolph (2012), HYSPLIT (HYbrid Single-Particle Lagrangian Integrated Trajectory) Model access via NOAA ARL READY Website (<http://ready.arl.noaa.gov/HYSPLIT.php>), NOAA Air Resources Laboratory, Silver Spring, MD.

Draxler R., B. Stunder, G. Rolph, A. Stein, and A. Taylor (2012), HYSPLIT4 User's Guide, version 4, March 2012, (www.arl.noaa.gov/documents/reports/hysplit_user_guide.pdf).

Duderstadt, K. A., M. A. Carroll, S. Sillman, T. Wang, G. M. Albercook, L. Feng, D. D. Parrish, J. S. Holloway, F. C. Fehsenfeld, D. R. Blake, N.J. Blake, and G. Forbes (1998), Photochemical production and loss rates of ozone at Sable Island, Nova Scotia during the North Atlantic Regional Experiment (NARE) 1993 summer intensive, *J. Geophys. Res.*, *103*, 13531-13555.

Ehhalt, D.H. (1999), Gas phase chemistry of the troposphere. In: *Global Aspects of Atmospheric Chemistry, Vol. 6* [Baumgaertel, H., W. Gruenbein, and F. Hensel (eds.)]. Springer Verlag, Darmstadt, pp. 21–110.

Emmons, L. K., S. Walters, P. G. Hess, J. F. Lamarque, G. G. Pfister, D. Fillmore, C. Granier, A. Guenther, D. Kinnison, T. Laepple, J. Orlando, X. Tie, G. Tyndall, C. Wiedinmyer, S. L. Baughcum, and S. Kloster (2010), Description and evaluation of the Model for Ozone and Related chemical Tracers, version 4 (MOZART-4), *Geosci. Model Dev.*, *3*, 43–67, doi:10.5194/gmd-3-43-2010.

Enting, I. G. (2002), *Inverse Problems in Atmospheric Constituent Transport*, Cambridge Univ. Press, Cambridge, U. K.

Fiedler, V., R. Nau, S. Ludmann, F. Arnold, H. Schlager, and A. Stohl (2009), East Asian SO₂ pollution plume over Europe – Part 1: Airborne trace gas measurements and source identification by particle dispersion model simulations, *Atmos. Chem. Phys.*, *9*, 4717-4728, doi:10.5194/acp-9-4717-2009.

- Fiore, A. M., D. J. Jacob, J. A. Logan, and J. H. Yin (1998), Long-term trends in ground level ozone over the contiguous United States, 1980–1995, *J. Geophys. Res.*, *103*(D1), 1471–1480, doi:10.1029/97JD03036.
- Fiore, A. M., D. J. Jacob, I. Bey, R. M. Yantosca, B. D. Field, A. C. Fusco, and J. G. Wilkinson (2002), Background ozone over the United States in summer: Origin, trend, and contribution to pollution episodes, *J. Geophys. Res.*, *107*(D15), 4275, doi:10.1029/2001JD000982.
- Fiore, A. M., *et al.* (2009), Multimodel estimates of intercontinental source-receptor relationships for ozone pollution, *J. Geophys. Res.*, *114*, D04301, doi:10.1029/2008JD010816.
- Fishman, J., S. Solomon, and P. J. Crutzen (1979), Observational and theoretical evidence in support of a significant in-situ photochemical source of tropospheric ozone, *Tellus*, *31*, 432-446.
- Fishman J., A. E. Wozniak, and J. K. Creilson (2003), Global distribution of tropospheric ozone from satellite measurements using the empirically corrected tropospheric ozone residual technique: Identification of the regional aspects of air pollution, *Atmos. Chem. & Phys.*, *3*, 893 – 907.
- Forster, P.M. de F., and K. P. Shine (1997), Radiative forcing and temperature trends from stratospheric ozone changes, *J. Geophys. Res.*, *102*, 10,841–10,855,
- Forster, P., V. Ramaswamy, P. Artaxo, T. Berntsen, R. Betts, D.W. Fahey, J. Haywood, J. Lean, D.C. Lowe, G. Myhre, J. Nganga, R. Prinn, G. Raga, M. Schulz and R. Van Dorland (2007), Changes in Atmospheric Constituents and in Radiative Forcing. In: *Climate Change 2007: The Physical Science Basis*. Contribution of Working Group I to the Fourth Assessment Report of

the Intergovernmental Panel on Climate Change [Solomon, S., D. Qin, M. Manning, Z. Chen, M. Marquis, K.B. Averyt, M. Tignor and H.L. Miller (eds.)], *Cambridge University Press*, Cambridge, United Kingdom and New York, NY, USA.

Francey, R.J., et al. (1999), A history of $\delta^{13}\text{C}$ in atmospheric CH_4 from the Cape Grim Air Archive and Antarctic firn air, *J. Geophys. Res.*, *104 (D19)*, 23633–23643.

Frankenberg, C., J. Meirink, M. Van Weele, U. Platt, and T. Wagner (2005), Assessing methane emissions from global space-borne observations, *Science*, *308*, 1010–1014.

Fuhrer, J., L. Skarbi, M. R. Ashmore (1997), Critical levels for ozone effects on vegetation in Europe, *Environ. Poll.* *97*, 91e106.

Fujimoto, T., T. Sato, K. Nagai, T. Nakano, M. Shitamichi, Y. Kamata, S. Miyauchi, K. Akagi, and T. Sasaki (2004), Further evaluation and improvements of Japanese KC-Ozonesonde through JOSIE-2000, paper presented at Quadrennial Ozone Symposium 2004, *Int. Ozone Comm.*, Kos, Greece.

Ganguly N. D., and Chris Tzanis (2011), Study of Stratosphere-Troposphere exchange events of ozone in India and Greece using ozonesonde ascents, *Meteorol. Appl.* *18*: 467 – 474.

Ganzeveld, L. and J. Lelieveld (1995): Dry deposition parameterization in a chemistry general circulation model and its influence on the distribution of reactive trace gases, *J. Geophys. Res.*, *100*, 20 999–21 012.

- Gauss, M., et al. (2006), Radiative forcing since preindustrial times due to ozone changes in the troposphere and the lower stratosphere, *Atmos. Chem. Phys.*, *6*, 575–599.
- Gautam, R., Z. Liu, R.P. Singh, N.C. Hsu (2009), Two contrasting dust-dominant periods over India observed from MODIS and CALIPSO data, *Geophys. Res. Lett.*, *36*, p. L06813 doi: 10.1029/2008GL036967.
- Ghude, S. D., et al. (2008a), Ozone in ambient air at a tropical megacity, Delhi: characteristics, trends and cumulative ozone exposure indices, *J. Atmos. Chem.*, *60*: 237-252, DOI 10.1007/s10874-0099119-4.
- Ghude, S. D., S. Fadnavis, G. Beig, S. D. Polade and R. J. van der A (2008b), Detection of surface emissions hot spots, trends, and seasonal cycle from satellite-retrieved NO₂ over India, *J. Geophys. Res.*, *113*, D20305, doi: 10.1029/2007JD009615.
- Giglio, L., J. D. Kendall, and R. Mack (2003), A multi-year active fire dataset for the tropics derived from the TRMM VIRS, *Int. J. Remote Sens.*, *24*, 4505–4525, doi:10.1080/0143116031000070283.
- Giles, D. M., et al. (2011), Aerosol properties over the Indo-Gangetic Plain: A mesoscale perspective from the TIGERZ experiment, *J. Geophys. Res.*, *116*, D18203, doi:10.1029/2011JD015809.
- Goroshi, S. K., R. P. Singh, S. Panigrahy, J. S. Parihar (2011), Analysis of Seasonal Variability of Vegetation and Methane Concentration over India using SPOT-VEGETATION and ENVISAT-SCIAMACHY Data, *J. Indian Soc*

Remote Sens (September 2011) 39(3):315–321, DOI 10.1007/s12524-011-0097-z.

Grell, G. A., S. E. Peckham, S. A. McKeen, R. Schmitz, and G. Frost (2005), Fully coupled “online” chemistry within the WRF model, *Atmos. Environ.*, *39*, 6957– 6975.

Guenther, A., T. Karl, P. Harley, C. Wiedinmyer, P. I. Palmer, and C. Geron (2006), Estimates of global terrestrial isoprene emissions using MEGAN (Model of Emissions of Gases and Aerosols from Nature), *Atmos. Chem. Phys.*, *6*, 3181–3210, doi:10.5194/acp-6-3181-2006.

Gupta, S., S. Lal, S. Venkataramani, T. A. Rajesh and Y. B. Acharya (2007), Variability in the vertical distribution of ozone over a subtropical site in India during a winter month, *J. Atmos Sol-Terr Phys (UK)*, *69*, 1502.

Gurney, K. R., Rachel M. Law, A. Scott Denning, Peter J. Rayner, David Baker, Philippe Bousquet, Lori Bruhwiler, Yu-Han Chen, Philippe Ciais, Songmiao Fan, Inez Y. Fung, Manuel Gloor, Martin Heimann, Kaz Higuchi, Jasmin John, Takashi Maki, Shamil Maksyutov, Ken Masarie, Philippe Peylin, Michael Prather, Bernard C. Pak, James Randerson, Jorge Sarmiento, Shoichi Taguchi, Taro Takahashi & Chiu-Wai Yuen (2002), Towards robust regional estimates of CO₂ sources and sinks using atmospheric transport models, *Nature*, *415*, 626-630, doi:10.1038/415626a.

Haagenson, P. L., M. A. Shapiro, P. Middleton, A. R. Laird (1981), A case study relating high ground level ozone to enhanced photochemistry and isentropic transport from the stratosphere, *J. Geophys. Res.*, *86*, 5231-5237.

Hack, J. J., B. A. Boville, J. T. Kiehl, P. J. Rasch, and D. L. Williamson (1994): Climate statistics from the National Center for Atmospheric Research community climate model CCM2, *J. Geophys. Res.*, 99, 20 785–20 813.

Hansen, J., M. Sato, R. Ruedy, A. Lacis, V. Oinas (2000), Global warming in the twenty-first century: An alternative scenario. *Proc Natl Acad Sci USA*, vol. 97 no. 18 9875-9880, doi: 10.1073/pnas.170278997 PNAS.

Hauglustaine, D.A., and G.P. Brasseur (2001), Evolution of tropospheric ozone under anthropogenic activities and associated radiative forcing of climate, *J. Geophys. Res.*, 106 (D23), 32337–32360, doi:10.1029/2001JD900175.

Heard, D. E. (2006), Analytical Techniques for Atmospheric Measurement, *Blackwell Publishing*, ISBN-13: 978–1–4051–2357–0.

HEMISPHERIC TRANSPORT OF AIR POLLUTION (HTAP) PART A: OZONE AND PARTICULATE MATTER (2010), *AIR POLLUTION STUDIES No. 17*, Edited by Frank Dentener, Terry Keating, and Hajime Akimoto, Prepared by the Task Force on Hemispheric Transport of Air Pollution acting within the framework of the Convention on Long-range Transboundary Air Pollution, UNITED NATIONS, New York and Geneva.

Holton, R. James., Peter, H. Haynes, Michael, E. McIntyre, Anne, R. Douglass, Richard, B. Rood and Leonhard Pfister (1995), Stratosphere-Troposphere Exchange, *Reviews of Geophys.* 33, 4, pages 403-409.

Holtlag, A. A. M., and B. A. Boville (1993): Local versus nonlocal boundary-layer diffusion in a global climate model, *J. Climate*, 6, 1825–1842.

Holton, J. R. and J. Lelieveld, (1996), Stratosphere-troposphere exchange and its role in the budget of tropospheric ozone, in: *Clouds, Chemistry and Climate*,

edited by: Crutzen, P. J. and Ramanathan, V., NATO ASI Series, Springer-Verlag, Berlin, pp. 173–190.

Houghton, R.A. (2003), Revised estimates of the annual net flux of carbon to the atmosphere from changes in land use and land management, *Tellus*, 55B, 378–390.

Hudman, R. C., D. J. Jacob, O. R. Cooper (2004), Ozone production in transpacific Asian pollution plumes and implications for ozone air quality in California, *J. Geophys. Res.*, 109, D23S10.

Hurst, D. F., E. G. Hall, A. F. Jordan, L. M. Miloshevich, D. N. Whiteman, T. Leblanc, D. Walsh, H. Vömel, and S. J. Oltmans (2011), Comparisons of temperature, pressure and humidity measurements by balloon-borne radiosondes and frost point hygrometers during MOHAVE-2009, *Atmos. Meas. Tech. Discuss.*, 4, 4357-4401, doi: 10.5194/amtd-4-4357-2011.

Hwang, S.H., J. Kim, and G.-R. Cho (2007), Observation of secondary ozone peaks near the tropopause over the Korean peninsula associated with stratosphere-troposphere exchange, *J. Geophys. Res.*, 112, D16305, doi:10.1029/2006JD007978.

Jacob, D. J. (1999a), Effect of rising Asian emissions on surface ozone in the United States, *Geophys. Res. Lett.*, 26, NO. 14, 2175-2178.

Jacob, D. J. (1999b), Introduction to Atmospheric Chemistry. *Princeton University Press*.

Jaffe, D. et al. (1999), Transport of Asian air pollution to North America, *Geophys. Res. Lett.*, 26, 711-714.

- Jaffe, D., H. Price, D. Parrish, A. Goldstein, and J. Harris (2003), Increasing background ozone during spring on the west coast of North America, *Geophys. Res. Lett.*, 30, 1613, doi:10.1029/2003GL017024, 12.
- Jain, S. L., B. C. Arya, Arun Kumar, Sachin D. Ghude, and P. S. Kulkarni (2005), Observational study of surface ozone at New Delhi, India, *Int. J. Remote Sens.*, 26(16), 3515-3524.
- Janjic, J. I. (2002), Nonsingular Implementation of the Mellor-Yamada Level 2.5 Scheme in the NCEP Meso model, *NCEP Office Note*, 437, 61pp.
- Jethva, H., S. K. Satheesh, and J. Srinivasan (2005), Seasonal variability of aerosols over the Indo-Gangetic basin, *J. Geophys. Res.*, 100, D21204, doi: 10.1029/2005JD005938.
- Justice, C. O., L. Giglio, S. Korontzi, J. Owens, J. T. Morisette, D. Roy, J. Descloitres, S. Alleaume, F. Petitcolin, Y. Kaufman (2002), The MODIS fire products. *Remote Sens. of Environ*, 83 (2002), 244-262.
- Kai, F. M., Stanley C. Tyler, James T. Randerson, and Donald R. Blake (2011), Reduced methane growth rate explained by decreased Northern Hemisphere microbial sources, *Nature*, 476, 194–197, doi:10.1038/nature10259.
- Kain, J. S. (2004), The Kain-Fritsch convective parameterization: An update, *J. Appl. Meteorol.*, 43, 25 170–181.
- Kanaya, Y., P. Pochanart, Y. Liu, J. Li, H. Tanimoto, S. Kato, J. Suthawaree, S. Inomata, F. Taketani, K. Okuzawa, K. Kawamura, H. Akimoto, and Z. F. Wang (2009), Rates and regimes of photochemical ozone production over Central East China in June 2006: a box model analysis using comprehensive measurements of ozone precursors, *Atmos. Chem. & Phys.*, 9, 7711–7723.

- Kar, J. et al. (2010), Wintertime pollution over the Eastern Indo-Gangetic Plains as observed from MOPITT, CALIPSO and tropospheric ozone residual data, *Atmos. Chem. & Phys.*, *10*, 12273-12283.
- Kasting, J. F., and H. B. Singh (1986), Nonmethane hydrocarbons in the troposphere: Impact on the odd hydrogen and odd nitrogen chemistry, *J. Geophys. Res.*, *91(D12)*, 13239–13256, doi:10.1029/JD091iD12p13239.
- Kaufman, Y. J., et al. (1998), Potential global fire monitoring from EOSMODIS, *J. Geophys. Res.*, *103*, 32,215–32,238, doi:10.1029/98JD01644.
- Keeling C. D., R. B. Bacastow, A.E. Bainbridge, C.A. Ekdahl, P.R. Guenther, and L.S. Waterman (1976), Atmospheric carbon dioxide variations at Mauna Loa Observatory, Hawaii, *Tellus*, *vol. 28*, 538-551.
- Keeling, C.D., T.P. Whorf, M. Wahlen, and J. van der Plicht (1995), Interannual extremes in the rate of rise of atmospheric carbon dioxide since 1980, *Nature*, *375*, 666–670.
- Keeling, C.D., and T.P. Whorf (2005), Atmospheric CO₂ records from sites in the SIO air sampling network. In: Trends: A Compendium of Data on Global Change. Carbon Dioxide Information Analysis Center, Oak Ridge National Laboratory, U.S. Department of Energy, *Oak Ridge, TN*, <http://cdiac.esd.ornl.gov/trends/co2/sio-keel-flask/sio-keel-flask.html>.
- Keppler, F., J. T. G. Hamilton, M. Brass, and T. Röckmann (2006), Methane emissions from terrestrial plants under aerobic conditions, *Nature*, *439*, 187–191, doi:10.1038/nature04420.

- Kerr, J. B., H. Fast, C. T. McElroy, S. J. Oltmans, J. A. Lathrop, E. Kyro, A. Paukkunen, H. Claude, U. Kohler, C. R. Sreedharan, T. Takao and Y., Tsukagoshi (1994), The 1991 WMO International Ozonesonde Intercomparison at Vanscoy, Canada, *Atm. Ocean*, 32, 685-716.
- Khalil, M. A. K., and R. A. Rasmussen (1988), Carbon monoxide in the Earth's atmosphere: Indications of a global increase, *Nature*, 332, 242-245.
- Khalil, M. A. K., and R. A. Rasmussen (1994), Global decrease in atmospheric carbon monoxide concentration. *Nature*, 370, 639-641.
- Kleinman, L. I. (1986), Photochemical formation of peroxides in the boundary layer, *J. Geophys. Res.*, 91, 10,889-10,904.
- Kleinman, L. et al. (1994), Ozone formation at a rural site in the southern United States, *J. Geophys. Res.*, 99, 3469-3482.
- Kobayashi, J., and Y. Toyama (1966), On various methods of measuring the vertical distribution of atmospheric ozone (III)—Carbon iodide type chemical ozonesonde, *Pap. Meteorol. Geophys.*, 17, 113– 126.
- Komhyr. W. D. (1969), Electrochemical concentration cells for gas analysis, *Ann. Geoph.*, 25, 203-210.
- Komhyr, W.D., R. A. Barnes, G. B. Brothers, J. A. Lathrop, & D. P. Opperman (1995), Electrochemical concentration cell ozonesonde performance evaluation during STOIC 1989, *J. Geophys. Res.*, 100 (D5), 9231–9244.
- Krupa, S. V. and M. Nosal (1989), Effects of Ozone on Agricultural crops, *Studies in Environ. Sci.*, Vol 35, Pages 229–238.

- Kummerow, C., W. Barnes, T. Kozu, J. Shiue, and J. Simpson (1998), The Tropical Rainfall Measuring Mission (TRMM) sensor package. *J. Atmos. Oceanic Technol.*, *15*, 809–816.
- Kumar, R., M. Naja, S. Venkataramani and O. Wild (2010), Variations in surface ozone at Nainital, a high altitude site in the Central Himalayas, *J. Geophys. Res.*, *115*, D16302, doi: 10.1029/2009JD013715.
- Kumar, R., M. Naja, S. K. Satheesh, N. Ojha, H. Joshi, T. Sarangi, P. Pant, U. C. Dumka, P. Hegde, and S. Venkataramani (2011), Influences of the springtime northern Indian biomass burning over the central Himalayas, *J. Geophys. Res.*, *116*, D19302, doi: 10.1029/2010JD015509.
- Kumar, R., M. Naja, G. G. Pfister, M. C. Barth, and G. P. Brasseur (2012a), Simulations over South Asia using the Weather Research and Forecasting model with Chemistry (WRF-Chem): set-up and meteorological evaluation, *Geosci. Model Dev.*, *5*, 321-343, doi: 10.5194/gmd-5-321-343-2012.
- Kumar, R., M. Naja, G. G. Pfister, M. C. Barth, C. Wiedinmyer, and G. P. Brasseur (2012b), Simulations over South Asia using the Weather Research and Forecasting model with Chemistry (WRF-Chem): chemistry evaluation and initial results, *Geosci. Model Dev.*, *5*, 619-648, doi: 10.5194/gmd-5-619-2012.
- Kunhikrishnan, T., Mark G. Lawrence, Rolf von Kuhlmann, Andreas Richter, Annette Ladstatter-Weißenmayer, John P. Burrows (2004), Analysis of tropospheric NO_x over Asia using the model of atmospheric transport and chemistry (MATCH-MPIC) and GOME-satellite observations, *Atmos. Environ.*, *38*, 581–596.

- Lacis, A. A., D. J. Wuebbles, and J. A. Logan (1990), Radiative forcing of climate by changes in the vertical distribution of ozone. *J. Geophys. Res.*, *95*, 9971-9981.
- Lal, S., M. Naja, A. Jayaraman (1998), Ozone in the marine boundary layer over the tropical Indian Ocean, *J. Geophys. Res.*, *103*, 18907–18917.
- Lal, S., M. Naja, and B. H. Subbaraya (2000), Seasonal variations in surface ozone and its precursors over an urban site in India, *Atmos. Environ.*, *34*, 2713-2724, doi: 10.1016/S1352-2310(99)00510-5.
- Lal, S., and M. G. Lawrence (2001), Elevated mixing ratios of surface ozone over the Arabian Sea, *Geophys. Res. Lett.*, *28*(8), 1487-1490.
- Lal, S., L. K. Sahu and S. Venkataramani (2007), Impact of transport from the surrounding continental regions on the distributions of ozone and related trace gases over the Bay of Bengal during February 2003, *J. Geophys. Res.*, *112*, D14302, doi: 10.1029/2006JD008023.
- Lamarque, J. F., and P. G. Hess (1994), Cross-Tropopause Mass Exchange and Potential Vorticity Budget in a simulated Tropopause Folding, *J. Atmos. Sci.*, *51*, 2246-2269.
- Lamarque, J. F., et al. (2005), Tropospheric ozone evolution between 1890 and 1990, *J. Geophys. Res.*, *110*, D08304, doi: 10.1029/2004JD005537.
- Landgraf, J. and P. J. Crutzen (1998): An efficient method for online calculations of photolysis and heating rates, *J. Atmos. Sci.*, *55*, 863–878.
- Lawrence, M. G. and P. J. Crutzen (1998): The impact of cloud particle gravitational settling on soluble trace gas distributions, *Tellus*, *50B*, 263–289.

- Lawrence, M. G., P. J. Crutzen, P. J. Rasch, B. E. Eaton, and N. M. Mahowald, N. M. (1999), A model for studies of tropospheric photochemistry: Description, global distributions, and evaluation, *J. Geophys. Res.*, *104*, 26 245–26 277.
- Lawrence, M. G., P. J. Rasch, R. von Kuhlmann, J. Williams, H. Fischer, M. de Reus, J. Lelieveld, P. J. Crutzen, M. Schultz, P. Stier, H. Huntrieser, J. Heland, A. Stohl, C. Forster, H. Elbern, H. Jakobs, and R. R. Dickerson (2003a), Global chemical weather forecasts for field campaign planning: predictions and observations of large scale features during MINOS, CONTRACE, and INDOEX. *Atmos. Chem. Phys.*, *3*, 267-289.
- Lawrence, M. G., R. von Kuhlmann, M. Salzmann, and P. J. Rasch (2003b), The balance of effects of deep convective mixing on tropospheric ozone, *Geophys. Res. Lett.*, *30*, 1940, doi:10.1029/2003GL017644.
- Lawrence, M. G., and J. Lelieveld (2010), Atmospheric pollutant outflow from southern Asia: a review, *Atmos. Chem. Phys.*, *10*, 11017-11096.
- Lefohn, A.S., H. Wernli, D. Shadwick, S. Limbach, S. J. Oltmans, M. Shapiro (2011), The importance of stratospheric-tropospheric transport in affecting surface ozone concentrations in the Western and Northern Tier of the United States, *Atmos. Environ.* *45*, 4845-4857.
- Lelieveld, J. et al. (2001), The Indian Ocean Experiment: Widespread Air Pollution From South and Southeast Asia, *Science*, *291*, 1031-1036.
- Lelieveld, J., J. van Aardenne, H. Fischer, M. de Reus, J. Williams, and P. Winkler (2004), Increasing Ozone over the Atlantic Ocean, *Science*, *304* (5676), 1483-1487, doi:10.1126/science.1096777.

- Lemoine, R. (2004), Secondary maxima in ozone profiles, *Atmos. Chem. Phys.*, *4*, 1085-1096, doi:10.5194/acp-4-1085-2004.
- Le Treut, H., R. Somerville, U. Cubasch, Y. Ding, C. Mauritzen, A. Mokssit, T. Peterson and M. Prather (2007), Historical Overview of Climate Change. In: *Climate Change 2007: The Physical Science Basis. Contribution of Working Group I to the Fourth Assessment Report of the Intergovernmental Panel on Climate Change* [Solomon, S., D. Qin, M. Manning, Z. Chen, M. Marquis, K.B. Averyt, M. Tignor and H.L. Miller (eds.)]. Cambridge University Press, Cambridge, United Kingdom and New York, NY, USA.
- Levy, H. II (1971), Normal Atmosphere: large radical and formaldehyde concentrations predicted, *Science*, *173*, 141-143.
- Levy, H. II, J. D. Mahlman, W. J. Moxim, and S. C. Liu (1985), Tropospheric ozone: The role of transport, *J. Geophys. Res.*, *90*, 3753-3772.
- Li, Q. B., D. J. Jacob, R. M. Yantosca, J. W. Munger, and D. D. Parrish (2004), Export of NO_y from the North American boundary layer: Reconciling aircraft observations and global model budgets, *J. Geophys. Res.*, *109*, D02313, doi: 10.1029/2003JD004086.
- Lin, X., M. Trainer and S. C. Liu (1988), On the nonlinearity of tropospheric ozone production, *J. Geophys. Res.*, *93*, D12, 15879-15888.
- Lin, J.T., M. B. McElroy, and K. F. Boersm (2010), Constraint of anthropogenic NO_x emissions in China from different sectors: a new methodology using multiple satellite retrievals, *Atmos. Chem. Phys.*, *10*, 63–78, doi:10.5194/acp-10-63-2010.

- Liu, H., D. J. Jacob, I. Bey, R. M. Yantosca, B. N. Duncan, and G. W. Sachse (2003), Transport pathways for Asian pollution outflow over the Pacific: Interannual and seasonal variations, *J. Geophys. Res.*, *108(D20)*, 8786, doi:10.1029/2002JD003102.
- Ludwig, F.L. et al. (1977) The relation of oxidant levels to precursor emissions and meteorological features, Vol I: Analysis and findings, *Final Report, SRI Project 4432*, EPA Contract 68-02-2084, SRI International, Menlo Park, California, 153 pp.
- Logan, J. A. (1985), Tropospheric ozone: Seasonal behavior, trend and anthropogenic influences, *J. Geophys. Res.*, *90 (D6)*, 10463-10482.
- Logan, J. A. (1994), Trends in the vertical distribution of ozone: An analysis of ozonesonde data, *J. Geophys. Res.*, *99 (D12)*, 25553-25585.
- Logan, J. A. (1999), An analysis of ozonesonde data for the troposphere: Recommendations for testing 3-D models and development of a gridded climatology for tropospheric ozone, *J. Geophys. Res.*, *104*, NO. D13, PAGES 16,115-16,149.
- Logan, J. A., et al (2012), Changes in ozone over Europe: Analysis of ozone measurements from sondes, regular aircraft (MOZAIC) and alpine surface sites, *J. Geophys. Res.*, *117*, D09301, doi: 10.1029/2011JD016952.
- Lowe, D.C., et al. (2004), Seasonal cycles of mixing ratio and ¹³C in atmospheric methane at Suva, Fiji, *J. Geophys. Res.*, *109*, D23308 doi:10.1029/2004JD005166.

- MacFarling Meure, C., et al. (2006), The Law Dome CO₂, CH₄ and N₂O ice core records extended to 2000 years BP, *Geophys. Res. Lett.*, *33*, L14810, doi:10.1029/2006GL026152.
- Machida, T., H. Matsueda, Y. Sawa, Y. Nakagawa, K. Hirotani, N. Kondo, K. Goto, T. Nakazawa, K. Ishikawa, and T. Ogawa (2008), Worldwide Measurements of Atmospheric CO₂ and Other Trace Gas Species Using Commercial Airlines, *J. Atmos. Oceanic. Technol.*, *25*, 1744–1754, doi:10.1175/2008JTECHA1082.1.
- Madronich, S., S. Flocke (1999), The role of solar radiation in atmospheric chemistry. In: Boule, P. (Ed.), *Handbook of Environmental Chemistry. Springer, Heidelberg*, pp. 1–26 (version 4.2 of the TUV model is available from the author).
- Madronich, S. (2006), Chemical evolution of gaseous air pollutants down-wind of tropical megacities: Mexico City Case Study, *Atmos. Environ.*, *40*, 6012–6018.
- Mandal, T. K., J. Y. N. Cho, P. B. Rao, A. R. Jain, S. K. Peshin, S. K. Srivastava, A. K. Bohra, and A. P. Mitra (1998), Stratosphere-troposphere ozone exchange observed with the Indian MST radar and a simultaneous balloon-borne ozonesonde, *Radio Sci.*, *33(4)*, 861–893, doi:10.1029/97RS03553.
- Manning, M.R., A. Gomez, and G.W. Brailsford (1997): Annex B11: The New Zealand CO₂ measurement programme. In: *Report of the Ninth WMO Meeting of Experts on Carbon Dioxide Concentration and Related Tracer Measurement Techniques*. WMO Global Atmosphere Watch No. 132; WMO

TD No. 952, Commonwealth Scientific and Industrial Research Organisation, Melbourne, pp. 120–123.

Marenco, A., H. Gouget, P. Nedelec, J. P. Pages, and F. Karcher (1994), Evidence of a long term increase in tropospheric ozone from Pic du Midi data series: Consequences: Positive radiative forcing, *J. Geophys. Res.*, *99*, 16617-16632.

Matsuda, K. et al. (2005), Ozone dry deposition above a tropical forest in the dry season in northern Thailand, *Atmos. Environ.*, *39* (14), 2571-2577.

Mauzerall, D. L., and X. P. Wang (2001), Protecting agricultural crops from the effects of tropospheric ozone exposure: Reconciling science and standard setting in the United States, Europe, and Asia, *Ann. Rev. Energy & Environ.*, *26*, 237– 268.

Mills, G., A. Buse, B. Gimeno, V. Bermejo, M. Holland, L. Emberson, and H. Pleijel (2007), A synthesis of AOT40-based response functions and critical levels of ozone for agricultural and horticultural crops, *Atmos. Environ.*, *41*, 2630– 2643.

Miyazaki, Y., et al. (2005), Contribution of particulate nitrate to airborne measurements of total reactive nitrogen, *J. Geophys. Res.*, *110*, 1–11, 2005, doi: 10.1029/2004JD005502.

Mlawer, E. J., S. Taubman, P. Brown, M. Iacono, and S. Clough (1997), Radiative transfer for inhomogeneous atmosphere: RRTM, a validated correlated-k model for the long-wave, *J. Geophys. Res.*, *102*, 16663–16682, doi: 10.1029/97JD00237.

- Nair, P. R., et al. (2002), Temporal variations in surface ozone at Thumba (8.6°N, 77°E): A tropical coastal site in India, *Atmos. Environ.*, 36, 603–610, doi:10.1016/S1352-2310(01)00527-1.
- Naja, M. and S. Lal (1996), Changes in surface ozone amount and its diurnal and seasonal patterns, from 1954-55 to 1991-93 measured at Ahmedabad (23 N), India, *Geophys. Res. Lett.*, 231(1), 81-84, doi: 10.1029/95GL03589.
- Naja, M., and S. Lal (2002), Surface ozone and precursor gases at Gadanki (13.5° N, 79.2° E), tropical rural site in India, *J. Geophys. Res.*, 107(D14), doi: 10.1029/2001JD000357.
- Naja, M., H. Akimoto, and J. Staehelin (2003a), Ozone in background and photochemically aged air over central Europe: Analysis of long-term ozonesonde data from Hohenpeissenberg and Payrene, *J. Geophys. Res.*, 108(D2), 4063, doi: 10.1029/2002JD002477.
- Naja, M., D. Chand, L. Sahu and S. Lal (2004), Trace gases over marine regions around India, *Indian Journal of Marine Sciences*, 33(1), 95-106.
- Nassar, R., et al. (2008), Validation of Tropospheric Emission Spectrometer (TES) nadir ozone profiles using ozonesonde measurements, *J. Geophys. Res.*, 113, D15S17, doi:10.1029/2007JD008819.
- Novelli, P. C., K. A. Masarie, P. M. Lang, B. D. Hall, R. C. Myers, and J. W. Elkins (2003), Reanalysis of tropospheric CO trends: Effects of the 1997–1998 wildfires, *J. Geophys. Res.*, 108, 4464, doi:10.1029/2002JD003031, D15.
- O’Doherty, S., et al. (2004), Rapid growth of hydrofluorocarbon 134a and hydrochlorofluorocarbons 141b, 142b, and 22 from Advanced Global Atmospheric Gases Experiment (AGAGE) observations at Cape Grim,

Tasmania, and Mace Head, Ireland, *J. Geophys. Res.*, *109*, D06310, doi:10.1029/2003JD004277.

Ohara, T., H. Akimoto, J. Kurokawa, N. Horri, K. Yamaji, X. Yan and T. Hayasaka (2007), An Asian emission inventory of anthropogenic emission sources for the period 1980-2020, *Atmos. Chem. & Phys.*, *7*, 4419-4444.

Ojha, N., M. Naja, K. P. Singh, T. Sarangi, R. Kumar, S. Lal, M. G. Lawrence, T. M. Butler, and H. C. Chandola (2012), Variabilities in ozone at a semi-urban site in the Indo-Gangetic Plain region: Association with the meteorology and regional processes, *J. Geophys. Res.*, *117*, D20301, doi: 10.1029/2012JD017716.

Olivier, J. G. J., J. P. J. Bloos, J. J. M. Berdowski, A. J. H. Visschedijk, and A. F. Bouwman (1999), A 1990 global emission inventory of anthropogenic sources of carbon monoxide on $1^{\circ} \times 1^{\circ}$ developed in the framework of EDGAR/GEIA, *Chemosphere: Global Change Science*, *1*, 1–17.

Oltmans, S. J. (1981), Surface ozone measurements in clean air, *J. Geophys. Res.*, *86*, 1174-1180.

Oltmans, S.J., et al. (2006), Long-term changes in tropospheric ozone, *Atmos. Environ.*, *40*, 3156–3173.

Park, M., W. J. Randel, A. Gettelman, S. T. Massie and J. H. Jiang (2007), Transport above the Asian summer monsoon anticyclone inferred from Aura Microwave Limb Sounder tracers, *J. Geophys. Res.*, *112*, D16309, doi: 10.1029/2006JD008294.

- Parrish, D.D., et al. (2004), Changes in the photochemical environment of the temperate North Pacific troposphere in response to increased Asian emissions, *J. Geophys. Res.*, *109*, D23S18, doi:10.1029/2004JD004978.
- Parrish, D. D., D. B. Millet, and A. H. Goldstein (2009), Increasing ozone in marine boundary layer inflow at the west coasts of North America and Europe, *Atmos. Chem. Phys.*, *9*, 1303-1323, 2009.
- Parrish, D. D., K. S. Law, J. Staehelin, R. Derwent, O. R. Cooper, H. Tanimoto, A. Volz-Thomas, S. Gilge, H. E. Scheel, M. Steinbacher, and E. Chan (2012), Long-term changes in lower tropospheric baseline ozone concentrations at northern mid-latitudes, *Atmos. Chem. Phys. Discuss*, *12*, 13881-13931.
- Patra, P. K., S. Maksyutov, Y. Sasano, H. Nakajima, G. Inoue, and T. Nakazawa, T. (2003), An evaluation of CO₂ observations with Solar Occultation FTS for Inclined-Orbit Satellite sensor for surface source inversion, *J. Geophys. Res.*, *108(D24)*, 4759, doi:10.1029/2003JD003661, 2003.
- Patra, P. K., et al. (2006), Sensitivity of inverse estimation of annual mean CO₂ sources and sinks to ocean-only sites versus all-sites observational networks, *Geophys. Res. Lett.*, *33*, L05814, doi:10.1029/2005GL025403.
- Patra, P. K., et al. (2011), Carbon balance of South Asia constrained by passenger aircraft CO₂ measurements, *Atmos. Chem. Phys.*, *11*, 4163-4175, doi: 10.5194/acp-11-4163-2011.
- Pitts, B. J. F. and J. N. Pitts (2000), Chemistry of the Upper and Lower Atmosphere: Theory , Experiments and Applications, *Academic Press*, 24-28, Oval Road, London, UK.

- Pio, C. A., M. S. Feliciano, A. T. Vermeulen, E. C. Sousa (2000), Seasonal variability of ozone dry deposition under southern European climate conditions, in Portugal, *Atmos. Environ.*, 34 (2), 195-205.
- Prather, M. J., et al. (2001), Atmospheric chemistry and greenhouse gases. In: *Climate Change 2001: The Scientific Basis. Contribution of Working Group I to the Third Assessment Report of the Intergovernmental Panel on Climate Change* [Houghton, J.T., et al. (eds.)]. Cambridge University Press, Cambridge, United Kingdom and New York, NY, USA, pp. 239–287.
- Prinn, R.G., R.F. Weiss, P.J. Fraser, P.G. Simmonds, D.M. Cunnold, F.N. Alyea, S. O'Doherty, P. Salameh, B.R. Miller, J. Huang, R.H.J. Wang, D.E. Hartley, C. Harth, L.P. Steele, G. Sturrock, P.M. Midgley, and A. McCulloch (2000), A History of Chemically and Radiatively Important Gases in Air deduced from ALE/GAGE/AGAGE, *J. of Geophys. Res.*, 105 (D14), 17,751-17,792.
- Ramanathan, V., R. J. Cicerone, H. B. Singh, and J. T. Kiehl (1985), Trace gas trends and their potential role in climate change, *J. Geophys. Res.*, 90, 5547-5566.
- Ramaswamy, V., et al. (2001), Radiative forcing of climate change. In: *Climate Change 2001: The Scientific Basis. Contribution of Working Group I to the Third Assessment Report of the Intergovernmental Panel on Climate Change* [Houghton, J.T., et al. (eds.)]. Cambridge University Press, Cambridge, United Kingdom and New York, NY, USA, pp. 349–416.

- Randel, W. J., D. J. Seidel, and L. L. Pan (2007), Observational characteristics of double tropopauses, *J. Geophys. Res.*, *112*, D07309, doi:10.1029/2006JD007904.
- Rao, S. T., Ku, Jia-Yeaong., S. Berman, K. Zhang, H. Mao (2003), Summertime characteristics of the atmospheric boundary layer and relationships to ozone levels over the eastern United States, *Pure Appl. Geophys.*, *160*, 21-55.
- Rasch, P. J., N. M. Mahowald, and B. E. Eaton (1997): Representations of transport, convection and the hydrologic cycle in chemical transport models: Implications for the modeling of short lived and soluble species, *J. Geophys. Res.*, *102*, 28 127–28 138.
- Rasch, P. J. and M. G. Lawrence (1998): Recent developments in transport methods at NCAR, Tech. Rep. 265, *Max-Planck-Institut für Meteorologie, Bundesstrasse 55*, 20146, Hamburg, Germany.
- Rasch, P. J. and J. E. Kristjansson (1998): A comparison of the CCM3 model climate using diagnosed and predicted condensate parameterizations, *J. Climate*, *11*, 1587–1614.
- Rayner, P. J., and D. M. O'Brien (2001), The utility of remotely sensed CO₂ concentration data in surface source inversions, *Geophys. Res. Lett.*, *28*, NO.1, PAGES 175-178.
- Reddy, R. R. et al. (2008), Measurements of surface ozone at semi-arid site Anantapur (14.62° N, 77.65° E, 331 m asl) in India, *J. Atmos. Chem.*, *59*:47-59, doi: 10.1007/s10874-008-9094-1.
- Reed, R. J. (1955), A study of a characteristic type of upper-level frontogenesis, *J. Atmos. Sci.*, *12*(3), 226–237.

Regener, E., Ozonschicht und Atmosphärische Turbulenz, Ber. deut. Wetterdienstes US-zone 11, 45.

Reichler, T., M. Dameris, and R. Sausen (2003), Determining the tropopause height from gridded data, *Geophys. Res. Lett.*, 30, 2042, doi: 10.1029/2003GL018240, 20.

Richter, Andreas, J. P. Burrows, H. Nüß, C. Granier, U. Niemeier (2005), Increase in tropospheric nitrogen dioxide over China observed from space, *Nature* 437, 129-132.

Rinsland, C., M. Luo, J. Logan, R. Beer, H. Worden, S. Kulawik, D. Rider, G. Osterman, M. Gunson, A. Eldering, A. Goldman, M. Shephard, S. Clough, C. Rodgers, M. Lampel, and L. Chiou, L. (2006), Nadir measurements of carbon monoxide distributions by the Tropospheric Emission Spectrometer instrument onboard the Aura Spacecraft: Overview of analysis approach and examples of initial results, *Geophys. Res. Lett.* 33(22): doi: 10.1029/2006GL027000. issn: 0094-8276.

Royal Society (2008), Ground-level ozone in the 21st century: future trends, impacts and policy implications, *RS Policy document 15/08*, ISBN: 978-0-85403-713-1.

Roy, S. D., G. Beig, and Sachin D. Ghude (2009): Exposure-plant response of ambient ozone over the tropical Indian region, *Atmos. Chem. Phys.*, 9, 5253-5260, doi:10.5194/acp-9-5253-2009.

Sagar, R., B. Kumar, U. C. Dumka, K. Krishna Moorthy, and P. Pant (2004), Characteristics of aerosol optical depths over Manora Peak: A high-altitude

- station in the central Himalayas, *J. Geophys. Res.*, *109*, D06207, doi:10.1029/2003JD003954.
- Sahu, L. K., and S. Lal (2006), Changes in surface ozone levels due to convective downdrafts over the Bay of Bengal, *Geophys. Res. Lett.*, *33*, L10807, doi:10.1029/2006GL025994.
- Saigusa et al. (2005) Inter-annual variability of carbon budget components in a cool-temperate deciduous forest in Japan (Takayama, AsiaFlux), *Phyton* *45*: 81-88.
- Saraf, N., and G. Beig (2004), Long-term trends in tropospheric ozone over the Indian tropical region, *Geophys. Res. Lett.*, *31*, L05101, doi:10.1029/2003GL018516.
- Schmidt, T., S. Heise, J. Wickert, G. Beyerle, and C. Reigber, C. (2005), GPS radio occultation with CHAMP and SAC-C: global monitoring of thermal tropopause parameters, *Atmos. Chem. Phys.*, *5*, 1473–1488, doi:10.5194/acp-5-1473-2005.
- Schmitt, A. and B. Brunner (1997), Emissions from aviation and their development over time, in: Pollutants from air traffic—results of atmospheric research 1992-1997, Final Report on the BMBF Verbundprogramm “Schadstoffe in der Luftfahrt”, *Tech. report, DLR-Mitteilung 97-04*, pp. 1–301.
- Schwarzkopf, M. D., and V. Ramaswamy (1993), Radiative forcing due to ozone in the 1980s: Dependence on altitude of ozone change, *Geophys. Res. Lett.*, *20*(3), 205–208, doi:10.1029/93GL00209.

- Seinfeld, J. H., and S. N. Pandis (2006), Atmospheric Chemistry and Physics: From Air Pollution to Climate Change, *A Wiley-Interscience Publication*, New Jersey.
- Shapiro, M. A. (1980), Turbulent Mixing within Tropopause Folds as a Mechanism for the Exchange of Chemical Constituents between the Stratosphere and Troposphere. *J. Atmos. Sci.*, *37*, 994–1004.
- Sillman, S., J. A. Logan, and S. C. Wofsy (1990), The sensitivity of ozone to nitrogen oxides and hydrocarbons in regional ozone episodes, *J. Geophys. Res.*, *95*, 1837-1851.
- Sillman, S. (1991), A numerical solution to the equations of tropospheric chemistry based on analysis of sources and sinks of odd hydrogen, *J. Geophys. Res.*, *96*, 20,735-20,744.
- Sillman, S. (1995), The use of NO_y, H₂O₂ and HNO₃ as indicators for O₃-NO_x-VOC sensitivity in urban locations, *J. Geophys. Res.*, *100*, 14,175 –14,188.
- Sillman, S. (1999), The relation between ozone, NO_x and hydrocarbons in urban and polluted rural environments, *Atmos. Environ.*, *33*, 1821-1845.
- Simmonds, P. G., R. G. Derwent, A. L. Manninge, and G. Spain (2004), Significant growth in surface ozone at Mace Head, Ireland, 1987–2003, *Atmos. Environ.*, *38*, 4769–4778.
- Simpson, I.J., D.R. Blake, F.S. Rowland, and T.Y. Chen (2002), Implications of the recent fluctuations in the growth rate of tropospheric methane, *Geophys. Res. Lett.*, *29* (10), doi:10.1029/2001GL014521.

- Slingo, J. M. (1987), The development and verification of a cloud prediction scheme for the ECMWF model, *Q. J. R. Meteorol. Soc.*, 113, 899–927.
- Smit, H. G. J., *et al.* (2007), Assessment of the performance of ECC-ozonesondes under quasi-flight conditions in the environmental simulation chamber: Insights from the Juelich Ozone Sonde Intercomparison Experiment (JOSIE), *J. Geophys. Res.*, 112, D19306, doi: 10.1029/2006JD007308.
- SPARC Report N°1 (1998), Trends in the Vertical Distribution of Ozone, Edited by N. Harris, R. Hudson and C. Phillips, *WMO Ozone Research and Monitoring Project Report No. 43*.
- Sreedharan, C. R. (1968), An Indian electrochemical ozonesonde, *Journal of Physics E Sci. Inst. Sr 2* (1), 995–997.
- Srivastava S. (2010), Study of trace gases and related meteorological parameters in the lower atmosphere, *PH. D. thesis, M. S. D. University, Udaipur*.
- Srivastava S., S. Lal, S. Venkataramani, S. Gupta and Y. B. Acharya (2011), Vertical distribution of ozone in the lower troposphere over the Bay of Bengal and the Arabian sea during ICARB-2006: Effects of continental outflow, *J. Geophys. Res.*, 116, D13301, doi:10.1029/2010JD015298.
- Srivastava, S., S. Lal, M. Naja, S. Venkataramani, S. Gupta (2012), Influence of regional pollution and long range transport over western India: Analysis of ozonesonde data, *Atmos. Environ.*, 47, Pages 174-182, ISSN 1352-2310, 10.1016/j.atmosenv.2011.11.018.
- Staehelin, J., J. Thudium, R. Buehler, A. Volz-Thomas, and W. Graber (1994), Trends in surface ozone concentrations at Arosa (Switzerland), *Atmos. Environ.*, 28, 75– 87.

- Stamnes, K., S. Tsay, W. J. Wiscombe, K. Jayaweera (1988), Numerically stable algorithm for discrete-ordinate-method radiative transfer in multiple scattering and emitting layered media, *Applied Optics* 27, 2502–2509.
- Stevenson, D.S., et al. (2006), Multi-model ensemble of present-day and near-future tropospheric ozone, *J. Geophys. Res.*, 111, D8301, doi:10.1029/2005JD006338.
- Stockwell, R. W., F. Kirchner, M. Kuhn, and S. Seefeld (1997), A new mechanism for regional atmospheric chemistry modeling, *J. Geophys. Res.*, 102, 25847–25879.
- Stohl, A., N. Spichtinger-Rakowsky, P. Bonasoni, H. Feldmann, M. Memmesheimer, H. E. Scheel, T. Trickl, S. Hübener (2000), The influence of stratospheric intrusions on alpine ozone concentrations, *Atmos. Environ.* 34, 1323-1354.
- Stohl, A., et al. (2003), Stratosphere-troposphere exchange: A review, and what we have learned from STACCATO, *J. Geophys. Res.*, 108, 8516, doi:10.1029/2002JD002490, D12.
- Stohl, A., C. Forster, H. Huntrieser, H. Mannstein, W. W. McMillan, A. Petzold, H. Schlager, and B. Weinzierl (2007), Aircraft measurements over Europe of an air pollution plume from South-east Asia aerosol and chemical characterization, *Atmos. Chem. Phys.*, 7, 913–937, <http://www.atmos-chem-phys.net/7/913/2007/>.
- Suntharalingam, P., D. J. Jacob, P. I. Palmer, J. A. Logan, R. M. Yantosca, Y. Xiao, M. J. Evans, D. G. Streets, S. L. Vay, and G. W. Sachse (2004), Improved

- quantification of Chinese carbon fluxes using CO₂/CO correlations in Asian outflow, *J. Geophys. Res.*, *109*, D18S18, doi: 10.1029/2003JD004362.
- Tanimoto, H., T. Ohara, and I. Uno (2009), Asian anthropogenic emissions and decadal trends in springtime tropospheric ozone over Japan: 1998-2007, *Geophys. Res. Lett.*, *36*, L23802, doi: 10.1029/2009GL041382.
- Tarasick, D.W., et al. (2005), Changes in the vertical distribution of ozone over Canada from ozonesondes: 1980-2001. *J. Geophys. Res.*, *110*, D02304, doi: 10.1029/2004JD004643.
- Thompson, A. M. (1992), The oxidizing capacity of the Earth's atmosphere: Probable past and future changes, *Science*, *256*, 1157-1165.
- Thompson, G., R. M. Rasmussen, and K. Manning (2004), Explicit forecasts of winter precipitation using an improved bulk microphysics scheme, Part I (2004): Description and sensitivity analysis, *Mon. Weather Rev.*, *132*, 519–542.
- Thompson, A. M., Samuel J. Oltmans, David. W. Tarasick, Peter von der Gathen, Herman G.J. Smit, and Jacquelyn C. Witte (2011), Strategic ozone sounding networks: Review of design and accomplishments, *Atmos. Environ.* *45*, 2145-2163.
- Thoning, K.W., P. P. Tans, and W.D. Komhyr (1989), Atmospheric carbon dioxide at Mauna Loa Observatory 2. Analysis of the NOAA GMCC data, 1974-1985, *J. Geophys. Research*, *vol. 94*, 8549-8565.
- T. P. Marcy, D. W. Fahey, R. S. Gao, P. J. Popp, E. C. Richard, T. L. Thompson, K. H. Rosenlof, E. A. Ray, R. J. Salawitch, C. S. Atherton, D. J. Bergmann, B. A. Ridley, A. J. Weinheimer, M. Loewenstein, E. M. Weinstock, and M. J. Mahoney (2004), Quantifying Stratospheric Ozone in the Upper Troposphere

with in Situ Measurements of HCl, *Science*, 304 (5668), 261-265, doi:10.1126/science.1093418.

Trickl, T., H. Feldmann, H.J. Kanter, H.E. Scheel, M. Sprenger, A. Stohl, and H. Wernli (2010), Forecasted deep stratospheric intrusions over Central Europe: case studies and climatologies, *Atmos. Chem. Phys.*, 10, 499–524, doi:10.5194/acp-10-499-2010.

U. S. Environmental Protection Agency (U.S. EPA) (2010), Our Nation's Air: STATUS AND TRENDS THROUGH 2008, EPA-454/R-09-002 (<http://epa.gov/airtrends/reports.html>).

Umezawa, T., T. Machida, K. Ishijima, H. Matsueda, Y. Sawa, P. K. Patra, S. Aoki, and T. Nakazawa (2012), Carbon and hydrogen isotopic ratios of atmospheric methane in the upper troposphere over the Western Pacific, *Atmos. Chem. Phys.*, 12, 8095–8113.

van der A, R. J., H. J. Eskes, K. F. Boersma, T. P. C. Van Noije, M. Van Roozendaal, I. De Smedt, D. Peters, and E. W. Meijer (2008), Trends, seasonal variability and dominant NO_x source derived from a ten year record of NO₂ measured from space, *J. Geophys. Res.*, 113, D04302, doi:10.1029/2007jd009021.

van der Werf, G. R., J. T. Randerson, G. J. Collatz, L. Giglio, P. S. Kasibhatla, A. F. Arellano, S. C. Olsen, and E. S. Kasischke (2004), Continental-scale partitioning of fire emissions during the 1997 to 2001 El Niño/La Niña period, *Science*, 303, 73–76.

Van der Werf, G. R., J. T. Randerson, L. Giglio, G. J. Collatz, P. S. Kasibhatla, and A. F. Arellano Jr. (2006), Interannual variability in global biomass burning

emissions from 1997 to 2004, *Atmos. Chem. Phys.*, 6, 3423-3441, doi:10.5194/acp-6-3423-2006.

Van Dingenen R., F. J. Dentener, F. Raes, M. C. Krol, L. Emberson, J. Cofala (2009), The global impact of ozone on agricultural crop yields under current and future air quality legislation, *Atmos. Environ.* 43, 604-618.

Varshney, C. R., and M. Aggarawal (1992), Ozone pollution in the urban atmosphere of Delhi, *Atmos. Environ.*, 26B, 291-294.

Volz, A. and D. Kley (1988), Evaluation of the Montsouris series of ozone measurements made in the nineteenth century, *Nature*, 332, 240-242, doi:10.1038/332240a0.

Von Kuhlmann, R (2001), Photochemistry of Tropospheric Ozone, its Precursors and the Hydroxyl Radical: A 3D-Modeling Study Considering Non-Methane Hydrocarbons, *Ph.D. thesis, Johannes Gutenberg-Universität at Mainz, Mainz, Germany.*

Von Kuhlmann, R., M. G. Lawrence, P. J. Crutzen, and P. J. Rasch (2003), A model for studies of tropospheric ozone and nonmethane hydrocarbons: Model description and ozone results, *J. Geophys. Res.*, 108, 4294, doi:10.1029/2002JD002893.

Wang, W. C., J. P. Pinto, and Y. L. Yung (1980), Climatic effects due to halogenated compounds in the Earth's atmosphere, *J. Atmos. Sci.*, 37, 333-338.

- Wang, W. C., D. J. Wuebbles, W. M. Washington, R. G. Isaacs, G. Molnar (1986), Trace Gases and other potential perturbations to global climate, *Rev. of Geophysics*, *24*, 110-140.
- Wang, X., D. L. Mauzerall, (2004), Characterizing distributions of surface ozone and its impact on grain production in China, Japan and South Korea: 1990 and 2020, *Atmos. Environ.*, *38*, 4383-4402.
- Wang, Y., J. W. Munger, S. Xu, M. B. McElroy, J. Hao, C. P. Nielsen, and H. Ma (2010), CO₂ and its correlation with CO at a rural site near Beijing: implications for combustion efficiency in China, *Atmos. Chem. Phys.*, *10*, 8881-8897, doi:10.5194/acp-10-8881-2010.
- Wang, Y., P. Konopka, Y. Liu, H. Chen, R. Müller, F. Plöger, M. Riese, Z. Cai, and D. Lü (2012), Tropospheric ozone trend over Beijing from 2002–2010: ozonesonde measurements and modeling analysis, *Atmos. Chem. Phys.*, *12*, 8389-8399, doi:10.5194/acp-12-8389-2012.
- Wiedinmyer, C., S. K. Akagi, R. J. Yokelson, L. K. Emmons, J. A. Al-Saadi, J. J. Orlando, and A. J. Soja (2011), The Fire Inventory from NCAR (FINN): a high resolution global model to estimate the emissions from open burning, *Geosci. Model Dev.*, *4*, 625–641, doi: 10.5194/gmd-4-625-2011.
- Wild, O., M. J. Prather, H. Akimoto, J. K. Sundet, I. S. A. Isaksen, J. H. Crawford, D. D. Davis, M. A. Avery, Y. Kondo, G. W. Sachse, and S. T. Sandholm (2004), Chemical transport model ozone simulations for spring 2001 over the western Pacific: Regional ozone production and its global impacts. *J. Geophys. Res.* *109*: D15S02 1-14.

- Wild, O. (2007), Modelling the global tropospheric ozone budget: exploring the variability in current models, *Atmos. Chem. Phys.*, 7, 2643-2660, doi:10.5194/acp-7-2643-2007.
- Worden, H. M., et al. (2007), Comparisons of Tropospheric Emission Spectrometer (TES) ozone profiles to ozonesondes: Methods and initial results, *J. Geophys. Res.*, 112, D03309, doi:10.1029/2006JD007258.
- World Meteorological Organization (WMO) (1957), Meteorology A Three-Dimensional Science: Second Session of the Commission for Aerology, *WMO Bulletin IV(4)*, WMO, Geneva, 134– 138.
- World Meteorological Organization (WMO) (2003), Scientific Assessment of Ozone Depletion: 2002. Global Ozone Research and Monitoring Project Report No. 47, *World Meteorological Organization, Geneva*, 498 pp.
- World Meteorological Organization (WMO) (2012), WMO greenhouse gas bulletin, The state of greenhouse gases in the atmosphere based on global observations through 2011, no. 8, 19 November 2012.
- Wu, S., et al. (2007), Why are there large differences between models in global budgets of tropospheric ozone?, *J. Geophys. Res.*, 112, D05302, doi: 10.1029/2006JD007801.
- Xiao, Y., D. J. Jacob, J. S. Wang, J. A. Logan, P. I. Palmer, P. Suntharalingam, R. M. Yantosca, G. W. Sachse, D. R. Blake, and D. G. Streets (2004), Constraints on Asian and European sources of methane from CH₄-C₂H₆-CO correlations in Asian outflow, *J. Geophys. Res.*, 109, D15S16, doi:10.1029/2003JD004475.
- Yienger, J. J. and H. Levy (1995), Empirical model of global soil-biogenic NO_x emissions, *J. Geophys. Res.*, 100, 11 447–11 464.

- Zhang, G. J. and N. A. McFarlane (1995), Sensitivity of climate simulations to the parameterization of cumulus convection in the Canadian Climate Centre general circulation model, *Atmos. Ocean*, 33, 407–446.
- Zhang J. and S. T. Rao (1999), The role of vertical mixing in the temporal evolution of ground-level ozone concentrations, *J. Appl. Meteor.*, 38, 1674-1691.
- Zhang, L., D. J. Jacob, K. F. Boersma, D. A. Jaffe, J. R. Olson, K. W. Bowman, J. R. Worden, A. M. Thompson, M. A. Avery, R. C. Cohen, J. E. Dibb, F. M. Flock, H. E. Fuelberg, L. G. Huey, W. W. McMillan, H. B. Singh, and A. J. Weinheimer (2008), Transpacific transport of ozone pollution and the effect of recent Asian emission increases on air quality in North America: an integrated analysis using satellite, aircraft, ozonesonde, and surface observations, *Atmos. Chem. Phys.*, 8, 6117-6136, doi:10.5194/acp-8-6117-2008.
- Zhang, Q., D. G. Streets, G. R. Carmichael, K. B. He, H. Huo, A. Kannari, Z. Klimont, I. S. Park, S. Reddy, J. S. Fu, D. Chen, L. Duan, Y. Lei, L. T. Wang, and Z. L. Yao (2009), Asian emissions in 2006 for the NASA INTEX-B mission (2009), *Atmos. Chem. Phys.*, 9, 5131–5153, doi:10.5194/acp-9-5131-2009.